



Science

15 March 2013 | \$10

10 Years After **SARS**

More affordable BD Research Reagents

Lower pricing on over one thousand high-quality products.

Welcome to
affordable
a more colorful
world.SM

Lower pricing means you don't have to sacrifice quality.

Enjoy the best combination of product quality and value when you select BD Biosciences multicolor flow cytometry reagents.

For over 25 years BD PharmingenTM brand reagents have been developed and manufactured with strict controls and high standards to ensure high lot-to-lot consistency and performance on BD flow cytometers.

Our ever expanding portfolio is the most cited on the market and includes rare combinations of antibodies and fluorochromes that let you use BD reagents across your entire multicolor panel. Recent portfolio additions include the innovative



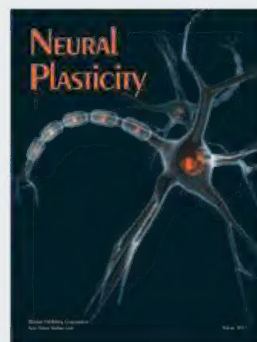
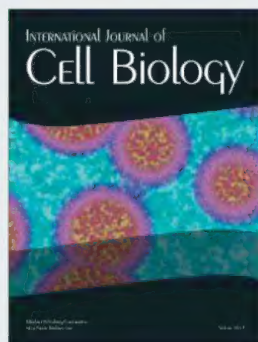
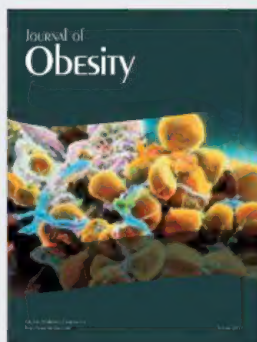
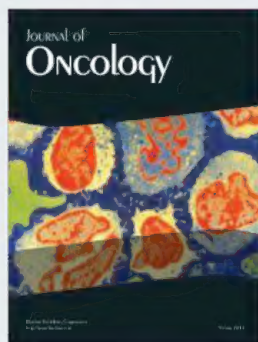
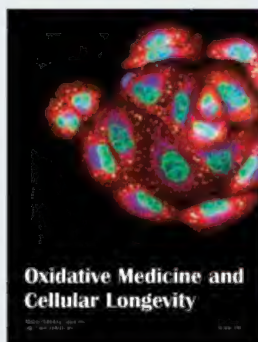
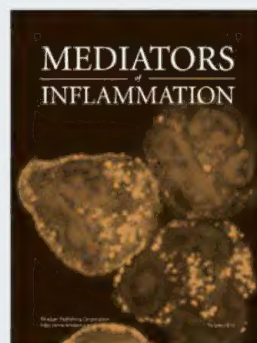
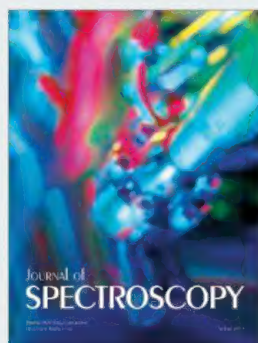
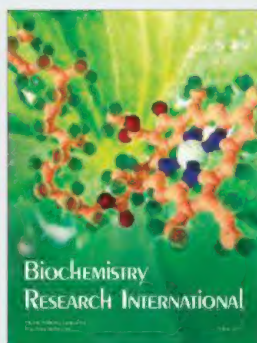
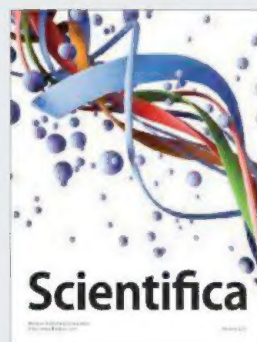
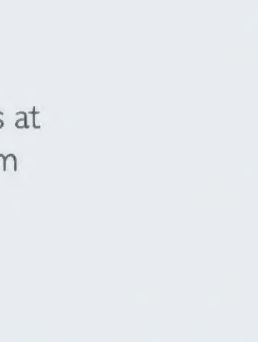
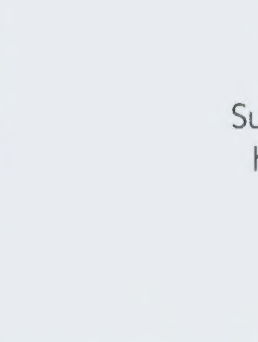
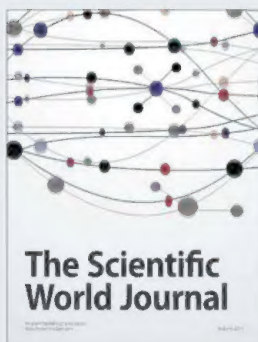
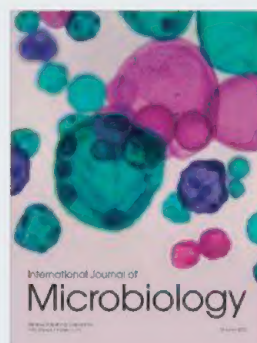
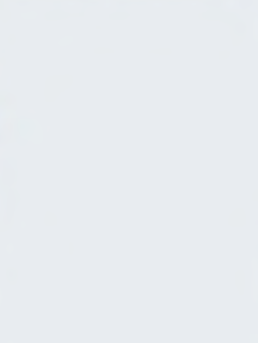
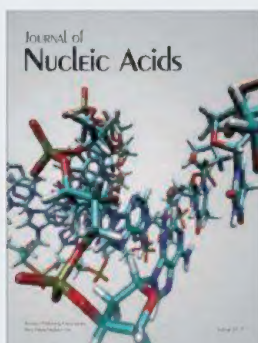
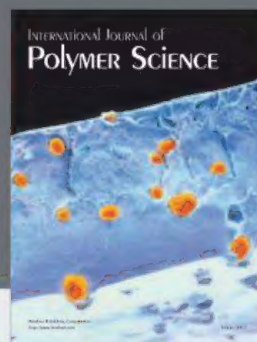
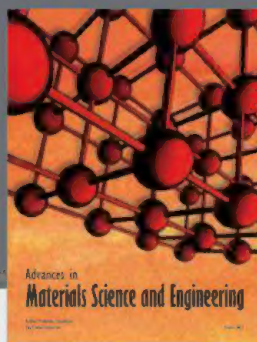
BD

Helping all people
live healthy lives

new BD HorizonTM Brilliant VioletTM dyes which are 5–10X brighter than conventional dyes to assist the resolution of rare or dim populations.

All BD Biosciences reagents are backed with expert technical support and a variety of tools and information to enable you get the most from your multicolor panels and help speed your research. Now, new pricing makes high quality and reliability more affordable.

You may also be eligible for a more attractive institutional discount—contact your BD Biosciences sales representative to find out more at bdbiosciences.com/reagents



Hindawi

Submit your manuscripts at
<http://www.hindawi.com>

For more information, visit
www.Q5PCR.com

Fidelity at its finest.

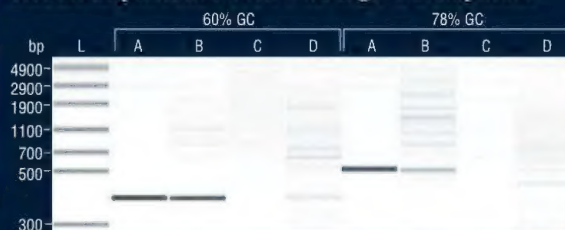
Q5[®] High-Fidelity DNA Polymerase

Q5 High-Fidelity DNA Polymerase sets a new standard for both fidelity and performance. With the highest fidelity amplification available (>100X higher than *Taq*), Q5 DNA Polymerase results in ultra-low error rates. Its unique buffer system provides superior performance for a broad range of amplicons, regardless of GC content. Available in master mix and hot start formulations, Q5 DNA Polymerase represents the finest in fidelity.

ALSO AVAILABLE: Optimized NEBNext[®] formulation for next generation sequencing library amplification

Mandarin Ducks (*Aix galericulata*) are frequently featured in Chinese art and are regarded as a symbol of fidelity.

Robust amplification even with high GC amplicons



Amplification of two human genomic amplicons of mid to high GC content. All reactions were conducted using 30 cycles of amplification and visualized by microfluidic LabChip[®] analysis. All polymerases were cycled according to manufacturer's recommendations. For the 78% GC amplicon, GC Buffers or enhancers were used when supplied with the polymerase.

A = Q5[®] High-Fidelity DNA Polymerase (NEB)
B = Phusion[®] High-Fidelity DNA Polymerase (NEB)
C = KOD DNA Polymerase (EMD)
D = PfuUltra[™] High-Fidelity DNA Polymerase (Agilent)

PHUSION[®] is a registered trademark and property of Thermo Fisher Scientific. Phusion[®] DNA Polymerase was developed by Finnzymes Oy, now a part of Thermo Fisher Scientific. PFUULTRA[™] is a trademark of Agilent Technologies, Inc. LABCHIP[®] is a registered trademark of Caliper Life Sciences, part of Perkin Elmer, Inc. NEBNext[®] and Q5[®] are registered trademarks of New England Biolabs, Inc.

EDITORIAL

- 1252 Am I Wrong?
Bruce Alberts

NEWS OF THE WEEK

- 1258 A roundup of the week's top stories

NEWS & ANALYSIS

- 1260 Gravity-Wave Observatory Debates Fake-Data Tests
- 1261 Dramatic Fossils Suggest Early Birds Were Biplanes
>> *Report p. 1309*
- 1262 Subset of CD4 Cells May Hold Key to Reaching HIV Cure
- 1263 Australian Researchers Rattled by Export Control Law

NEWS FOCUS

- 1264 War Stories
SARS: Chronology of the Epidemic
>> *Perspective p. 1287*
- 1269 Understanding the Enemy
The Metropole, Superspreaders, and Other Mysteries
>> *Science Podcast*

LETTERS

- 1274 Latin American Science: Much Work Remains
J. A. Huete-Pérez
Latin American Science: Sustainable Careers
C. G. Acevedo Rocha
University Rankings Could Bias Funding
P. De Souto Barreto
The Race to Name Earth's Species
W. F. Laurance
- 1275 CORRECTIONS AND CLARIFICATIONS

BOOKS ET AL.

- 1276 Harvesting the Biosphere
V. Smil, reviewed by S. W. Running
- 1277 Mind and Cosmos
T. Nagel, reviewed by K. Musholt

POLICY FORUM

- 1278 End the Deadlock on Governance of Geoengineering Research
E. A. Parson and D. W. Keith
>> *Science Podcast*

PERSPECTIVES

- 1280 Cracking the Mercury Methylation Code
A. J. Poulain and T. Barkay
>> *Report p. 1332*
- 1281 Creating Flexible Calcite Fibers with Proteins
I. Sethmann
>> *Report p. 1298*
- 1282 RNA That Gets RAN in Neurodegeneration
J. P. Taylor
>> *Report p. 1335*
- 1284 The Brain Activity Map
A. P. Alivisatos et al.
- 1285 How HIF-1 α Handles Stress
L. E. Huang
- 1286 Not All About Consumption
D. J. Davidson and J. Andrews
- 1287 The SARS Wake-Up Call
I. Nuttall and C. Dye
>> *News story p. 1264*

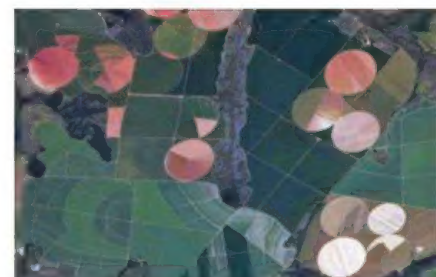
REVIEW

- 1289 Planar Photonics with Metasurfaces
A. V. Kildishev et al.
Review Summary; for full text:
<http://dx.doi.org/10.1126/science.1232009>

CONTENTS continued >>



pages 1261 & 1309



page 1276



COVER

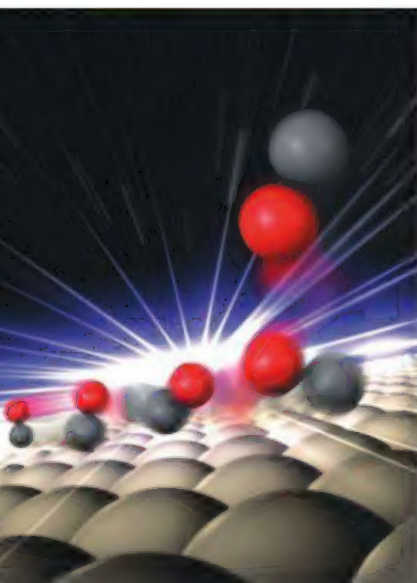
A woman in Beijing covers her face at the peak of the severe acute respiratory syndrome (SARS) outbreak in April 2003. Two News stories (pages 1264 and 1269) and a Perspective (page 1287) describe what happened when the world was confronted with this deadly new virus and ask whether we are better prepared today.

Photo: Guang Niu/Reuters/Newscom

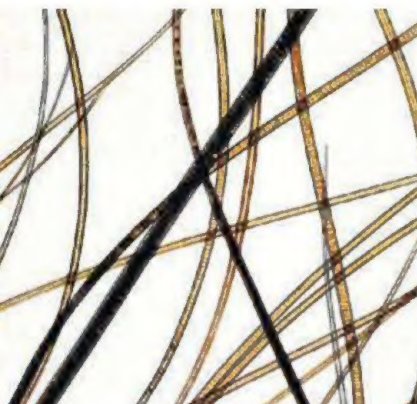
Explore our rich online offerings, including multimedia, news, *Science Careers*, and our two research journals—*Science Signaling* and *Science Translational Medicine*—at www.sciencemag.org

DEPARTMENTS

- 1251 This Week in *Science*
1253 Editors' Choice
1256 *Science Staff*
1339 New Products
1340 *Science Careers*



page 1302



page 1312

RESEARCH ARTICLE

- 1290 A Neural Circuit for Memory Specificity and Generalization**
W. Xu and T. C. Südhof
 Projections to and from the nucleus reunions in the thalamus regulate the specificity of contextual fear memory.

REPORTS

- 1295 Spin Torque–Generated Magnetic Droplet Solitons**
S. M. Mohseni et al.
 Transport measurements reveal a self-reinforcing traveling wave in a magnetic system.
- 1298 Flexible Minerals: Self-Assembled Calcite Spicules with Extreme Bending Strength**
F. Natalio et al.
 Spicules from aligned calcite nanocrystals and silicatein- α show enhanced bending strength linked to protein content.
 >> *Perspective p. 1281*
- 1302 Real-Time Observation of Surface Bond Breaking with an X-ray Laser**
M. Dell'Angela et al.
 Changes in x-ray absorption and emission features reveal a weakly interacting precursor state to the chemisorbed state.
- 1305 Evidence for Microbial Carbon and Sulfur Cycling in Deeply Buried Ridge Flank Basalt**
M. A. Lever et al.
 Active methane- and sulfur-cycling microbial communities exist in deep basaltic ocean crust.
- 1309 Hind Wings in Basal Birds and the Evolution of Leg Feathers**
X. Zheng et al.
 Fossils of basal birds have feathers on all four limbs, suggesting that the present two-winged condition is a derived state.
 >> *News story p. 1261*

- 1312 Adaptive Evolution of Multiple Traits Through Multiple Mutations at a Single Gene**
C. R. Linnen et al.
 The light color of mice living in the Nebraska Sand Hills is not the result of a single large-effect mutation.
- 1316 Circadian Control of Chloroplast Transcription by a Nuclear-Encoded Timing Signal**
Z. B. Noordally et al.
 In plants, day/night information is communicated from a nuclear-encoded circadian oscillator to the chloroplast.
- 1320 Quantitative Phosphoproteomics Reveal mTORC1 Activates de Novo Pyrimidine Synthesis**
A. M. Robitaille et al.
- 1323 Stimulation of de Novo Pyrimidine Synthesis by Growth Signaling Through mTOR and S6K1**
I. Ben-Sahra et al.
 In addition to its role in stimulating protein and lipid synthesis, the kinase mammalian target of rapamycin stimulates nucleotide biosynthesis.
- 1328 Proteomic Mapping of Mitochondria in Living Cells via Spatially Restricted Enzymatic Tagging**
H.-W. Rhee et al.
 A modern update of a classic peroxidase-based anatomical methodology opens a window into mitochondria in live cells.
- 1332 The Genetic Basis for Bacterial Mercury Methylation**
J. M. Parks et al.
 A two-gene cluster encodes proteins required for the production of the neurotoxin methylmercury in bacteria.
 >> *Perspective p. 1280*
- 1335 The C9orf72 GGGGCC Repeat Is Translated into Aggregating Dipeptide-Repeat Proteins in FTL/ALS**
K. Mori et al.
 A new class of proteins links a common genetic mutation to the predominant pathology in certain neurodegenerative diseases.
 >> *Perspective p. 1282*

SCIENCE (ISSN 0036-8075) is published weekly on Friday, except the last week in December, by the American Association for the Advancement of Science, 1200 New York Avenue, NW, Washington, DC 20005. Periodicals Mail postage (publication No. 484460) paid at Washington, DC, and additional mailing offices. Copyright © 2013 by the American Association for the Advancement of Science. The title SCIENCE is a registered trademark of the AAAS. Domestic individual membership and subscription (51 issues): \$149 (\$74 allocated to subscription). Domestic institutional subscription (51 issues): \$990; Foreign postage extra: Mexico, Caribbean (surface mail) \$55; other countries (air assist delivery) \$85. First class, airmail, student, and emeritus rates on request. Canadian rates with GST available upon request, GST #1254 88122. Publications Mail Agreement Number 1069624. Printed in the U.S.A.

Change of address: Allow 4 weeks, giving old and new addresses and 8-digit account number. Postmaster: Send change of address to AAAS, P.O. Box 96178, Washington, DC 20090-6178. Single-copy sales: \$10.00 current issue, \$15.00 back issue prepaid includes surface postage; bulk rates on request. Authorization to photocopy material for internal or personal use under circumstances not falling within the fair use provisions of the Copyright Act is granted by AAAS to libraries and other users registered with the Copyright Clearance Center (CCC) Transactional Reporting Service, provided that \$30.00 per article is paid directly to CCC, 222 Rosewood Drive, Danvers, MA 01923. The identification code for Science is 0036-8075. Science is indexed in the Reader's Guide to Periodical Literature and in several specialized indexes.



<< Four-Winged Birds?

Recently, nonavian dinosaurs with feathers on their fore- and hindlimbs have been described. **Zheng *et al.*** (p. 1309) describe eleven basal avialan fossils with clear evidence of feathered hindlimbs. Together these fossils show that early avialans possessed four wings, rather than two. A gradual reduction in hindlimb feathering eventually yielded the two-wing condition in today's birds. Such a transition may have accompanied a locomotory decoupling of the fore- and hindlimbs, which facilitated the development of the forelimbs into flight-capable wings.

A Move to Planar Optics

Metamaterials allow light to be manipulated in ways that cannot be done with naturally available materials. Subwavelength metallic nanoantenna arrays patterned onto a surface can provide the basis for planar optical devices, in which bulk optical elements that are typically thousands of wavelengths in size can be "flattened" into a two-dimensional sheet less than a wavelength thick. **Kildishev *et al.*** (p. 1289) review progress in the optics of metasurfaces and discuss promising applications for surface-confined planar photonics components.

Flexi-Fibers

Glass or metal fibers can show incredible flexibility. **Natalio *et al.*** (p. 1298; see the Perspective by **Sethmann**) used the protein silicatein- α , which is responsible for the biomineralization of silicates in sponges, to guide the formation of spicules made of calcite. These synthetic spicules could be bent to a high degree because of their inherent elasticity, whilst retaining the ability to guide light.

The Thalamus in Fear and Memory

The medial prefrontal cortex (mPFC) mediates the cognitive control of many high-level brain functions. However, it is unclear which synaptic projections from the mPFC to subcortical regions are critical for maintaining the proper balance between retention and generalization of fear

memory details. Using an array of behavioral, physiological, and anatomical techniques, **Xu and Südhof** (p. 1290) describe a neural circuit that controls memory generalization and specificity. This circuit involves the nucleus reunions (NR), a thalamic nucleus of largely unknown function. Optogenetic activation of NR neurons in awake behaving mice revealed the role of the NR in fear memory generalization.

Additive Effects

Although specific genes involved in animal coloration have been identified, the underlying selection for genetic variation in color-specific adaptation is not well understood. Examining the *Agouti* gene and other loci in the deer mice of Nebraska, where predation selects for light-colored mice in light environments and dark-colored mice in dark environments, **Linnen *et al.*** (p. 1312) find evidence of multiple genetic variants under selection affecting coloration. The light color of Sand Hills mice is not the result of a single large-effect mutation, but is because of many accumulated mutations, each with a smaller phenotypic effect.

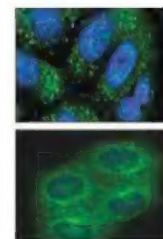
Magnetic Droplet

When a solitary wave travels atop the surface of a fluid, its shape generally changes with time, with some of its components traveling at velocities slightly different than others. In nonlinear media, this spreading effect may be countered by a slimming effect stemming from the non-

linearity, which generates an object with perfectly preserved shape, called a soliton. Solitons have been observed in fluids, granular media, and other systems. **Mohseni *et al.*** (p. 1295) detected a dissipative soliton (one that also balances gain and dissipation) in a magnetic system, in the form of a magnetic droplet consisting of a core of spins pointing opposite to the external magnetic field. The droplet exhibited peculiar dynamics and could be controlled by electric current.

Coordinating Metabolism

Growth factors help to coordinate metabolism with growth in part by stimulating the activity of the protein kinase mTORC1 (mechanistic target of rapamycin complex 1). **Ben-Sahra *et al.*** (p. 1323, published online 21 February) and **Robitaille *et al.*** (p. 1320, published online 21 February) independently identified a key target of mTORC1—carbamoyl-phosphate synthase 2, or CAD, the rate-limiting enzyme for de novo synthesis of pyrimidines. Metabolomic profiling and phosphoproteomic analyses of normal cells and cells lacking signaling by mTORC1 converged on CAD as a key point at which growth-promoting signals also ramp up production of nucleic acids.



Under the Sea Floor

Microorganisms living in basaltic sea floor buried beneath sediments derive energy from inorganic components from the host rocks that interact with infiltrating seawater, which brings dissolved oxygen and other trace nutrients with it. **Lever *et al.*** (p. 1305) directly sampled the subseafloor community off the eastern flank of the Juan de Fuca Ridge in the Pacific Ocean and found evidence for ongoing microbial sulfate reduction and methanogenesis. Multiyear incubation experiments with samples of host rock confirmed the microbial activities measured in situ.

Synchronizing Photosynthetic Capacity

Coordination of photosynthetic activity with sunlight benefits plant productivity. **Noordally *et al.*** (p. 1316) analyzed how the *Arabidopsis* circadian clock keeps the chloroplasts working in tune with the Sun. SIGMA FACTOR5 (SIG5) is encoded in the cell nucleus and reflects circadian cycles with changes in its own transcript abundance. SIG5 acts, however, in the chloroplast, where it supports photosystem II production.

Am I Wrong?

I HAVE SEVEN GRANDCHILDREN, AND I WORRY ABOUT THEIR FUTURE. THE NATION THAT I WAS RAISED in, the United States, has clearly lost its way at a time when the world badly needs wise leadership. Nations with a long-term view are making huge investments in their infrastructure—transportation, water, energy, waste, and recreation. And they have a laserlike focus on supporting science and engineering research with government resources. As examples, Germany, China, and South Korea come to mind. Meanwhile, the United States is living off its past. Not only do we face a crumbling infrastructure* but our federal investments in fundamental long-term R&D have been stagnant, dropping from 1.25% of the gross domestic product (GDP) in 1985 to 0.87% in 2013.† Now, on top of that comes a mindless budget “sequester” that will make the situation considerably worse, causing the U.S. National Science Foundation to announce last week that it may award 1000 fewer research grants in 2013 than it did in 2012.

Governments might justifiably be considered deranged when they fail to take actions today that will generate tremendous future benefits. Consider the fact that human lifespan is increasing, and, without a medical breakthrough, 1 in 5 of those who reach the age of 85 are projected to have Alzheimer's disease. Without research that reduces this terrible burden, the Alzheimer's Association estimates that the costs associated with this disease and other forms of dementia in the United States will increase fivefold by 2050, to \$1.1 trillion a year. Given that 70% of such costs are expected to be billed to Medicare and Medicaid,‡ the U.S. government is clearly being “penny wise and pound foolish” by cutting the fundamental research in physics, chemistry, mathematics, and biomedicine that can be expected, in some way that is completely unpredictable today, to prevent this terrible disease. And of course, no financial cost can begin to reflect the terrible toll of old-age dementia on human happiness.

I was fortunate to become a scientist at a time when the U.S. system of research was flourishing, thanks to visionary national leadership. It is no accident that the U.S. economy and global status subsequently flourished, or that the success was built in partnership with many of the best minds from other nations. The brilliance of U.S. science and engineering enabled its universities to attract a very large number of the most energetic and talented students from around the globe. A major fraction of these young scientists and engineers decided to remain here after their training, where they have made enormous contributions not only as academic leaders but also as leaders in industry and government. As one indicator, for both the U.S. National Academy of Sciences and National Academy of Engineering, 25% of members were born outside of the United States, even though they had to be U.S. citizens to be elected. It is hard to imagine a Silicon Valley, or any of the other U.S. centers of innovation, prospering without such talented immigrants.

Other nations have been increasing their research intensity at an impressive pace. With the latest cuts created by the shortsighted political gridlock in Washington, DC, are we headed to a future where the world's most talented young scientists and engineers no longer want to pursue careers in the United States? If so, in what nation will the next Silicon Valley be developed? The declining opportunities for research funding have made survival for some of the most able researchers resemble a lottery—or perhaps Russian roulette is a better analogy. The effect on the U.S. research system seems devastating. Am I wrong? To what extent do you think the current grant-funding environment is undermining the intellectual environment and creativity in your institution? Post comments at http://scim.ag/wrong_comments, and take the *Science* poll at http://scim.ag/wrong_poll.§

Online
sciencemag.org
Take the poll
(http://scim.ag/wrong_poll).

— Bruce Alberts

10.1126/science.1237434

*www.asce.org/reportcard. †www.aaas.org/spp/rd/guihist.shtml. ‡www.alz.org/alzheimers_disease_facts_and_figures.asp#expanding. §Polling results reflect only the votes of those who choose to participate.



Bruce Alberts is Editor-in-Chief of *Science*.





SIGNAL TRANSDUCTION

Transcription Takes a Back Seat

When a bacterial cell responds to environmental changes in carbon sources available as food, how would you say this occurs—through changes in gene expression directed by appropriate transcription factors, perhaps? Berthoumieux *et al.* show that this seemingly likely scenario actually accounted for little of the response of *Escherichia coli* to nutritional stress. Rather, it was the “physiological state of the cell” that coordinated the gene expression program. That is, it was not the binding of transcription factors to particular target genes that produced the changes in gene expression in the bacteria, but instead global changes in transcription and translation mediated by changes, for example, in the abundance of RNA polymerase, ribosomes, and the pools of available amino acids and nucleotides. Mathematical modeling used to measure the relative contributions of specific transcriptional control and global changes in physiological state showed the primary mechanism to be the latter, which ironically is almost never accounted for in diagrams of cellular regulatory networks. — LBR
Mol. Syst. Biol. **9**, 634 (2013).

SIGNAL TRANSDUCTION

See-Saw Gene Expression

Upon wounding, the body must act quickly to initiate a repair or regeneration response. Using a human-skin *ex vivo* organ-culture system, Sundaram *et al.* found that the small noncoding RNA miR-198, which is encoded in the 3' untranslated region of follistatin-like 1 (FSTL1), is expressed at high levels in healthy epidermis but is suppressed after wounding. FSTL1 showed the opposite pattern of expression. Knockdown studies demonstrated that FSTL1 promoted keratinocyte migration, which is important for wound healing, whereas miR-198 suppressed this. Examination of chronic nonhealing ulcer wounds from individuals with diabetes mellitus revealed that miR-198 rather than FSTL1 was expressed, which explains

ECOLOGY

Getting It Just Right

North American monarch butterflies are known for the massive southern migrations they undertake each year. During these migrations, a single butterfly may fly over 2500 miles south to the overwintering site, where it enters diapause, a hibernation-like state. This same butterfly will then fly northward in the spring, where it will become reproductive before dying and leaving the remainder of the return trip to its offspring. Monarchs coordinate their southward flight on the basis of a Sun compass mediated through circadian clocks located in the antennae. Guerra and Reppert now show that northbound flight is mediated by the same Sun compass mechanism. This finding begs the question, however, of how individuals are able to “switch” their compasses to fly south in the fall and north in the spring. Exposure of fall remigrants to variations of the day length and temperature conditions encountered at overwintering sites revealed that although day length has no effect on flight direction, temperature was able to facilitate the directional switch. Specifically, butterflies exposed to temperatures that were too warm did not switch their flight directions, whereas those exposed to appropriately cold temperatures flew north as expected. Thus, cold temperatures during overwintering are necessary for the completion of the enigmatic migration. Furthermore, warmer winters at these sites, due to climate change, may interfere with the monarch's migration home. — SNV

Curr. Biol. **10.1016/j.cub.2013.01.052** (2013).

the lack of keratinocyte migration and tissue repair seen in these lesions. A posttranscriptional regulatory mechanism allows for this “see-saw” pattern of expression: Transforming growth factor-1 helped to stabilize FSTL1 by down-regulating the splicing regulatory protein KSRP, which is necessary for miR-198 expression. — BAP
Nature **10.1038/nature11890** (2013).

MATERIALS SCIENCE

Welded Together

Welding depends on a strong bond forming between two pieces that have been heated to the point where they partially melt at the area that is being fused together. In joining two polymer pieces together, it was thought that the welded area would attain the same strength as the bulk material when the polymer chains had diffused by a distance close to their radius of gyration, but experimentally, bulk strength has been obtained in much shorter times. Ge *et al.* use molecular dynamics simulations to probe the weld region between two homopolymer segments in order to determine the correlation between individual chain motion and the shear strength of the welded pieces. At short weld times, the

dominant failure mode is caused by the pullout of individual chains at the interface. Then there is a transition, once the interface chains are sufficiently embedded and entangled into the opposite region, where chain pullout decreases and bond breaking occurs. At first, this chain scission occurs primarily at the interface region, but then evolves so that bonds break uniformly across the specimen, showing that the welded region has achieved the bulk strength. This corresponds to when the areal density of entanglements matches the bulk value, and confirms that this is the key parameter to determining the time needed to achieve a strong weld. — MS�

Phys. Rev. Lett. **110**, 098301 (2013).

BIOMEDICINE

RAS Helping RAS

Solid tumors contain not only malignant cells but also a wide array of host-derived cells that can have dramatic effects on tumor behavior. These include macrophages, immune cells that enhance tumor progression in part by promoting inflammation and whose presence in tumors

Continued on page 1255

Stem Cell Lawsuit Finally Over. Russian Team Retrieves First Sample from Lake Vostok. Surprise Choices Mark New Leadership on U.S. House Science Panel. India Unveils Ambitious Science Policy.



Now, more than ever, developments in the lab are directly connected to decisions made in the halls of government.

*Science*Insider, the policy blog from the journal *Science*, is your source for news from the intersection of science and policy. From budget debates in the United States Congress, to climate change agreements at the United Nations, *Science*Insider covers the issues that have an impact on your work, your field, and your world.

Keep up to date and keep informed. Go inside the issues at www.ScienceInsider.org



ScienceInsider

Breaking news and analysis from the world of science policy



Continued from page 1253

correlates with reduced patient survival times. Macrophages must be continually replenished as the tumor grows, but little is known about this replenishment process.

Studying mice bearing lung cancers produced by activation of the RAS oncogene, Cortez-Retamozo *et al.* found that tumor-associated macrophages are supplied by the spleen, through amplification of hematopoietic stem cells and macrophage progenitor cells. This cell amplification process was stimulated by angiotensin II, a peptide hormone better known for its role in the renin-angiotensin system (RAS), which regulates blood pressure. Notably, mice treated with the blood pressure medication enalapril, which inhibits angiotensin II production, had fewer tumor-associated macrophages and fewer lung tumor nodules than control mice. Whether these results can be extrapolated to human lung cancer remains to be determined. — PAK

Immunity **38**, 296 (2013).

GEOCHEMISTRY

Mercury Gas in Neptune Grass

Not far off the coast of the Mediterranean Sea, meadows of the flowering seagrass *Posidonia oceanica*, or Neptune grass, cover the seafloor. The vast network of ancient mat deposits in the sediments in and below the root layer preserve a rich record of the water chemistry over thousands of years. Serrano *et al.* show that a Neptune grass mat deposit in a bay off the northeast coast of the Iberian Peninsula—a region with a complex

legacy of mercury (Hg) mining activities—preserves a ~2500-year record of anthropogenic Hg pollution. In coastal zones, Hg present in runoff from local rivers is added

to the water column in addition to the more common dissolved gaseous Hg that was originated in remote regions and was deposited from the atmosphere. Variable mat Hg concentrations,

which reflect uptake and bioaccumulation into plant tissues during growth, correspond to known mining and metalworking activities in European history, including Roman mining, metallurgy in the Late Middle

Ages, and modern industrial practices. Moreover, Hg concentrations decreased or leveled off after periods when drastic economic changes halted mining activities, such as the fall of the Roman Empire and the spread of the plague across Europe in the 14th century. — NW

Global Biogeochem. Cycles **27**, 10.1029/2012GB004296 (2013).

PHYSICS

Following a Single Imperfection

Quantum simulation aims to explain the behavior of a complicated physical system by using a more ordered and controllable equivalent. Over the past decade, such quantum simulators have been realized in quantum gases loaded in optical lattices, which simulate crystal structures in real materials and are formed by counterpropagating laser beams. Quantum magnetism, which is thought to play a major role in high-temperature superconductors and spin liquids, is a prime goal for such efforts. Fukuhara *et al.* observed the dynamics of a single spin impurity in a linear chain of ~10 atoms with magnetic interactions as the regime was varied from deep confinement to a delocalized superfluid state. The impurity was created with exquisite control by flipping the direction of the middle spin in the chain, whereas the other spins remained in the initial uniform state; the propagation of the impurity was tracked by imaging individual sites. The results agreed well with numerics and showed evidence of collective polaronic behavior in the superfluid limit. — JS

Nat. Phys. 10.1038/nphys2561 (2013).

AAAS Travels

MADAGASCAR

Explore the Unique Heritage of this Enchanting Land!
August 3-18, 2013

Explore the natural heritage and unique wildlife of Madagascar with 95% of the lemurs and reptiles, and 98% of the palms that are simply found nowhere else. Look for indri, ring-tailed lemurs, sifakas, and more! \$3,995 + air.

For a detailed brochure, please call (800) 252-4910

All prices are per person twin share + air



BETCHART EXPEDITIONS Inc.

17050 Montebello Rd, Cupertino, CA 95014

Email: AAASInfo@betchartexpeditions.com

www.betchartexpeditions.com



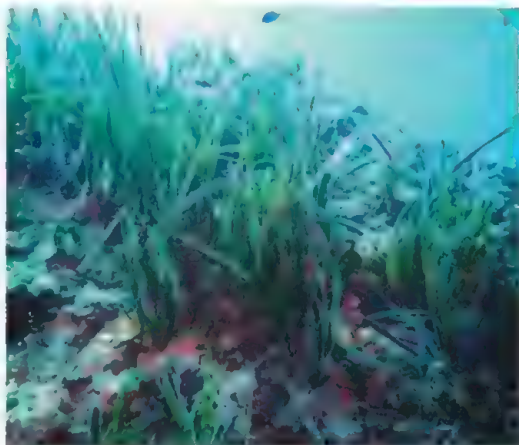
Join the Conversation!

Twitter is a great way to connect with AAAS members and staff about the issues that matter to you most. Be a part of the discussion while staying up-to-date on the latest news and information about your personal member benefits.

Follow us @AAASmember
and join the conversation
with #AAAS

AAAS
MEMBERCENTRAL

MemberCentral.aaas.org



1200 New York Avenue, NW
Washington, DC 20005

Editorial: 202 326-6550, FAX 202 289 7562
News: 202-326-6591, FAX 202-371-9227

Bateman House, 82-88 Hills Road

Cambridge, UK CB2 1LQ

+44 (0) 1223 326500, FAX +44 (0) 1223 326501

SUBSCRIPTION SERVICES For change of address, missing issues, new orders and renewals, and payment questions: 866-434-AAAS (2227) or 202-326-6417, FAX 202-482-1065. Mailing addresses: AAAS, P.O. Box 96178, Washington, DC 20090-6178 or AAAS Member Services, 1200 New York Avenue, NW, Washington, DC 20005

INSTITUTIONAL SITE LICENSES please call 202 326-6755 for any questions or information

REPRINTS: Author Inquiries 800-635-7181

Commercial Inquiries 803-359-4578

PERMISSIONS 202-326-7074, FAX 202-682-0816

MEMBER BENEFITS AAAS Travels: Betchart Expeditions 800-252-4910; Apple Store www.store.apple.com/us/go/epstore/aaas; NASA Federal, 1-888-NASA-FCU (1-888-627-2328) or www.nasa.fcui.com; Cold Spring Harbor Laboratory Press Publications www.cshlpress.com/affiliates/aaas.htm; GEICO Auto Insurance www.geico.com/landingpage/go51.htm?logo=17624; Hertz 800-654-2200 CDP#343457; Office Depot https://bsd.officedepot.com/portalLogin.do; Seabury & Smith Life Insurance 800-424-9883; Subaru VIP Program 202-326-6417; VIP Moving Services www.vipmayflower.com/domestic/index.html; Other Benefits: AAAS Member Services 202-326-6417 or www.aaasmember.org.

science_editors@aaas.org (for general editorial queries)

science_letters@aaas.org (for queries about letters)

science_reviews@aaas.org (for returning manuscript reviews)

science_bookrevs@aaas.org (for book review queries)

Published by the American Association for the Advancement of Science (AAAS), *Science* serves its readers as a forum for the presentation and discussion of important issues related to the advancement of science, including the presentation of minority or conflicting points of view, rather than by publishing only material on which a consensus has been reached. Accordingly, all articles published in *Science*—including editorials, news and comment, and book reviews—are signed and reflect the individual views of the authors and not official points of view adopted by AAAS or the institutions with which the authors are affiliated.

AAAS was founded in 1848 and incorporated in 1874. Its mission is to advance science, engineering, and innovation throughout the world for the benefit of all people. The goals of the association are to: enhance communication among scientists, engineers, and the public; promote and defend the integrity of science and its use; strengthen support for the science and technology enterprise; provide a voice for science on societal issues; promote the responsible use of science in public policy; strengthen and diversify the science and technology workforce; foster education in science and technology for everyone; increase public engagement with science and technology; and advance international cooperation in science.

INFORMATION FOR AUTHORS

See pages 716 and 717 of the 8 February 2013 issue or access www.sciencemag.org/about/authors

SENIOR EDITORIAL BOARD

A. Paul Alivisatos, Lawrence Berkeley Nat'l. Laboratory
Cori Bargmann, The Rockefeller Univ.
Ernst Fehr, Univ. of Zurich
Erin O'Shea, Harvard Univ.
Michael S. Turner, University of Chicago

BOARD OF REVIEWING EDITORS

Adriano Aguzzi, Univ. Hospital Zürich
Takuzo Aida, Univ. of Tokyo
Leslie Aiello, Wenner-Gren Foundation
Sonia Altshuler, Univ. of Georgia
Sant'Anna Amigorena, Institut Curie
Angelika Amon, MIT
Kathryn Anderson, Memorial Sloan-Kettering Cancer Center
Siv G. E. Andersson, Uppsala Univ.
Peter Andolfatto, Princeton Univ.
Meinrat O. Andreae, Max Planck Inst., Mainz
Paola Arlotta, Harvard Univ.
Johan Auwerx, EPFL
David Awschalom, Univ. of California Santa Barbara
Ben Barres, Stanford Medical School
Jordi Bascompte, Estación Biológica de Doñana, CSIC
Facundo Batista, London Research Inst.
Ray H. Baughman, Univ. of Texas, Dallas
David Baum, Univ. of Wisconsin
Mark Bear, Massachusetts Inst. of Technology
Yasmine Belkaid, NIAID, NIH
Philip Benfey, Duke Univ.
Stephen J. Benkovic, Penn State Univ.
Christophe Bernard, Aix-Marseille Univ.
Gregory C. Berzins, Stanford Univ.
Gabriele Bergers, Univ. of California, San Francisco
Peer Bork, EMBL
Bernard Bourdon, Ecole Normale Supérieure de Lyon
Chris Bowler, Ecole Normale Supérieure
Ian Boyd, Univ. of St. Andrews
Christian Büchel, Universitätsklinikum Hamburg-Eppendorf
Joseph A. Burns, Cornell Univ.
William P. Butz, Population Reference Bureau
Gyorgy Buzsáki, New York Univ., School of Medicine
Mats Carlsson, Univ. of Oslo
Mildred Cho, Stanford Univ.
David Clapham, Children's Hospital, Boston
David Clary, Univ. of Oxford
Jonathan D. Cohen, Princeton Univ.
Robert Cook-Deegan, Duke Univ.
James Collins, Boston Univ.
Alan Cowman, Walter & Eliza Hall Inst.
Robert H. Crabtree, Yale Univ.
Wolfgang Cramer, Mediterranean Inst. of Biodiversity and Ecology
Jeff L. Dangl, Univ. of North Carolina

Tom Daniel, Univ. of Washington
Frans de Waal, Emory Univ.
Stanislas Dehaene, Collège de France
Robert Desimone, MIT
Claude Desplan, New York Univ.
Ap Dijksterhuis, Radboud Univ. of Nijmegen
Dennis Discher, Univ. of Pennsylvania
Gerald W. Dorn II, Washington Univ. School of Medicine
Jennifer A. Doudna, Univ. of California, Berkeley
Julian Downward, Cancer Research UK
Bruce Dunn, Univ. of California, Los Angeles
Christopher Dye, WHO
David Ehrhardt, Carnegie Inst. of Washington
Tim Eiston, Univ. of North Carolina at Chapel Hill
Gerhard Ertl, Fritz-Haber-Institut, Berlin
Barry Everitt, Univ. of Cambridge
Paul G. Falkowski, Rutgers Univ.
Ernst Fehr, Univ. of Zurich
Tom Fenchel, Univ. of Copenhagen
Michael Feuer, The George Washington Univ.
Alain Fischer, INSERM
Susan Fiske, Princeton Univ.
Anne C. Ferguson-Smith, Univ. of Cambridge
Peter Fratzl, Max Planck Inst.
Elaine Fuchs, Rockefeller Univ.
Wulfraim Gerstner, EPFL Lausanne
Andrew Gewirth, Univ. of Illinois
Karl-Heinz Glassmeier, TU Braunschweig
Elizabeth Grove, Univ. of Chicago
David Hale, Univ. of Cambridge
Taekjip Ha, Univ. of Illinois at Urbana-Champaign
Christian Haass, Ludwig Maximilians Univ.
Steven Hahn, Fred Hutchinson Cancer Research Center
Gregory J. Hannon, Cold Spring Harbor Lab.
Martin Heilmann, Max Planck Inst., Jena
Yka Helariutta, Univ. of Finland
Isaac Held, NOAA
James A. Hendler, Rensselaer Polytechnic Inst.
Janet G. Heuser, Swiss Fed. Inst. of Aquatic Science & Technology
Ray Hilborn, Univ. of Washington
Michael E. Himmel, National Renewable Energy Lab.
Kai-Uwe Hinrichs, Univ. of Bremen
Kei Hirose, Tokyo Inst. of Technology
David Holtzman, Univ. of Cambridge
David Holden, Imperial College
Lora Hooper, UT Southwestern Medical Ctr at Dallas
Jeffrey A. Hubbell, EPFL Lausanne
Thomas Hudson, Ontario Inst. for Cancer Research
Ray Huey, Univ. of Washington
Steven Jacobsen, Univ. of California, Los Angeles
Kai Johnson, EPFL Lausanne
Peter Jonas, Universität Freiburg
Matt Kaeblerlein, Univ. of Washington

William Kaelin Jr., Dana-Farber Cancer Inst.
Daniel Kahne, Harvard Univ.
Daniel Kammen, Univ. of California, Berkeley
Joel Kingsolver, Univ. of North Carolina at Chapel Hill
Robert Kingston, Harvard Medical School
Roberto Kolter, Harvard Medical School
Alberto R. Kornblitt, Univ. of Buenos Aires
Leonid Kruglyak, Princeton Univ.
Thomas L. Lander, Harvard Univ.
Mitchell A. Lazar, Univ. of Pennsylvania
David Lazer, Harvard Univ.
Virginia Lee, Univ. of Pennsylvania
Ottoline Leyser, Cambridge Univ.
Marcia C. Lian, Univ. of California, Berkeley
Jianqiao Liu, Michigan State Univ.
Luis Liz-Marzan, CIC bioGUNE
Jonathan Losos, Harvard Univ.
Ke Lu, Chinese Acad. of Sciences
Christian Lüscher, Univ. of Geneva
Laura Mackey, CRUK Beatson Inst. for Cancer Research
Anne Magurran, Univ. of St. Andrews
Oscar Marin, CSIC & Univ. Miguel Hernández
Charles Marshall, Univ. of California, Berkeley
Chris Marshall, Inst. of Cancer Research
Martin M. Matzuk, Baylor College of Medicine
C. Robertson McClung, Dartmouth College
Graham Medley, Univ. of Warwick
Yasushi Miyashita, Univ. of Tokyo
Richard Morris, Univ. of Edinburgh
Edward Moseley, Norwegian Univ. of Science and Technology
Sean Munro, MRC Lab. of Molecular Biology
Thomas Murray, The Hastings Center
Naoto Nagao, Univ. of Tokyo
James Nelson, Stanford Univ. School of Med.
Daniel Neuman, Univ. of California, Berkeley
Stuart Newman, New York Medical College
Timothy W. Nilsen, Case Western Reserve Univ.
Pär Nordlund, Karolinska Inst.
Helga Nowotny, European Research Advisory Board
Luke O'Neill, Trinity College, Dublin
Stuart Newman, New York Medical College
N. Phuan Ong, Princeton Univ.
Joe Orenstein, Univ. of California, Berkeley & Lawrence Berkeley National Lab
Harry Orr, Univ. of Minnesota
Andrew Oswald, Univ. of Warwick
Steve Palumbi, Stanford Univ.
Jane Parker, Max-Planck Inst. of Plant Breeding Research
Donald R. Paul, Univ. of Texas at Austin
P. David Pearson, Univ. of California, Berkeley
John H. J. Petrini, Memorial Sloan-Kettering Cancer Center
Simon Philpott, Univ. of Florida
Joshua Plotkin, Univ. of Pennsylvania
Philippa Poulin, CNRS

Colin Renfrew, Univ. of Cambridge
Trevor Robbins, Univ. of Cambridge
Tim Roberts, Fred Hutchinson Cancer Research Ctr.
Barbara A. Romanowicz, Univ. of California, Berkeley
Jens Rostrup-Nielsen, Haldor Topsøe
Mike Ryan, Univ. of Texas, Austin
Shimon Sakaguchi, Kyoto Univ.
Miquel Salmeron, Lawrence Berkeley National Lab
Jürgen Sandkühner, Medical Univ. of Vienna
Alexander Schier, Harvard Univ.
Randy Seeley, Univ. of Cincinnati
Vladimir Shalaev, Purdue Univ.
Joseph Silk, Institut d'Astrophysique de Paris
Denis Simon, Arizona State Univ.
Alison Smith, John Innes Centre
Davor Solter, Inst. of Medical Biology, Singapore
Peter Sorger, Harvard Medical School
John Speakman, Univ. of Aberdeen
Allan C. Spradling, Carnegie Institution of Washington
Jonathan Sprent, Garvan Inst. of Medical Research
Paula Stephan, Georgia State Univ. and National Bureau of Economic Research
Elisabeth Stern, ETH Zürich
V. S. Subrahmanian, Univ. of Maryland
Ira Tabas, Columbia Univ.
Yoshiko Takahashi, Kyoto University
Sarah Teichmann, Cambridge Univ.
John Thomas, Duke Univ.
Herbert Virgin, Washington Univ.
Bert Vogelstein, Johns Hopkins Univ.
Cynthia Volkert, Univ. of Göttingen
Bruce D. Walker, Harvard Medical School
Douglas Wallace, Dalhousie Univ.
Ian Walsley, Univ. of Oxford
David A. Wardle, Swedish Univ. of Agric Sciences
David Waxman, Fudan Univ.
Jonathan Weissman, Univ. of California, San Francisco
Kathy Willis, Oxford Univ.
Ian A. Wilson, The Scripps Res. Inst.
Timothy D. Wilson, Univ. of Virginia
Rosemary Wyse, Johns Hopkins Univ.
Jan Zaenen, Leiden Univ.
Kenneth Zaret, Univ. of Penn. School of Medicine
Jonathan Zehr, Univ. of California, Santa Cruz
Maria Zuber, MIT

BOOK REVIEW BOARD

John Aldrich, Duke Univ.
David Bloom, Harvard Univ.
Angela Creager, Princeton Univ.
Richard Shweder, Univ. of Chicago
Ed Wasserman, DuPont
Lewis Wolpert, Univ. College London

EXECUTIVE EDITOR
Monica M. Bradford

MANAGING EDITOR, RESEARCH JOURNALS Katrina L. Kelnar

DEPUTY EDITORS Barbara R. Jasny, Andrew M. Sugden, Valda J. Vinson

EDITORIAL SENIOR EDITORS/COMMENTARY Lisa D. Chong, Brad Wible; SENIOR EDITORS Gilbert J. Chin, Pamela J. Hines, Paula A. Kiberstis (Boston), Marc S. Lavine (Toronto), Beverly A. Purnell, L. Bryan Ray, Guy Riddihough, H. Jesse Smith, Philip D. Szurovi (Tennessee), Jake S. Veston, Laura M. Zahn (San Diego); ASSOCIATE EDITORS Melissa R. McCartney (Education Projects), Kristen L. Mueller, Jelena Stajic, Sacha Vignier (Oregon), Nicholas S. Wigginton (Michigan); BOOK REVIEW EDITOR Sherman J. Suter; ASSOCIATE LETTERS EDITOR Jennifer Sills; EDITORIAL MANAGER Cara Tate; SENIOR COPY EDITORS Jeffrey E. Cook, Cynthia Howe, Harry Jach, Lauren Kneer, Barbara P. Ordway, Trista Waggoner; COPY EDITOR Chris Filatreat; SENIOR EDITORIAL COORDINATORS Carolyn Kyle, Beverly Shields; EDITORIAL COORDINATORS Joi S. Granger, Anita Wynn; PUBLICATIONS ASSISTANTS Ramatoulaye Diop, Aneera Dobbins, Jeffrey Hearn, Lisa Johnson, Dona Mathieu, Le-Toya Mayne Flood, Shannon McMahon, Scott Miller, Jerry Richardson, Teresa R. Sakon, Brian White; EDITORIAL ASSISTANT Patricia M. Moore; EXECUTIVE EDITORIAL ASSISTANT Yolanda O'Bannon (San Francisco); EXECUTIVE ASSISTANT Alison Crawford; ADMINISTRATIVE SUPPORT Maryrose Madrid

EDITORIAL DIRECTOR, WEB AND NEW MEDIA Stewart Willis; SENIOR WEB EDITOR Sarah Crespi; WEB EDITOR Kerry Klein; WEB DEVELOPMENT MANAGER Martyn Green; WEB DEVELOPER Cornelia Cohn
NEWS DEPUTY NEWS EDITORS Robert Coontz, Elizabeth Culotta, David Grimm (Online), Eliot Marshall, Jeffrey Mervis, Leslie Roberts, Richard Stone, John Travis; CONTRIBUTING EDITOR Polly Shulman; NEWS WRITERS Yudhijit Bhattacharjee, Adrian Cho, Jennifer Couzin-Frankel, Carolyn Gramling, Jocelyn Kaiser, Richard A. Kerr, David Malachukoff, Elizabeth Pennisi, Robert F. Service (Pacific NW), Erik Stokstad, Emily Underwood; WEB DEVELOPER Daniel Berger; SOCIAL MEDIA STRATEGIST Meghna Sachdev; INTERN Lizzie Wade; CONTRIBUTING CORRESPONDENTS John Bohannon, John Cohen (San Diego, CA), Ann Gibbons, Sam Kean, Eli Kintisch, Andrew Lawler, Mitch Leslie, Charles C. Mann, Virginia Morell, Gary Taubes; COPY EDITORS Melissa Ramondini, Kara Estelle; ADMINISTRATIVE SUPPORT Scherraine Mack; BUREAU: San Diego, CA: 760-942-3252, FAX 760-942-4979; Pacific Northwest: 503-963-1940

PRODUCTION DIRECTOR Wendy K. Shank; ASSISTANT MANAGER Rebecca Doshi; SENIOR SPECIALISTS Steve Forrester, Christopher Redwood, Anthony Rosen; PREFLIGHT DIRECTOR David M. Tompkins; MANAGER Marcus Spiegel; SPECIALISTS Jason Hillman, Tara Kelly
ART DIRECTOR Yael Fitzpatrick; ASSOCIATE ART DIRECTOR Laura Creveling; SENIOR ILLUSTRATORS Chris Bickel, Katharine Stultiff; ILLUSTRATOR Yana Hammond; SENIOR ART ASSOCIATES Holly Bishop, Preston Huey; ART ASSOCIATES Kay Engman, Garvin Grullion, Chrystal Smith; PHOTO EDITOR Leslie Blizard

SCIENCE INTERNATIONAL

EUROPE (science@science-int.co.uk) EDITORIAL: INTERNATIONAL MANAGING EDITOR Andrew M. Sugden; SENIOR EDITOR/COMMENTARY Julia Fahrenkamp-Uppenbrink; SENIOR EDITORS Caroline Ash, Stella M. Hurlley, Ian S. Osborne, Peter Stern; ASSOCIATE EDITOR Maria Cruz; CONTRIBUTING EDITOR Helen Pickersgill; EDITORIAL SUPPORT Rachel Roberts, Alice Whaley; ADMINISTRATIVE SUPPORT Janet Clements, Michelle Pegrum; NEWS DEPUTY NEWS EDITOR, U.K. Daniel Clerly; CONTRIBUTING EDITOR, EUROPE Martin Enserink; CONTRIBUTING CORRESPONDENTS Michael Balter (Paris), Kai Kupferschmidt (Berlin), Gretchen Vogel (Berlin)

ASIA Japan Office: Asca Corporation, Tomoko Furusawa, Rustic Bldg. 7F, 77 Tenjin-cho, Shinjuku-ku, Tokyo 162-0808, Japan; +81 3 6802 4616, FAX +81 3 6802 4615, inquiry@sciencemag.jp; CONTRIBUTING EDITOR, ASIA Mara Hvistendahl [China: mhvisten@aaas.org]; CONTRIBUTING CORRESPONDENTS Dennis Normile [Japan: +81 (0) 3 3391 0630, FAX +81 (0) 3 5936 3531; dnormile@gol.com]; Hao Xin [China: cindyhao@gmail.com]; Pallava Bagla [South Asia: +91 (0) 11 2271 2896; pbagla@vsnl.com]

EXECUTIVE PUBLISHER Alan I. Leshner
PUBLISHER Beth Rosner

FULFILLMENT SYSTEMS AND OPERATIONS (membership@aaas.org); CUSTOMER SERVICE SUPERVISOR Pat Butler; SPECIALISTS LaToya Casteel, Michelle Ofordire, April Marshall; MANAGER, DATA ENTRY Mickie Napoleoni; DATA ENTRY SPECIALISTS JJ Regan, Jaimee Wise, Fiona Giblin

BUSINESS OPERATIONS AND ADMINISTRATION DIRECTOR Deborah Rivera-Wienhold; BUSINESS SYSTEMS AND FINANCIAL ANALYSIS DIRECTOR Randy Yi; SYSTEMS ANALYST Nicole Mehmedovich; MANAGER, BUSINESS ANALYSIS Eric Knott; MANAGER, BUSINESS OPERATIONS Jessica Tierney; BUSINESS ANALYSTS Cory Lipman, Celeste Troxler; FINANCIAL ANALYST Jeremy Clay; RIGHTS AND PERMISSIONS: ADMINISTRATOR Emilie David; ASSOCIATE Elizabeth Sandler; MARKETING DIRECTOR Ian King; MARKETING MANAGERS Alison Chandler, Julianne Wielga, Justin Sawyers; MARKETING ASSOCIATES Mary Ellen Crowley, Elizabeth Sattler, Rebecca Riffkin; SENIOR MARKETING EXECUTIVE Jennifer Reeves; DIRECTOR, SITE LICENSING Tom Ryan; DIRECTOR, CORPORATE RELATIONS Eileen Bernadette Moran; SENIOR PUBLISHER RELATIONS SPECIALIST Kiki Forsythe; PUBLISHER RELATIONS MANAGER Catherine Holland; PUBLISHER RELATIONS, EASTERN REGION Keith Layson; PUBLISHER RELATIONS, WESTERN REGION Ryan Keroth; CUSTOMER RELATIONS MANAGER Iquo Edim; CUSTOMER RELATIONS ANALYSTS Simon Chong, Lana Guz; MARKETING MANAGER Christina Schlecht; MARKETING ASSOCIATES Paulina Curto, Mitchell Edmund; ELECTRONIC MEDIA DIRECTOR Lizbeth Hamann; ASSISTANT MANAGER Lisa Stanford; PRODUCTION SPECIALISTS Antoinette Hodal, Nichole Johnston, Lori Murphy, Kimberly Oster; WEB AND NEW MEDIA: SENIOR PROJECT MANAGER Trista Smith, PROJECT LEADER Luke Johnson COMPUTER SPECIALISTS Walter Jones, Kai Zhang, WEB DEVELOPER Chris Coleman; PROGRAM DIRECTOR, AAAS MEMBER CENTRAL Peggy Mhlich

DIRECTOR, GLOBAL COLLABORATION, CUSTOM PUBLICATIONS, ADVERTISING Bill Moran
EDITOR, CUSTOM PUBLISHING Sean Sanders: 202-326-6430

ASSISTANT EDITOR, CUSTOM PUBLISHING Tianna Hicklin 202-326-6463

ASSOCIATE DIRECTOR, COLLABORATION, CUSTOM PUBLICATIONS/CHINA/TAIWAN/KOREA/ SINGAPORE Ruolei Wu +86-1367-101-5294

PRODUCT (science.advertising@aaas.org); MIDWEST Rick Bongiovanni: 330-405-7080, FAX 330-405-7081; EAST COAST/E. CANADA Laurie Faraday: 508-747-9395, FAX 507-507-8189; WEST COAST/W. CANADA Lynne Stickrod: 415-931-9782, FAX 415-520-6940; UK EUROPE/ASIA Roger Gonçalves: TEL/ FAX +41 43 243 1358; JAPAN, Makiko Hara: +81 (0) 3 6802 4616, FAX +81 (0) 3 6802 4615; ads@sciencemag.jp; CHINA/TAIWAN Ruolei Wu: +86 1367 1015 294 rhu@aaas.org

WORLDWIDE ASSOCIATE DIRECTOR OF SCIENCE CAREERS Tracy Holmes: +44 (0) 1223 326525, FAX +44 (0) 1223 326532

CLASSIFIED (advertise@sciencereaders.org); U.S./CANADA/SOUTH AMERICA Tina Burks: 202-326-6577; SALES ADMINISTRATOR Marci Gallun; EUROPE/NOW SALES Lucy Nelson; SALES ASSISTANT Kelly Grace; JAPAN Yuri Kobayashi +81 (0)90-9110-1719; careerads@sciencemag.jp; CHINA/TAIWAN Ruolei Wu: +86 1367 1015 294 rhu@aaas.org; ADVERTISING SUPPORT MANAGER Karen Foote: 202-326-6740; ADVERTISING PRODUCTION OPERATIONS MANAGER Deborah Tompkins; SENIOR PRODUCTION SPECIALIST/GRAPHIC DESIGNER Amy Hardcastle; PRODUCTION SPECIALIST Yuse Lajiminshup; SENIOR TRAFFIC ASSOCIATE Christine Hall; SALES COORDINATOR Shirley Young; MARKETING MANAGER Allison Pritchard; MARKETING ASSOCIATE Aimee Aponte

AAAS BOARD OF DIRECTORS RETIRING PRESIDENT, CHAIR William H. Press; PRESIDENT Phillip A. Sharp; PRESIDENT-ELECT Gerald R. Fink; TREASURER David Evans Shaw; CHIEF EXECUTIVE OFFICER Alan I. Leshner; BOARD BONNIE L. BASSLER, May R. Berenbaum, Claire M. Fraser, Elizabeth Loftus, Stephen L. Mayo, Raymond Orbach, Sue V. Rosser, Inder M. Verma



A UNIQUE OPPORTUNITY FOR SCIENTISTS FROM AROUND THE WORLD: LIFE SCIENCES AT THE WISSENSCHAFTSKOLLEG



Wissenschaftskolleg zu Berlin

INSTITUTE FOR ADVANCED STUDY

For 30 years the Wissenschaftskolleg zu Berlin (Institute for Advanced Study) has served as an intellectual resort for internationally recognised researchers as well as promising younger scholars, in



a variety of disciplines in the natural sciences, social sciences, humanities, literature, music etc., to pursue their pet projects for a year, unhindered by the normal teaching and administrative duties of their home institutions. In a typical year the Kolleg consists of some 40 Fellows from different countries and cultures, speaking different languages and pursuing specialized intellectual tasks in their chosen disciplines, but at the same time presenting their work and their ideas to each other during weekly colloquia and daily meals and other informal occasions. In doing so they benefit

from critique provided by an outstanding community of scholars coming from diverse intellectual disciplines and academic traditions. The local environment of the Grunewald forest and indeed the rapidly changing city of Berlin make no small contribution to make the Fellows' year at the Kolleg a memorable one.

Over the years, Rüdiger Wehner, Raghavendra Gadagkar and Paul Schmid-Hempel have been working with the Wissenschaftskolleg to make a special effort to bring into this milieu, scholars from the broad area of life sciences, giving outstanding biologists and biomedical researchers the opportunity to spend a year away from their laboratories, rethinking the foundations of their disciplines, writing synthetic reviews and monographs or simply to chart a new course for their future research.

Distinguished scientists including Janis Antonovics, Robert Boyd, Ansgar Büschges, Tecumseh Fitch, Steven Frank, Yoh Iwasa, Alex Kacelnik, Axel Meyer, Cynthia Moss, Robert Page, Andrew Read, Mandyam Srinivasan, Luc Steels, and Eörs Szathmáry have availed of this opportunity. Many influential books, e.g. *The Wisdom of the Hive* (Thomas Seeley, Harvard, 1995), *Social Evolution in Ants* (A. Bourke and Nigel Franks, Princeton, 1995), *Foundations of Social Evolution* (S. Frank, Princeton, 1998), *Self-Organization in Biological Systems* (Scott Camazine et al, Princeton, 2001), *The Evolution of Social Wasps* (James Hunt, Oxford, 2007), *Deceit and Self-Deception* (Robert Trivers, 2011), were wholly or partly written at the Wissenschaftskolleg.

The Wissenschaftskolleg provides an excellent library service, arranges accommodation and helps with practical matters connected with relocation, including schooling of children where needed. Fellows are invited singly or in small focus groups. While the normal fellowship is for 10 months (mid-September to mid-July), in exceptional cases younger scholars (post-doc, early career) who cannot be away from their institutions for a whole year, are offered the opportunity to spend 3 months at the Kolleg. Fellows who are unable to obtain paid leave of absence from their institutions are either offered a stipend or the Kolleg may pay their institutions to hire a replacement for the year.

If you are interested in such an opportunity you find more information at (<http://www.wiko-berlin.de>) and may write to Permanent Fellows Paul Schmid-Hempel (psh@env.ethz.ch), Raghavendra Gadagkar (ragh@ces.iisc.ernet.in), or to Katharina Biegger (admission@wiko-berlin.de) of the Kolleg administration.

WISSENSCHAFTSKOLLEG ZU BERLIN WALLOTSTRASSE 19 D-14193 BERLIN

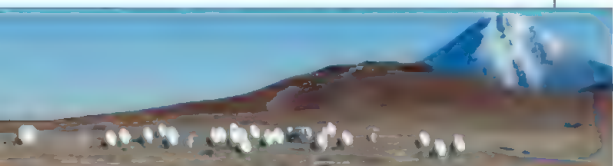
AROUND THE WORLD



Atacama Desert, Chile 1

ALMA Unveiled

The world's biggest telescope held its inauguration ceremony this week on a high desert plateau in northern Chile. Nearly all the 66 antennas that make up the Atacama Large Millimeter/submillimeter Array (ALMA) are now receiving data at the telescope site 5000 meters above sea level. The telescope, built at a cost of more than \$1.3 billion, will help astronomers study the cold universe at wavelengths that fall between microwaves and infrared light. Observing in that part of the electromagnetic spectrum will enable researchers to gain new insights into the origins of stars, galaxies, and planets.



Funded by the United States, Japan, and Europe, ALMA began delivering science long before its 13 March inauguration ceremony, discovering that certain galaxies in the infant universe went through a phase of intense star birth more than 12 billion years ago. The finding, reported in *Nature* this week—and based on observations made by only 16 antennas—suggests that the universe became a fertile birthing ground for stars long before when was previously thought.

Science LIVE

Join us on Thursday, 21 March, at 3 p.m. EDT for a live chat on **emerging diseases**. Ten years after SARS, are we better prepared? <http://scim.ag/science-live>

Arlington, Virginia 2

Audit Flags Alleged Plagiarism In Funded NSF Proposals

The National Science Foundation (NSF) is investigating nearly 100 cases of suspected plagiarism drawn from a single year's worth of proposals funded by the agency.

The cases were spotted in an internal examination by NSF's Office of Inspector General (IG) of every proposal that NSF funded in fiscal year 2011. The use of plagiarism software on some 8000 awards made that year resulted in a "hit rate" of 1% to 1.5%.

Plagiarism is one of three categories, along with fabrication and falsification, recognized as research misconduct by federal research agencies. NSF IG Allison Lerner told a congressional panel recently that the number of "substantive allegations of misconduct associated with NSF proposals and awards ... has more than tripled in the past 10 years, as has the number of findings of research mis-

conduct." She said her office has issued 120 findings of research misconduct since 2003 and that "more than 80%" involved plagiarism. <http://scim.ag/NSFplag>

Naples, Italy 3

Calls to Rebuild Burned Science Museum

The *Città della Scienza* (City of Science) complex in Naples, including a 12-year-old interactive museum and an education and conference center, went up in smoke last week. The fire took hours to extinguish; just one of the museum's buildings survived. Calls for rebuilding began almost immediately, and by late last week the Italian Ministry of Economic Development, Infrastructure and Transport, the Ministry for

Territorial Cohesion, the local government, and the mayor of Naples agreed on a plan to make available €20 million for its reconstruction, according to an article in Italy's *La Repubblica*. Several online campaigns for money to rebuild, including a crowdsourcing effort by the social platform DeRev and the online platform Cambiomerici, have received pledges to contribute both money and expertise to help the complex resume its activities. The origin of the fire is now under investigation. The Italian media is reporting growing suspicions of arson as the cause.

Bangkok 4

Bid to Restrict Polar Bear Trade Fails

With melting habitats, polar bears are in danger of extinction; hunting and trade in body parts also pose a threat. But last week, delegates to the Convention on International Trade in Endangered Species of Wild Fauna and Flora (CITES) meeting in Bangkok voted down a motion, proposed by the U.S. Department of the Interior, to restrict trade in polar bear parts. The motion failed with 38 votes for, 42 against, and 46 abstentions.

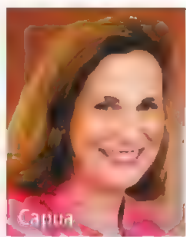
Polar bears are currently listed on CITES's Appendix II, which means that countries that export body parts must vouch that the animals were legally killed and that the deaths will not harm the survival of the species. The United States and Russia, which both already ban sales within their borders, proposed to shift polar bears from Appendix II to I, which is stricter, outlawing commercial trade in the species.



The other three countries that have polar bears—Canada, Greenland, and Norway—opposed the additional protection. The Canadian delegation argued that the extent of trade does not endanger the species and that banning trade could boost the price of trophies, perhaps leading to illegal hunting. The World Wildlife Fund also did not support the change in listing. <http://scim.ag/polbear>

NEWSMAKERS

Scientist Enters Italian Senate



Virologist **Ilaria Capua**, of the Istituto Zooprofilattico Sperimentale delle Venezie in Legnaro, Italy, will enter the Italian parliament this week for the first time as a newly elected deputy for the Civic Choice

party. The party is led by outgoing Prime Minister Mario Monti, who asked Capua to join his crew for her commitment to meritocracy and transparency and for her expertise in science and public health.

The offer came at the right time; Capua had been considering leaving Italy, as her current laboratory space is not sufficiently equipped to continue her group's research projects. "His call came on the sixth of January, after I had spent my Christmas holidays looking for a place abroad where I could go working," Capua says. She hopes her new role as a politician could also help prevent other scientists from going abroad.

Marrett to Fill in at NSF When Suresh Leaves

Cora Marrett will become acting director of the National Science Foundation (NSF) when Subra Suresh steps down on 22 March to become president of Carnegie Mellon University.

It's a familiar drill for Marrett, 70, a sociologist and longtime academic administrator. She kept the trains running between the departure of former NSF Director Arden Bement in May 2010 and Suresh's arrival that October, and has held the deputy director's job for nearly 4 years. Before that, she ran NSF's education programs and, in the 1990s, its social and behavioral sciences directorate.

Several former NSF directors would like to see her considered for the real job. "They couldn't do any better than to nominate Cora," says John Slaughter, an engineer who led NSF in the early 1980s. "She's helped to define the agency's programs in several areas." Neal Lane, a physicist who headed NSF in the mid-1990s, calls her "smart, dependable, and organized. I'm very high on her."



Random Sample

You Are What You Like

Every day, millions of people click on Facebook "Like" buttons, declaring preferences for books, movies, and cat videos. But likes may reveal much more, including sexual orientation, drug use, and religious affiliation, according to a study that analyzed the online behavior of 58,000 Facebook users.

To get data on personal attributes for comparison with the likes, a team of psychologists at the University of Cambridge in the United Kingdom created a Facebook app called myPersonality. After agreeing to volunteer as a research subject, app users answer questions and take psychological tests that measure things such as intelligence, competitiveness, extraversion versus introversion, and general satisfaction with life. With those data, and data from the user's Facebook profile and friends network, the researchers built a statistical model that predicted personal attributes based on likes.

It turns out that likes can predict many private details, the team reported on 11 March in the *Proceedings of the National Academy of Sciences*. The most accurate predictions were for gender (93%) and race (95%) (Caucasian versus African-American). But likes also accurately predicted more sensitive attributes: homosexuality (88% for men, 75% for women); religion (82%); political party membership (85%); and even use of cigarettes, alcohol, and drugs (73%, 70%, and 65%, respectively). Some predictions for likes make intuitive sense, such as "Jesus" for Christians and "Glee" for gay men. But others are harder to explain, such as the strong association between liking curly fries and having a high IQ. "What was traditionally laboriously assessed on an individual basis can be automatically inferred for millions of people without them even noticing," says lead author Michal Kosinski, "which is both amazing and a bit scary."

Like



{High IQ}

Like smart. High IQs correlate to "liking" curly fries, Morgan Freeman's voice, *The Colbert Report*, thunderstorms, Mozart, and science.

FINDINGS

Thirteen New Solutions To Three-Body Problem

It's an abstract puzzle to keep a scientist awake at night: How will three objects orbit one another in a repeating pattern? Isaac Newton raised the "three-body problem" in the 1680s when he showed that the law of gravity predicts the orbit of two bodies, such as a star and a planet, but not three. Since then, just three families of solutions have been found. Now, two physicists have discovered 13 more—which could help astrophysicists understand new planetary systems.

Mathematicians eventually determined that the motion of three bodies is non-repeating, except under specific conditions, and sorted those into three families: the Lagrange-Euler family (objects chasing one another like merry-go-round horses), the self-explanatory figure-eight family, and the Broucke-Hénon family (two objects dashing back and forth while a third orbits them).

To find the 13 new families, physicists Milovan Šuvakov and Veljko Dmitrašinović at the Institute of Physics Belgrade started with an existing solution on a computer simulation and tweaked its initial conditions until a new type of orbit materialized, they report in a paper in press at *Physical Review Letters*. The next step is to see how many of their new solutions are stable—and might be glimpsed in space. <http://scim.ag/threebody>

NOTED

>What life might lurk in Lake Vostok remains a mystery. Days after Russian scientists announced a new species of bacteria found in water collected from the subglacial Antarctic lake, **that discovery was negated—by another member of the team.** Geneticist Vladimir Korolyov of the St. Petersburg Nuclear Physics Institute said the bacteria weren't denizens of the lake but were mostly in the drilling fluid.

PHYSICS

Gravity-Wave Observatory Debates Fake-Data Tests

It was only 11 a.m., early in the day to serve champagne, but Jay Marx thought it might take the sting out of the news he was about to deliver. His team of physicists had gathered at a California hotel on a March day in 2011 to discuss what could be one of the greatest discoveries of all time: the first detection of gravitational waves, which Einstein had predicted nearly a century ago.

The researchers had spent months checking and rechecking their analysis of a signal seen by the Laser Interferometer Gravitational-Wave Observatory (LIGO) and had concluded that it looked like the signature of a wave emanating from the merger of two black holes. They had spent hundreds of hours writing a discovery paper that was ready to be submitted to a journal. Now, it was time for Marx—then LIGO's director—to reveal that the signal had been a well-intentioned hoax known as a blind injection.

"I had been thinking, 'Will there be a riot in the room? Will they hang me?'" Marx recalls. Loud moans arose from the audience. After the wave of disappointment passed, there was applause—and more champagne. Marx says most researchers acknowledged that the exercise—nicknamed "the Big Dog" after the bogus signal's apparent source in the constellation Canis Major—had left them better prepared to make a real detection in the future by clarifying "what our real criteria should be for claiming an event."

But did it go too far? That question—and how future blind injections should be conducted—will be discussed next week, when researchers from the LIGO Scientific Collaboration and their counterparts at the Virgo

gravitational wave detector in Italy meet in Bethesda, Maryland, to prepare for the next phase of the search for gravitational waves. Among other things, the researchers will debate how many blind injection exercises a year to hold once LIGO's successor, Advanced LIGO, goes online in 2015. "It is our intention to continue the blind injection program," says David Reitze, a physicist at the California Institute of Technology in Pasadena who succeeded Marx as LIGO's executive director in August 2011. "What form it will take will likely be different from the last one."

Gravitational waves are ripples in space-time caused by the acceleration of massive objects, like binary stars spiraling in toward one another. Detecting them is one of the big quests of modern physics. It should be possible because the distance between stationary objects changes slightly as the ripples pass through. But spotting those changes is challenging because even the most powerful gravitational waves from space have a minuscule effect by the time they reach Earth.

Gravitational-wave detectors such as LIGO and Virgo aim to measure those tiny effects. LIGO has three interferometers: two in Hanford, Washington, and one in Livingston, Louisiana. In each of these instruments, a beam of laser light is split into two beams that travel through two 4-kilometer-long perpendicular vacuum tubes. Reflected by mirrors at the ends of the tubes, the beams bounce back and forth several times before reuniting. If the mirrors in both arms are the same distance apart, the two beams should return to the laser with their light waves still in step. Because of how the arms are configured, however, a passing gravita-

Wave machine. LIGO's detector in Louisiana aims to detect ripples in space-time through minute changes in the length of its 4-kilometer-long perpendicular arms.

tional wave would change their lengths by different amounts, causing the beams to reunite out of sync. As a result, some light would leak out, providing a measurable signal.

LIGO has conducted blind injections since it began operations in 2002, primarily as a way of testing the hardware and software and helping researchers learn to pick out signal from noise. But the injection made on 16 September 2010 was more dramatic: It was made to look like an unambiguous gravitational wave signal. Scientists created it by moving the mirrors in the tubes ever so slightly. Only Marx and a few others knew the secret.

When researchers in the collaboration saw the signal, they were electrified. They knew it *could* be a blind injection, "but we were very hopeful" that it would prove to be a real cosmic event, says Gabriela González, a physicist at Louisiana State University, Baton Rouge, and the scientific spokesperson for LIGO. The researchers spent the next few months analyzing the result and writing a paper. "We dotted all the i's and crossed all the t's," González says. Their hopes were dashed when Marx opened the "blind injection envelope" at the March 2011 meeting to reveal that Big Dog was a big fake.

When Advanced LIGO—an upgrade of the current observatory—goes online, blind injection exercises will likely be kept secret from the collaboration for a shorter time. "We will certainly not be writing a paper," Reitze says. He says the collaboration needs to reach a consensus on how often to stage blind injections (current plans would limit them to one or two a year) and whether to let astronomical observatories spend time trying to locate non-events in the sky, as NASA's SWIFT observatory did in 2010.

Not everybody is gung ho about continuing the exercises. "My preference would be for every search pipeline trigger to be viewed by collaboration members as a potentially real event and not to have them second-guess themselves as to whether it might be a blind injection," says Nelson Christensen, a physicist at Carleton College in Northfield, Minnesota. "But to be fair," he says of the 2010 injection, "that exercise did display to us that we were not fully prepared for what was necessary to make a discovery. We did learn some things in the process."

—YUDHIJIT BHATTACHARJEE

CREDIT: LIGO LABORATORY

PALEONTOLOGY

Dramatic Fossils Suggest Early Birds Were Biplanes

When the Wright brothers took to the skies from Kitty Hawk in December 1903, they did it in a biplane, a craft with two pairs of parallel wings. Most early aircraft were biplanes, but by the 1930s, the faster monoplane design, with just two wings, dominated aviation. On page 1309, a Chinese team presents dramatic new fossils suggesting that early birds went through a similar evolution, starting off with wings on both arms and legs and only later adopting the arms-only, monoplane configuration.

The 11 beautifully preserved skeletons of early birds with intact leg feathers are “spectacular,” says Stephen Brusatte, a paleontologist at the University of Edinburgh in the United Kingdom who was not involved in the work. David Alexander, an expert in animal flight at the University of Kansas, Lawrence, adds that “these new fossils fill in many gaps in our view of the early evolution of birds.”

Almost all paleontologists agree that birds evolved from other feathered dinosaurs. So researchers have zeroed in on fossils from the Lower Cretaceous period, about 150 million to 100 million years ago, when one group of dinosaurs evolved into birds. In 2000, paleontologists discovered a nonavian dinosaur with feathers on both arms and legs called *Microraptor*, which probably could fly—although researchers debate just how it did so (*Science*, 2 November 2012, p. 591). Some scientists, most notably famed dino hunter Xing Xu of the Institute of Vertebrate Paleontology and Paleoanthropology in Beijing, suspected that the earliest birds also had feathers on all four limbs and used all four as wings. Some specimens of *Archaeopteryx*, the earliest claimed bird, seem to have leg

feathers, as does one other early bird specimen.

But the preservation of many of these specimens is so poor, Brusatte says, that “you really have to squint” to see the feathers. Researchers had little evidence to support the notion that leg feathers were an ancestral feature. Until now, that is.

The new specimens come from the famed Lower Cretaceous Jehol formation in Liaoning, northeastern China. Over the past decade, collectors donated the fossils to China’s Shandong Tianyu Museum of Nature, where Xu and his colleagues verified their authenticity and studied them.

All the fossils have leg feathers—not just soft, fluffy ones like those on some modern raptors, but stiff feathers that jut straight out from the limb and provide enough surface area to play an aerodynamic role, the team contends. These birds had “big leg feathers with vanes and the whole shebang,” Brusatte agrees.

Crucially, the fossils are from at least four diverse groups of early birds, including the genera *Sapeornis* and *Yanornis*, several specimens related to *Confuciusornis*, and two species from the *Enantiornithes* group.

Thus, leg feathers were not just a rare quirk of evolution, the authors say. “These new fossils leave no doubt that the four-winged morphology was common among basal birds and their relatives,” Alexander says.

That implies that having four wings was the ancestral condition for early birds. Indeed, the team analyzed the feather arrangements of nonavian dinosaurs and early and later birds, and it concluded that feathers covering the entire leg—including the feet—arose first among dinosaurs, continued on in the earliest birds, and then

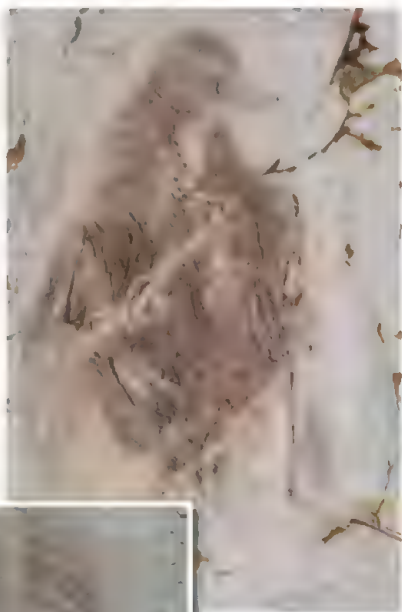
receded. Feathers disappeared from the feet first and gradually vanished from the length of the leg. Today’s birds use only their arms for flight and their legs for terrestrial locomotion. “From their work, it becomes clear that the four-wing form was exhibited not just by *Microraptor*, but also retained ... in successive lineages of early birds,” says Sankar Chatterjee, a paleontologist at Texas Tech University in Lubbock.

However, the finds leave open the critical questions of whether and how these leg wings were used in flight. Xu and colleagues argue that the perpendicular arrangement of stiff feathers, which they contend formed a large flat surface, could have provided lift and enhanced maneuverability, arguments that have also been made for *Microraptor*. The feathers “must surely have had some aerodynamic function,” Alexander agrees, “although whether as stabilizers, steering vanes, or full-blown wings remains to be seen. There really is no other logical function for that kind of feather on a limb.” Chatterjee suggests that the early biplane configuration might have provided greater stability, especially when gliding, but later gave way to a monoplane style that favored maneuverability.

But Kevin Padian, a paleontologist at the University of California, Berkeley, who calls the paper a “great study,” nevertheless argues that the authors have provided no evidence “that these feathers contributed to any sort of flight.” Padian thinks that the apparent large surface area of the supposed wings might be due to flattening during preservation. He adds that “it is indisputable that such feathers would create drag,” and thus have made flight more difficult. Indeed, Richard Prum, an evolutionary biologist at Yale University, says the earliest leg feathers could have been used for courtship display rather than flight.

Resolving these questions will require biomechanical studies carried out in a lab, Brusatte says. Xu, whose team is working its way through thousands of specimens at the Shandong museum, says more fossils should also help. “We are working hard to extract new information from these wonderful specimens and hopefully can produce more interesting results in the future.”

—MICHAEL BALTER



Winging it. This ancient bird had stiff feathers on both arms and legs.



HIV/AIDS

Subset of CD4 Cells May Hold Key To Reaching HIV Cure

ATLANTA—"What do you think of the baby?" became the most asked question at the 20th Conference on Retroviruses and Opportunistic Infections held here last week. But the Mississippi case that grabbed international headlines after a report at the meeting described how a child had been cured of an HIV infection represents a single intriguing observation rather than a significant advance (*Science*, 8 March, p. 1134). New findings about how a subset of CD4+ white blood cells invaded by HIV may control the course of the disease promise to have a far more profound impact on the field. These "central memory cells" might even help explain the underlying mechanism behind the child's apparent cure.

central memory cell, a type of CD4+ T lymphocyte known in shorthand as T_{cm} , churns out clones of itself and can almost refill the body's pool of CD4 cells as fast as HIV drains it. However, the downside is that some infected T_{cm} cells become reservoirs of latent virus that rekindle infection if antiretrovirals (ARVs) are stopped.

The researchers who presented the case of the Mississippi child contend that success occurred because treatment was started unusually early, 31 hours after birth, which they say may have severely limited the size of the child's reservoir and given the infant's body a better chance to clear those cells. They have no direct evidence for this—but another report at the meeting lends credence to the idea.

At the Thai Red Cross AIDS Research Center in Bangkok, Jintanat Ananworanich and a team from the U.S. Armed Forces Research Institute of Medical Sciences have been identifying people shortly after they become infected and then encouraging them to start ARVs immediately. It typically takes 3 weeks after infection for people to test positive on standard screens for viral proteins and antibodies, but Ananworanich uses more sensitive tests that can identify infections earlier. Some

people are so recently infected that the researchers detect only HIV genetic material in their blood, while others who are a little further along have viral proteins, and a third group also has antibodies that are detected by an ultrasensitive test, a sign of a slightly longer infection.

This study separated 75 acutely infected people into these three groups and started them on ARVs within 5 days of taking a blood test. An analysis by immunologist Nicolas Chomont of the Vaccine and Gene Therapy Institute of Florida in Port St. Lucie

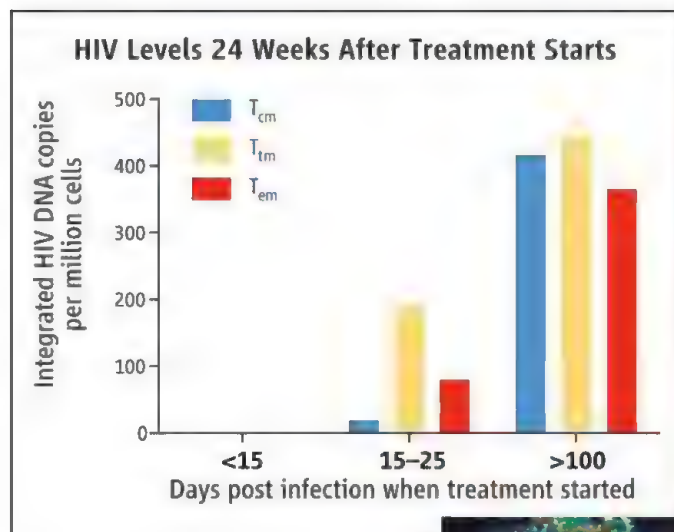
found that all three groups started out with fewer HIV-infected T_{cm} cells than seen in untreated people who have been infected for several years. What's more, after 24 weeks of treatment, the HIV DNA integrated into the T_{cm} cells remained undetectable or extremely low in each group. "Early [treatment] prevents the seeding of latent reservoirs in long-lived central memory T cells," Ananworanich concluded. She suggested that these people might be "ideal candidates" for future cure studies that she and her colleagues plan to conduct with novel interventions aimed at purging reservoirs. UCSF's Deeks suspects that the Mississippi child's T_{cm} cells were protected by extraordinarily early treatment and that the child's body was able to clear the tiny reservoir that was established.

Some people naturally control HIV better than others and protect their T_{cm} cells without the help of ARVs. Christina Ramirez Kitchen of the University of California, Los Angeles, collaborated with Deeks to look at "elite controllers," HIV-infected people who retain low HIV levels in their blood and high CD4 counts without treatment. The study compared nearly 300 infected people who had low levels of HIV in their blood, two-thirds of whom received treatment. The researchers found that elite controllers stood out in part because their T_{cm} cells downregulated a key receptor that HIV needs for entry and were less permissive to HIV infection. Conversely, Kitchen noted that people whose immune systems did not rebound even though ARVs controlled their infections had T_{cm} cells with impaired function.

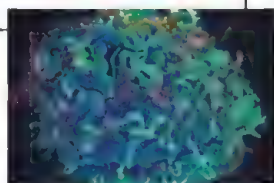
In yet another twist involving T_{cm} cells, a poster presentation by Nichole Klatt of the University of Washington, Seattle, examined an unusual group of five people who had been infected for more than 9 years and maintained relatively normal CD4 counts, but, unlike elite controllers, have high levels of HIV in their blood. None took ARVs. The researchers compared these "viremic nonprogressors" to seven recently infected, untreated people with similar viral loads and CD4 counts who they expect will progress. A key difference between the two groups: The viremic nonprogressors had significantly fewer HIV-infected T_{cm} cells, and those cells had the same downregulated receptor found in the T_{cm} cells of the elite controllers that Kitchen studied.

So while the "cured" baby stole the limelight at the retrovirus meeting this year, central memory cells occupied center stage, too.

—JON COHEN



Early does it. HIV invades various subsets of CD4+ T cells (T_{em} , T_{tm} , T_{cm}), but prompt intervention with antiretroviral therapy protects T_{cm} cells from infection.



"At the end of the day, what happens to central memory cells in the context of HIV infection may be the most important determinant of who you'll be able to cure and a patient's long-term outcome," said Steven Deeks of the University of California, San Francisco (UCSF), whose own lab focuses on curing HIV infections.

HIV preferentially invades T lymphocytes that have CD4 receptors on their surfaces. The resulting destruction of CD4 cells over a decade or so cripples the immune system and is the hallmark of AIDS. But the process takes many years because the

DUAL USE RESEARCH

Australian Researchers Rattled by Export Control Law

CANBERRA—An emerging controversy over an Australian government effort to tighten controls on research that could be used for good and evil is getting some high-level attention. On 25 March, a special 11-member advisory panel led by Australia's chief scientist will meet here. Its task: to assess how recently adopted regulations on the export of a long list of "dual use" technologies—such as missile designs and knowledge about viruses that could be used to make bioweapons—will affect Australian science.

Some researchers fear that the new export controls—approved late last year as part of a defense treaty between Australia and the United States—will stifle the ability of Australian researchers to communicate with colleagues abroad. "It's explicitly stated that researchers would be prohibited from communicating by any means—e-mails, papers, or speeches—to a person outside Australian borders without a defense permit," says biophysicist Jill Trehwella, a deputy vice-chancellor at the University of Sydney. Such constraints could prompt some Australian scientists to abandon certain lines of research or move abroad, she warns.

But Ian Chubb, the government's independent chief scientist, says such concerns are premature—and that his panel will be working to clarify the new rules, which will be phased in over the next 2 years. "I'm tired of shadowboxing and speculating about what might happen," Chubb says. "We have an opportunity to jump in and make recommendations that will eliminate any problems."

The issue has been simmering since October 2012 when Australia's Parliament approved the Defence Trade Controls Act (DTCA), which implements a 2007 U.S.-Australia pact designed to streamline trade in defense-related technology and know-how. DTCA is not Australia's first effort to keep problematic technologies out of the hands of potential enemies. Like the United

States and most other industrialized nations, Australia has long regulated the export of dual-use technologies, requiring researchers and companies working on things like new weapons and certain software and electronics to get special permits before sharing their innovations.

In recent years, growing concern about bioterrorism has prompted nations to extend export controls to the life sciences and impose new restrictions on the sharing of information and samples for researchers working with dangerous bacteria, viruses, and toxins. The issue gained global prominence last year, during the controversy

over two studies involving the H5N1 avian influenza virus, when the governments of the United States and the Netherlands required some scientists to obtain export control licenses before discussing the studies at international meetings and submitting final manuscripts to journals (*Science*, 1 March, p. 1025). Some influenza scientists have chafed at the licensing requirement, arguing that it violated other policies that exempt communication about basic research from export controls.

One problem with Australia's new law, critics say, is that it appears to do away with similar, long-standing exemptions from export controls for basic research. Prior to passage of the law, for example, Australia's customs regulations excluded scientific publications and e-mail communication with international research collaborators. Now, analysts say,

researchers working with any of the items on the export control list will have to think twice before hitting the send button. "The implications of the legislation are complex and important," says Belinda Robinson, chief executive of the umbrella group Universities Australia, which was one of several groups that urged the government to appoint a special panel to examine the law's impact on research.

The government responded late last year, creating the Strengthened Export Controls Steering Group. Its members are major movers and shakers, including Chubb, the heads of Australia's two major research funding agencies, senior administrators from the Queensland and Newcastle universities, and leading defense and industry officials. The panel, which meets quarterly and reports to the defense and research ministries, plans to keep a close watch on how the export licensing process is working and whether it is unnecessarily entangling scientists. It also plans to launch a series of studies examining the law's impact on different fields. It will make the results of those and other studies public and file a final report with Parliament at the end of DTCA's 2-year implementation period.

In the meantime, Australia's medical research funding body is drafting guidelines to help scientists comply with the new rules. And the government has tried to reassure scientists, agreeing not to prosecute those who fail to comply during the transition period.

Chubb says he expects the panel to find problems—and solutions. "Did anyone say the act was perfect yet? Not to my knowledge. Are we working to make it better? Yes," he says. "We need to get a balance here," he adds. "My view is that we do not toss away the notion of freedom of research. Equally, I don't want people to believe

they can publish anything in any way they like. The aim of the exercise is to allow research to be as unrestricted as possible, but to stop damaging material and knowledge falling into the wrong hands."

—LEIGH DAYTON



Dual role. Ian Chubb, the Australian government's chief scientist, is leading a high-level panel that is examining how new controls on dual use research are affecting scientists.



Concerned. Biophysicist Jill Trehwella says that export control rules will make it more difficult for Australian scientists to communicate with colleagues overseas.



War Stories

In 2003, the world successfully fought off a new disease that could have become a global catastrophe. A decade after the SARS outbreak, how much safer are we?

GENEVA, SWITZERLAND—What were they going to call it? That was the final question for a small group of men huddling in a room here at the headquarters of the World Health Organization (WHO) on the morning of Saturday, 15 March 2003. They were about to issue a second global alert on a serious new disease that was spreading rapidly, and it needed a name.

Three days earlier, WHO had warned about the illness, known simply as “atypical pneumonia,” for the first time. Then, it was known to have occurred in mainland China, Hong Kong, and Vietnam. Now, there were suspected cases in Canada, Singapore, Thailand, Indonesia, and the Philippines. And at 2 a.m. that Saturday, WHO epidemiologist Michael Ryan had learned that a Singaporean doctor who was likely infected with the disease was on his way home from New

York; he would be taken off the plane during a stopover in Frankfurt. A new statement, in which then WHO Director-General Gro Harlem Brundtland described the disease as a “worldwide health threat,” was about to be sent to the press.

“We had to give the disease a name,” says David Heymann, then WHO’s executive director of communicable diseases. “If we hadn’t, the media might have come up with something stigmatizing like Chinese flu.” Heymann wanted a name that rolled off the tongue easily—something like AIDS.

Dick Thompson, a former science reporter for *Time* who joined WHO as a press officer in 2001, says he eventually coined “severe acute respiratory syndrome” based on what they knew so far. It worked well as an acronym, he said. The alert went out later that

CREDIT: CHRISTIAN KEENAN/STRINGER/GETTY IMAGES



morning. The first global health threat of the 21st century had a name: SARS.

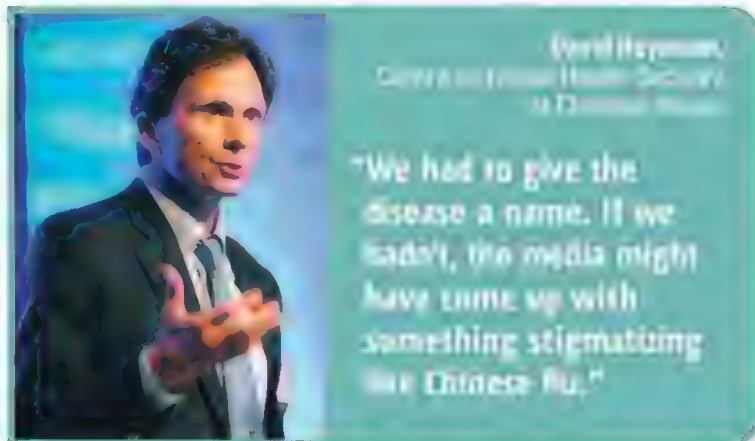
• • • • •

In the following months, just over 8000 people in almost 30 countries were infected with SARS, and 774 died. Initially, it seemed that SARS might be unstoppable—that it would sweep the globe and infect millions. But aggressive countermeasures by health care workers, public health officials, and scientists put the genie back into the bottle—not using a drug or a vaccine, but simply by preventing patients from infecting others. By 5 July, it was all over.

The two alerts were issued a decade ago this week. To mark the occasion, *Science* asked many of the key players at WHO, as well as public health agencies and research labs, about what happened—and about the lasting lessons they learned from those frightening months. Many said that SARS was the most dramatic episode in their career; a time of 18-hour workdays, anxiety, and the occasional fight—but also of cour-

age, unprecedented collaboration, and scientific excitement. Some said it resembled a war and called the SARS virus “the enemy.”

Umesh Parashar, an epidemiologist at the U.S. Centers for Disease Control and Prevention (CDC) in Atlanta, helped battle SARS in Hong Kong. Parashar had investigated the U.S. anthrax attacks in 2001 and would work on the influenza pandemic in 2009; neither matched SARS “in its intensity and sheer enormity,” he says. Among his most vivid memories: entering a meeting room at Hong Kong’s Prince of Wales Hospital, which had a big SARS outbreak, and seeing everybody wearing masks. “I had never had that sense of personal vulnerability,” he says.



CREDIT: U.K. HEALTH PROTECTION AGENCY

As to SARS’s legacy, many agree that the world is better prepared today for the emergence of infectious diseases that have the potential to go global. Disease surveillance has improved, and scientific advances make it easier to fish an unknown pathogen from a sample and characterize it. SARS also spurred the introduction in 2005 of new international rules on how to report and handle disease threats. The outbreak drove home that the world is an awfully small place, and collaboration is essential.

At the same time, many countries lack the ability to detect a breakaway virus early on, and producing new vaccines quickly is still difficult for almost any disease. Although SARS painfully demonstrated that sweeping an epidemic under the rug, as China tried to do, is counterproductive, few people believe that this age-old reflex won’t occur again.

The recent emergence of a distant cousin of SARS on the Arabian Peninsula has highlighted some of the remaining problems. After the first case, it took 3 months for information about the new virus, now named NCoV for novel coronavirus, to come out. Many questions remain about where it came from, how it got into humans, and its potential to spread—and they “probably aren’t pursued aggressively enough,” says virologist John Mackenzie of Curtin University, Bentley, in Australia, who led a WHO mission to Beijing when SARS was exploding there.

• • • • •

The SARS outbreak didn’t start in March 2003. Scientists later discovered that the first known case, in November 2002, was a 45-year-old man in Foshan, a city in the southern Chinese province of Guangdong. Studies would also show that the virus originated in bats and infected humans most likely through animals traded in China’s wild animal markets.

The provincial government initially banned the press from writing about the disease and downplayed its significance; an official bulletin issued on 11 February finally acknowledged 305 cases, including five deaths, but said the outbreak was under control. In neighboring Hong Kong, experts were “very concerned,” says University of Hong Kong virologist Malik Peiris. “If something untoward was happening across the border, it would come to Hong Kong pretty quickly.”

And it did. Hong Kong became the virus’s springboard to the globe on 21 February, when a 64-year-old nephrologist from Guangzhou, the capital of Guangdong, checked into room 911 of the Metropole Hotel in Kowloon. He went to a nearby hospital the next day with severe pneumonia. At least 16 other hotel guests and a visitor became infected and they carried the disease to 3 new countries (see sidebar, p. 1272).

In Geneva, WHO had an experienced team to respond. Heymann, an American epidemiologist who today heads the U.K. Centre on Global Health Security at Chatham House and is a professor at the London School of Hygiene and Tropical Medicine, had helped eradicate smallpox in India and had battled many diseases in Africa; in 1995, he led WHO’s response to the largest Ebola outbreak until then, in Kikwit, in what was then Zaire. Guénaél Rodier, a Frenchman and WHO’s then-director of communicable disease surveillance, had an equally international resume and had worked alongside Heymann in Kikwit.

Now, as they were coordinating a global response from their desks in the tidy city of Geneva, their collective field experience was essential, says Ryan, an energetic Irishman and a junior member of the team. “You’re not just sitting there clicking buttons and looking at things on screen,” he says. “When you talk to national authorities or to people in hospitals, they know: This person knows my situation. They’ve been there.”

In several ways, the international health community was only half prepared. Heymann's team was convinced that a new pandemic disease could emerge; to help identify and respond to such threats, they had already set up the Global Outbreak Alert and Response Network, consisting of institutes and labs around the world. Health Canada had set up a system called GPHIN that allowed WHO to monitor a wide range of online sources, including news outlets, for anything suggesting unusual disease patterns. (It was initially called the "rumor list," Rodier says.)

At WHO's helm, Brundtland, a former Norwegian prime minister, backed the new, more activist role for the U.N. agency, but it raised hackles among member states, who were used to reporting such information in their own time. "Countries would scream at us," Ryan recalls. "We would pick up an event in the media, and go to a country and say, 'Look, what's happening?' They would ask us: 'What right do you have?'"

WHO was also hamstrung by the existing legal framework. An agreement last revised in 1969, the International Health Regulations (IHR), spelled out how countries should report and handle diseases that can cross borders, but it was outmoded and ineffective; for one, it only covered plague, cholera, and yellow fever. As a result, there was nothing that compelled China, or any other country, to tell the rest of the world what was happening within its borders early in 2003.

• • • • •

Henk Bekedam, a tall, outspoken Dutchman who led the WHO office in Beijing at the time, experienced the problem firsthand. At first, WHO believed that the Guangdong outbreak might be the start of a pandemic of the avian flu virus H5N1—a few cases were detected in February in humans in Hong Kong—or it might be something completely different. WHO pressed China to find out more, but little information was forthcoming.

In late February, Bekedam received help from a three-member mission of foreign experts: Hitoshi Oshitani of WHO's regional office in Manila; Keiji Fukuda, then at CDC in Atlanta; and Masato Tashiro from Japan's National Institute of Infectious Diseases. But the trio couldn't get an appointment with Chinese health officials. After spending 9 days at WHO's Beijing office, Oshitani and Fukuda finally met with the China CDC, Bekedam says, but they learned little and were denied a trip to Guangdong. Even after SARS was acknowledged as a new disease, Chinese officials long downplayed its extent.



All of that changed when new leadership—Hu Jintao took over as China's president on 15 March—realized the problem was too big to hide or neglect. On 20 April, Chinese Health Minister Zhang Wenkang and Beijing Mayor Meng Xue-nong were dismissed. Hu started championing the fight, and China began opening up to WHO. "From that moment, you couldn't work with a better country," Bekedam says. "It was very impressive."

Ten years on, the world's most populous country has made major strides in public health, improving its surveillance and expanding its laboratory capacity, says Bekedam, who left Beijing in 2007 and now works in WHO's regional office in Manila. Peiris says that China's labs have "improved dramatically over the last 10 years."

But the most important consequence of SARS, many say, was that it made clear the inadequacies of the IHR. In 2005, the World Health Assembly adopted a revision of the IHR that took effect in 2007, requiring countries to report within 24 hours anything that "may constitute a public health emergency of international concern" including unknown diseases. Each country must have the ability to detect such threats and assess their risk. The rules also allow WHO

to follow up on informal reports about diseases—thus giving the "rumor list" a formal basis.

But implementation has lagged. More than 100 countries did not meet the June 2012 deadline for establishing the necessary surveillance and lab capacity and had to ask WHO for a 2-year extension. Among the least prepared are poor countries with high biodiversity that are also seen as a likely cradle for new pathogens. Money is a key problem.

"There was supposed to be a massive investment in national and international public health infrastructure," after the revision of the IHR, Ryan says, "and I don't think we have seen that yet. It's one thing to set in motion a set of rules; it's another thing to create the infrastructure you need." Ryan left WHO in 2011 to become an adjunct professor of international health at University College Dublin, in part because he was frustrated by a shifting culture at WHO that he characterizes as more about "discussion, discussion, and discussion" than about getting things done.

• • • • •

Pascale Brudon, the French head of WHO's Hanoi office, had more luck convincing the Vietnamese government that SARS was a problem. And the outbreak there, with only 63 cases in total, taught the world some key lessons about the disease early on.

SARS: Chronology of the Epidemic

NOVEMBER 2002 — JULY 2003



First known case of SARS, not identified until much later in Foshan of Guangdong Province, China.

16 November

Guangdong Health Bureau sends official document on atypical pneumonia to provincial health bureaus and medical institutions.

23 January

Seafood seller in Guangzhou infects more than 50 hospital staff members and 19 relatives, the first known "super-spreading event."

30 January

World Health Organization's (WHO's) Beijing office receives e-mail warning of a "strange contagious disease" in Guangdong.

10 February

Guangdong officials report 305 cases and five deaths of acute respiratory syndrome between 16 November 2002 and 9 February 2003.

11 February

On 27 February, doctors at the French hospital in Hanoi asked Carlo Urbani, a parasitologist in the WHO office, to look at an unusual case: a Chinese-American businessman who suffered from severe pneumonia with an unknown cause. Within days, hospital staff members were falling ill as well. Urbani—a “very Italian” man, Brudon says, who loved wine, food, music, and life in Hanoi—was worried, and he sent a report to the WHO office in Manila on 3 March.

Soon, staff members at the French hospital started falling ill. The Vietnamese government “considered it a private problem in a private hospital,” says Brudon, who is now retired and living in Paris. In a 4-hour meeting on Sunday, 9 March, she and Urbani tried to convince Vice-Minister of Health Nguyen Van Thuong that it wasn’t. “If you want to do something good for Vietnam and the world, you should take this seriously,” Brudon recalls telling him, “because it may be very important.” Finally, Nguyen promised to inform the prime minister, set up a task force, and ask for foreign help.

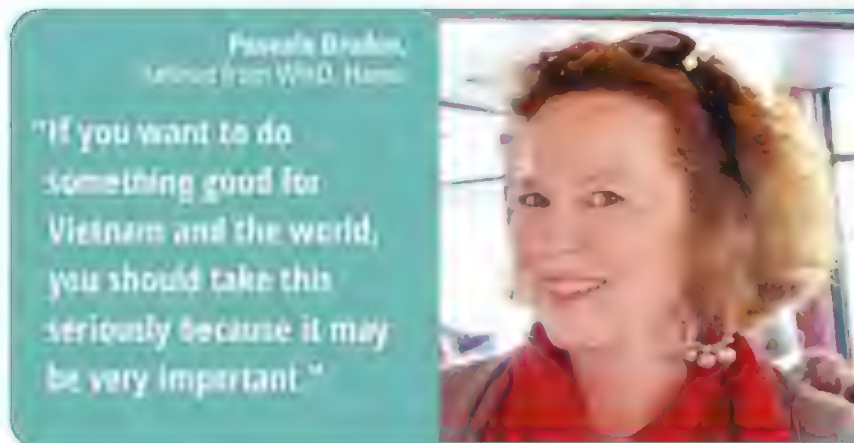
Urbani became one of the heroes in the SARS story, because he helped raise the alarm at WHO. Until then, the new disease appeared to be confined to Guangdong and Hong Kong; now, it was clear that it had spread further. (The American businessman was one of the guests on the ninth floor of Hong Kong’s Metropole Hotel.) “Vietnam was the trigger” for the first alert on 12 March, Heymann says.

On 12 March, Urbani traveled to Bangkok, where he was scheduled to give a presentation at a parasitology meeting. He called Brudon before boarding a plane in Hanoi to say he wasn’t feeling well and was considering canceling the trip. “I told him to go—he had wanted to go to this meeting,” Brudon says. “I said he was probably just tired. We were all exhausted.” But after Urbani had boarded the plane, she started worrying, and she called the WHO office in Manila, which helped arrange an ambulance to pick him up at the Bangkok airport. It was soon clear that he had the as-yet unnamed new disease.

Brudon had a few phone calls with Urbani in the following days, but he deteriorated rapidly and died on 29 March. “We were all devastated,” she says. Colleagues streamed into WHO’s office that Saturday, Brudon says; there were flowers, photos, and music. “We all drank too much.”

SARS was an extraordinarily dangerous disease for health care workers; they accounted for more than one-fifth of all cases. Doctors and nurses weren’t used to such high infection risks, and interventions such as intubation of the trachea and the use of drug nebulizers exacerbated them because they set loose virus-laden aerosols. “We learned that health care is part of the solution, but it can also amplify the problem,” Ryan says.

WHO started to advocate the kind of rigorous infection control that it had used during the viral hemorrhagic fever outbreaks in Africa, including strict isolation of the patient and the use of gloves,



gowns, surgical masks, and protective eyewear. “We realized quickly that the measures used to stop the spread of Ebola and Marburg worked for SARS as well,” Rodier says.

As the weeks passed, it became clear that other measures could help curtail the virus in the community at large. There were a few so-called superspreading events, such as the Metropole Hotel outbreak and a big outbreak in Amoy Gardens, a Hong Kong apartment complex. But most SARS patients infected few others. If public health systems were able to find and isolate suspected cases early, and if they could quarantine the people they had been in touch with, they might be able to stop the virus.

Vietnam became the first country to show that this strategy could work; on 28 April, WHO declared it SARS-free, inspiring hope that the virus could be wiped out worldwide. “When Vietnam was able to stop transmission, we knew it was possible,” Heymann says.

• • • • •

Within days after the initial alerts, WHO’s modernist headquarters in Geneva became the center of a virtual conference room that spanned the globe. The agency set up networks of doctors treating SARS patients to exchange information and of epidemiologists assembling and analyzing data on the virus’s spread. A third network consisted of virology labs that joined hands to find the cause of SARS—a very unusual arrangement for the competitive field (see p. 1269). Led by Klaus Stöhr, a German epidemiologist in charge of WHO’s influenza network, the effort “was pretty phenomenal,” says Larry Anderson, who was at CDC at the time and is now at Emory University in Atlanta. Peiris says it’s a model for similar crises in the future.

Yet in the end, 21st century lab science had little impact on the fight against SARS; the disease was stopped using 19th century hygiene measures. Diagnostic tests developed soon after the virus was isolated weren’t needed to manage the outbreak, and the

CREDITS (TOP TO BOTTOM): M. A. CIPRUT/AP PHOTO/VINCENT YU

The Chinese Ministry of Health informs WHO that the Guangdong outbreak is under control.

14 February

A Guangdong physician falls ill in Hong Kong’s Metropole Hotel. Other guests carry SARS to Hanoi, Singapore, and Toronto.

21 February

A Chinese-American businessman from New York who stayed at the Metropole Hotel is admitted to the French Hospital in Hanoi.

26 February

Carlo Urbani examines the Hanoi case and notifies WHO’s regional office in Manila of unusual disease.

3 March

Health care workers at Hong Kong’s Prince of Wales Hospital start falling ill.

7 March



sequence, completed by Canadian scientists on 12 April, had little direct impact. Scientists launched programs to develop antivirals and vaccines against SARS—and some of the work is still going on—but they never came to fruition; the direct need for them disappeared in July 2003, when the epidemic was declared over.

Today, identifying and characterizing a new agent takes much less time, says virologist Christian Drosten of the University of Bonn in Germany. High-throughput sequencing allows researchers to pull out an infectious agent from a patient sample without culturing it first. Sequencing SARS would now take hours, not weeks, and diagnostic tests can be developed much faster, Drosten says.

• • • • •

But although the science may be better, many of the social issues remain the same. No country likes to admit having a new health threat within its borders, especially when the economic and political consequences can be huge. The situation with the new NCoV has driven that point home.

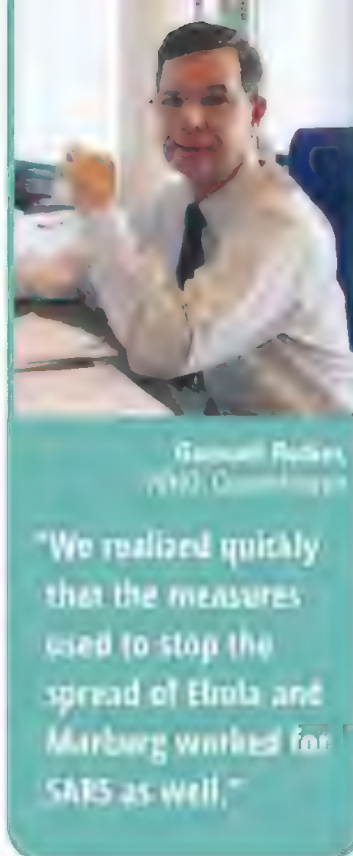
To Maria Zambon, a virologist at the United Kingdom's Health Protection Agency whose lab identified four NCoV cases, the parallels with SARS are striking: Here's another coronavirus that can cause severe disease and can spread from one person to another. So far, it does not appear to do so very efficiently, but Zambon is concerned nonetheless. "It could become as much a threat as SARS," she says.

And again, similar questions have arisen, starting with the timeliness of the reporting. News about the NCoV virus was reported on ProMED, an internet service providing outbreak news, on 20 September 2012, by Ali Mohamed Zaki, an Egyptian microbiologist working in a hospital in Jeddah, Saudi Arabia. Zaki identified the virus in June in a man who died of pneumonia and shared samples with Ron Fouchier of Erasmus MC in the Netherlands, who sequenced it.

Accounts differ on why 3 months passed between the discovery and the ProMED report. Fouchier says that Zaki notified the Saudi government of the finding and urged reporting it to WHO; only when Saudi officials refused did he send the e-mail to ProMED, Fouchier says. (Zaki did not respond to questions from *Science*.) But Ziad Memish, Saudi Arabia's deputy minister for public health, says that Zaki never told the government anything. "We were surprised to hear about this whole thing from ProMED," Memish tells *Science*.

The sequence of the virus is closely related to those of other viruses found in bat species, and researchers assume that the new virus also originated in bats. So far, 14 people have been found to be infected with the virus, eight fatally. Seven came from Saudi Arabia, two from Qatar, two from Jordan, and in February, the United Kingdom reported three cases in people residing there. One of them had traveled to the Middle East and Pakistan, but the others had not, suggesting that the virus can spread between humans.

But many questions remain, and Fouchier says they're not being answered fast enough. The fact that five of the cases were diagnosed



in Europe means there must be unrecognized cases in the Middle East, he says; a program of antibody testing could reveal how many and yield more information on how the virus spreads. If bats are indeed the virus's reservoir, it's important to know how it got into humans. Infected bat urine or feces may have ended up in human food, for instance, but it's also possible that there is an intermediate host—for instance some farm animal. Surveys of goats, camels, cattle, and other domestic animals could quickly confirm or rule out these species as carriers.

Memish says Saudi Arabia is working to answer these questions, but that will take time; for instance, there aren't sufficiently reliable antibody tests at the moment. Fouchier disagrees. "You can answer a

lot of these questions within a month," he says. WHO held a meeting in Cairo in January to discuss the new virus with experts from the region and established labs elsewhere; Fouchier, who attended, says the meeting's goal of more international collaboration has not panned out. His own lab has offered technology, expertise, and training free of charge, he says, but there have been no takers. Drosten has had the same experience. WHO is less proactive than it was during SARS, Fouchier adds: "It's all handled much more cautiously."

Fukuda, who is now WHO's assistant director-general for health, security, and environment, chaired the Cairo meeting. He says that his own experience—including the frustrating 2003 visit to Beijing—has taught him to be patient. "In an ideal world, yes, we would have all the primary questions answered really quickly," Fukuda says. "But I accept it takes time for some of this information to come up." But the time for studies is now, Drosten says: NCoV may be only weakly transmissible between humans, but if it's circulating at low levels, it may evolve to become more adept at jumping from person to person: "For a virus, every day in the human host is a new day full of experiments."

Stöhr, who left WHO in 2007 and is now vice-president of Novartis Vaccines and Diagnostics, says WHO is in a difficult position. "Do you want to be criticized for overreacting, or do you want to be criticized at the end, when things have gotten out of hand, for not having gone far enough?" Given everything that happened 10 years ago, Stöhr says the former is probably the safer option.

—MARTIN ENSERINK

CREDITS (TOP TO BOTTOM): WHO; PETER PARKS/AFP/NEWS.COM

Outbreak explodes in Hanoi hospital; at least 22 staff members fall ill with influenzalike symptoms.

10 March

WHO issues a rare global alert about a severe form of "atypical pneumonia."

12 March



In second alert, WHO names disease SARS, calls it "a worldwide health threat" and issues travel advisories.

15 March

WHO sets up network of 11 labs to hunt for the agent causing SARS. Networks for clinicians and epidemiologists will follow.

17 March

Scientists in the lab network finger new coronavirus.

24 March

No touching. Patient isolation and staff member protection halts SARS transmission in hospitals.

Understanding the Enemy

Research sparked by the SARS outbreak increased the understanding of emerging diseases, though much remains to be learned

In the end, what made SARS such a threat to human health turned out to be surprisingly and alarmingly simple. Thirty months after the causative agent was found to be a novel coronavirus and 2 years after the disease had been stamped out, scientists determined that what gave the agent the ability to infect and sicken humans came down to two key amino acid changes in a viral protein. More digging has since uncovered still other tricks that SARS and all other coronaviruses have hidden in their genomes to bolster their chances of thriving and causing illness.

The findings are part of a legacy of an unprecedented scientific effort. The SARS outbreak came and went in just 8 months, infecting almost 8100 people in 29 countries and killing 774 (see p. 1264). But as soon as it emerged, dozens of labs around the world jumped into the fray. Working on parallel tracks, they tried to figure out the causative agent, where it came from, what made it so deadly, and how to stop it. Their effort and the work it spawned are continuing to increase our understanding of how zoonotic diseases emerge and spread and how they might be contained, if not prevented.

Online sciencemag.org

S Podcast interview with author Dennis Normile (http://scim.ag/pod_6125).

"SARS was the first pandemic of the 21st century and one of the best studied as it was ongoing and in retrospect," says Kathryn Holmes, a coronavirus specialist at the University of Colorado, Denver. "Over 3000 papers were published on the SARS coronavirus in the last 10 years," adds Kwok-yung Yuen, a microbiologist at the University of Hong Kong (HKU). Researchers have identified dozens of new coronaviruses in nature that could also threaten human health.

The understanding of the SARS virus and other coronaviruses came together piece by painstaking piece. Almost like a mystery writer planting misleading clues in a story, nature delivered a number of false leads. Even today, many aspects of the virus, the disease, and the epidemic remain a puzzle. That leaves nagging worries about how well prepared the world is if SARS or something like it stages a comeback.

An unexpected culprit

Shortly after the World Health Organization (WHO) issued its alerts about SARS in mid-March 2003, scientists at 11 labs in nine countries joined forces to try to understand the new threat. Putting aside their rivalries, they agreed to daily teleconferences to share their findings. Job one was to identify the cause of the disease, as that would lead to diagnostic tests and, possibly, treatments and vaccines.

WHO's Urbani dies of SARS in Bangkok.

29 March

Start of SARS outbreak in Amoy Gardens apartment complex in Hong Kong. More than 300 become infected.

30 March



WHO says that macaque study in Rotterdam clinches the case for a new coronavirus as the cause of SARS.

16 April

WHO team in Beijing expresses strong concern over inadequate reporting of SARS cases.

18 April

Beijing acknowledges 339 previously undisclosed cases. China's minister of health and mayor of Beijing are fired.

20 April

Several groups in Asia had started hunting for the causative agent soon after rumors surfaced of an unusual pneumonia circulating in China's southern Guangdong Province in January 2003. Scientists at the Chinese Center for Disease Control and Prevention in Beijing suspected chlamydia infection, as traces of that bacterium were found in lung tissue recovered from early SARS victims. Others focused on the avian influenza virus H5N1. When it had first emerged in Hong Kong in 1997, H5N1 killed six of 18 victims. The H5N1 hypothesis got a boost in mid-February, when it caused one death and one illness in a Hong Kong family that had visited Fujian Province, which neighbors Guangdong. But when clusters of atypical pneumonia cases surfaced in Hong Kong in early March, HKU researchers found no evidence of H5N1 infection. Then "we knew we were dealing with something completely out of the blue," HKU virologist Malik Peiris told *Science* in 2003 (9 May, p. 886).

The first breakthrough came on 24 March when WHO confirmed that three labs had independently concluded that a new coronavirus was the cause of SARS. "It was a surprise. Coronaviruses were considered quite harmless to humans," says Christian Drosten, a virologist then at the Bernhard Nocht Institute for Tropical Medicine in Hamburg, Germany, who led one of the groups. The other groups were at HKU and at the U.S. Centers for Disease Control and Prevention (CDC) in Atlanta. Although they had long posed a threat to livestock health, "in humans, coronaviruses were common cold agents, nobody had them on their list" of suspects for SARS, explains Drosten, now at the University of Bonn.

Before SARS, Drosten says, few human virologists worked on coronaviruses, which are named for the crownlike spikes on their surface. But that quickly changed.

Out of the wild

Several groups, including Drosten's, set about developing diagnostic tests. Others began looking for the virus's origins. It was natural to assume there was an animal reservoir "because 70% of emerging infections come from animals," Yuen says. The Hong Kong group, which was already monitoring flu viruses circulating in poultry in southern China, was perfectly positioned for the hunt.

Early epidemiological evidence suggested that many of the first suspected SARS cases had connections to the trade in wild mammals in Guangdong Province, which is home to distinctive culinary traditions. In addition to vegetables, poultry, fish, and reptiles of all kinds, wild beavers, rabbits, badgers, and other small animals were sold at live animal markets and either butchered on the spot or at restaurants specializing in exotic dishes. In early May 2003, Yi Guan, another HKU virologist, and his field team collected samples from animals at a large market in Shenzhen, just over the border from Hong Kong, and retrieved a virus similar to the SARS coronavirus from Himalayan palm civets (*Paguma*

larvata) and a raccoon dog (*Nyctereutes procyonoides*). The group also found that 12 of 55 market workers carried antibodies to the SARS virus, with the highest rates in those who handled wild animals. None of them reported having had any SARS-like symptoms within the previous 6 months. Guan and his colleagues concluded that the precursor to the human SARS virus had been circulating asymptotically among the animals and market workers. "The markets provided an environment for the virus to circulate and adapt," Guan says.

But Guan's team was unable to find the virus in civets in the wild, which suggested that the animals were an intermediary. So the hunt for the natural reservoir continued.

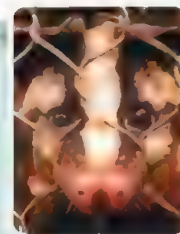
In September 2005, two groups simultaneously reported finding "SARS-like" viruses in Chinese horseshoe bats in Guangdong. One group, led by Australian researchers, had made an inspired guess that bats might be involved, knowing that bats harbor both Nipah and Hendra viruses, which had both recently caused human outbreaks. Similarly, a Chinese group had set its sights on fruit bats and got lucky when a young researcher grabbed and tested samples from horseshoe bats by mistake. The coronaviruses found in the bats were related to but still different from both the human and civet SARS viruses; their sequences were between 88% and 92% identical to the human coronavirus.

This means there is either a closer SARS progenitor virus lurking in nature or the virus found in the horseshoe bats underwent extensive mutation in unidentified intermediate hosts either in the wild or in Guangdong's animal markets.

The first 11 documented human cases of SARS came from different cities in a region within Guangdong Province. The patients had



Uncaged. Guangdong's live animal markets provided an ideal environment for a SARS precursor to mutate and adapt to humans.



Scientists announce detection of SARS-like virus in the Himalayan palm civet and raccoon dog.

Outbreaks in Hanoi, Hong Kong, Singapore, and Toronto show signs of peaking.

Vietnam becomes first country to successfully end SARS outbreak.

Toronto declared SARS-free.

Canada reports new SARS cluster in Toronto.

25 April

28 April

14 May

22 May

23 May

CREDITS (TOP TO BOTTOM): AP PHOTO/STR; PAUL HILTON/EPA/NEWS.COM

not been in contact with each other; seven of them had connections to the wild game trade, according to a 12 March 2004 *Science* paper (p. 1666) by a Chinese SARS consortium led by Guo-Ping Zhao of the Chinese National Human Genome Center in Shanghai. These initial cases likely contracted a virus from live animals in the markets. After that, the evidence suggests that with one or two exceptions, virtually all later patients were infected through human-to-human transmission. Apparently, one or more final changes had given the virus the ability to spread efficiently between humans, making it a truly global threat.

In sequence

But exactly what had changed in the virus during this exquisite adaptation to the human host? A new generation of faster and cheaper DNA sequencing technology gave researchers unprecedented power to find out.

The genomes of the human and civet coronaviruses turned out to be 99.8% identical. One glaring difference was a 29-nucleotide stretch that was present in samples from civets but missing in the human samples available then, which mostly came from patients in Hong Kong, who were infected at a later stage of the outbreak than those in Guangdong. Scientists initially thought this 29-nucleotide deletion might be involved in making the virus transmissible among and infectious in humans.

But that hypothesis was soon proven wrong. In the 12 March 2004 issue of *Science*, the Chinese SARS Consortium reported that some samples retrieved from early human cases in China did contain the suspect 29 nucleotides after all. And samples isolated from patients who became ill late in the outbreak had deletions in the same genomic region, but these were far larger—89 or even 415 nucleotides. The significance of the lost nucleotides, which all turned out to be in what is known as open reading frame (ORF) 8, is still not understood.

Mutations that changed the virus's spike, or S, glycoprotein turned out to be more important. Coronaviruses use their spike protein to attach to host cells, and if a cell does not have compatible receptors then the virus cannot infect it efficiently. Several groups started focusing on how the spike differed between the civet and human viruses and how it changed as the virus circulated among humans. Zhao's group found that the sequence of the spike protein changed rapidly as the virus moved from person to person early in the outbreak, but stabilized as it went on, presumably because the spike had become well adapted to human-to-human transmission.

Zhao's team and a second group from Harvard Medical School in Boston and other institutions narrowed their focus to differences in amino acids between the animal and human viruses at two key locations on the spike protein. At one, the civet S protein encoded for a serine, while the human virus encoded a threonine. And at the other

position, the civet's asparagine became a lysine in the spike protein of the human virus.

Then, a 16 September 2005 *Science* paper, by Fang Li of Harvard Medical School *et al.*, reported crystallizing both the spike protein binding domain and the human receptor, clarifying the significance of the amino acid changes (p. 1864). In the spike of the animal virus, the residues at the two key locations inhibited binding to human receptors. But the human SARS virus had a loop structure that could nestle snugly against human angiotensin-converting enzyme 2 (ACE2), a protein found on lung epithelial cells that the virus used as its entry point. The two key changes in the viral spike increased the binding affinity a thousandfold.

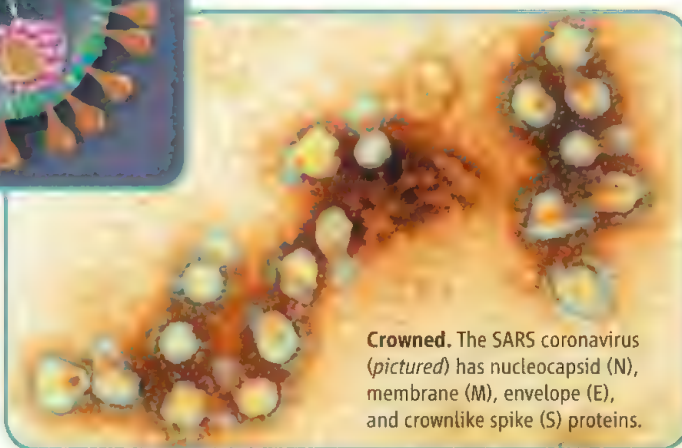
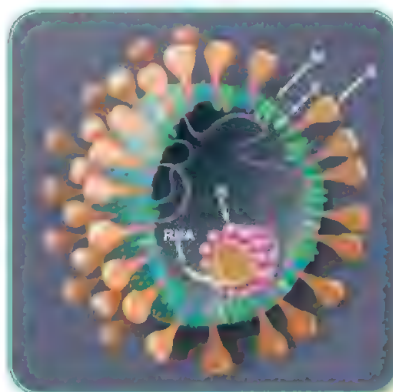
Those two adaptations were enough to give the virus the ability to infect humans and spread from person to person and cause lethal disease.

Accessories to the crime

Once the virus made the leap to humans, it caused serious disease. A better understanding of how it did so emerged only years later as researchers continued studying SARS and other coronaviruses.

All coronaviruses share four "core" genes—the spike, envelope, membrane, and nucleocapsid genes. They also have so-called accessory genes that are scattered through the genome between the core genes.

The accessory genes are not essential to viral survival and replication, but they do benefit the virus. Take the bit of extra genetic material designated ORF6 in the human SARS virus. In a series



Crowned. The SARS coronavirus (pictured) has nucleocapsid (N), membrane (M), envelope (E), and crownlike spike (S) proteins.

of experiments, Ralph Baric, a virologist at University of North Carolina, Chapel Hill, and colleagues found that ORF6 helps the virus escape detection by the human immune system. "Infect a cell with flu, and you have [an immune response] within 6 hours. In the case of SARS virus, it takes 36," Baric says. That delay gives the virus a head start on replicating and causing more serious disease. Accessory genes

Singapore declared
SARS-free.

31 May

Hong Kong declared
SARS-free.

23 June

Beijing declared
SARS-free.

24 June



Toronto declared SARS-
free a second time.

2 July

Taiwan declared SARS-
free. After 8096 cases
and 774 deaths, WHO
declares the end of the
SARS epidemic.

5 July

The Metropole, Superspreaders, and Other Mysteries

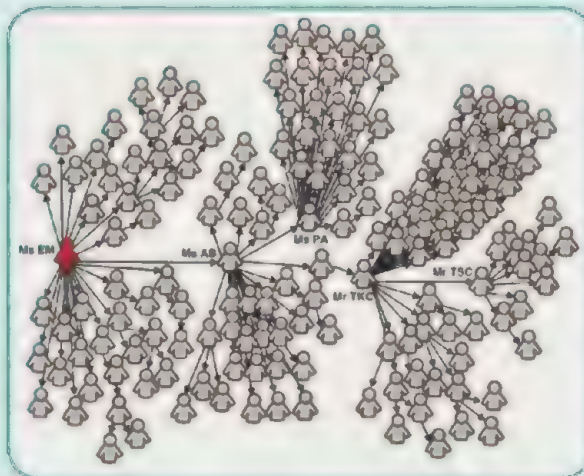
For all that has been learned about SARS in the intervening 10 years, some mysteries endure. Foremost is what happened at the Metropole Hotel in Hong Kong the night of 21 February 2003. A physician from Guangdong Province in southern China who worked at a hospital treating patients suffering from what was then called atypical pneumonia stayed in room 911 at the Metropole that night. He checked out the next morning but was admitted to a local hospital, where he died several days later.

Sixteen other guests who stayed at the hotel that night and one visitor contracted what was later identified as SARS and carried the novel coronavirus to Hanoi, Singapore, and Toronto, sparking outbreaks in those cities. Epidemiologists later traced close to half of the 8100 cases of SARS worldwide back to the Metropole Hotel. Whatever happened on the ninth floor turned what might have been a local outbreak of a new disease into an alarming global threat, underscoring just how quickly a new virus can spread with modern air travel.

But how the other guests were infected is not clear. It is unlikely they all met in the hallway or ele-

vator. And, strangely, no hotel staff members became sick.

A World Health Organization (WHO) investigative team from Canada visited the hotel, which



Links of contagion. One-hundred-forty-four of Singapore's 206 probable SARS cases were traced to a chain of five individuals that included four "superspreaders."

has since changed its name, in late April 2003 and collected samples from numerous surfaces in rooms on the ninth floor, the hallway, and even

the vacuum cleaner used in that wing and analyzed them for genetic material from the SARS virus. They tested the flow of air through the ventilation system and seals in the plumbing and ruled them out as avenues of transmission. The team made one surprising discovery: copious amounts of viral remnants on the carpet in front of room 911 but, curiously, not in the room itself. In a report dated July 2003, they speculate that the man vomited on the floor in front of his room and then, embarrassed perhaps, cleaned it up himself. Subsequently, other guests could have been exposed by walking through the contaminated area. While "there is no definite proof for the ... outlined scenario," as the July 2003 report concludes, many say it's as good a guess as any.

Another peculiar event at the Amoy Gardens, a high-rise apartment building complex in Hong Kong, in late March and early April 2003 also sent confusing signals about how easily the virus was spreading in the community. At the time, it was not clear if the causative agent was being transmitted by airborne particles, as measles and tuberculosis spread, or by infected respiratory droplets, which carry most flu viruses, for example, only a short distance. It was later determined that a man who lived in Guangdong possibly became

vary in number, location, and function among the different coronavirus groups. How coronaviruses acquired and adapted this genetic material is a mystery.

Lucky break

When the first clusters of SARS cases occurred in quick succession in cities around the world, public health experts feared this new disease would quickly circle the globe and threaten millions. Several alarming events—such as a cluster of more than 300 infections at an apartment complex and the spread of infection through guests at a hotel, both in Hong Kong—heightened those fears (see sidebar, above). But in retrospect, "SARS was nowhere near as infectious as influenza," Holmes says. Both flu and SARS spread through respiratory droplets that usually travel within about a 1-meter circumference of a person. But flu patients start producing and expelling virus through sneezing and coughing before they start feeling feverish. This means that they are likely to continue normal activities and come into contact with strangers.

However, SARS patients did not start shedding virus until the onset of symptoms, 7 to 10 days after infection. By that time, they tended to be so sick that they stayed home or checked into a hospital, which is one reason why secondary infections occurred mostly among household members and health care workers.

Early on, before the virus was identified and its transmission dynamics understood, hospital practices unwittingly aided its spread. On 4 March, a patient was admitted to Hong Kong's Prince of Wales Hospital with severe pneumonia. A week later, more than 112 health

care workers and patients came down with SARS. It turns out the patient was given a nebulizer to deliver antibiotics to his lungs. But nebulizers can atomize respiratory droplets, enabling them to waft about the room. In other early cases, patients suffering from advanced pneumonia were intubated, a procedure in which a tube is passed through the mouth into the trachea to force air into the lungs. This also exposed health care workers to infectious respiratory droplets. Hospital infections—including staff members, other patients, and visitors—accounted for more than 70% of SARS cases in Toronto and Singapore.

Hospitals soon recognized the problem. "But in the beginning, it was an uphill battle, it was very difficult to prevent hospital infections," says Joseph Sung, who is now university president and who was then chief of medicine and therapeutics at Prince of Wales Hospital, which is affiliated with the Chinese University of Hong Kong. Sung explains that wards were congested and didn't have proper isolation facilities; the staff members were not familiar with protection procedures; and there was a shortage of basic equipment such as masks.

"Hospital-based infections were hugely important in the expansion of SARS, and shutting them down through good infection control was essential to stamping out the outbreak," says James Lloyd-Smith, an epidemiologist and disease ecologist at University of California, Los Angeles.

For controlling infections outside hospitals, "We were a bit lucky," Baric says. The 7- to 10-day gap between infection and the onset of viral shedding gave officials a window of opportunity to trace contacts and quarantine them, even though there was spotty compliance with some quarantine regimes.

CREDIT: WHO/WPRO



Lingering mystery. A man who spent one night at Hong Kong's Metropole Hotel (left) spread SARS to other ninth floor guests who later sparked outbreaks in Hanoi, Toronto, and Singapore.

infected at Hong Kong's Prince of Wales Hospital where he was being regularly treated for a chronic renal condition. Already ill and suffering diarrhea, he spent the nights of 14 and 19 March with his brother, who lived in Amoy Gardens. Over the next month, more than 300 Amoy Gardens residents contracted SARS.

Studies and experiments by the Hong Kong government later identified a possible scenario. The bathrooms of the Amoy Gardens apartments had drains in the floors with standard water traps of the kind seen in plumbing throughout the

world. However, investigators found that few residents relied on the drains, mopping bathroom floors instead of hosing them. This allowed the water traps to dry out. The same piping was connected to the toilets. Investigators concluded that the diarrhea from the patient flushed into the system and produced aerosols that traveled through the piping and into bathrooms, where the moist environment allowed the virus to survive. This transmission route likely spread the infections through one block of apartments and from there, through person-to-person contact.

The Amoy and Metropole index cases remain at the center of another unsolved puzzle: They were among what came to be called "super-spreaders," who accounted for a disproportionate number of further infections, in some cases passing the virus on to more than a dozen other people (see graphic). "SARS made superspreading impossible to ignore," says James Lloyd-Smith, an epidemiologist at the University of California, Los Angeles. But he adds that his own investigations and modeling, reported in a 17 November 2005 *Nature* letter, have shown that the superspreader phenomenon occurs with other infectious diseases, including measles and smallpox. He says superspreading likely results from a combination of biological factors, transmission routes, contact rates, and travel patterns of the infected people. Kwok-yung Yuen, a microbiologist at the University of Hong Kong who was heavily involved in understanding the SARS outbreak, agrees that superspreading "is still a mystery." Like Lloyd-Smith, he suspects a confluence of factors. For instance, superspreaders could have been suffering from another illness at the same time that caused coughing and sneezing that helped spread the SARS virus. Lloyd-Smith says that in epidemiology, it is important to be wary of averages: Many infected with disease don't pass it on at all, but some become superspreaders.

—D. N.

Can it return?

SARS may be the second human pathogen, after smallpox, to ever be eradicated. But is it gone for good? "Coronaviruses are important emerging pathogens," Baric says. "They are highly mobile, can jump between species by recombination or mutation, and when they do, they cause micro-outbreaks with the potential to drive additional mutations that enhance person-to-person transmission," he adds.

Recent research suggests that most, if not all, of the known human coronaviruses originated in animals, sometimes in the not too distant past. In the February 2005 *Journal of Virology*, virologist Marc Van Ranst and colleagues at the Catholic University of Leuven in Belgium concluded that the human coronavirus OC43, which causes the common cold, likely resulted from an adaptation of a bovine coronavirus around 1890. Drosten's group claimed in *Emerging Infectious Diseases* in September 2009 that human coronavirus 229E, another common cold culprit, likely diverged from a bat coronavirus between 1686 and 1800.

Last September, a group at the University of Maryland, Baltimore, and other institutions reported, also in the *Journal of Virology*, that the human coronavirus NL63 likely diverged from a common ancestor in bats 563 to 822 years ago. Just discovered in 2004, NL63 causes a type of lung inflammation common in infants.

Researchers and public health officials are now closely watching the latest new human coronavirus to make the jump, alternately called EMC or NCoV. First discovered in Saudi Arabia last June, the virus has sickened 14 people and killed eight. This virus, too, seems to have originated in bats. So far "it is not as transmissible

as SARS," says Drosten, who was involved in identifying the virus and in developing a diagnostic test. He and colleagues reported in the 11 December 2012 issue of *mBio* that the new virus does not latch onto the ACE2 receptor that provided such efficient entry for the SARS virus. In a letter in this week's issue of *Nature*, the group identifies dipeptidyl peptidase 4 as a receptor for the new virus. "It remains to be seen how important the disease will be epidemiologically," Holmes says.

Meanwhile, few researchers rule out a repeat performance by the SARS virus or something very close to it. Indeed, it almost came back. During the winter of 2003 to 2004, four people in Guangdong contracted a SARS-like illness. They had no contact with one another, and each developed mild disease. Sequence analysis by Zhao and his collaborators revealed that all four were infected with the same coronavirus—and it had one of the two key mutations found in the lethal SARS virus that caused the global epidemic. The group also found civets carrying a nearly identical virus with the same mutation. They concluded in a 15 February 2005 paper in the *Proceedings of the National Academy of Sciences* that the precursor to the SARS virus had continued to circulate in animals in the province, and in late 2003, one of the two key proteins mutated again, allowing it to infect humans and cause illness, but not with the same transmissibility or virulence of the 2002 to 2003 strain. Scientists convinced authorities to ban wild game from the markets. Aside from a few incidents of laboratory infections, no further human cases of SARS have ever been found.

—DENNIS NORMILE

LETTERS

edited by Jennifer Sills

Latin American Science:
Much Work Remains

AT A TIME WHEN REMARKABLY FEW LATIN AMERICAN countries are improving their research capacity, it seems incongruous to display much enthusiasm about the future of science, technology, and innovation in the region. The Editorial "Growing Latin American science" asserts that the region is swiftly improving its research capacity (C. R. S. Garcia *et al.*, 30 November 2012, p. 1127). By not clarifying that only a handful of Latin American countries are experiencing scientific growth, the optimism reflected in the Editorial is somewhat misleading.

Despite increasing its share of publications from 1 to 4% in the past 30 years, Latin America remains a small player on the world scale, ranking behind Europe, Asia, North America, and the Middle East (1). In Latin America, scientific growth is far from uniform. Brazil, Mexico, Argentina, Chile, and Colombia combined contribute 95% of all scientific publications in the region (2). The remaining countries lag far behind the rest of the world.

Insufficient investment in R&D has resulted not only in subpar academic quality, but also in minimal synergy between industry and universities. In 2009, investment in R&D in Latin America was equivalent to 0.69% of GDP, compared to 2.40% in Organization for Eco-



nomomic Co-operational and Development (OECD) countries (3). In some countries in the region, meager increases in public spending on R&D reflect an overall increase in spending as the economies grow, rather than a greater ratio in R&D.

Although some training fellowships have been established in the region, they are generally limited to the largest economies. To move from scientifically lagging to scientifically proficient, smaller countries need to create a weightier pool of scientists, invest more resources, and strengthen their science programs. Most important, they would benefit from improved science, technology, and innovation strategies to lead them toward knowledge-based economies.

Although positive news regarding science in powerhouse nations such as Brazil is encouraging, we shouldn't be blind to the fact that much remains to be done to advance science in Latin America.

JORGE A. HUETE-PÉREZ

Molecular Biology Center, University of Central America, Managua, Apartado 69, Nicaragua.
E-mail: jorgehuete@uca-cbm.org

References

1. E. Archambault, "Thirty years in science: Secular movements in knowledge creation" (Montreal, Quebec, Monograph, Science-Metrix, 2010); www.science-metrix.com/30years-Paper.pdf.
2. The SCImago Journal & Country Rank (www.scimagojr.com).
3. RICYT (Network for Science and Technology Indicators), Database of Indicators (2011); www.ricyt.org [in Spanish].

Latin American Science:
Sustainable Careers

IN THEIR EDITORIAL "GROWING LATIN American science" (30 November 2012, p. 1127), C. R. S. Garcia *et al.* embrace a new hope for science in Latin America thanks to the boost in the region's economy. In the past, first-world nations have made huge investments in scientific research to foster international competitiveness, under the premise that the production of knowledge is an essential strategy for economic development. Between 1998 and 2008, the number of awarded doctorates grew annually by nearly 40% in countries belonging to the Organization for Economic Co-operation and

Development (OECD) (1). Similar trends in numbers of postdocs have been documented in other parts of the world (2).

However, in the United States and parts of Europe, there is now an excessive supply of young researchers and lack of academic demand for them (3). Industry, government, and other organizations can mitigate the effect in some places (1), but in others such imbalance cannot be sustained. This is true in the life sciences and particularly in biomedicine (4).

Scientists in Latin America should think in advance about these issues, learn from the Western world, and work to prevent a collapse of the academic system while offering sustainable research careers for young scientists.

CARLOS G. ACEVEDO ROCHA

Max-Planck-Institut für Kohlenforschung, Kaiser-Wilhelm-Platz, Muelheim an der Ruhr, Germany; World Association of Young Scientists (WAYS). E-mail: acevedor@kofo.mpg.de

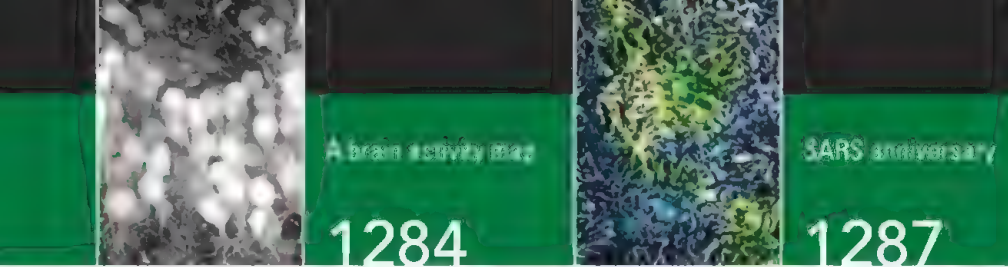
References

1. D. Cyranoski, N. Gilbert, H. Ledford, A. Nayar, M. Yahia, *Nature* **472**, 276 (2011).
2. R. Van Noorden, *Nature* **490**, 326 (2012).
3. V. Uskokovic, *J. Postdoc. Affairs* **1**, 31 (2011).
4. M. Wadman, *Nature* **486**, 304 (2012).

University Rankings
Could Bias Funding

THE NEWS & ANALYSIS STORY "BRUSSELS ranking' of universities off to a rocky start" (T. Rabesandratana, 25 January, p. 383) discusses a new plan for ranking universities called the U-Multirank, which rates universities according to their quality. This plan may

CREDIT: ISTOCKPHOTO



lead to a polarization of research funding.

The misuse of such a university ranking list may aggravate an existing bias in the review process: Research teams from well-rated universities, which in most cases already have good funding, have an advantage compared with research groups at low-rated universities when competing for funding resources (1). Ranking universities may also aggravate the already difficult access to financial support for junior research groups; senior research groups, with larger and well-funded laboratories (2), are more likely to be affiliated with well-rated universities.

Ranking universities is not new (for example, the Academic Ranking of World Universities has existed for a decade), but emphasizing the importance of such lists, as seems to be the European Union's intent for the U-Multirank, may harm the research enterprise. If a university's rank is used to judge research proposals and allocate funding, high-quality and innovative research ideas proposed by researchers at low-rated universities may never see the light of day.

PHILIPPE DE SOUTO BARRETO

Gérontopôle de Toulouse, Institut du Vieillessement, Centre Hospitalo-Universitaire de Toulouse (CHU Toulouse), 31000, Toulouse, France. E-mail: philipebarreto81@yahoo.com.br

References

1. InterAcademy Council and IAP (The Global Network of Science Academies), "Responsible conduct in the global research enterprise: A policy report" (2012); www.interacademies.net/10878/19787.aspx.
2. A. A. Hyman, *Science* **339**, 119 (2013).

The Race to Name Earth's Species

IN THEIR REVIEW "CAN WE NAME EARTH'S species before they go extinct?" (25 January, p. 413), M. J. Costello *et al.* answer in the affirmative. I am not so sure.

Costello *et al.* could be underestimating global biodiversity by concluding that Earth likely sustains only 2 to 8 million species of eukaryotes. Studies they review suggest that there might be 6.1 to 7.8 million species of terrestrial arthropods alone, as well as 0.3 to 1.0 million marine species and 0.3 to 0.4 million species of plants (1). Even if one ignores the relatively small number of vertebrate spe-

cies, many other taxa—including nematodes and other worm phyla, fungi, and other terrestrial and freshwater invertebrates—could be impressively species-rich. Beyond this, there are myriad microscopic eukaryotes (2). I am also less sanguine than are Costello *et al.* about the world's undescribed biodiversity. Such "missing" species likely include many local endemics (3), small-sized or non-descript species, species that live in poorly explored places such as the rainforest canopy or deep oceans, morphologically cryptic species, and those that simply are very good at hiding (1). Even with improving genetic and other technologies, some of these taxa may be extremely difficult to find or catalog. Moreover, because the missing species are almost certainly a nonrandom component of all biodiversity, our incomplete view of life on Earth likely suffers from various selective biases. Finally, even with growing taxonomic expertise in developing nations, it is far from certain that sufficient effort will be focused on the world's imperiled biodiversity hotspots (4), which are likely to house the bulk of undescribed species (3, 5).

I agree with Costello *et al.* that lower to intermediate extinction rates (0.1 to 1% per decade) for contemporary species are most plausible at present, but feel they might be too optimistic about future extinction rates. Forests are indeed regenerating in certain parts of the world, and this could aid some species (6). However, many regrowth forests are being recleared before they become old enough to sustain much biodiversity (7), and considerable forest "recovery" worldwide involves monocultures of nonnative species such as oil palm, rubber, and eucalyptus trees that have limited value for endangered wildlife (8). Threats to biodiversity from increasing land-use pressures and climate change are likely to intensify.

By focusing on species, Costello *et al.* overlook other facets of the modern biodiversity crisis. Losses of large-sized species such as many vertebrates (9) and old-growth trees (10), in concert with myriad species invasions and other environmental stresses, are causing marked ecological distortions in terrestrial and marine ecosystems worldwide (9–11). Beyond this, many species are losing sub-

stantial genetic variation as their populations collapse. Human-caused population bottlenecks have led to deleterious genetic effects and reduced viability in many endangered species or subspecies, including the Florida panther (12), Speke's gazelle (13), and fritillary butterfly (14).

Great strides are being made in technical fields that could improve the pace and quality of species descriptions. Beyond this, however, major uncertainties still cloud our understanding of the amount of extant biodiversity and its fate in the coming centuries.

WILLIAM F. LAURANCE

Centre for Tropical Environmental and Sustainability Science and School of Marine and Tropical Biology, James Cook University, Cairns, QLD 4878, Australia. E-mail: bill.laurance@jcu.edu.au

References

1. B. R. Scheffers, L. N. Joppa, S. L. Pimm, W. F. Laurance, *Trends Ecol. Evol.* **27**, 501 (2012).
2. J. Pawlowski *et al.*, *PLoS Biol.* **10**, e1001419 (2012).
3. L. N. Joppa, D. L. Roberts, N. Myers, S. L. Pimm, *Proc. Natl. Acad. Sci. U.S.A.* **108**, 13171 (2011).
4. N. Myers *et al.*, *Nature* **403**, 853 (2000).
5. W. F. Laurance, D. P. Edwards, *Proc. Natl. Acad. Sci. U.S.A.* **108**, 12971 (2011).
6. S. J. Wright, H. C. Muller-Landau, *Biotropica* **38**, 287 (2006).
7. C. A. Almeida, D. Valeriano, M. Escada, C. E. Rennó, *Acta Amazonica* **40**, 289 (2010).
8. W. F. Laurance, *Trends Ecol. Evol.* **22**, 65 (2007).
9. G. Ceballos, P. R. Ehrlich, *Science* **296**, 904 (2002).
10. D. B. Lindenmayer, W. F. Laurance, J. F. Franklin, *Science* **338**, 1305 (2012).
11. J. A. Estes *et al.*, *Science* **333**, 301 (2011).
12. M. E. Roelke, J. S. Martenson, S. J. O'Brien, *Curr. Biol.* **3**, 340 (1993).
13. S. T. Kalinowski, P. W. Hedrick, P. S. Miller, *Conserv. Biol.* **14**, 1375 (2000).
14. I. Saccheri *et al.*, *Nature* **392**, 491 (1998).

CORRECTIONS AND CLARIFICATIONS

Editorial: "Designing scientific meetings" by B. Alberts (15 February, p. 737). The first paragraph states that Gordon Research Conferences are often confined to fewer than 125 attendees. The conferences are limited to 200 attendees. The statement "There is no longer a Gordon Conference called Nucleic Acids" is incorrect. The Nucleic Acid Gordon Research Conference is ongoing and scheduled to take place 2 to 7 June 2013 at the University of New England in Biddeford, Maine.

Articles: "A new boson with a mass of 125 GeV observed with the CMS experiment at the Large Hadron Collider" by The CMS Collaboration (21 December 2012, p. 1569). In the abstract, the mass of the new particle should have been 125 giga-electron volts. The HTML and PDF versions online have been corrected.

Letters to the Editor

Letters (~300 words) discuss material published in *Science* in the past 3 months or matters of general interest. Letters are not acknowledged upon receipt. Whether published in full or in part, Letters are subject to editing for clarity and space. Letters submitted, published, or posted elsewhere, in print or online, will be disqualified. To submit a Letter, go to www.submit2science.org.

ENVIRONMENT

Approaching the Limits

Steven W. Running

One of the foundational principles of biology is that a population cannot grow forever in a finite ecosystem—a progressive system feedback of starvation, predation, and disease limits uncontrolled growth. The global human population has now nearly tripled since 1950, and economic activity increased tenfold, leading many to suggest that humanity is heading toward a population and consumption overshoot (resource depletion and correction, as economists would say). In *Harvesting the Biosphere*, Vaclav Smil traces the historical development of human consumption of biological resources and evaluates whether we could be approaching important global limits. Smil (an economist at the University of Manitoba) has written several books on global energy and other resource issues; here, he focuses on human consumption of the plant and animal life and whether current trends are sustainable.

To begin, Smil addresses whether the total plant and animal biomass on Earth can be measured adequately. Of greater value is the annual plant production of new biomass [net primary production (NPP)], which serves as the foundation of all food chains. The introduction of Earth-observing satellites in the 1980s provided the first defensible measure of plant growth at global scales, and Smil illustrates the latest capability with a NASA image of global annual NPP (which should have been reproduced in color). Smil traces the history of global estimates of NPP through to the now commonly accepted range of 53 to 59 Pg carbon per year for land and 50 Pg carbon for oceans, estimates rather well constrained by mass balancing

the global carbon cycle with the atmosphere and human emissions.

Smil next addresses the key question of what fraction of this global NPP humans currently consume. He critiques the methodology of estimates of the human appropriation of NPP (HANPP), beginning with Peter Vitousek *et al.*'s original (1986) calculation of 32 to 40% (1). Most authors define



Intensively farmed. Agricultural lands in Minas Gerais, Brazil (10 February 2011).

HANPP rather expansively as all biospheric production used for human benefit, a conceptually satisfying but methodologically challenging interpretation that includes crops, forest plantations, grazing land, and the negative impacts of habitat destruction and environmental degradation. Choosing to estimate HANPP using only agricultural and forestry harvest statistics, Smil arrives at a lower estimate of 17 to 20%, a level that might appear to be sustainable.

However, one cannot assume that all of global NPP is potentially available for human use. Some regions of the Amazon or Siberia, for example, are too remote for harvest. More important, do we really want to plow and clear the whole world? Most of us want to preserve some natural systems for biodiversity, ecosystem services (such as water and air purification), recreation, or aesthetic beauty. Human settlements and infra-

structure, termed impervious surfaces, presently cover only 0.44% of Earth's continental surface, whereas agriculture and grazing lands cover about 40%. Although global NPP currently appears stable, Smil suggests the great potential for pollution, exhaustion of soil nutrients, and irrigation depletion to substantially reduce the future NPP available for humanity. In addition, bioenergy is emerging as a massive new demand on NPP. Should fossil fuels become scarce, expensive, or unwanted, biofuels could, if allowed by policy and economic strategies, consume all remaining available NPP (2).

The future limits of HANPP become an urgent policy issue when one considers the

40% increase in global population expected over the next three or four decades and the expansion in living standards aspired to by the underdeveloped world. Smil expects that current policies will lead to a two- to threefold increase in HANPP demand in the next half century, and he rightfully asks if this increase is possible.

Scholars around the world have been asking roughly this same question since 1972, when the landmark *Limits to Growth* book appeared (3). More recent analyses—such as the global human footprint, planetary boundaries, and Gaia—address the question from various angles. Each has indicated that another half-century of the current trajectory of human development, consumption, and economic aspirations does not appear possible (4–7).

Smil's final recommendations echo others: global population must be stabilized at or below 9 billion; agriculture has to become sustainable, no longer relying on fossil-fuel-based fertilizers and mining groundwater for irrigation; meat consumption must be moderated; and food storage and processing must be improved and wastage minimized. Crucially, the rich nations have to share global resources more equitably with emerging countries, as simply growing more does not appear possible.

Full of recent references and statistics, *Harvesting the Biosphere* adds to the growing chorus of warnings about the current trajectory of human activity on a finite planet, of which climate change is only one dimen-

Harvesting the Biosphere
What We Have Taken from Nature

by Vaclav Smil

MIT Press, Cambridge, MA, 2012

315 pp. \$29, £19.95

ISBN 9780262018562

The reviewer is at the Numerical Terradynamic Simulation Group, University of Montana, Missoula MT 59812, USA. E-mail: swr@ntsg.umd.edu

CREDIT: ISS02&E02537/IMAGE SCIENCE AND ANALYSIS LABORATORY, NASA-JOHNSON SPACE CENTER

sion. One can quibble with some assumptions or tweak Smil's calculations, but the bottom line will not change, only the time it may take humanity to reach a crisis point. Systems ecology teaches that the human population and consumption trajectories need a stronger feedback control than currently exists. Either we are smart enough to craft that feedback mechanism ourselves, or the Earth system will ultimately provide it. Unfortunately, the tragedy of the commons suggests that collective international actions to voluntarily reduce consumption are contrary to human nature.

References

1. P. M. Vitousek, P. R. Ehrlich, A. H. Ehrlich, P. A. Matson, *Bioscience* **36**, 368 (1986).
2. W. K. Smith et al., *Bioscience* **62**, 911 (2012).
3. D. H. Meadows et al., *The Limits to Growth: A Report for the Club of Rome's Project on the Predicament of Mankind* (Universe, New York, 1972).
4. www.footprintnetwork.org.
5. J. Lovelock, *The Vanishing Face of Gaia: A Final Warning* (Basic, New York, 2010).
6. J. Randers, *2052: A Global Forecast for the Next Forty Years* (Chelsea Green, White River Junction, NH, 2012).
7. A. Wijkman, J. Rockstrom, *Bankrupting Nature: Denying Our Planetary Boundaries* (Routledge, London, ed. 2, 2012).

10.1126/science.1235886

PHILOSOPHY OF SCIENCE

A Flawed Challenge Worth Pondering

Kristina Musholt

What are the limits of the scientific method? This is the question that lies at the heart of *Mind and Cosmos*. With science laying ever-increasing claims on questions once regarded as unanswerable by empirical means, philosopher Thomas Nagel argues that science is—in principle—unable to explain the mind. And because “mind is not just an afterthought or an accident or an add-on, but a basic aspect of nature,” science’s inability to account for mentality strikes at the core of its endeavor to make sense of the world.

Nagel (New York University) has long been concerned with the problem of consciousness and the question of whether consciousness can be reduced to its biological basis. In his famous paper “What is it like to be a bat?” (1), he argued that however much we may come to know about the physiology

of bats, we will never be able to know what it feels like to be one. Accordingly, the scientific method, in this case physiology, fails to provide us with a certain kind of knowledge—the understanding of what the phenomenal experience of a bat would be. Similarly, although neuroscience and psychology are currently making great strides toward a better understanding of the neural and functional correlates of consciousness, one can always ask why a particular brain state or function should be associated with a particular (or indeed any) conscious experience. Consciousness simply does not seem to be reducible to the functional role played by states or processes in the brain.

In *Mind and Cosmos*, Nagel picks up this argument and takes it a step further. He contends that the irreducibility of the mental to the physical also has implications for evolutionary theory. In his view, an evolutionary explanation for the appearance of consciousness would have to show “why the appearance of conscious organisms, and not merely of behaviorally complex organisms, was likely.” To do so, presumably, evolutionary theory would have to give an account of the adaptive role played by consciousness. However, if consciousness cannot be reduced to the functional role played by processes in the brain, natural selection has nothing to work on. For every adaptive function we can identify, one can always ask why it should have a particular (or any) phenomenal character. The alternative, that consciousness could be seen as a mere by-product (or spandrel) of evolution, appears equally unsatisfying to Nagel because he takes consciousness to be one of the “systematic features of the natural world.”

Thus, we are left with “a double mystery”: We can explain neither the relation between the mental and the physical nor how or why consciousness evolved. According to Nagel, this should encourage us to look for a radical alternative to the “materialist neo-Darwinian conception of nature.” Indeed, Nagel believes that to make progress with regard to these questions, we need a major conceptual revolution akin to the scientific revolution itself. More precisely, he holds, we should consider the possibility that life and consciousness might not just be a result of the laws of physics and chemistry in combination with natural selection. What else might there be? Nagel does not give us much detail about the alternative he envisages; his aim is “to present the problem rather than to

propose a solution.” He does, however, point to the Aristotelian notion of “natural teleology” for a possible alternative—that is, the idea that there is a purpose or direction in the evolution of life.

Although Nagel presents us with good reasons to reject reductionism (the view that everything that exists, including consciousness, can ultimately be explained in terms

of physics), his claims for the necessity of a major scientific revolution are much less compelling. Indeed, whereas he takes reductionism to be the mainstream position in philosophy and science, Nagel is in fact far from being alone in making the case for antireductionism. Yet the fact that not every phenomenon is fully explicable in terms of physics does not imply that materialism (the view that everything

that exists is ultimately physical) is false or that science is in need of radical overhaul. The problem of consciousness could be a conceptual problem, whose solution (or dissolution, as some philosophers would have it) simply falls outside the remit of empirical science.

Moreover, it remains unclear why Nagel insists that evolutionary theory must demonstrate that the appearance of consciousness was something to be expected in order to render it intelligible. We have perfectly reasonable explanations for many events that were unlikely to occur but did. It remains even more unclear how the alternative that Nagel gestures toward is any more illuminating than the theories he rejects. Why should it be any less mysterious to think that consciousness is the result of teleological principles in addition to natural selection than that it is the unlikely (though not impossible) result of natural selection alone? That said, Nagel's arguments against reductionism should give those who are in search of a reductionist physical “theory of everything” pause for thought.

Overall, many aspects of *Mind and Cosmos* are problematic. Nonetheless, the book serves as a challenging invitation to ponder the limits of science and as a reminder of the astonishing puzzle of consciousness. Whether or not you believe that this puzzle can ultimately be solved by science, it is certainly one worth thinking about.

References

1. T. Nagel, *Philos. Rev.* **83**, 435 (1974).

10.1126/science.1235036

The reviewer is at the Department of Philosophy, Lakatos Building, London School of Economics, Houghton Street, London WC2A 2AE, UK. E-mail: k.musholt.lse.ac.uk

End the Deadlock on Governance of Geoengineering Research

Edward A. Parson^{1*} and David W. Keith²

Proposals for research on geoengineering methods to offset greenhouse-gas-driven climate change have attracted controversy (1–6). Multiple methods have been proposed (7), but attention and controversy have centered on methods to reduce incoming sunlight—for example, spreading reflective aerosols in the stratosphere or spraying condensation nuclei to increase low ocean clouds (1, 2). Such high-leverage interventions offer the dual prospect of large benefits and harms. They may reduce climate-change risks faster than any other response. Yet they may also cause environmental harm or worsen policy failures—for example, undermining emissions cuts or triggering international conflict. Research is needed to develop capabilities and assess effectiveness and risks (field research as well as model and laboratory studies), but geoengineering requires competent, prudent, and legitimate governance (1, 2, 8). We propose specific steps to advance progress on research governance.

Questions of Scale and Self-Regulation

No such governance now exists beyond normal scientific review processes and national laws, so geoengineering outside national territory—from small field research to operational deployment—falls under no international legal control (9). Recognizing this void, several projects have tried to develop guidelines on governance of geoengineering research (10–13). These projects have achieved agreement on the need for research, the need for governance of research, and the principle that as the scale and anticipated risk of interventions increase, so does the need for assessment, scrutiny, and control. But these consensus statements have been at high levels of abstraction, lacking the specificity needed to help any body—governmental or scientific—enact operational

governance and assessment procedures.

In particular, no progress has been made on two questions that are basic to designing

NEAR-TERM STEPS TO BREAK THE DEADLOCK

Accept government authority over geoengineering research

- Scientific self-regulation insufficient to manage risks
- First steps: informal coordination; new laws or treaties not required

Declare moratorium on large-scale geoengineering

- Possible large-scale threshold: nondetectable global climate signal
- Solar methods: threshold defined by area, time, and size of RF perturbation
- Possible threshold: annual average $\Delta RF < \sim 10^{-2} \text{ Wm}^{-2}$

State small-scale threshold below which research may proceed

- Modest new requirements: existing regulations, transparency, no forum-shopping
- Possible threshold: annual average $\Delta RF < \sim 10^{-6} \text{ Wm}^{-2}$

a governance system. First, if large interventions need more control than small ones, how is the boundary between “small” and “large” defined? Second, can scientific self-regulation adequately control small-scale research, or is government regulation needed—and, if it is, what should be the relation between regulatory and scientific processes?

Debate on these questions is increasingly polarized. One view, advanced by some non-governmental organizations and a few scientists, invokes direct environmental risks (often exaggerated) and a slippery slope from research to deployment to seek strict control on a broad set of activities—for example, all geoengineering research, all field research, or all active environmental perturbation, no matter how small. Practical obstacles to this approach are considerable, because impacts of proposed research can be tiny relative to many activities not so restricted—for example, single aircraft flights, fish farms, or sewage outfalls. This approach would thus control activities by their purpose, targeting research but not similar nonresearch acts, or geoengineering research but not similar nongeoeengineering research, distinctions that would be hard to enforce and create incentives to avoid oversight by concealing an activity’s purpose.

An opposing view, widespread but quietly expressed, invokes these practical objections to regulation, plus broad appeals to freedom of inquiry, to reject any new controls on research. This view holds that geoengineering

Can scientific self-regulation control small-scale research, or is governmental regulation needed?

research should be treated as ordinary scientific research, acknowledging no special policy significance or need for scrutiny. It thus presumes that scientific processes and existing regulations can ensure that geoengineering research is done prudently and with minimal environmental risk and that the public will trust that this is so.

Controversy over a rogue ocean fertilization project in 2012 illustrates the risks of the current deadlock. Funded by a Haida village and conducted west of British Columbia, the project spread 100 metric tons of iron-rich dust over 10,000 km² of ocean to stimulate phytoplankton growth, aiming to restore depleted salmon stocks and create carbon credits (14, 15). Lacking adequate measurement and controls, the project was apparently done without knowledge of Canadian authorities, yet violated no international law (16–18). Worldwide controversy followed, including an attempt in the United Nations Convention on Biodiversity to strengthen a 2010 decision opposing all geoengineering research.

Such controversies should be expected because the stark tension inherent in geoengineering’s dual prospect—large risk reduction and grave new risks—breeds polarization. We thus expect both periodic recurrence of adventurers pushing reckless, scientifically weak projects and rejecting any control, and zealous opponents seeking to prohibit the entire domain of activities. As in so many conflicts, the extremes reinforce each other: Every irresponsible, ill-conceived intervention—even if tiny in scale and risk—empowers the abolitionists, risking broad bans or burdensome restrictions that frustrate even low-risk, high-value research. In turn, pursuit of such overbroad controls affirms the view of scientists who reject all geoengineering concern as uninformed and antiscientific and encourages adventurers and legitimate scientists alike to find ways to escape scrutiny.

Defining Thresholds, Accepting Oversight

This deadlock poses real threats to sound management of climate risk. Geoengineering may be needed to limit severe future risks, so

¹Emmett Center for Climate Change and Law, UCLA School of Law, Los Angeles, CA 90095, USA. ²Kennedy School of Government, Harvard University, Cambridge, MA 02138, USA.

*Author for correspondence. parson@law.ucla.edu

informed policy judgments require research on its efficacy and risks. If research is blocked, then in some stark future situation where geoengineering is needed, only unrefined, untested, and excessively risky approaches will be available. To avoid this policy train wreck, progress on research governance is needed that advances four aims: (i) letting low-risk scientifically valuable research proceed; (ii) giving scientists guidance on the design of socially acceptable research; (iii) addressing legitimate public concern about reckless interventions or a thoughtless slide from small research to planetary manipulation; and (iv) ending the current legal void that facilitates rogue projects. Although full specification of a governance regime will take time and broad consultation, we propose specific first steps (see the table).

To the extent that projects can raise support from nonscientific sources—as the Haida project did, based on hoped-for operational benefits—they escape peer review and other scientific controls. Effective governance must thus be backed by government authority and coordinated internationally to prevent shopping for lax jurisdictions. Initial steps need not require the delay and inflexibility of enacting new laws or treaties but can come from informal consultation and coordinated decisions by research-funding and regulatory agencies of participating governments.

On the thorny problem of defining regulatory thresholds of project scale and risk, we propose that the first step should state two separate thresholds. Interventions above the large threshold would be subject to a moratorium, with commitments by both scientists and governments: scientists stating that such large interventions serve no present scientific purpose and that they would not conduct them and governments stating that such interventions are not appropriate or prudent and that they would not conduct, fund, or allow them. The threshold's definition may vary for different project types. For solar geoengineering, it might be defined by the product of area, duration, and size of radiative forcing perturbation (ΔRF), perhaps at a level where global climate response is barely detectable—for example, global-annual-average $\Delta RF > \sim 10^{-2} \text{ Wm}^{-2}$. The moratorium terms—how long it lasts, or under what conditions—will need delicate negotiation. It cannot be a permanent unconditional ban, because global geoengineering may sometime be needed. Yet it must be long and firm enough to allay concern that small research will slide unexamined into deployment, and so give the assurance needed to let small, low-risk research proceed.

The small-scale threshold would define a

second boundary, below which participating governments agree that high-value research may proceed. Its level would reflect the fact that much promising process research has trivial environmental impact, smaller than common commercial activities—for example, average $\Delta RF \sim 10^{-6} \text{ Wm}^{-2}$. These are only “geoengineering” research by virtue of their purpose, and imposing large regulatory burdens on them will merely create incentives to misstate their purpose. Even this research must accept some additional regulatory scrutiny to earn public confidence, but the extra burden should be modest. Projects should meet strong transparency requirements: a registry giving advance notice of plans and goals, and full and timely disclosure of results. They must comply with all applicable environmental, health, and safety rules, and this requirement must be made internationally consistent to deter jurisdiction shopping by identifying some set of best-practice rules (perhaps from leading jurisdictions) that projects must follow, no matter where they are conducted.

The large and small thresholds are separated by a wide gulf—a factor of $\sim 10^4$ in our illustrative examples—and our proposal is silent on how to treat interventions that fall between them. We thus avoid the hard governance issues that lie in the wide middle ground, yet we contend that it is the two tails of the scale distribution that need action most urgently, and the simple treatment we propose in each tail meets current needs. Moreover, we expect little added scientific value from expanding interventions to this middle range, so these are unlikely to be pursued at present even without an explicit moratorium.

Geoengineering poses acute and novel challenges that require proactive management, starting with practical and effective governance of research. Opponents of such research must recognize risks of suppressing the study of technologies offering such large potential benefits. Supporters of such research—including scientists who, like one of us, want to do it (19)—must accept legitimate societal interests in environmental perturbations that inform and develop a capacity for planetary manipulation, even if the scale and risk of current activities are tiny. These interests justify a modest regulatory burden, enforced by governments, as a societal condition for allowing small-scale research to proceed.

Our proposals are only first steps and do not avoid all risks. Yet we are confident that they can help, in the near term, by framing a social bargain that lets research proceed and, in the long term, by starting to build international norms of cooperation and transparency in geoengineering. There may be a window for

cooperation on geoengineering now, because states' views appear more marked by fear of doing something destabilizing and worry over what others may do, than by seeking advantage through some lead in knowledge or capability. States' interests may thus now favor supporting a cooperative scheme such as we propose. Geoengineering is not arms control, at least for now. But if states fail to build cooperation and transparency now when stakes are low, it could become as difficult and fraught as arms control, or more so, in some future of severe climate change. Our proposals aim to nip these future risks in the bud by building shared knowledge and cooperative norms while it is relatively easy.

References and Notes

1. Royal Society, *Geoengineering the Climate: Science, Governance, and Uncertainty* (2009); <http://royalsociety.org/policy/publications/2009/geoengineering-climate/>.
2. National Research Council, *America's Climate Choices: Panel on Advancing the Science of Climate Change* (National Academies Press, Washington, DC, 2010), pp. 377–388.
3. E. Teller, R. Hyde, L. Wood, *Active Climate Stabilization: Practical Physics-Based Approaches to Prevention of Climate Change* (Report UCR/LJ-148012, Lawrence Livermore National Laboratory, 2002); <https://e-reports-ext.llnl.gov/pdf/244671.pdf>.
4. S. Levitt, S. Dubner, *Superfreakonomics* (HarperCollins, New York, 2011).
5. A. Robock, *Bull. At. Sci.* **64**, 14 (2008).
6. C. Hamilton, *The Guardian*, 5 December 2011.
7. D. Keith, *Annu. Rev. Energy Environ.* **25**, 245 (2000).
8. D. W. Keith, E. Parson, M. G. Morgan, *Nature* **463**, 426 (2010).
9. E. Parson, L. Ernst, *Theoret. Inq. Law* **14**, 311 (2013).
10. Asilomar Scientific Organizing Committee, Conference Report (Climate Institute, Washington, DC, 2010); www.climate.org/PDF/AsilomarConferenceReport.pdf.
11. Solar Radiation Management Governance Initiative, *Solar Radiation Management: The Governance of Research* (SRMGI, 2011); www.srmgi.org/report.
12. Bipartisan Policy Center Task Force on Climate Remediation Research, *Geoengineering: A national strategic plan for research on the potential effectiveness, feasibility, and consequences of climate remediation technologies* (BPC, Washington, DC, 2011); <http://bipartisanpolicy.org/library/report/task-force-climate-remediation-research>.
13. Oxford Geoengineering Programme, *Oxford Principles of Geoengineering Research* (Univ. of Oxford, Oxford, 2009); www.geoengineering.ox.ac.uk/oxford-principles/principles/.
14. M. Lukacs, *The Guardian*, 15 October 2012.
15. D. Biello, *Sci. Am.* (24 October 2012).
16. London Convention and Protocol, Resolution LC-LP.1 (2008) and Assessment Framework (LC 32/17, annex 6) (2008); www.imo.org/blast/mainframemenu.asp?topic_id=1969.
17. Convention on Biological Diversity, Decision X/33; www.cbd.int/decision/cop/?id=12299.
18. E. T. C. Group, *World's Largest Geoengineering Deployment off Coast of Canada's British Columbia* [news release], 17 October 2012; www.etcgroup.org.
19. D.W.K. is developing a stratospheric experiment to test ozone loss processes from aerosol geoengineering. The project will only proceed with public funding and authorization and will provide open data access and produce no patents. D.W.K. also serves as president of a company developing CO₂ air-capture technology. We regard air capture as so unlike high-leverage geoengineering that our arguments do not apply to it, but disclose this interest because some writers consider the two to be related.

10.1126/science.1232527

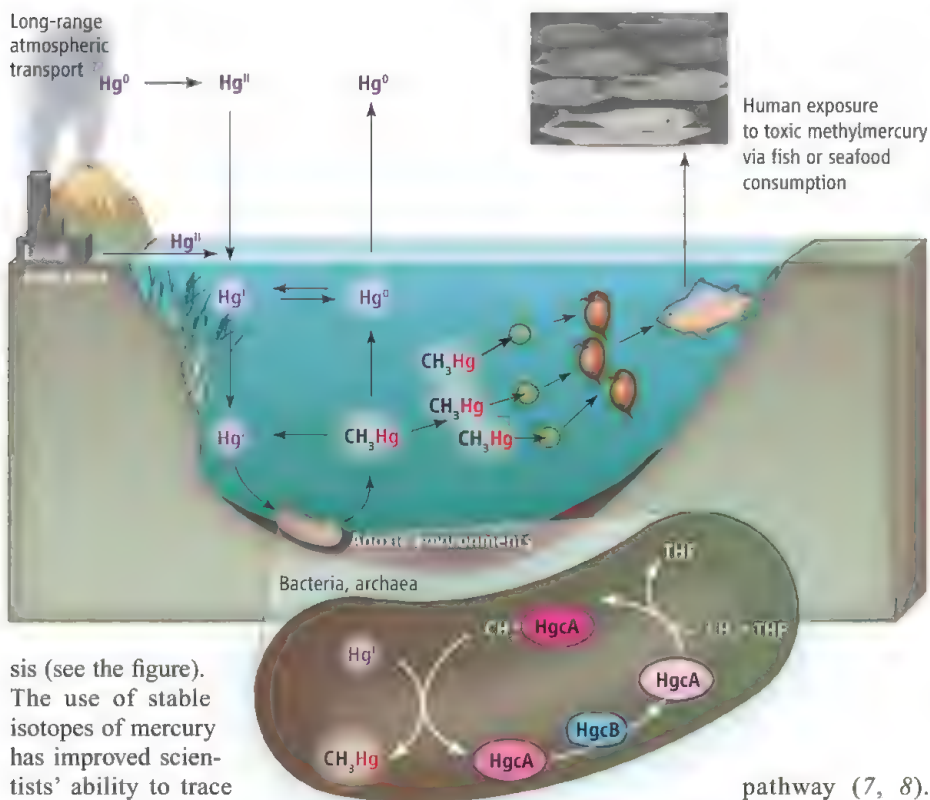
Cracking the Mercury Methylation Code

Alexandre J. Poulain¹ and Tamar Barkay²

Mercury (Hg) is a global pollutant that is transported over long distances. Although it occurs naturally, its concentration in the biosphere has increased dramatically over the past 200 years as a result of industrial activities. Mercury enters the environment in its inorganic form, but its bioaccumulation in organisms, biomagnification in food webs, and toxicity to humans depend on microbial methylmercury (MeHg) synthe-

The crippling and deadly effects of methylmercury have been recognized globally since the severe mercury poisoning event in Minamata, Japan in 1956, after the release of mercury from a nearby industry. Since then, studies have shown that mercury is methylated under anoxic conditions (4) by sulfate- and iron-reducing bacteria (5, 6). Biochemical studies suggested the possible involvement of corrinoid proteins in the methylation

Identification of two genes involved in mercury methylation may help to develop biomarkers to track and manage mercury contamination in the environment.



sis (see the figure). The use of stable isotopes of mercury has improved scientists' ability to trace and measure mercury in the environment (1, 2), but methods to predict methylmercury synthesis in the environment remain scarce. On page 1332 of this issue, Parks *et al.* (3) identify two genes required for mercury methylation. This discovery will be helpful for developing tools to study the synthesis and accumulation of methylmercury and to improve the management of contaminated environments.

¹Department of Biology, University of Ottawa, Ottawa, Ontario K1N 6N5, Canada. ²Department of Biochemistry and Microbiology, Rutgers University, New Brunswick, NJ 08901, USA. E-mail: apoulain@uottawa.ca

However, no specific mercury methylation genes were identified, limiting understanding of the methylation pathway and hence the ability to track methylmercury production.

Parks *et al.* used comparative genomics and structural biology tools to identify candidate genes. They performed targeted gene deletion and complementation experiments to show that two genes, *hgcA* (which encodes a putative corrinoid protein) and *hgcB* (which encodes a 2[4Fe-4S] ferredoxin), are required for mercury methylation.

On the basis of these findings, the authors

propose a mechanistic model where a methyl group is transferred from the methylated HgcA protein to inorganic Hg(II) and the HgcB protein is required for HgcA turnover (see the figure). This proposed pathway raises questions about the biophysical and biochemical mechanisms by which mercury is methylated. Most intriguing is the authors' prediction that the C terminus of HgcA may be membrane-embedded, possibly coupling methylation to the transport of Hg(II) and/or methylmercury across the cell wall.

The authors identified homologs of *hgcA* and *hgcB* in genomes of 52 bacteria and methanogenic archaea. Although most have not been tested for their ability to methylate mercury in pure culture, field studies have implicated methanogens in mercury

The mercury geochemical cycle. Mercury is methylated in anoxic environments by microorganisms, one of which is illustrated in the inset. Parks *et al.* show that the methylation reaction requires two genes, *hgcA* (encoding a putative methyltransferase corrinoid protein) and *hgcB* (encoding a putative [4Fe-4S] ferredoxin). Different colors for the HgcA protein indicate different redox states of the corrinoid HgcA enzyme. The toxic methylmercury accumulates in aquatic species (bioaccumulation), and its concentrations increase with each trophic level (biomagnification), causing a threat to humans whose diets rely on fish. THF, tetrahydrofolate.

methylation (9). The distribution of methylation ability is sporadic, with methylating and nonmethylating strains occurring in the same species (10). These observations raise the questions of how methylation evolved and what its purpose might be. Methylation may be a detoxification mechanism (11, 12), possibly an ancient pathway used to deal with toxic inorganic mercury. Further experiments and analyses of the genomes in which *hgcA* and *hgcB* are found will help establish the evolutionary path of mercury methylation (13).

The importance of mercury as a chemical of major concern to human health was underscored by the recent adoption of the Minamata Convention on Mercury, a legally binding treaty to be signed in fall 2013 by more than 140 countries. This treaty requires that government agencies

be equipped to monitor processes affecting global mercury transport and cycling. The United Nations Environment Programme recently identified two pressing global issues with regard to mercury pollution: establishing the link among deposition, methylation, and uptake by living organisms, and characterizing methylation and demethylation and how these reactions are affected by climate change (14).

The study by Parks *et al.* is important and timely for its promise to inform the development of such monitoring and management strategies. Knowing the sequences of mercury methylation genes will be useful for the development of molecular biomarkers for the detection and quantification of mercury methylation and the elucidation

of the environmental triggers of *hgcA/hgcB* expression. Given that quantitative and traditional polymerase chain reactions can now be performed in the field, these biomarkers would offer specific, fast analyses of whether or not methylation is likely to occur in a given environment, as well as enable evaluation of the efficiency of potential mitigation strategies. Further work may reveal additional determinants of mercury methylation under anoxic conditions and might explain puzzling observations of methylation under oxic conditions in surface marine waters (15).

References

1. H. Hintelmann, K. Keppel-Jones, R. D. Evans, *Environ. Toxicol. Chem.* **19**, 2204 (2000).
2. B. A. Bergquist, J. D. Blum, *Science* **318**, 417 (2007).
3. J. M. Parks *et al.*, *Science* **339**, 1332 (2013); 10.1126/science.1230667.
4. S. Jensen, A. Jernelöv, *Nature* **223**, 753 (1969).
5. G. Comeau, R. Bartha, *Appl. Environ. Microbiol.* **50**, 498 (1985).
6. E. J. Kerin *et al.*, *Appl. Environ. Microbiol.* **72**, 7919 (2006).
7. S.-C. Choi, T. Chase Jr., R. Bartha, *Appl. Environ. Microbiol.* **60**, 4072 (1994).
8. J. M. Wood, F. S. Kennedy, C. G. Rosen, *Nature* **220**, 173 (1968).
9. S. Hamelin, M. Amyot, T. Barkay, Y. Wang, D. Planas, *Environ. Sci. Technol.* **45**, 7693 (2011).
10. C. C. Gilmour *et al.*, *Appl. Environ. Microbiol.* **77**, 3938 (2011).
11. L. Landner, *Nature* **230**, 452 (1971).
12. J. K. Schaefer *et al.*, *Proc. Natl. Acad. Sci. U.S.A.* **108**, 8714 (2011).
13. L. Boto, I. Doadrio, R. Diogo, *Biol. Philos.* **24**, 119 (2009).
14. U.N. Environment Programme DTI/1636/GE (2013).
15. I. Lehnher, V. L. St. Louis, H. Hintelmann, J. L. Kirk, *Nat. Geosci.* **4**, 298 (2011).

10.1126/science.1235591

MATERIALS SCIENCE

Creating Flexible Calcite Fibers with Proteins

Ingo Sethmann

The process of biomineralization that forms structures such as bones, teeth, and shells of organisms incorporates biomacromolecules (proteins) into minerals as they precipitate. The composite nature of these materials confers flexibility and elasticity on otherwise brittle minerals, so biominerals can exhibit high performance rarely reproduced by synthetic or biomimetic materials. On page 1298 of this issue, Natalio *et al.* (1) describe the synthesis of intriguingly flexible fibrous spicules of calcite (CaCO_3) using silicatein- α , a protein involved in the formation of skeletal silica (hydrated SiO_2) spicules in sponges, to facilitate biomimetic precipitation. Transferring a protein from a biological silicification system to in vitro calcite precipitation led to the formation of spicules with extremely high flexibility. The high quality of these spicules allows them to be used as waveguides for visible light.

Organisms most commonly precipitate calcium carbonates, calcium phosphates, or silica to produce functional hard structures. A high degree of control is required to reproducibly form a biomineral structure

consisting of a specific mineral phase with a specific size and morphology in the correct location. This control is exerted by complex cellular machineries in which polyanionic macromolecules play a crucial role by binding dissolved mineral constituents and transporting them to the intended mineralization site in a chemically controlled microenvironment.

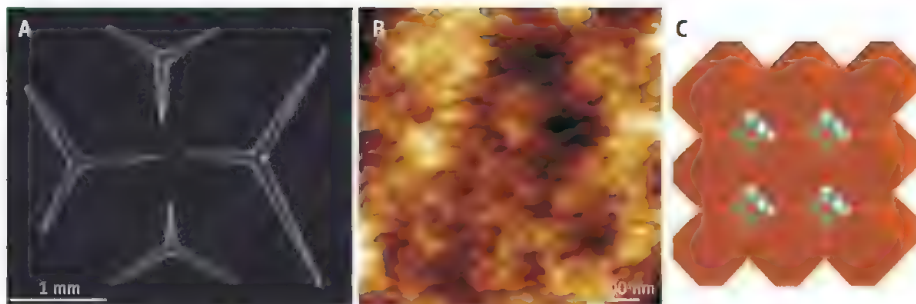
Controlled biomineralization is performed even by relatively simple organisms such as sponges, which lack differentiated tissues or organs. Most sponges form a multitude of mineral spicules with specific morphologies as an internal skeleton that prevents the body from collapsing. Sponges can be subdivided into two major groups: siliceous sponges producing spicules of amorphous silica (also known as bio-opal), and calcareous sponges that form calcite spicules. Silica spicules are initially formed inside specialized sponge cells where silicatein proteins catalytically mediate the polymerization of silica, leading to the formation of hydrated nanoparticles. These particles arrange in concentric clouds around a preformed central filament consisting of silicatein as well (2). Upon condensation, a silica-silicatein composite is formed in concentric cylindrical layers that build up the spicule (3). Highly laminated silica

Fracture-resistant calcium carbonate fibers were made by using a protein that normally directs silica spicule formation in sponges.

spicules show exceptionally high fracture resistance because the silicatein-reinforced layered structure counteracts catastrophic failure through enhanced toughness and reduced hardness, as well as through its ability to arrest microcracks (4).

In contrast to the silica spicules consisting of noncrystalline material, calcareous sponges produce spicules that represent single crystals of calcite but with specific elaborate morphologies, basically elongated single rods or triradiate stars (see the figure, panel A). Despite being well-defined crystals, calcite sponge spicules contain small amounts of polyanionic macromolecules incorporated within the mineral phase (5). These proteins presumably play a role in the precipitation mechanism, equivalent to that of silicatein in silica spicule formation, because calcite sponge spicules also appear to be constructed by aggregation of nanoparticles (see the figure, panel B) to create smoothly curved morphologies (6). The proteins are assumed to temporarily stabilize the particles as an amorphous phase of CaCO_3 , which then crystallizes after particle aggregation into a calcite single crystal. The granular structure with intercalated proteins deflects fracture propagation and dissipates strain energy, reducing the brittleness of the material.

Institut für Angewandte Geowissenschaften, Technische Universität Darmstadt, 64287 Darmstadt, Germany. E-mail: sethmann@geo.tu-darmstadt.de



Increasing flexibility with proteins. Calcareous sponge spicules and their microstructure are shown. (A) A light microscopic image reveals relatively large triactine spicules with smoothly curved surfaces. Each spicule represents a transparent single crystal of calcite, CaCO_3 . (B) Atomic force microscopic topography image of a spicule surface shows the microstructure of aggregated nanogranules. (C) Schematic drawing of a possible mesocrystalline composite structure with crystallographically aligned calcite granules (brown) and intercalated proteins (green) that leads to greater flexibility with increasing organic content. The sponge sample was provided by G. Wörheide, Ludwig-Maximilians-Universität, München.

By crossing the systems, Natalio *et al.* discovered that originally biosilica-specific silicatein- α can also mediate the precipitation of calcium carbonate with fibrous morphology, even without biological control. Hence, a high degree of self-assembly on the nano- to micrometer scale must be involved in the formation of synthetic calcite spicules, and the same can be inferred for the biomineral counterpart. Because crystallographically aligned structures are assembled from prenucleated mineral particles instead of “classical” ion-by-ion growth, the spicules can be classified as mesocrystals (7).

However, a peculiarity of these mesocrystals is that the alignment develops only after aggregation by conformable crystallization of the amorphous particles, whereas nanocrystals assemble in a crystallographically aligned fashion from the start. Crystallization of one particle conformably to another one implies some semicoherence of the crystal lattice bridging particle boundaries despite the presence of intercalated proteins (see the figure, panel C). The authors attribute the extreme flexibility of the biomimetic spicules to the relatively high content of organic material, which is consistent with

mechanical studies on various biomineral structures: Nature tunes the mechanical performance of biominerals not only by varying the microstructures but also by adjusting the organic content (8).

Rarely has bioinspired mineralization been successful in reproducing combinations of advanced material properties, such as specific morphology and flexibility, in one material. In the biomimetic fibrous calcite-silicatein- α spicules, rubberlike toughness and elasticity prevent fractures. The light-guiding studies of Natalio *et al.* show that the spicules go beyond biomimetic cross-breed mineralization and enter the realm of flexible fiber optics, for which smoothly curved fiber surfaces are a prerequisite. A challenge for future applications will be the elongation of these fibers while maintaining their microscopic width.

References

1. F. Natalio *et al.*, *Science* **339**, 1298 (2013).
2. W. E. G. Müller *et al.*, *Micron* **37**, 107 (2006).
3. X. Wang *et al.*, *Pure Appl. Chem.* **82**, 175 (2010).
4. A. Miserez *et al.*, *Adv. Funct. Mater.* **18**, 1241 (2008).
5. J. Aizenberg, M. Ilan, S. Weiner, L. Addadi, *Connect. Tissue Res.* **34**, 255 (1996).
6. I. Sethmann, R. Hinrichs, G. Wörheide, A. Putnis, *J. Inorg. Biochem.* **100**, 88 (2006).
7. H. Cölfen, M. Antonietti, *Mesocrystals and Nonclassical Crystallization* (Wiley, Chichester, UK, 2008).
8. J. D. Currey, *J. Exp. Biol.* **202**, 3285 (1999).

10.1126/science.1235357

NEUROSCIENCE

RNA That Gets RAN in Neurodegeneration

J. Paul Taylor

Amyotrophic lateral sclerosis (ALS) and frontotemporal dementia (FTD) are devastating neuromuscular and cognitive diseases, respectively, with substantial clinical, genetic, and neuropathological overlap (1). Mutation in the gene *C9orf72* is the most common genetic defect underlying these two diseases (2, 3). On page 1335 of this issue, Mori *et al.* (4) report that a “repeat expansion” mutation in *C9orf72* causes an unusual defect in RNA metabolism that may contribute to ALS, FTD, and other neurological disorders.

The pathogenic mutation in *C9orf72* consists of a hexanucleotide repeat expansion in a noncoding region (intron 1) (see the figure). Typically, normal individuals have 23 or fewer repeats [(GGGGCC)_n], but aberrant expansion can result in hundreds to thousands of repeats. This type of mutation in *C9orf72* suggests three possible disease mechanisms. Repeat expansion might impair expression of the gene product, as seen in the neurodegenerative disease Friedreich’s ataxia (5). But Friedreich’s ataxia involves impairment of both alleles and is recessively inherited. By contrast, the dominant inheritance pattern observed in *C9orf72* families makes a loss-of-function mechanism unlikely to be the sole cause of disease.

A common neurodegenerative disease is associated with unconventional translation of mutant expanded RNA.

A more favored mechanism is RNA-mediated toxicity. Presence of a noncoding repeat expansion and nuclear foci of RNA (2) in *C9orf72*-related disease are reminiscent of traits in myotonic dystrophy types 1 and 2 (6). In these disorders, characterized by progressive dementia, myopathy, and myotonia, RNA-binding proteins (of the muscleblind-like family) associate with repeat-expanded RNA, leading to abnormal RNA splicing, which underlies certain clinical features. RNA-binding proteins that bind to (GGGGCC)_n repeats have been identified as well (7). Interestingly, among these were heterogeneous nuclear ribonucleoprotein A1 (hnRNP A1) and hnRNP A2B1, both recently identified as dis-

Department of Developmental Neurobiology, St. Jude Children’s Research Hospital, Memphis, TN 38105, USA. E-mail: jpaul.taylor@stjude.org

ease genes in ALS and related disorders (8).

A third potential mechanism that has drawn little attention until now is repeat-associated non-ATG (RAN) translation. This type of unconventional translation occurs in the absence of an initiating AUG codon (9). RAN translation was first described in the context of trinucleotide repeat expansions causative of spinocerebellar ataxia type 8 and myotonic dystrophy type 1. Remarkably, in both of these diseases, RAN translation of pathologically expanded RNA occurs in all reading frames, generating long homopolymeric peptides.

Mori *et al.* describe the presence of RAN translation products in the neuropathology

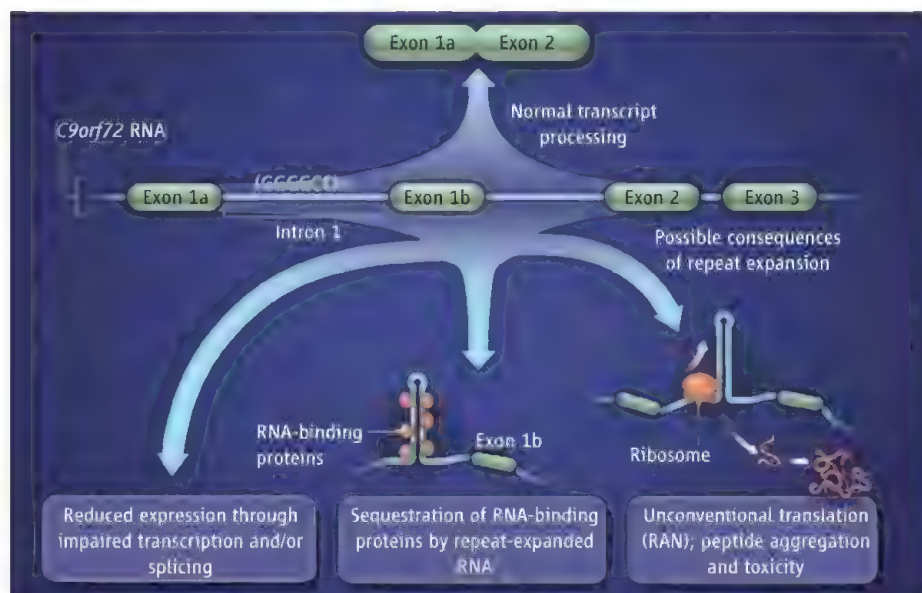
(Gly-Ala)] in these starlike inclusions. Ash *et al.* also observed high-molecular weight RAN translation products in the insoluble material of brain homogenates from *C9orf72* FTD patients, as well as neuronal inclusions of RNA throughout the central nervous system (11).

The studies by Mori *et al.* and Ash *et al.* raise the question of whether RAN translation products have a role in disease. Although patients with the *C9orf72* repeat expansion show cerebellar atrophy that is not present in other FTD variants, it remains to be determined how widespread this pathology is and whether the burden of dipeptide protein aggregates correlates with

stabilized antisense transcript, indicating that the mutant *C9orf72* allele is bidirectionally transcribed. Thus, RAN translation could also occur in the opposite orientation, which means that there could be as many as six different RAN translation products made from mutant *C9orf72* alleles.

The relationship between RAN translation and the pathological RNA foci described in *C9orf72* patients is another question. Nuclear translation has been described (12); could accumulation of repeat-expanded RNA serve as a transcript for RAN translation in the nucleus?

It remains unclear how RAN translation is initiated. Presumably, secondary structure formed by the expanded repeat is important, analogous to the secondary structures that underlie internal ribosomal entry site (IRES)-mediated translation initiation. However, even this type of translation depends on an initiating AUG codon; thus, the mechanism underlying RAN translation is unprecedented in mammalian translation. There is, however, a precedent for non-AUG-dependent, IRES-mediated translation in some picornaviruses (13). Could RAN translation use a similar mechanism? Alternatively, RNA editing might introduce a translational start site, or an initiating AUG codon could be introduced by a translicing event of the sort observed in *Caenorhabditis elegans* (14). However it occurs, RAN translation is sure to involve some unconventional mechanism that could provide new targets for therapeutic intervention for the growing list of diseases caused by pathogenic expansion of microsatellite repeats. The discovery of RAN translation in some pathologies also challenges us to consider how some cellular RNAs may use this mechanism to produce proteins that are currently unrecognized.



Expansion problems. The human gene *C9orf72* contains a repeat within intron 1. Three mechanisms may contribute to disease (such as ALS and FTD) when there is pathological expansion of the repeat.

of *C9orf72*-related FTD (2). Translation of the repeat in all reading frames would result in three dipeptide repeat proteins: poly-(Gly-Ala), poly-(Gly-Pro), and poly-(Gly-Arg), all of which were detected in high-molecular weight, insoluble material of cerebellar extracts from postmortem brains of *C9orf72* patients. A unique feature of patients with *C9orf72*-related FTD is the abundance of “starlike” inclusions in the cerebellum and hippocampus. These inclusions are characterized by the presence of the ubiquitin-binding protein p62/SQSTM1 and the absence of TDP-43 [the former is present in neuronal inclusions of numerous neurodegenerative diseases; the latter is an RNA-binding protein that is a unifying pathological feature of most sporadic and familial cases of ALS, and also the most common subtype of FTD (10)]. Mori *et al.* found all three dipeptide repeat proteins [mostly poly-

degeneration in other clinically relevant regions of the central nervous system. If the RAN translation products are toxic, it will be important to determine their relationship to TDP-43 pathology, which is present in *C9orf72* cases. Could RAN translation products work upstream of TDP-43 to initiate pathology?

There is also the issue of what transcript is used for these deviant translation products. One possibility is an aberrantly spliced RNA that retains intron 1 and somehow evades normal quality control processes that would otherwise destroy the transcript. However, Mori *et al.* detected a substantially increased amount of intron 1 relative to mature, normally spliced transcript in *C9orf72*-related FTD. This suggests that intron 1 is successfully excised but selectively stabilized by the repeat expansion. Interestingly, Mori *et al.* also detected a

References

1. R. Ferrari, D. Kapogiannis, E. D. Huey, P. Momeni, *Curr. Alzheimer Res.* **8**, 273 (2011).
2. M. DeJesus-Hernandez *et al.*, *Neuron* **72**, 245 (2011).
3. A. E. Renton *et al.*, *Neuron* **72**, 257 (2011).
4. K. Mori *et al.*, *Science* **339**, 1335 (2013); 10.1126/science.1232927.
5. M. Anheim, C. Tranchant, M. Koenig, *N. Engl. J. Med.* **366**, 636 (2012).
6. B. Udd, R. Krahe, *Lancet Neurol.* **11**, 891 (2012).
7. K. Mori *et al.*, *Acta Neuropathol.* **125**, 413 (2013).
8. H. J. Kim *et al.*, *Nature* **10.1038/nature11922** (2013).
9. T. Zu *et al.*, *Proc. Natl. Acad. Sci. U.S.A.* **108**, 260 (2011).
10. M. Neumann *et al.*, *Science* **314**, 130 (2006).
11. P. E. Ash *et al.*, *Neuron* **77**, 639 (2013).
12. A. David *et al.*, *J. Cell Biol.* **197**, 45 (2012).
13. R. J. Jackson, *Cold Spring Harb. Perspect. Biol.* **10.1101/cshperspect.a011569** (2013).
14. E. L. Lasda, T. Blumenthal, *Wiley Interdiscip. Rev. RNA* **2**, 417 (2011).

10.1126/science.1236450

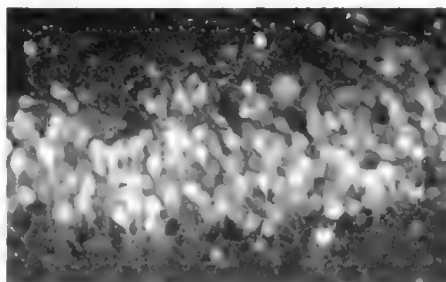
NEUROSCIENCE

The Brain Activity Map

A. Paul Alivisatos,^{1*} Miyoung Chun,² George M. Church,³ Karl Deisseroth,⁴ John P. Donoghue,⁵ Ralph J. Greenspan,⁶ Paul L. McEuen,⁷ Michael L. Roukes,⁸ Terrence J. Sejnowski,^{9*} Paul S. Weiss,¹⁰ Rafael Yuste^{11*}

Neuroscientists have made impressive advances in understanding the microscale function of single neurons and the macroscale activity of the human brain. One can probe molecular and biophysical aspects of individual neurons and also view the human brain in action with magnetic resonance imaging (MRI) or magnetoencephalography (MEG). However, the mechanisms of perception, cognition, and action remain mysterious because they emerge from the real-time interactions of large sets of neurons in densely interconnected, widespread neural circuits.

It is time for a large-scale effort in neuroscience to create and apply a new generation of tools to enable the functional mapping and control of neural activity in brains with cellular and millisecond resolution. This initiative, the Brain Activity Map (BAM), could put neuroscientists in a position to understand how the brain produces perception, action, memories, thoughts, and consciousness and be a major step toward a complete understanding of brain function and dysfunction. The BAM project will seek to fill the gap in our knowledge of brain activity at the circuit level, a scale between single-neuron and whole-brain function (1–3). It will provide a bridge that will



Neuronal activity in the hippocampus. Activity is shown by two-photon calcium imaging.

enable recording and manipulating the activity of circuits, networks, and possibly eventually whole brains with single-neuron precision.

The BAM project is essentially a technology-building research program with three goals: (i) to build new classes of tools that can simultaneously image or record the individual activity of most, or even all, neurons in a brain circuit, including those containing millions of neurons; (ii) to create tools to influence the activity of every neuron individually in these circuits, because testing function requires intervention; and (iii) to understand circuit function. The third goal will require developing methods for storing, managing, and sharing large-scale imaging and physiology data, as well as developing methods for analyzing data and modeling underlying neuronal circuits, leading to emergent principles of brain function. It will be carried out by providing access for all investigators to the methods and data needed for developing, testing, and verifying theories of how the brain operates.

The BAM project will be timely; we perceive a critical coalescence of technologies from diverse fields. Model organisms could be a cornerstone of this project, as a means to extend these technologies to the human brain in a minimally invasive fashion. Invertebrates such as the worm, fly, or leech are ideal for testing new technologies, where the results can be compared to extensive, growing bodies of data on the functions of identified neurons and smaller-scale circuits. They could also be used to spearhead new capabilities for data acquisition and analysis and for theory development. Small vertebrates, such as the zebrafish, mouse, and rat, may permit scaling up of new technologies to achieve increasingly greater depth, temporal resolution, chemical

Researchers propose building technologies to enable comprehensive mapping of neural circuit activity to understand brain function and disease.

sensitivity, and number of recorded neurons. With advances in technology, as yet unexplored systems could also become accessible. Finally, from the outset, we will seek to develop techniques to perform related measurements and controls in human scientific or clinical applications.

We envision the BAM project as an open, international collaboration of scientists, engineers, and theoreticians, throughout academia and industry, with work carried out both by individual laboratories and in new collective efforts. Within 5 years, it should be possible to monitor and/or to control tens of thousands of neurons, and by year 10 that number will increase at least 10-fold. By year 15, observing 1 million neurons with markedly reduced invasiveness should be possible. With 1 million neurons, scientists will be able to evaluate the function of the entire brain of the zebrafish or areas from the cerebral cortex of the mouse or primate, for example.

In parallel, we envision developing nanoscale neural probes that can locally acquire, process, and store accumulated data. Networks of “intelligent” nanosystems would be capable of providing specific responses to externally applied signals, or to their own readings of brain activity. These, together with noninvasive optical methods, could have clinical applications for diagnosing or treating neuropsychiatric disorders, and restoring lost functions after stroke, as well as helping to generate theories of human cognition and behavior and brain disease at a neural network scale of explanation.

Many of the most devastating human brain disorders, such as epilepsy, depression, schizophrenia, autism, and dementia, may emerge when large-scale interactions within the brain are disrupted. Similarly, voluntary movements are lost when strokes, cerebral palsy, amyotrophic lateral sclerosis, or spinal cord injury disconnect the brain and body. We believe that tools and knowledge created by the BAM project may lead to new approaches to rebalance disordered networks and treat such diseases. Early studies have already shown that an individual can overcome profound depression when deep brain stimulation modulates disrupted neural circuits (4), and emerging brain-computer interfaces allow a person completely paralyzed from a stroke

¹Materials Science Division, Lawrence Berkeley National Laboratory and Department of Chemistry, University of California, Berkeley, CA 94720, USA. ²The Kavli Foundation, Oxnard, CA 93030, USA. ³Department of Genetics, Harvard Medical School and Wyss Institute for Biologically Inspired Engineering, Boston, MA 02115, USA. ⁴Howard Hughes Medical Institute (HHMI) and Departments of Bioengineering and Psychiatry, Stanford University, Stanford, CA 94305, USA. ⁵Rehabilitation Research and Development Service, Veterans Affairs Medical Center, Providence, RI 02908, USA and Brown Institute of Brain Science, Department of Neuroscience and School of Engineering, Brown University, Providence, RI 02912, USA. ⁶Kavli Institute for Brain and Mind, University of California, San Diego, La Jolla, CA 92093, USA. ⁷Kavli Institute at Cornell for Nanoscale Science, Department of Physics, Cornell University, Ithaca, NY 14850, USA. ⁸Kavli Nanoscience Institute and Departments of Physics, Applied Physics, and Bioengineering, California Institute of Technology, Pasadena, CA 91125, USA. ⁹HHMI, Computational Neurobiology Laboratory, Salk Institute, La Jolla, CA 92037, USA and Division of Biological Sciences, University of California, San Diego, La Jolla, CA 92093, USA. ¹⁰California NanoSystems Institute, Department of Chemistry and Biochemistry, and Department of Materials Science and Engineering, University of California at Los Angeles, Los Angeles, CA 90095, USA. ¹¹HHMI, Departments of Biological Sciences and Neuroscience, Kavli Institute for Brain Science, Columbia University, New York, NY 10027, USA.

*Corresponding author. E-mail: alivis@berkeley.edu (A.P.A.); terry@salk.edu (T.J.S.); rafaelyuste@columbia.edu (R.Y.)

to feed themselves using a robotic arm controlled by their thoughts (5).

The BAM project will generate a trove of techniques for the neuroscience community. Just as better sequencing methods arose as a result of the Human Genome Project, concerted technology development will likely make imaging, electrophysiological, and computational techniques more powerful, more robust, and less expensive, thus supporting future neuroscience research and create clinical and commercial applications.

This proposal is meant to stimulate discussion and debate among scientists and administrators; our role is merely to help catalyze action. We believe this initiative should be funded by a partnership between federal and

private organizations. It is essential that those funds not be taken away from existing neuroscience initiatives, which we view as crucial. Also, data from the BAM project should be made immediately public and accessible to all researchers, with oversight on ethical, legal, social, and safety issues.

In addition to the fundamental, clinical, and technological advances described, the BAM project will also provide fertile ground for the training of new generations of interdisciplinary researchers, equally at home in the neurosciences, the physical sciences, and engineering. The economic activities galvanized by the BAM project are expected to be comparable to those of the Human Genome Project, in which a \$3.8 billion investment

generated \$800 billion in economic impact (6). We believe that when devoted and passionate groups of people join together to achieve these extraordinary goals, they will have transformational benefits for humanity.

References and Notes

1. A. P. Alivisatos *et al.*, *Neuron* **74**, 970 (2012).
2. A. M. Andrews, P. S. Weiss, *ACS Nano* **6**, 8463 (2012).
3. C. Koch, R. C. Reid, *Nature* **483**, 397 (2012).
4. A. M. Lozano *et al.*, *J. Neurosurg.* **116**, 315 (2012).
5. L. R. Hochberg *et al.*, *Nature* **485**, 372 (2012).
6. Battelle, Economic impact of the human genome project (2011); battelle.org/publications/humangenomeproject.pdf.

Acknowledgments: We thank all participants in BAM workshops for input and support.

Published online 7 March 2013

10.1126/science.1236939

BIOCHEMISTRY

How HIF-1 α Handles Stress

L. Eric Huang

Metazoans cope with hypoxia—oxygen deficiency in the tissues—by eliciting elaborate cellular responses to balance oxygen supply and demand. At the molecular level, adaptation relies primarily on the hypoxia-inducible factor 1 α (HIF-1 α), a transcription factor, and its binding partner ARNT (also called HIF-1 β). This complex activates numerous target genes to limit oxygen consumption and push the cell into survival mode (1). The scope of HIF-1 α action is expanding, though, as it seems to have nontranscriptional activities that reduce DNA replication and slow down cell proliferation when oxygen becomes scarce (see the figure).

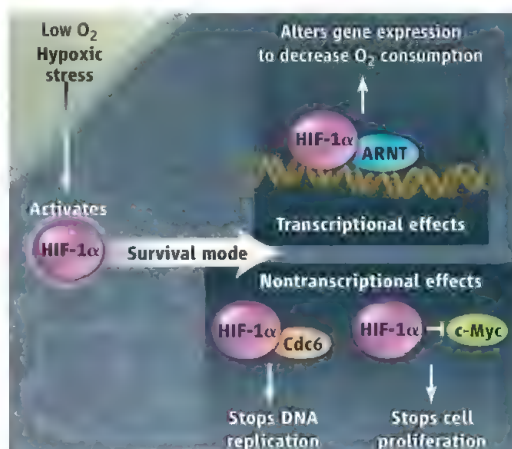
The activity of the HIF-1 α –ARNT heterodimer is determined by hypoxic stabilization of HIF-1 α (2). Under normal oxygen conditions, HIF-1 α is marked by prolyl hydroxylation for proteolytic degradation (3). Under acute hypoxia, cells cease to proliferate as a means to reduce oxygen consumption. A recent study by Hubbi *et al.* (4) examined the effect of oxygen stress on DNA replication and found that HIF-1 α arrests the process by interacting with the protein Cdc6. Cdc6 is an adenosine triphosphatase that loads chromatin with a helicase called minichromosome maintenance (MCM). MCM forms a pre-replication complex at the origins of DNA

replication (5). Once the helicase is activated, the protein Cdc45 associates with it, and in turn, recruits DNA polymerase to initiate replication. Hubbi *et al.* report that HIF-1 α not only increases the abundance of chromatin-bound Cdc6 but also promotes Cdc6 interaction with MCM; this boosts the loading of the MCM complex onto chromatin. To complete the initiation of DNA replication, however, cells require the MCM helicase to be converted to an active state through phosphorylation by Cdc7. This is where HIF-1 α steps in: By luring Cdc6 and the MCM complex into the early process of DNA replication, HIF-1 α leaves the helicase inactivated by preventing this critical phosphorylation.

Consequently, DNA replication ceases.

Hubbi *et al.* observed this mechanism of action by HIF-1 α in both normal cells and cancer cells, the latter of which frequently experience various degrees of hypoxia because of the imbalance between rapid cancer cell proliferation and an insufficient vasculature supply. The authors further noticed that hypoxic inhibition of DNA replication occurs even in quiescent fibroblasts, suggesting that the effect is not secondary to the arrest of the cell division cycle (6).

Despite the controversies surrounding the involvement of HIF-1 α and the isoform HIF-2 α (4) in regulating the oxygen stress response, the mechanisms underlying hypoxic inhibition of cell proliferation continue to be elucidated. Genetic studies of the mouse *Hif1a* gene indicate a role for HIF-1 α in increasing the expression of p21^{cip1} (7, 8), a cyclin-dependent kinase inhibitor that stops the cell cycle. In response to low oxygen, HIF-1 α activates the expression of *CDKN1A* (which encodes p21^{cip1}) by displacing c-Myc, a repressive transcription factor (in this setting), from the *CDKN1A* gene. Remarkably, this requires neither HIF-1 α binding to DNA nor its transcriptional activities (6). This unconventional way of increasing *CDKN1A* expression revealed a nontranscriptional role of HIF-1 α in antagonizing another transcription factor. Unexpectedly, HIF-2 α does the opposite



Survival mode. In response to low oxygen, HIF-1 α acts in transcriptional and also in nontranscriptional responses to control oxygen consumption.

Department of Neurosurgery, Department of Oncological Sciences, University of Utah, Salt Lake City, UT 84132, USA. E-mail: eric.huang@hsc.utah.edu

by increasing c-Myc repressive activity. This decreases *CDKN1A* expression and alters the expression of other cell-cycle relevant genes to promote hypoxic cell proliferation (9). The role of HIF-2 α in DNA replication is unclear.

Consistently, for the inhibition of DNA replication, HIF-1 α DNA-binding and transcriptional activities are nonessential; likewise, ARNT has been shown to be dispensable. Hence, HIF-1 α possesses an innate, ARNT-independent ability to curtail oxygen consumption, which argues against the notion of a “dead mutant” for a transcriptionally inactive form. Through functional antagonism to c-Myc and suppression of MCM activation, HIF-1 α appears to multitask in meeting the demands of survival during hypoxia.

Although functional links between HIF-1 α and Cdc6 or c-Myc have been established, details of these interactions are only beginning to be understood. It is unclear how HIF-1 α simultaneously increases the abundance of chromatin-bound Cdc6 but prevents Cdc7-mediated phosphorylation of an MCM subunit (MCM2) (4). Also unclear is whether the decreased MCM2 phosphorylation is accompanied by an increase in phosphorylation of MCM3 and MCM4 by Chk2, a pro-

tein kinase that is activated by hypoxia (10), because these modifications block MCM helicase activity under stressed conditions (11). Likewise, although phosphorylation serves as a molecular determinant distinguishing between HIF-1 α and HIF-2 α in c-Myc antagonism (12), the signaling pathway controlling the phosphorylation is not known. The same HIF-1 α polypeptide fragment engages in both cell cycle and DNA replication control, albeit in disparate ways (4, 6). Assuming that HIF-1 α fulfills its function as a transcription factor, could it be that HIF-1 α handles its nontranscriptional roles by partitioning in a spatiotemporal order? The answer requires investigation of molecular signaling and biochemistry, and real-time imaging of events in cells. It remains a challenge to validate the nontranscriptional role of HIF-1 α in vivo without compromising the transcriptional role. Thus, a loss-of-function approach (the gold standard to validate gene function) will not work unless transcriptional and nontranscriptional roles can be uncoupled functionally. Recognizing the nontranscriptional roles of HIF-1 α has advanced the understanding of hypoxic responses in new contexts, including cell proliferation, carbon metabolism,

DNA repair, and protein synthesis (13, 14). HIF-1 α now appears to be a complex molecule that possesses, for instance, both pro- and antitumor functions. Moreover, HIF-1 α and HIF-2 α have unique and sometimes opposing biological activities (15). Although HIF inhibitors are in clinical trials as cancer therapeutics, precise targeting of these molecules functionally, rather than molecularly, may improve their efficacies.

References and Notes

1. G. L. Semenza, *Cell* **148**, 399 (2012).
2. L. E. Huang *et al.*, *J. Biol. Chem.* **271**, 32253 (1996).
3. W. G. Kaelin Jr., P. J. Ratcliffe, *Mol. Cell* **30**, 393 (2008).
4. M. E. Hubbi *et al.*, *Sci. Signal.* **6**, ra10 (2013).
5. R. A. Sclafani, T. M. Holzen, *Annu. Rev. Genet.* **41**, 237 (2007).
6. M. Koshiji *et al.*, *EMBO J.* **23**, 1949 (2004).
7. P. Carmeliet *et al.*, *Nature* **394**, 485 (1998).
8. N. Goda *et al.*, *Mol. Cell. Biol.* **23**, 359 (2003).
9. J. D. Gordan *et al.*, *Cancer Cell* **11**, 335 (2007).
10. R. A. Freiberg *et al.*, *Mol. Cell. Biol.* **26**, 1598 (2006).
11. I. Ilves, N. Tamberg, M. R. Botchan, *Proc. Natl. Acad. Sci. U.S.A.* **109**, 13163 (2012).
12. K. K.-W. To *et al.*, *EMBO J.* **25**, 4784 (2006).
13. J. D. Gordan *et al.*, *Cancer Cell* **12**, 108 (2007).
14. L. E. Huang, *Cell Death Differ.* **15**, 672 (2008).
15. B. Keith *et al.*, *Nat. Cancer Rev.* **12**, 9 (2012).

Acknowledgments: Supported in part by the National Cancer Institute, NIH.

10.1126/science.1236966

ECOLOGY

Not All About Consumption

Debra J. Davidson and Jeffrey Andrews

The average barrel of oil on the market today has a larger ecological footprint than did the average barrel in 1950, and the average barrel in 2050 will have a larger ecological footprint than that of today. This tendency is most obvious in the increasing energy inputs required for production (1); production of all fossil fuels has an ecological impact, and increases in energy inputs thus translate into increased environmental impact. But exploiting less-accessible resources also requires more inputs, like diluents, water, and land, and produces more waste. Furthermore, once resources near population centers are depleted, more geographically remote reserves are accessed, increasing the ecological costs of transport. The implication is simple: Even if consumption is held constant, ecological impact can increase—not only for energy but also for other resources.

Ricardo offered a similar insight in his law of diminishing returns (2), observing that marginal agricultural land requires more inputs and generates less profit, but the perceived implications were entirely economic. Today, environmental awareness is greater, yet the wider implications of Ricardo's Law have gone unnoticed. According to the dominant paradigm in the environmental sciences, ecological impact is a function of consumption, as captured by the IPAT formula (Impact = Population \times Affluence \times Technology) introduced by Ehrlich and Holdren (3–5), but it lacks a variable that captures the condition of ecosystems. Humans could continue to extract oil, coal, natural gas, and many minerals for decades, but the escalating ecological implications of doing so demand research and policy attention.

The inverse relationship between resource richness and ecological impact shows in human efforts to meet oil demand. As oil fields decline, more effort must be expended to maintain production (6), and due to domes-

Resource exploitation can lead to increased ecological impacts even when overall consumption levels stay the same.

tic production declines in consuming nations, exports now constitute 75% of global production (7). Newly discovered fields are smaller and geographically dispersed, requiring greater transit distances. They are also deeper, requiring more energy to extract, and entail greater ecological risks, which became clear when BP's 10.7-km-deep Deepwater Horizon well exploded in 2010.

Capturing this relationship empirically can be challenging, particularly at the global scale, but the story becomes vivid once we consider a particular production zone. Alberta has been the seat of Canada's oil production for half a century. Oil production has several ecological impacts, but the most immediate is the consumption of land. If the area of land consumed per barrel of oil produced were constant or improving, the rate of oil production would increase at least as fast as land consumption. This is not the case, however. During an initial period of extraction at a reservoir there may be efficiency gains, but as the reservoir ages the opposite will be true. Alberta's conventional

Department of Resource Economics and Environmental Sociology, Edmonton, Alberta, T6G2H1, Canada. E-mail: debra.davidson@ualberta.ca

oil production follows this trend: From 1955 to 2006, the area of land required to extract a barrel of oil has increased 12-fold (8).

Conventional oil well pads in Alberta consume 3.3 ha on average (9), but the ecosystem fragmentation caused by the roads and pipelines required to support the wells results in a much higher total impact (10). By law, land cleared for an oil well must be reclaimed after abandonment, but the ecological value of reclaimed sites is not equivalent to their pre-development condition. Furthermore, reclamation has not kept up. The average number of wells abandoned annually in the past decade was 4111; the number reclaimed averaged 1682 (11).

Alberta's declining conventional oil industry has been surpassed by rapidly growing oil-sands exploitation, representing a further escalation of impact. A recent study found that emission levels in oil-sands mines are 23 times that of conventional production (9). Because less than 20% of the deposit can be accessed from the surface, production will soon be dominated by in situ drilling, substantially increasing cumulative land disruption: Three times as much land is disturbed to produce the natural gas required for oil-sand drilling as is consumed by the wells themselves (10).

If the thesis holds that resource quality declines over time as a given reserve is depleted, one would expect the same to hold true for oil sands. But even before evidence of this tendency emerges for the oil-sands reserves themselves, the impact caused by the energy inputs required for oil-sands extrac-



Diminishing returns and increasing environmental impacts. The effects of oil production from oil sands in Alberta provide an example of the increasing environmental impacts of energy production.

tion and processing will escalate. Currently, this energy mostly comes from regional natural gas supplies, which are in steep decline. In the very near future, oil-sands exploitation will require other sources of natural gas, which have a higher ecological impact than do the conventional, regional sources.

Declining conventional fossil fuel reserves have motivated much more investment in nonconventional fossil fuel enterprises than in renewable alternatives, representing a global trend toward increased ecological impact per unit of fuel produced. Coal production, which is growing at a faster rate than any other fossil fuel, is increasingly dominated by surface (including mountain-top) mining, which allows more efficient extraction of lower-density deposits but is also more ecologically disruptive than underground mining.

Signs of diminishing returns and increasing environmental impacts are also evident in nonenergy sectors. In China, production efficiency gains in land use for grain production leveled off 30 years ago, but inputs continue to increase, including a 10-fold increase in

groundwater extraction to support irrigation since 1961 (12) and a nearly 17-fold increase in fertilizer use between 1961 and 2009 (13). Global fish catch peaked in the past 10 years at ~90 million tons, yet fishing effort has continued to increase by 1.1% per year (14), resulting in more by-catch, damage from fishing equipment, and fuel consumption. Meanwhile, the mean trophic level of fish harvest has declined (15).

Even if consumption leveled off, increases in ecological impact could result as global reserves become depleted. The question is not when resources will run out, but how much ecological impact we can tolerate.

References and Notes

1. D. J. Murphy, C. A. S. Hall, *Ann. N. Y. Acad. Sci.* **1219**, 52 (2011).
2. D. Ricardo, *Economic Essays: Edited with Introductory Essay and Notes*, E. C. K. Gonner, Ed. (A. M. Kelley, New York, 1966).
3. P. R. Ehrlich, J. P. Holdren, *Science* **171**, 1212 (1971).
4. R. York, E. A. Rosa, T. Dietz, *Ecol. Econ.* **46**, 351 (2003).
5. T. Dietz, E. A. Rosa, *Proc. Natl. Acad. Sci. U.S.A.* **94**, 175 (1997).
6. D. Fantazzini, M. Höök, A. Angelantoni, *Energy Policy* **39**, 7865 (2011).
7. American Petroleum Institute, Basic Petroleum Data Book: Petroleum Industry Statistics 31 (2). Section IV. Table 1 and Section IX, Table 9 (American Petroleum Institute, Washington, DC, 2011).
8. Energy Resources and Conservation Board ST98-2012: Alberta's Energy Reserves 2011 and Supply/Demand Outlook—Appendix D, www.ercb.ca/sts/ST98/ST98-2012.pdf.
9. S. Yeh et al., *Environ. Sci. Technol.* **44**, 8766 (2010).
10. S. M. Jordaan, D. W. Keith, B. Stelfox, *Environ. Res. Lett.* **4**, 024004 (2009).
11. www.environment.alberta.ca/02862.html. Accessed 27 August 2012.
12. <http://faostat3.fao.org/home/index/>. Accessed 20 August 2012.
13. J. Wang et al., *Environ. Res. Lett.* **7**, 014035 (2012).
14. J. A. Anticamara, R. Watson, A. Gelchu, D. Pauly, *Fish. Res.* **107**, 131 (2011).
15. R. Clausen, R. York, *Conserv. Biol.* **22**, 458 (2008).

10.1126/science.1234205

EPIDEMIOLOGY

The SARS Wake-Up Call

Isabelle Nuttall and Christopher Dye

In February 2003, a 64-year-old doctor was treating patients with atypical pneumonia in his home town of Guangzhou, in Guangdong Province, China (1). He himself had developed a respiratory complaint but felt well enough to travel to Hong Kong and go sightseeing with his brother-in-law. Unknown to him or anyone else, his symptoms were the early stages of “severe acute

respiratory syndrome” caused by a previously unknown coronavirus (SARS-CoV) (2). The doctor, who had been staying in a hotel during his visit, checked into a Hong Kong hospital, warning staff that he had contracted a virulent disease. He succumbed 10 days later. During his short illness he had infected his brother-in-law (who died shortly after), at least two hospital nurses, and seven hotel guests including three from Canada, Singapore, and Vietnam. One hotel guest admitted to a hospital infected at least 88 health work-

Ten years ago, the SARS outbreak spurred efforts by the World Health Organization to improve global responses to health threats and crises.

ers and 18 medical students. Another patient discharged from the same hospital started an outbreak affecting more than 200 residents of a housing estate. Infection continued to spread rapidly and widely. Within 5 months, 8096 people had been affected in 30 countries and 774 died, a fatality rate of about 1 in 10. As the emergency unfolded over the following 134 days, it stimulated renewed debate about how countries should work together to combat public health crises that run across national boundaries.

World Health Organization, 1211 Geneva 27, Switzerland.
E-mail: nuttalli@who.int; dyec@who.int

The international response to SARS was an extraordinary challenge and eventually a collaborative success. Among other things, a network of 13 laboratories in 10 countries identified the virus and sequenced the genome within a month. Through the World Health Organization's (WHO's) Global Outbreak Alert and Response Network, case reports from all affected countries were analyzed in real time, and daily guidance was provided on clinical management and infection control. By early July, all known chains of transmission had been interrupted, and the SARS outbreak was declared to have been contained (3).

The spread of SARS-CoV quickly overtook the continuing but unhurried debate about how to create a more efficient system for reporting on, and responding to, international health threats in the highly connected modern world. During the 1990s, widely publicized outbreaks of Ebola hemorrhagic fever in Africa and pneumonic plague in India led WHO's World Health Assembly to call for revisions to the International Health Regulations (IHR). WHO's member states had recognized that the regulations, which focused on just three infectious diseases—cholera, pneumonic plague, and yellow fever—were inadequate to combat new and emerging infectious diseases and other cross-national health threats. But the rapid global spread of SARS in 2003 and “bird flu” (avian influenza A, H5N1) in 2004–2005 were a spur to action. The revised IHR (2005) emerged from WHO's 58th World Health Assembly, and entered into force in June 2007. IHR (2005) gave the world a new legal framework with which to mount a collective defense against international health threats.

The influence of the SARS on IHR (2005) is evident. It is now mandatory to report to WHO any case of smallpox, polio, new viral subtypes of human influenza, and SARS. Other infections must be reported after an assessment of their public health impact, including cholera, pneumonic plague, yellow fever, and viral hemorrhagic fevers.

The scope of the new regulations is now wider and includes other events such as those with unknown causes or sources, and those involving events other than infections, such as chemical and nuclear accidents. Signatories to IHR (2005), the “states parties,” have

more extensive obligations in surveillance and response and are required to notify WHO through national IHR focal points. They must ensure that designated international ports, airports, and ground crossings can prevent the spread of disease (by disinfecting, decontaminating, etc.). Furthermore, IHR (2005) gives new powers and obligations to WHO: to maintain continual global epidemic intelligence and risk assessment, and to detect and respond to all public health events of potential international concern.

In the event of delayed reports from governments, WHO may use information from unofficial sources to assess the situation, and may share this information with other member states and the public, as deemed necessary.

With 195 signatories and a comprehensive legal framework, is IHR (2005) now fit for purpose? The critical test comes not from scrutiny of the legislative fine print but from the way the regulations work in practice. The H1N1 influenza pandemic of 2009 has been the biggest test so far. The report of the Review Committee on the Functioning of IHR (2005) during the pandemic was unequivocal: The new regulations allowed better preparation for the 2009 pandemic, but the world remained ill-prepared for a severe influenza pandemic, or for any large global, sustained threat to public health (4).

Some challenges should be noted (5, 6). One is that the national and local capacities called for in IHR (2005) are not yet up to standard. There are weaknesses in the ability to detect, assess, and report potential health threats, and to respond in key areas such as infection control. There have been, however, some notable successes, such as China's post-SARS installation of real-time surveillance for 39 infectious diseases.

Another challenge is that the establishment of IHR (2005) as international law is not always consistent with, or supported by, national legal arrangements. For example, European countries differ in the range and the nature of interventions that are authorized by law. There are also differences in the extent to which national pandemic policies and plans have been integrated within national public health laws (7).

Instituting mechanisms to ensure compliance is another obstacle. For its signatories there are, at the very least, reputations at stake in a world where information is even more contagious than SARS. At the other end of the spectrum, a failure to comply with IHR

(2005) could lead to travel and trade restrictions. It is important to emphasize, however, that the focus of the regulations is not on punitive measures and sanctions, but rather on conciliation, mediation, and negotiation. The goal is to ensure that control measures are commensurate to the risk.

The H1N1 pandemic, like the outbreak of SARS and H5N1 before it, put mutual trust to the test—in the way virus samples were shared, and in giving access to vaccines, antiviral drugs, and diagnostics. Drawing together the experiences of managing H1N1, the intensely negotiated Pandemic Influenza Preparedness Framework established the roles and obligations of key players (8). It focuses on influenza, but is an important example of conduct for health threats of all kinds.

As if to remind us of the threat posed by SARS-CoV 10 years ago, a new human coronavirus (HCoV-EMC) emerged in 2012 (9, 10). As of February 2013, 13 cases of HCoV-EMC have been reported from Saudi Arabia, Qatar, Jordan, and the United Kingdom, of whom 7 have died. After news of the first case, IHR (2005) sprang into action, and WHO made full use of its power to collate and distribute information among affected countries and other concerned parties (11). Fortunately, this new coronavirus is distantly related to SARS-CoV and does not appear, so far, to be transmitted easily among people.

IHR (2005) set a deadline of June 2012 for countries to implement core capacities to detect, assess, inform, and respond to public health threats. Of the 195 signatories, 119 asked for an extension beyond the deadline. Although we cannot know what, where, or when, another major international health threat is inevitable. Will we be fully prepared?

References and Notes

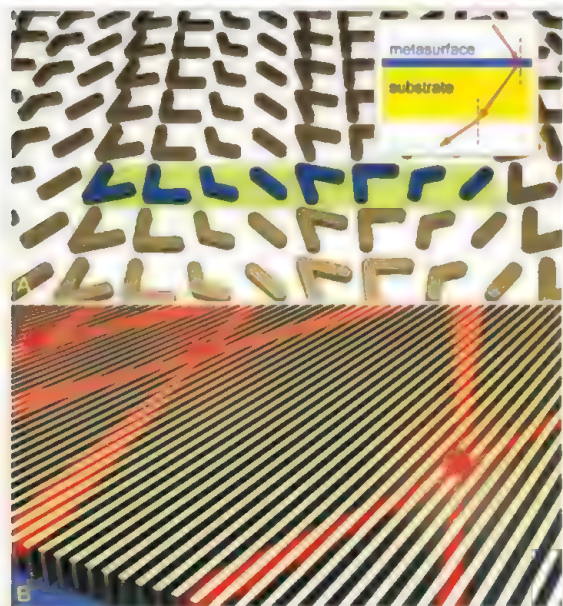
1. World Health Organization, Global Alert and Response (GAR). Update 95—SARS: Chronology of a serial killer (2013); www.who.int/csr/don/2003_07_04/en/.
2. W. Li et al., *Science* **310**, 676 (2005).
3. D. L. Heymann, *Philos. Trans. R. Soc. Lond. B Biol. Sci.* **359**, 1127 (2004).
4. World Health Organization, Implementation of the International Health Regulations, (2005). http://apps.who.int/gb/ebwha/pdf_files/WHA64/A64_10-en.pdf.
5. K. Wilson et al., *CMAJ* **179**, 44 (2008).
6. J. E. Fischer, S. Kornblat, R. Katz, The International Health Regulations (2005): Surveillance and Response in an Era of Globalization (Stimson Global Health Security Program, Washington, DC, 2011).
7. R. Martin et al., *BMC Public Health* **10**, 532 (2010).
8. WHO, Pandemic influenza preparedness framework for the sharing of influenza viruses and access to vaccines and other benefits (WHO, Geneva, 2011).
9. WHO, www.who.int/csr/disease/coronavirus_infections/update_20121221/en/index.html.
10. A. M. Zaki et al., *N. Engl. J. Med.* **367**, 1814 (2012).
11. WHO, Statement to the meeting of the States Parties to the Biological and Toxin Weapons Convention, 10 December 2012 (WHO, Geneva, 2012).

Planar Photonics with Metasurfaces

Alexander V. Kildishev, Alexandra Boltasseva, Vladimir M. Shalaev*

Background: Metamaterials (MMs) are smartly engineered structures with rationally designed, nanostructured building blocks that allow us to build devices with distinct responses to light, acoustic waves, and heat flows that are not attainable with naturally available materials.

Advances: The latest developments have shown that optical metasurfaces comprising a class of optical MMs with a reduced dimensionality can exhibit exceptional abilities for controlling the flow of light; achieve the anomalously large photonic density of states; and, similar to their bulk analog, provide superresolution imaging. Such a planar photonics technology is expected to facilitate new physics and enhanced functionality for devices that are distinctly different from those observed in their three-dimensional MM counterparts. As a result, this technology will enable new applications in imaging, sensing, data storage, quantum information processing, and light harvesting.



Plasmonic metasurfaces at work. (A) A nanoantenna-array plasmonic metasurface used to experimentally demonstrate negative refraction (inset) and reflection angles. The unit cell of a representative metasurface (blue) consists of eight gold V-shaped antennas repeated periodically. (B) A hyperbolic metasurface enhancing the radiation rate of quantum emitters. The metasurface is arranged of a thin subwavelength metallic grating deposited on a dielectric substrate.

result in the development of new types of ultrathin metasurface designs with unparalleled properties, including increased operational bandwidths and reduced losses. These new designs would also be compatible with planar, low-cost manufacturing. In turn, these advances will lead to ultrathin devices with unprecedented functionalities, ranging from dynamic spatial light modulation to pulse shaping and from subwavelength imaging or sensing to novel quantum optics devices.

Outlook: The recent progress in optical metasurfaces can address the major issues hampering the full-scale development of MM technology, such as high loss, cost-ineffective fabrication, and challenging integration. The studies of new, low-loss, tunable plasmonic materials—such as transparent conducting oxides and intermetallics—that can be used as building blocks for metasurfaces will complement the exploration of smart designs and advanced switching capabilities. This progress in metasurface design and realization will lead to novel functionalities and improved performance and may

READ THE FULL ARTICLE ONLINE
<http://dx.doi.org/10.1126/science.1232009>

Cite this article as A. V. Kildishev *et al.*, *Science* **339**, 1232009 (2013). DOI: 10.1126/science.1232009

ARTICLE OUTLINE

Nanoantenna-Array Metasurfaces
 Hyperbolic Metasurfaces
 Improved Plasmonic Materials for Metasurfaces

RELATED ITEMS IN SCIENCE

- J. B. Pendry, D. Schurig, D. R. Smith, *Science* **312**, 1780 (2006). DOI: 10.1126/science.1125907
- Z. Liu, H. Lee, Y. Xiong, C. Sun, X. Zhang, *Science* **315**, 1686 (2007). DOI: 10.1126/science.1137368
- N. I. Zheludev, *Science* **328**, 582 (2010). DOI: 10.1126/science.1186756
- C. M. Soukoulis, M. Wegener, *Science* **330**, 1633 (2010). DOI: 10.1126/science.1198858
- A. Boltasseva, H. A. Atwater, *Science* **331**, 290 (2011). DOI: 10.1126/science.1198258
- N. Engheta, *Science* **334**, 317 (2011). DOI: 10.1126/science.1213278
- N. Yu *et al.*, *Science* **334**, 333 (2011). DOI: 10.1126/science.1210713
- X. Ni, N. K. Emani, A. V. Kildishev, A. Boltasseva, V. M. Shalaev, *Science* **335**, 427 (2012). DOI: 10.1126/science.1214686
- O. Hess, K. L. Tsakmakidis, *Science* **339**, 654 (2013). DOI: 10.1126/science.1231254

BACKGROUND READING

New physics of optical MMs expands the functionality of modern photonic devices. Reduction in thickness of the bulk MMs, along with the use of alternative plasmonic materials, gives a new class of advanced, ultrathin optical elements: optical metasurfaces, which exhibit extended or completely new capabilities.

- N. I. Zheludev, Y. S. Kivshar, *Nat. Mater.* **11**, 917 (2012). DOI: 10.1038/nmat3431
- G. V. Naik, J. Liu, A. V. Kildishev, V. M. Shalaev, A. Boltasseva, *Proc. Natl. Acad. Sci. U.S.A.* **109**, 8834 (2012). DOI: 10.1073/pnas.1121517109
- F. Aieta *et al.*, *Nano Lett.* **12**, 1702 (2012). DOI: 10.1021/nl300204s
- J. Kim *et al.*, *Opt. Express* **20**, 8100 (2012). DOI: 10.1364/OE.20.008100

School of Electrical and Computer Engineering and Birck Nanotechnology Center, Purdue University, West Lafayette, IN 47907, USA.

*Corresponding author. E-mail: shalaev@purdue.edu

Support the sciences. **Get rewarded.**

Show your AAAS pride and reward yourself with the new AAAS Platinum Advantage Rewards Card from NASA Federal Credit Union.

Apply now and get
10,000 bonus points!

Go to nasa.fcuhq.com/AAASpromo



Get **10,000 bonus points** if you sign up for a card and spend \$3,000 within 90 days of account opening.

Learn more at
nasa.fcuhq.com/AAASpromo.

Subject to credit approval.
Membership in AAAS and NASA FCU is required.
NASA FCU is federally insured by NCUA.



Planar Photonics with Metasurfaces

Alexander V. Kildishev, Alexandra Boltasseva, Vladimir M. Shalaev*

Metamaterials, or engineered materials with rationally designed, subwavelength-scale building blocks, allow us to control the behavior of physical fields in optical, microwave, radio, acoustic, heat transfer, and other applications with flexibility and performance that are unattainable with naturally available materials. In turn, metasurfaces—planar, ultrathin metamaterials—extend these capabilities even further. Optical metasurfaces offer the fascinating possibility of controlling light with surface-confined, flat components. In the planar photonics concept, it is the reduced dimensionality of the optical metasurfaces that enables new physics and, therefore, leads to functionalities and applications that are distinctly different from those achievable with bulk, multilayer metamaterials. Here, we review the progress in developing optical metasurfaces that has occurred over the past few years with an eye toward the promising future directions in the field.

With the recent advances in micro- and nanofabrication methods, one can now control the flow of light in a way that was not possible before. Metamaterials (MMs) are engineered structures with rationally designed, nanostructured building blocks (“meta-atoms”). MMs allow us to build devices with responses to light, acoustic waves, and heat flows that are unattainable with naturally available materials (1–3). In the artificial patterns of meta-atoms, the propagation of electromagnetic energy can be defined by the spatial and spectral dispersions of the effective dielectric and magnetic properties. These synthetic structures offer the distinct potential to guide and control the flow of electromagnetic energy in an engineered optical space (2) and open the door to a number of applications that were previously considered impossible (4). We are no longer constrained by the electromagnetic response of natural materials and their chemical compounds. Instead, we can tailor the shape and size of the structural units of a MM, tune the composition and morphology of the nanostructure, and achieve new, desired functionalities. The extraordinary properties of optical MMs and transformation optics (TO) devices (2), which were conceived by MMs, enable a negative refractive index, imaging with the nanometer-scale resolution, invisibility cloaks, efficient light concentrators, nano-optics and quantum information applications (1–4).

Optical metasurfaces comprise a class of optical MMs with a reduced dimensionality that demonstrate exceptional abilities for controlling the flow of light beyond that offered by conventional, planar interfaces between two natural materials (5). Such two-dimensional (2D) and quasi-2D MMs provide us with the distinct possibility to fully control light with planar (or nearly

planar) MM elements and, thus, to realize “planar photonics.” Metasurfaces enable new physics and phenomena that are distinctly different from those observed in their 3D counterparts. Moreover, they are compatible with on-chip nanophotonic devices, which is of critical importance for future applications in opto-electronics, ultrafast information technologies, microscopy, imaging, and sensing.

A metasurface structured on the subwavelength scale in the lateral directions can be deterministic (i.e., periodic and aperiodic) or random. In practice, such a metasurface is represented by a patterned metal-dielectric layer that is very thin compared with the wavelength of the incident light and is typically deposited on a supporting substrate. The functionality of a device based on such a metasurface depends directly on the effective, surface-confined, optical dispersion. Effective optical properties, along with nonconventional far-field responses of ultrathin metasurfaces, for example, have been found to deviate from classical reflection and refraction laws (5, 6). Hence, the responses of metasurfaces cannot be inferred from the experimental responses for bulk materials. To design reliable flat photonic devices, a fundamental understanding of the extraordinary properties, as a function of the lateral dimensional features and the structural ordering, is required. There is a critical need to develop innovative theoretical, experimental, and fabrication approaches to unleash the power of functional optical metasurfaces.

In a long-wavelength regime (from radio to terahertz waves), surface-confined metallic antenna arrays, or “metafilms” (7–9), containing multiple antenna elements have already been successfully used for communication applications (10–12) or as highly confined cavity resonators (13, 14). Similar to optical metasurfaces, the antenna elements in such “reflectarrays” (10) and “transmitarrays” (12) also act as phase-controlling resonators for manipulating the direction in which radio or microwave signals are received or broadcast. Nevertheless, the desired phase shifts in

the reflect- and transmitarrays are obtained with the dimensions of resonant elements and array periods of a magnitude comparable in size to the incident or transmitted free-space wavelength (15).

The importance and power of planar photonics was demonstrated earlier for the specially designed case of planar chiral elements (16–19). The recently discovered generalized Snell’s law suggests a way toward ultimate control of light propagation (5). As demonstrated by Yu *et al.* (5), special nanoantenna-array metasurfaces create phase discontinuities for light propagating through the interfaces and drastically change the flow of reflected and refracted light, as initially demonstrated for the mid-infrared (mid-IR) wavelength of 8 μm (5). This phenomenon has recently been extended to the near-IR wavelength region (6), where it was also shown that the effect is robust and broadband. With these new approaches, metasurfaces could be used to fully control all light parameters, including frequency, phase, polarization, momentum, and angular momentum (20–23). Metasurface-based optical vortex plates (21), aberration-free and ultrathin flat lenses, and axicons at telecommunication wavelengths (24) have recently been demonstrated. Ni *et al.* also reported that extremely thin (30 nm) and very small (2 μm in radius) metalenses based on Babinet complementary nanoantennas (V-shaped slots in a metal sheet) can be used for the extra-strong focusing of light (with a focal length as short as 2.5 μm) in the visible wavelength range (25). In addition, ultrathin terahertz planar lenses have also been proposed (26).

Another recent demonstration showed that 3D effects on light propagation can be obtained without the need for complex inclusions in bulk MMs. Instead, planarized, broadband, bianisotropic MMs consisting of stacked nanorod arrays can be used (27). These nanorod arrays contain a tailored rotational twist and were shown to constitute an ultrathin, broadband circular polarizer that can be directly integrated within nanophotonic systems (27). Plasmonic metasurfaces have also been proposed and realized as quarter-wave plates (28, 29). Metasurfaces can be used to effectively couple propagating waves to surface waves (30), which could be of great importance for on-chip nanophotonic applications. Kang *et al.* have also shown that thin, U-shaped aperture antennas can be used to completely convert circularly polarized light into its cross-polarized counterpart (31). As shown by Shu *et al.* (32), transformation media can generate optical beams with desirable orbital angular momenta (OAM) [see also (33)]. Simon *et al.* have reported that specially engineered metasurface-based OAM states can be used also for high-efficiency quantum cryptography and a new quantum-key distribution protocol, exploiting, for example, the recursive properties of the Fibonacci sequence (34). Finally, it has been shown that so called fishnet and multilayer MM structures can be used for

School of Electrical and Computer Engineering and Birck Nanotechnology Center, Purdue University, West Lafayette, IN 47907, USA.

*To whom correspondence should be addressed. E-mail: shalaev@purdue.edu

computer-generated holograms (35, 36). Conventionally, phase holograms are made by changing either the thickness or the refractive index of a material. In contrast, metasurfaces can create ultrathin holograms that rely on subwavelength-sized antennas to modulate the phase appropriately and create the hologram image.

We note that the control of the phase with metasurfaces can be related, in some cases, to the fundamental physics associated with the Pancharatnam-Berry phase. This geometrical phase appears when the light polarization follows a geodesic triangle on the Poincaré sphere (37, 38). The phase difference between the initial and final states differs in this case by an amount representing half of the solid angle encompassing by the triangle. It has been demonstrated that continuous, space-variant, subwavelength gratings can result in this phase change, which is not due to optical path differences but rather stems from local changes in polarization, representing the geometrical space-domain Pancharatnam-Berry phase [see, for example, (39)]. The subwavelength, periodic structure in this case behaves as a uniaxial crystal. By controlling the local orientation of such a grating, one can form space-variant wave plates. Based on these computer-generated, space-variant, subwavelength dielectric gratings, a family of Pancharatnam-Berry phase optical elements has been demonstrated; this family includes blazed diffraction gratings and polarization-dependent focusing lenses (39), image-encrypting devices (40), vectorial vortices, and spiral phase elements producing helical beams with different topological charges (41, 42), as well as near- and mid-IR holograms employing circularly polarized illumination (43). For example, in the design of the experiments by Hasman *et al.* and Niv *et al.* (39, 42), for incident light with a wavelength of 10.6 μm , the typical depth and period of a designed GaAs dielectric grating structure were $\sim 2 \mu\text{m}$ each. It was also shown that when plasmons are involved, one can develop an important quantum weak measurement tool (44) and observe various fundamental phenomena, such as the plasmonic Aharonov-Bohm effect and the optical spin Hall effect (45, 46).

To advance the emerging metasurface technology further and enable real-life applications for metasurfaces, there is a critical need to develop a new material platform that provides performance enhancements and new functionalities combined with manufacturing and integration capabilities. To enable the large-scale fabrication and chip integration of metasurfaces, customizable, cost-effective, and semiconductor-compatible materials are required (47). Metasurfaces that incorporate such materials can contribute to a new class of hybrid, chip-scale devices (48) that are expected to revolutionize nanophotonic and optoelectronic circuitry through smart integration of multiple functions in the metallic, dielectric, and semiconductor building blocks. Due to their 2D nature that is advantageous for wafer-scale processing and complex integration, metasurfaces

hold great promise to win the race for the most technologically important research among artificially structured materials. We will focus on three areas that we believe are important for the current and future developments of the field: (i) nanoantenna-based metasurfaces, (ii) hyperbolic metasurfaces (HMSs), and (iii) the use of new material platforms for metasurfaces, enabling a generation of switchable devices that could be integrated with the existing semiconductor technology into complex, multifunctional systems.

Nanoantenna-Array Metasurfaces

By engineering a phase discontinuity along an interface, one can fully steer light and accomplish unparalleled control of anomalous reflection and refraction described by the generalized Snell's law (5)

$$\sin(\theta_t)n_t - \sin(\theta_i)n_i = \lambda_0 \nabla \Phi / 2\pi \quad (1)$$

$$\sin(\theta_r) - \sin(\theta_i) = n_i^{-1} \lambda_0 \nabla \Phi / 2\pi \quad (2)$$

where θ_t , θ_r , and θ_i are the angles of refraction, incidence, and reflection, respectively; n_t and n_i are the refractive indices of the two media at the transmission and incident side, respectively, and λ_0 is the free-space wavelength. These expressions indicate that a gradient in a phase discontinuity, $\nabla \Phi$, along an interface can modify the direction of the rays refracted and reflected by the device, and this can be achieved in a very thin layer. Note that $\nabla \Phi$ is essentially an additional momentum contribution that is introduced by coupling to the nanoantennas (NAs) and breaking the symmetry at the interface; hence, the light wave bends accordingly to conserve the momentum.

The degree of light control is illustrated in Fig. 1. Metasurface functionalities are combined with low losses due to the fact that they are ultrathin. This could lead to a variety of devices enabling extraordinary light modulation and control.

Metasurfaces with symmetry-breaking V-shaped nanoantennas create abrupt phase shifts from 0 to 2π in cross-polarized light and, thus, can be used for a number of planar optical elements. For example, to achieve the lensing functionality, the NAs can be arranged in concentric rings (24, 25). Along with their different shapes, the NAs can be distributed in such a way that the abrupt phase shifts cause the wave propagating through the interface to experience a fully constructive interference at a distance f . Therefore, the outgoing cross-polarized light is focused at a focal length f (24, 25). Such ultrathin metalenses can be designed to generate, for example, non-diffracting Bessel beams (24), which are extremely important for laser machining, high-precision position alignment, and sensing. By using Babinet-complementary NAs, one can significantly increase the signal-to-noise ratio, which is the ratio of the cross-polarized light that experiences the anomalous refraction to the transmitted light with the original polarization (25).

One of most interesting applications for metasurfaces could be related to ultrathin, deeply subwavelength spatial light modulators (SLMs). It is important to note that such SLMs can also provide ultrafast, dynamically controlled responses.

Metasurfaces can also be used as broadband mid-IR chemical sensors. The mid-IR range is an important part of the spectrum, especially for

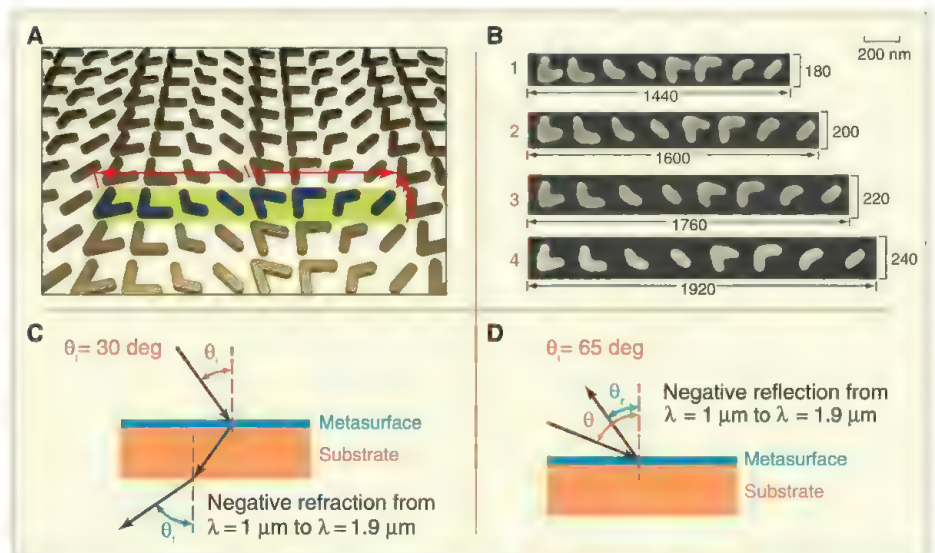


Fig. 1. Nanoantenna-array metasurfaces. (A) Schematic view of a representative nanoantenna array. The unit cell of the plasmonic interface (blue) consists of eight gold V-shaped antennas with 40-nm arm width and 30-nm thickness, repeated with a periodicity of Λ in the x direction and $\Lambda/8$ in the y direction. The phase delay for cross-polarized light increases along the x axis from right to left. (B) Scanning electron microscope images of the unit cells of four antenna arrays with different periods fabricated on a single silicon wafer. (C and D) Negative refraction (θ_t) (C) and reflection (θ_r) (D) angles are obtained experimentally for incident cross-polarized light with 30° and 65° incidence angles (θ_i), respectively, for the range of near-IR wavelengths (λ) from 1.0 to 1.9 μm (6).

chemical sensing, because many chemicals exhibit signature absorption spectra in the mid-IR. It is well known that plasmonic structures with their local-field enhancement can dramatically increase sensitivity and, thus, can be used for efficient sensing. With metasurfaces, one can further increase the sensitivity. Unlike conventional plasmonic structures, which translate the change in the local environment into the intensity of the detected light, metasurfaces can transform the local environmental changes into a shift in the angle of the anomalous reflection and refraction ($\Delta\theta_r$ and $\Delta\theta_t$, respectively) as depicted in Fig. 2A. The detection of angular shifts can be substantially more sensitive than the detection of small intensity changes. Thus, metasurfaces could be an efficient way to produce ultrasensitive chemical sensors in the mid-IR.

Because metasurfaces can precisely control the phase of the incident light at the nanoscale, they can also be used as building blocks for metastructures with extremely large values of refractive index in the optical range. Such materials with an extra-large refractive index could find very important applications in nanophotonics, super-resolution imaging, and sensing devices. Access to extreme refractive index values that are unattainable with natural materials can be achieved by using the large phase changes over the deeply subwavelength scale provided by a single layer of a NA-based metasurface. With two or more layers of such metasurfaces, one can slow down the light inside the layers by creating additional phase shifts in the propagation direction. Figure 2B illustrates how a multilayer of metasurfaces can operate as a MM with an extra-large refractive index. The right panel of Fig. 2B illustrates the phase change accumulated by a beam of light propagating through a normal homogeneous material (the green line) and through a MM consisting of several metasurfaces (the red curve). The slope of each curve indicates the effective

refractive index. Because of the abrupt phase changes due to metasurfaces, the beam in the MM can accumulate phase much faster than in normal materials; hence, the MM provides a much larger effective refractive index than in normal materials.

In addition to the control of incident light, metasurfaces can also control and manipulate surface electromagnetic waves. Applications can be realized by designing metasurfaces that support and transform surface waves. For example, cloaking of 3D objects using bulk MMs can be extended to surface structures that cloak surface discontinuities from detection via propagating surface waves (e.g., surface plasmon polaritons). As mentioned previously, metasurfaces allow one to very effectively couple propagating waves to surface waves (30). One can apply the transformation optics approach to control the propagation of surface-confined waves with metasurfaces. This extends the previously proposed TO approach for the surface plasmon waves (49) to the generalized TO concept for waves supported by metasurfaces.

To advance the proposed functionalities further, it is important to add switching and modulation capabilities to metasurface devices. Switchable metasurfaces could be extremely important for applications involving dynamic beam steering. One can employ phase-changing materials such as chalcogenide glass, transition-metal oxides (e.g., vanadium oxide), and liquid crystals as possible candidates for switching. By precisely controlling the phase change acquired by the beam passing through a metasurface, one can also develop an approach for advanced pulse shaping. Dynamically controlled pulse shaping can be enabled by combining ultrathin metasurfaces with phase-changing and nonlinear dielectrics.

Hyperbolic Metasurfaces

Highly anisotropic hyperbolic metamaterials (HMMs), which are usually made of alternating

metal and dielectric layers or using metal wires embedded in a dielectric host, are metallic in one direction and dielectric in the other directions (Fig. 3) (50–57). In HMMs, light encounters extreme anisotropy, causing its dispersion to become hyperbolic. This leads to dramatic changes in the light's behavior. For example, HMMs enable many exotic applications for nanoscale imaging and efficient light concentration (50–52, 58, 59). Additionally, HMMs can enhance the density of states for photons within a broad spectral range (53–55, 60, 61). The radiative decay rate for light emitters is proportional to the photonic density of states (PDOS); thus, the radiative decay can be efficiently enhanced in HMMs. This recent discovery of a broad-band singularity in the PDOS for HMMs (61) could revolutionize PDOS engineering, enabling light sources with dramatically increased photon extraction and, ultimately, leading to nonresonant single-photon sources, which could be used, for example, for quantum communication protocols and other quantum information applications (60).

However, bulk HMMs usually exhibit high loss. Moreover, it is difficult to place emitters inside 3D HMMs to efficiently use the high PDOS. Thus, it is important to develop quasi-2D HMSs that could offer important advantages over their 3D counterparts because such HMSs would be chip-compatible and would typically have small losses that are relatively easy to compensate. Planar and ultrathin HMSs also offer straightforward device fabrication and integration. Complementing the distinct properties of the NA-based metasurfaces considered above, HMSs would also provide broadband control over the PDOS.

One of the interesting surface phenomena that holds promise for developing efficient HMSs with a number of applications in nano-optics and imaging is a Dyakonov surface wave. Dyakonov plasmon surface waves occur at the interface between two media, at least one of which is

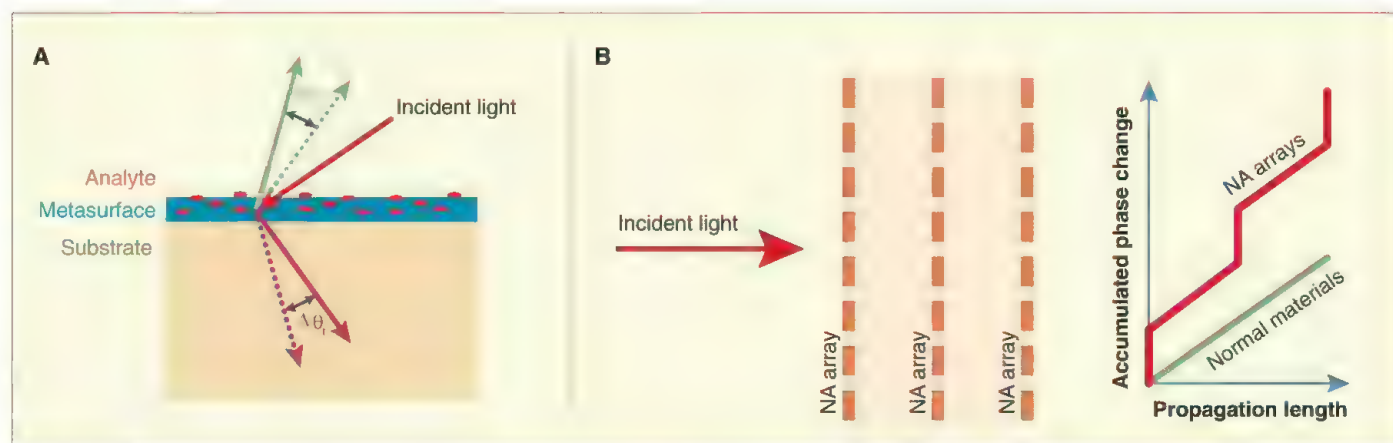


Fig. 2. Example applications of optical metasurfaces. (A) A metasurface acting as a chemical sensor: The analyte molecules adsorb onto the metasurface, causing a shift in the resonance of the constituent NAs. This results in shifts in the angle of the anomalously reflected and transmitted beams ($\Delta\theta_r$ and $\Delta\theta_t$, respectively). (B) Illustration of an extra-large refractive-

index MM consisting of three metasurfaces (left panel). The right panel shows the accumulated phase change for light propagating through a normal homogeneous material (green line) and through a MM consisting of three metasurfaces (red curve). The slope of each curve indicates the effective refractive index.

anisotropic, and where one component of the permittivity of either media has to be negative (56). These surface waves can be observed in two different geometries. The first is a layer of metal covered with a uniaxial dielectric material. The second possibility is to employ an HMM layer covered with an isotropic dielectric layer. Both of these configurations can support surface waves exhibiting hyperbolic dispersion, which causes highly directional propagation of the sur-

face waves with unbounded wave vectors (limited in magnitude only by the inverse of the size of the structural unit) in a broad wavelength range. It is important to note that the PDOS in HMSs diverges similarly to PDOS in their 3D counterparts. Naturally, the unbounded isofrequency curves of HMSs immediately suggest a diverging, anomalously large PDOS. Importantly, though, the hyperbolic dispersion can be achieved within a wide spectral range; thus, the expected enhancement of

the emission rate on HMSs has a broad bandwidth similar to that of their 3D counterparts.

We note that the anomalously large PDOS in HMSs could open up the exciting possibility of creating a new generation of active, on-chip light sources with dramatically increased photon extraction. Moreover, PDOS engineering achievable in HMS could lead to novel laser designs with extraordinary properties such as wide-band tunability and high directionality.

One of the interesting directions in this field is exploring how to use HMSs for quantum optical applications, such as the control of spontaneous emission and “single-photon guns,” which could be very important for quantum information applications (60). As follows from the considerations above, one can expect emission enhancement from quantum emitters on HMSs. In contrast to bulk HMMs, quantum emitters can be placed directly on the interfaces of HMSs. In addition, the hyperbolic dispersion relation of the Dyakonov surface waves implies that the emitted light on the surface is highly directional, which will improve the collection efficiency. The surface nature of this approach makes it inherently compatible with on-chip integration. Figure 4A illustrates an example of a geometry involving quantum emitters on a HMS.

Another important application for HMSs is a surface hyperlens for superresolution imaging, which was previously proposed and realized for the 3D case (52, 58, 62). Figure 4, B and C, illustrates the hyperlensing effect for HMSs consisting of metallic gratings on top of a dielectric substrate. Figure 4B shows a surface hyperlens without the magnification effect. Two scatterers on top of the grating are separated by a subwavelength distance and behave as sources. The surface waves are confined in a preferred angular direction, along which the wave vector of the Dyakonov plasmons is perpendicular to the isofrequency curve. For the hyperlensing condition (when the hyperbolas of the isofrequency curves are flat), the waves emerging from the two sources are parallel to each other and will be resolvable at a distance far away from the sources. The design can be readily changed to produce a magnifying effect,

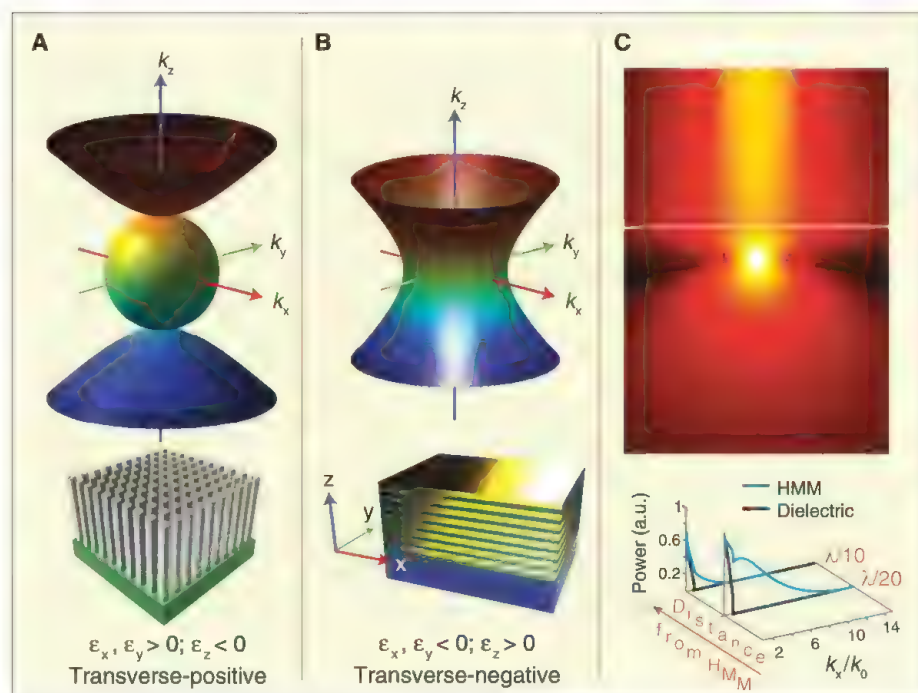


Fig. 3. Metamaterials with hyperbolic dispersion. (A and B) Examples of 3D HMMs with extreme anisotropy [transverse positive (TP) and transverse negative (TN)] made of plasmonic nanowires in a dielectric host (A) and alternating layers of metallic and dielectric materials (B). The sphere in the center of (A) represents the dispersion relation in a conventional, isotropic material, whereas the two hyperbolic surfaces describe the dispersion in a TP HMM. The dispersion for the TN HMM is shown in (B). The unbounded wave vectors in HMMs imply an extremely high effective refractive index and, thus, the possibility of super-resolution imaging. This also leads to a singularity in the density of states that occurs over the entire bandwidth where hyperbolic dispersion is achieved. k_x and k_0 , the tangential components of the normalized wave vector; ϵ_x, ϵ_y , and ϵ_z , the diagonal components of the permittivity tensor; λ , the free-space wavelength. (C) Simulated emission in an HMM (top) and power spectrum in an HMM as compared to conventional dielectric (bottom) (54). a.u., arbitrary units.

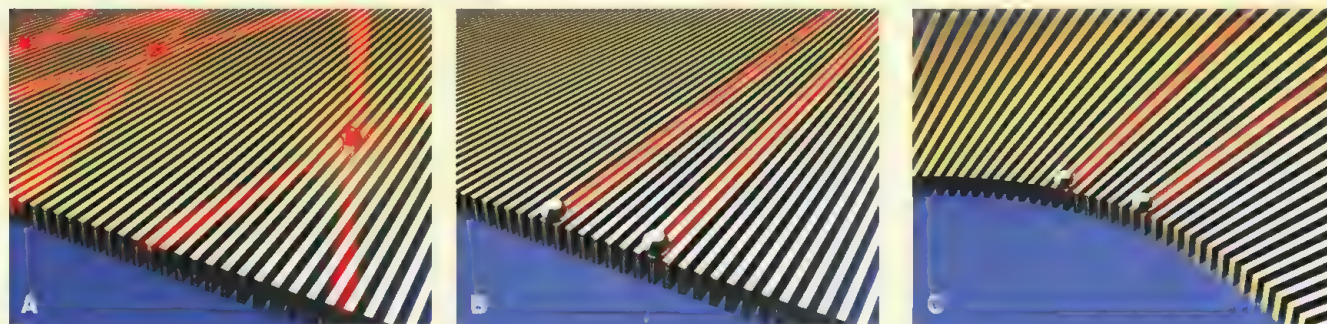


Fig. 4. Hyperbolic metasurfaces. (A) Illustration of a HMS enhancing the emission rate of quantum emitters on a metasurface consisting of a metallic grating on a dielectric substrate. (B and C) Illustration of a

surface hyperlens without magnification (B) and with magnification (C). The two scatterers are on the top of the grating and have a subwavelength separation.

as shown in Fig. 4C. A grating made of strips that become wider with distance from the sources will magnify the image of the sources. When the light is directed in the opposite direction, the same HMS designs can be employed as light concentrators. Such HMSs could focus light to a subwavelength-sized spot and could be used for efficient, on-chip light harvesting.

The enhancement in the PDOS provided by HMSs also enables the engineering of thermal radiation and near-field heat transport. Engineering the thermal radiation of emitters over a broad band of mid-IR frequencies that is enabled by HMSs also allows the efficient control over the flow of heat, which is essential for many applications such as surveillance, sensing, detection, and imaging.

Improved Plasmonic Materials for Metasurfaces

The search for novel, low-loss, tunable materials that can be used as building blocks for metasurfaces will no doubt complement the exploration of smart designs and lead to new functionalities and improved performance. Similar to other plasmonic systems, one of the largest obstacles to overcome in metasurfaces is optical loss arising in the metallic unit cells (47, 57). Metals such as silver and gold have traditionally been selected as the plasmonic materials of choice because they have large free-electron concentrations and high electrical conductivities. Although these metals work well in the infrared and microwave spectral regions, they suffer from high losses arising in part from interband transitions as the incident light approaches the technologically important telecommunication and visible wavelengths (57). One common approach to loss compensation is the addition of a gain medium in or around the plasmonic material. This approach can partially or fully compensate the loss in metals, but the incorporation of such active materials is very challenging (63). Often, the gain that can be provided by usual materials is barely enough to compensate the losses. Hence, an efficient alternative approach is needed to realize extremely low-loss or lossless devices. Another related fact limiting optical MM applications is the large plasma frequency of noble metals (~2000 THz) that cannot be adjusted (57). This is disadvantageous for a number of applications such as hyperlenses, transformation optics, and epsilon-near-zero materials (materials where the real part of the effective dielectric permittivity approaches zero) that enable subwavelength-resolution imaging, cloaking, and directional beaming, respectively. Ideally, for many applications, metals should not be too metallic (so that their permittivity would be comparable in magnitude to that of dielectrics but opposite in sign) and should have an adjustable or tunable plasma frequency to enable controllable or switchable devices. Moreover, noble metals are not compatible with the established semiconductor processing technologies, restricting MM and metasurface devices to the proof-of-concept stage only.

Those issues can be addressed by developing new material platforms that use low-loss, tunable materials for metasurface devices with improved performance, new functionalities, switchability, and compatibility with existing semiconductor technologies. The recent search for new plasmonic materials (47, 57, 64–66) defined new, intermediate carrier density materials as the best candidates that exhibit low loss, extraordinary tuning, and modulation capabilities and that are compatible with standard semiconductor fabrication and integration procedures.

Recently, the most promising classes of new plasmonic materials have been outlined and include materials such as inorganic ceramics [notably transparent conducting oxides (TCOs) (57, 64, 65) and transition metal nitrides (65, 66)], and the merits of these materials for different applications have been explored (57, 64–66). Heavily doped (10^{21} cm^{-3}) TCOs, such as indium tin oxide and zinc oxide doped with aluminum or gallium, have been shown to be promising plasmonic materials in the near-IR range (57, 64–66). In the visible range, intermetallics such as silicides, germanides, borides, and nitrides could serve as plasmonic materials (47). Naik *et al.* have demonstrated that the optical performance of gold can be at least matched by that of TiN (65, 66).

It is also important to study the possibility of incorporating tunability and switching and/or modulation capabilities into metasurface systems. Along with phase-change materials like liquid crystals, chalcogenide glasses, and transition-metal oxides (e.g., vanadium oxide), the usage of TCOs for electro-optical switching of metasurface devices can be explored. The addition of electro-optical capabilities to metasurface devices, particularly in the infrared domain, can be optimized by exploiting the shift of the electromagnetic response driven by an applied voltage. Feigenbaum and Atwater have shown that heavily doped semiconductor oxides and TCOs support extraordinary tuning and modulation of their complex refractive indices because their carrier concentrations can be changed by orders of magnitude through the application of an electric field (67). It is also important to look into the possibility of using the strong optical nonlinear responses that can be exhibited by the intermediate carrier density materials (68) proposed above to add new, useful functionalities to metasurface devices.

The recent progress in optical metasurfaces could address the major issues—such as high loss, cost-ineffective fabrication, and challenging integration—that are hampering the full-scale development of MM technology. This progress can result in the development of new types of ultrathin metasurfaces with unparalleled properties, including increased operational bandwidths and reduced losses; these metasurfaces would also be compatible with planar, low-cost manufacturing. In turn, this development could lead to novel, ultrathin devices that offer unprecedented functionalities ranging from dynamic spatial light modulation to pulse-shaping and beam-steering

and from nanoscale-resolution imaging and sensing to novel quantum optics devices.

References and Notes

- V. G. Veselago, The electrodynamics of substances with simultaneously negative values of ϵ AND μ . *Sov. Phys. Usp.* **10**, 509 (1968) and references therein. doi: 10.1070/PU1968v010n04ABEH003699
- J. B. Pendry, D. Schurig, D. R. Smith, Controlling electromagnetic fields. *Science* **312**, 1780 (2006) and references therein. doi: 10.1126/science.1125907; pmid: 16728597
- C. M. Soukoulis, M. Wegener, Optical metamaterials—more bulky and less lossy. *Science* **330**, 1633 (2010) and references therein. www.ncbi.nlm.nih.gov/entrez/query.fcgi?cmd=Retrieve&db=PubMed&list_uids=21164003&dopt=Abstract doi: 10.1126/science.1198858; pmid: 21164003
- N. I. Zheludev, Y. S. Kivshar, From metamaterials to metadevices. *Nat. Mater.* **11**, 917 (2012) and references therein. doi: 10.1038/nmat3431; pmid: 23089997
- N. Yu *et al.*, Light propagation with phase discontinuities: Generalized laws of reflection and refraction. *Science* **334**, 333 (2011). doi: 10.1126/science.1210713; pmid: 21885733
- X. Ni, N. K. Emani, A. V. Kildishev, A. Boltasseva, V. M. Shalae, Broadband light bending with plasmonic nanoantennas. *Science* **335**, 427 (2012). doi: 10.1126/science.1214686; pmid: 22194414
- E. F. Kuester, M. A. Mohamed, M. Piket-May, C. L. Holloway, Averaged transition conditions for electromagnetic fields at a metafilm. *IEEE Trans. Antenn. Propag.* **51**, 2641 (2003). doi: 10.1109/TAP.2003.817560
- C. L. Holloway, M. A. Mohamed, E. F. Kuester, A. Dienstfrey, Reflection and transmission properties of a metafilm: With an application to a controllable surface composed of resonant particles. *IEEE Trans. Electromagn. Compat.* **47**, 853 (2005). doi: 10.1109/TEMC.2005.853719
- Y. Zhao, N. Engheta, A. Alù, Homogenization of plasmonic metasurfaces modeled as transmission-line loads. *Metamaterials* **5**, 90 (2011). doi: 10.1016/j.metmat.2011.05.001
- D. M. Pozar, S. D. Targonski, H. D. Syrigos, Design of millimeter wave microstrip reflectarrays. *IEEE Trans. Antenn. Propag.* **45**, 287 (1997). doi: 10.1109/8.560348
- D. Sievenpiper, L. Zhang, R. F. J. Broas, N. G. Alexopolous, E. Yablonovitch, High-impedance electromagnetic surfaces with a forbidden frequency band. *IEEE Trans. Microwave Theory Tech.* **47**, 2059 (1999). doi: 10.1109/22.798001
- C. G. M. Ryan *et al.*, A wideband transmitarray using dual-resonant double square rings. *IEEE Trans. Antenn. Propag.* **58**, 1486 (2010). doi: 10.1109/TAP.2010.2044356
- M. Caiazzo, S. Maci, N. Engheta, A metamaterial surface for compact cavity resonators. *IEEE Antenn. Wireless Propag. Lett.* **3**, 261 (2004). doi: 10.1109/LAWP.2004.836576
- C. L. Holloway, D. C. Love, E. F. Kuester, A. Salandrino, N. Engheta, Sub-wavelength resonators: On the use of metafilms to overcome the $\lambda/2$ size limit. *IET Microwave Antenn. Propag.* **2**, 120 (2008). doi: 10.1049/iet-map:20060309
- N. Engheta, Antenna-guided light. *Science* **334**, 317 (2011). doi: 10.1126/science.1213278; pmid: 22021846
- A. Papakostas *et al.*, Optical manifestations of planar chirality. *Phys. Rev. Lett.* **90**, 107404 (2003).
- S. L. Prosvirnin, N. I. Zheludev, Polarization effects in the diffraction of light by a planar chiral structure. *Phys. Rev. E* **71**, 037603 (2005).
- S. L. Prosvirnin, N. I. Zheludev, Analysis of polarization transformations by a planar chiral array of complex-shaped particles. *J. Opt. A* **11**, 074002 (2009).
- Y. Svirko, N. Zheludev, M. Osipov, Layered chiral metallic microstructures with inductive coupling. *Appl. Phys. Lett.* **78**, 498 (2001). doi: 10.1063/1.1342210
- F. Aieta *et al.*, Out-of-plane reflection and refraction of light by anisotropic optical antenna metasurfaces with phase discontinuities. *Nano Lett.* **12**, 1702 (2012). doi: 10.1021/nl300204s; pmid: 22335616

21. P. Genevet *et al.*, Ultra-thin plasmonic optical vortex plate based on phase discontinuities. *Appl. Phys. Lett.* **100**, 013101 (2012). doi: [10.1063/1.3673334](https://doi.org/10.1063/1.3673334)
22. R. Blanchard *et al.*, Modeling nanoscale V-shaped antennas for the design of optical phased arrays. *Phys. Rev. B* **85**, 155457 (2012).
23. S. Larouche, D. R. Smith, Reconciliation of generalized refraction with diffraction theory. *Opt. Lett.* **37**, 2391 (2012). doi: [10.1364/OL.37.002391](https://doi.org/10.1364/OL.37.002391); pmid: 22739918
24. F. Aieta *et al.*, Aberration-free ultrathin flat lenses and axicons at telecom wavelengths based on plasmonic metasurfaces. *Nano Lett.* **12**, 4932 (2012). doi: [10.1021/nl302516v](https://doi.org/10.1021/nl302516v); pmid: 22894542
25. X. Ni, S. Ishii, A. V. Kildishev, V. M. Shalaev, Ultra-thin, planar, Babinet-inverted plasmonic metalenses. *Light Sci. Appl.* **10**, 1038/lsa.2013.28 (2013).
26. D. Hu *et al.*, <http://arxiv.org/abs/1206.7011v1> (2012).
27. Y. Zhao, M. A. Belkin, A. Alù, Twisted optical metamaterials for planarized ultrathin broadband circular polarizers. *Nat. Commun.* **3**, 870 (2012).
28. Y. Zhao, A. Alù, Manipulating light polarization with ultrathin plasmonic metasurfaces. *Phys. Rev. B* **84**, 205428 (2011).
29. N. Yu *et al.*, A broadband, background-free quarter-wave plate based on plasmonic metasurfaces. *Nano Lett.* **12**, 6328 (2012).
30. S. L. Sun *et al.*, Gradient-index meta-surfaces as a bridge linking propagating waves and surface waves. *Nat. Mater.* **11**, 426 (2012). doi: [10.1038/nmat3292](https://doi.org/10.1038/nmat3292); pmid: 22466746
31. M. Kang, T. H. Feng, H. T. Wang, J. S. Li, Wave front engineering from an array of thin aperture antennas. *Opt. Express* **20**, 15882 (2012). doi: [10.1364/OE.20.015882](https://doi.org/10.1364/OE.20.015882); pmid: 22772278
32. W. X. Shu *et al.*, Generation of optical beams with desirable orbital angular momenta by transformation media. *Phys. Rev. A* **85**, 063840 (2012).
33. N. M. Litchinitser, Structured light meets structured matter. *Science* **337**, 1054 (2012) and references therein. doi: [10.1126/science.1226204](https://doi.org/10.1126/science.1226204); pmid: 22936768
34. D. S. Simon, N. Lawrence, J. Trevino, L. Dal Negro, A. V. Sergienko, <http://arxiv.org/abs/1206.3548> (2012).
35. B. Walther, C. Helgert, C. Rockstuhl, T. Pertsch, Diffractive optical elements based on plasmonic metamaterials. *Appl. Phys. Lett.* **98**, 191101 (2011).
36. S. Larouche, Y. J. Tsai, T. Tyler, N. M. Jokerst, D. R. Smith, Infrared metamaterial phase holograms. *Nat. Mater.* **11**, 450 (2012). doi: [10.1038/nmat3278](https://doi.org/10.1038/nmat3278); pmid: 22426458
37. M. V. Berry, The adiabatic phase and Pancharatnam's phase for polarized light. *J. Mod. Opt.* **34**, 1401 (1987). doi: [10.1080/09500348714551321](https://doi.org/10.1080/09500348714551321)
38. S. Pancharatnam, Generalized theory of interference, and its applications. Part I. Coherent pencils. *Proc. Indiana Acad. Sci.* **44**, 247 (1956).
39. E. Hasman, V. Kleiner, G. Biener, A. Niv, Polarization dependent focusing lens by use of quantized Pancharatnam-Berry phase diffractive optics. *Appl. Phys. Lett.* **82**, 328 (2003). doi: [10.1063/1.1539300](https://doi.org/10.1063/1.1539300)
40. G. Biener, A. Niv, V. Kleiner, E. Hasman, Geometrical phase image encryption obtained with space-variant subwavelength gratings. *Opt. Lett.* **30**, 1096 (2005). doi: [10.1364/OL.30.001096](https://doi.org/10.1364/OL.30.001096); pmid: 15943278
41. A. Niv, G. Biener, V. Kleiner, E. Hasman, Spiral phase elements obtained by use of discrete space-variant subwavelength gratings. *Opt. Commun.* **251**, 306 (2005). doi: [10.1016/j.optcom.2005.03.002](https://doi.org/10.1016/j.optcom.2005.03.002)
42. A. Niv, G. Biener, V. Kleiner, E. Hasman, Manipulation of the Pancharatnam phase in vectorial vortices. *Opt. Express* **14**, 4208 (2006). doi: [10.1364/OE.14.004208](https://doi.org/10.1364/OE.14.004208); pmid: 19516574
43. U. Levy, H.-C. Kim, C.-H. Tsai, Y. Fainman, Near-infrared demonstration of computer-generated holograms implemented by using subwavelength gratings with space-variant orientation. *Opt. Lett.* **30**, 2089 (2005). doi: [10.1364/OL.30.002089](https://doi.org/10.1364/OL.30.002089); pmid: 16127919
44. Y. Gorodetski *et al.*, Weak measurements of light chirality with a plasmonic slit. *Phys. Rev. Lett.* **109**, 013901 (2012).
45. Y. Gorodetski, S. Nechayev, V. Kleiner, E. Hasman, Plasmonic Aharonov-Bohm effect: Optical spin as the magnetic flux parameter. *Phys. Rev. B* **82**, 125433 (2010).
46. N. Shitrit, I. Bretner, Y. Gorodetski, V. Kleiner, E. Hasman, Optical spin Hall effects in plasmonic chains. *Nano Lett.* **11**, 2038 (2011). doi: [10.1021/nl2004835](https://doi.org/10.1021/nl2004835); pmid: 21513279
47. A. Boltasseva, H. A. Atwater, Low-loss plasmonic metamaterials. *Science* **331**, 290 (2011). doi: [10.1126/science.1198258](https://doi.org/10.1126/science.1198258); pmid: 21252335
48. P. Y. Fan *et al.*, An invisible metal-semiconductor photodetector. *Nat. Photonics* **6**, 380 (2012). doi: [10.1038/nphoton.2012.108](https://doi.org/10.1038/nphoton.2012.108)
49. Y. M. Liu, T. Zentgraf, G. Bartal, X. Zhang, Transformational plasmon optics. *Nano Lett.* **10**, 1991 (2010). doi: [10.1021/nl1008019](https://doi.org/10.1021/nl1008019); pmid: 20465268
50. D. R. Smith, D. Schurig, Electromagnetic wave propagation in media with indefinite permittivity and permeability tensors. *Phys. Rev. Lett.* **90**, 077405 (2003).
51. X. D. Yang, J. Yao, J. Rho, X. B. Yin, X. Zhang, Experimental realization of three-dimensional indefinite cavities at the nanoscale with anomalous scaling laws. *Nat. Photonics* **6**, 450 (2012). doi: [10.1038/nphoton.2012.124](https://doi.org/10.1038/nphoton.2012.124)
52. Z. Jacob, L. V. Alekseyev, E. Narimanov, Optical hyperlens: Far-field imaging beyond the diffraction limit. *Opt. Express* **14**, 8247 (2006). doi: [10.1364/OE.14.008247](https://doi.org/10.1364/OE.14.008247); pmid: 19529199
53. H. N. S. Krishnamoorthy, Z. Jacob, E. Narimanov, I. Kretzschmar, V. M. Menon, Topological transitions in metamaterials. *Science* **336**, 205 (2012). doi: [10.1126/science.1219171](https://doi.org/10.1126/science.1219171); pmid: 22499943
54. Z. Jacob *et al.*, Engineering photonic density of states using metamaterials. *Appl. Phys. B* **100**, 215 (2010). doi: [10.1007/s00340-010-4096-5](https://doi.org/10.1007/s00340-010-4096-5)
55. M. A. Noginov *et al.*, Controlling spontaneous emission with metamaterials. *Opt. Lett.* **35**, 1863 (2010). doi: [10.1364/OL.35.001863](https://doi.org/10.1364/OL.35.001863); pmid: 20517443
56. Z. Jacob, E. E. Narimanov, Optical hyperspace for plasmons: Dyakonov states in metamaterials. *Appl. Phys. Lett.* **93**, 221109 (2008).
57. P. R. West *et al.*, Searching for better plasmonic materials. *Laser Photonics Rev.* **4**, 795 (2010) and references therein. doi: [10.1002/lpor.200900055](https://doi.org/10.1002/lpor.200900055)
58. A. Salandrino, N. Engheta, Far-field subdiffraction optical microscopy using metamaterial crystals: Theory and simulations. *Phys. Rev. B* **74**, 075103 (2006).
59. A. J. Hoffman *et al.*, Negative refraction in semiconductor metamaterials. *Nat. Mater.* **6**, 946 (2007). doi: [10.1038/nmat2033](https://doi.org/10.1038/nmat2033); pmid: 17934463
60. Z. Jacob, V. M. Shalaev, Plasmonics goes quantum. *Science* **334**, 463 (2011). doi: [10.1126/science.1211736](https://doi.org/10.1126/science.1211736); pmid: 22034423
61. Z. Jacob, I. I. Smolyaninov, E. E. Narimanov, Broadband Purcell effect: Radiative decay engineering with metamaterials. *Appl. Phys. Lett.* **100**, 181105 (2012).
62. Z. W. Liu, H. Lee, Y. Xiong, C. Sun, X. Zhang, Far-field optical hyperlens magnifying sub-diffraction-limited objects. *Science* **315**, 1686 (2007). doi: [10.1126/science.1137368](https://doi.org/10.1126/science.1137368); pmid: 17379801
63. S. M. Xiao *et al.*, Loss-free and active optical negative-index metamaterials. *Nature* **466**, 735 (2010). doi: [10.1038/nature09278](https://doi.org/10.1038/nature09278); pmid: 20686570
64. G. V. Naik, J. J. Liu, A. V. Kildishev, V. M. Shalaev, A. Boltasseva, Demonstration of Al:ZnO as a plasmonic component for near-infrared metamaterials. *Proc. Natl. Acad. Sci. U.S.A.* **109**, 8834 (2012) and references therein. doi: [10.1073/pnas.1121517109](https://doi.org/10.1073/pnas.1121517109); pmid: 22611188
65. G. V. Naik, J. Kim, A. Boltasseva, Oxides and nitrides as alternative plasmonic materials in the optical range. *Opt. Mater. Express* **1**, 1090 (2011) and references therein. doi: [10.1364/OME.1.001090](https://doi.org/10.1364/OME.1.001090)
66. G. V. Naik *et al.*, Titanium nitride as a plasmonic material for visible and near-infrared wavelengths. *Opt. Mater. Express* **2**, 478 (2012). doi: [10.1364/OME.2.000478](https://doi.org/10.1364/OME.2.000478)
67. E. Feigenbaum, H. A. Atwater, Resonant guided wave networks. *Phys. Rev. Lett.* **104**, 129 (2010).
68. J. A. Schuller *et al.*, Plasmonics for extreme light concentration and manipulation. *Nat. Mater.* **9**, 193 (2010). doi: [10.1038/nmat2630](https://doi.org/10.1038/nmat2630); pmid: 20168343

Acknowledgments: We thank A. Sokolov, X. Ni, and G. Naik for useful discussions. This work was partially supported by Air Force Office of Scientific Research grant FA9550-12-1-0024, U.S. Army Research Office grant 57981-PH (W911NF-11-1-0359), NSF grant DMR-1120923, and NSF award Meta-PREM no. 1205457.

[10.1126/science.1232009](https://doi.org/10.1126/science.1232009)



AAAS is here – bringing scientific expertise to policy making.

Good science policy is the result of politicians understanding science and scientists understanding policy. Toward this end, AAAS manages the Science & Technology Policy Fellowships program, which embeds scientists and engineers in the federal government for up to two years. From Congress to the State Department, each class of Fellows contributes to the policy-making process while getting hands-on experience at the intersection of science and policy. As a AAAS member your dues support these efforts. If you're not yet a AAAS member, join us. Together we can make a difference.

To learn more, visit aaas.org/plusyou/fellows



A Neural Circuit for Memory Specificity and Generalization

Wei Xu* and Thomas C. Südhof*

Increased fear memory generalization is associated with posttraumatic stress disorder, but the circuit mechanisms that regulate memory specificity remain unclear. Here, we define a neural circuit—composed of the medial prefrontal cortex, the nucleus reuniens (NR), and the hippocampus—that controls fear memory generalization. Inactivation of prefrontal inputs into the NR or direct silencing of NR projections enhanced fear memory generalization, whereas constitutive activation of NR neurons decreased memory generalization. Direct optogenetic activation of phasic and tonic action-potential firing of NR neurons during memory acquisition enhanced or reduced memory generalization, respectively. We propose that the NR determines the specificity and generalization of memory attributes for a particular context by processing information from the medial prefrontal cortex en route to the hippocampus.

Memories allow animals to adapt to a constantly changing environment. Memories are never completely precise but always partially generalized, which enables an animal to quickly and appropriately respond to novel stimuli that resemble a previous experience. The level of memory specificity and the degree of generalization are normally balanced. Generalization of fear memories protects animals

by alerting them to potential dangers when animals are exposed to situations that are similar to previously experienced harmful circumstances, but overgeneralization of fear memories can lead to inappropriate anxiety. This is evident with posttraumatic stress disorder (PTSD), in which the reexperiencing of a past trauma is triggered by cues existing in a normally safe environment (1). Similarly, overgeneralization of episodic memories is a consistent problem in patients with severe depression (2). Since its initial demonstration (3), memory generalization has been extensively characterized, and multiple theories have been developed to explain it. In addition to the hippocampus, which is critical for maintain-

ing the specificity of memories (4, 5), we recently found that the medial prefrontal cortex (mPFC) is essential for memory generalization (6). Specifically, we observed that global impairment of synaptic transmission in the mPFC unexpectedly caused overgeneralization of contextual fear memories. This observation is potentially interesting, because functional abnormalities of the mPFC have been consistently observed in patients with PTSD and other psychiatric disorders (7).

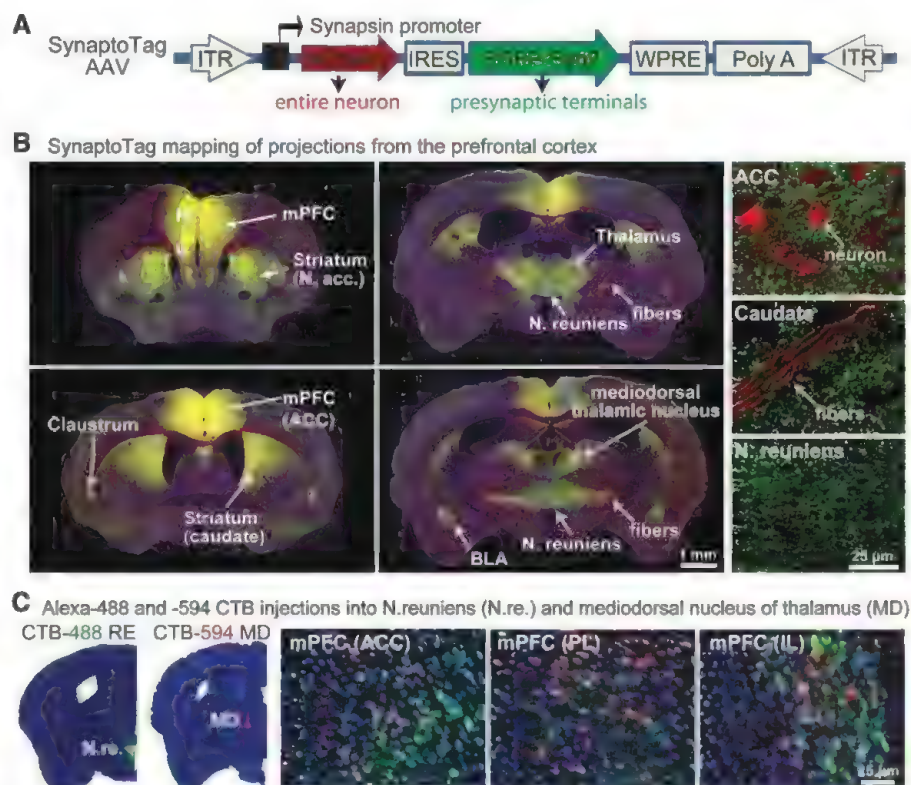
Mapping synaptic projections from the mPFC. The mPFC mediates the cognitive control of many high-level brain functions (7, 8). Consistent with such cognitive control, inactivation of synaptic transmission by expressing the light chain of tetanus toxin (TetTox) in the mPFC does not block fear memory, but leads to overgeneralization of such fear memory (6). However, it is unclear which synaptic projections from the mPFC to subcortical regions are critical for maintaining the proper balance between retention and generalization of fear memory details.

To quantitatively map the projections from the mPFC to subcortical regions, we developed a “SynaptoTag” adeno-associated virus (AAV), which coexpresses red fluorescent mCherry protein and enhanced green fluorescent protein (EGFP) fused to the synaptic vesicle protein synaptobrevin-2 (Fig. 1A) (9). Neurons infected with SynaptoTag AAV are filled with diffusible mCherry, which is present throughout their cytoplasm, including axon fibers. These neurons selectively localize green fluorescent synaptobrevin-2 to efferent synapses, allowing a quantitative assessment of

Department of Molecular and Cellular Physiology and Howard Hughes Medical Institute, Stanford University, 265 Campus Drive, Stanford, CA 94304–5453, USA.

*To whom correspondence should be addressed. E-mail: weixu@stanford.edu (W.X.); tcs1@stanford.edu (T.C.S.)

Fig. 1. Distinct mPFC neurons project to different synaptic targets. **(A)** Design of SynaptoTag AAV used for tracing synaptic connections. The synapsin promoter in the AAV drives bicistronic expression of soluble mCherry and a presynaptic EGFP–synaptobrevin-2 fusion protein (EGFP–Syb2). ITR, inverted terminal repeat; IRES, internal ribosome entry site; WPRE, woodchuck hepatitis posttranscriptional regulatory element. **(B)** SynaptoTag AAV mapping of mPFC projections. Representative low-resolution (left and middle panels) and high-resolution images (right panels) illustrate synaptic targets for mPFC neurons. Red mCherry labeling marks axonal fibers, whereas green EGFP labeling marks synapses projecting from the mPFC (yellow, coincident red and green labeling). BLA, basolateral nucleus of the amygdala; IL, infralimbic cortex; PL, prelimbic cortex; N. acc, nucleus accumbens (for complete sections, see fig. S1). **(C)** Retrograde labeling of mPFC neurons after injection of Alexa Fluor-488 and -594 labeled cholera toxin-B (CTB-488 and CTB-594) into the NR (N.re., green) and the mediodorsal thalamic nucleus (MD, red), respectively. Low-power micrographs (left panels) show injection areas, whereas high-power images (right panels) depict the three major mPFC regions. Most traced neurons were dominated by the presence of one fluorophore (for additional mPFC projections, see fig. S2).



the number of synapses formed in a target region by SynaptoTag AAV-infected neurons. This simple approach provides information about the distribution of both axonal fibers and synaptic terminals derived from a neuron.

We stereotactically injected SynaptoTag AAV into the mPFC of adult mice and imaged the localization of synapses formed by mPFC neurons 8 weeks later (Fig. 1B and fig. S1). Axons of mPFC neurons that were positive for mCherry formed a fiber bundle that extended caudoventrally through the corpus callosum, dorsal striatum, dorsal thalamus, hypothalamus, and midbrain structures. Axons continuously branched out of this bundle and formed synaptic connections with brain structures on the way. The intensity and density of the observed green synaptic puncta reflects the number of synaptic connections. Apart from a dense meshwork of synapses formed by mPFC neurons within the mPFC itself, mPFC neurons formed major synaptic pro-

jections in the mediodorsal striatum and nucleus accumbens, thalamus, claustrum, septohippocampal nucleus, and basolateral amygdala (Fig. 1B). In the thalamus, most projections were targeted to the mediodorsal nucleus (MD) and the nucleus reuniens (NR). The mPFC also sent substantial synaptic projections to the zona incerta, hypothalamic nuclei, midbrain, and periaqueductal gray.

The parallel connections of mPFC neurons to different subcortical nuclei raise the question of whether the same mPFC neurons project to multiple targets. Thus, we injected fluorescent cholera toxin B (CTB), tagged with Alexa Fluor-488 or Alexa Fluor-594 (Invitrogen, Carlsbad, California), into neighboring thalamic nuclei (the NR and the MD). We detected retrogradely labeled neurons in all three major subregions of the mPFC [the prelimbic cortex, the infralimbic cortex, and the anterior cingulate cortex (ACC)] (Fig. 1C and fig. S2). Most fluorescent mPFC neurons contained only one of

the two fluorophores, indicating that these neurons preferentially project to only one of the two neighboring thalamic regions examined. We also injected the fluorescent CTB tracers into the mediodorsal striatum and either the mediodorsal thalamic nucleus or the NR, and we observed a similar segregation of mPFC projection neurons (fig. S2).

Which mPFC projections control fear memory? We have previously observed overgeneralization of contextual fear memory induced by global expression of TetTox in the mPFC (6). Because distinct subpopulations of mPFC neurons project to different brain regions, it is unclear which of these projections participates in the circuit that controls fear memory generalization. To address this question, we used a trans-neuronally transported version of cre-recombinase that is fused to wheat-germ agglutinin (WGA-cre fusion protein) (10, 11).

We injected an AAV encoding a double-floxed, inverted EGFP and TetTox gene (2xFlx-TetTox) into the mPFC (Fig. 2A). This AAV expressed EGFP and TetTox only after inversion of the double-floxed expression cassette by cre-recombinase. At the same time, we injected a second AAV into one of the brain areas that are targeted by efferent synapses from the mPFC (Fig. 2B). The second AAV coexpressed red fluorescent mCherry and WGA-cre fusion protein (Fig. 2A). We then tested whether expression of WGA-cre in target areas for the mPFC activated EGFP and TetTox expression in the mPFC. We found that WGA-cre AAV injections specifically induced EGFP expression in the mPFC (Fig. 2B and fig. S3). Detection of WGA-cre-mediated trans-neuronal transport was made possible by modifications in the AAV vectors, especially by using a shorter synapsin promoter (~0.5 kb) and the AAV-DJ serotype (6). Substantially fewer mPFC neurons were labeled with EGFP by the WGA-cre/2xFlx-TetTox approach than were traced with CTB (Figs. 1C and 2B and figs. S3 and S4), suggesting that trans-synaptic WGA-cre transport is less efficient than retrograde labeling with an extracellular tracer. Quantifications showed that approximately one-third of the mPFC neurons projecting to the striatum were captured by trans-neuronal transport of WGA-cre from the target area (fig. S5). Despite its lower efficacy, we chose WGA-cre for our experiments instead of more efficacious rabies virus vectors (12), because rabies viruses in our hands induced rapid cytotoxicity, which may confound the interpretation of the behavioral results, whereas WGA-cre did not exhibit this problem.

We asked whether blocking specific projections from the mPFC to target areas alters fear memory generalization. We bilaterally injected the 2xFlx-TetTox AAV into the mPFC and the WGA-cre AAV into three target brain regions that receive synaptic inputs from the mPFC (the mediodorsal striatum, mediodorsal thalamic nucleus, and NR), as well as into the mPFC itself (as a positive control). We selected the mediodorsal striatum and the mediodorsal thalamic nucleus because they are major mPFC targets (Fig. 1B). We chose the NR because it forms an

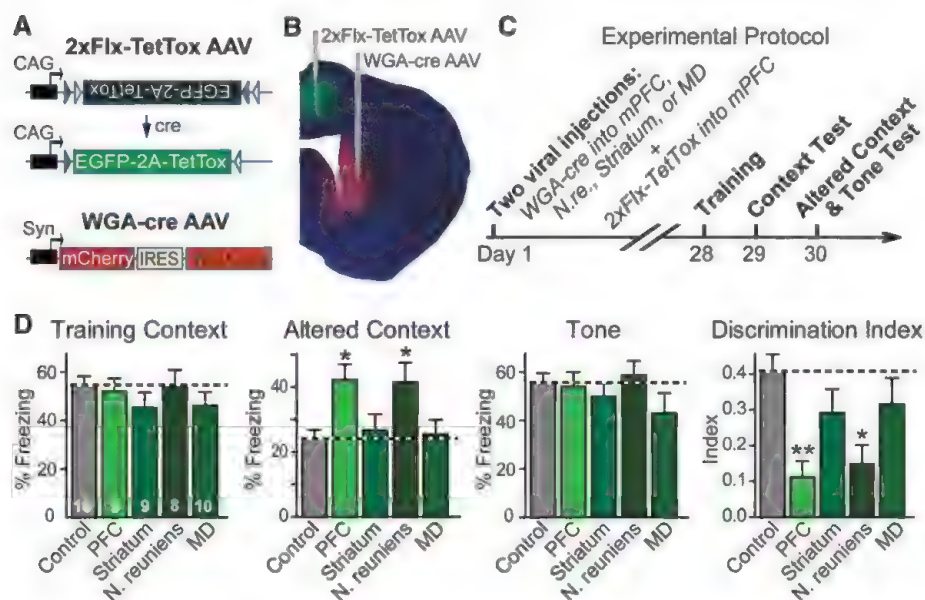


Fig. 2. mPFC projection to the NR controls memory specificity. (A) Design of AAVs used for inactivating synaptic transmission in subsets of projection neurons with specific synaptic targets. Double-floxed inverted TetTox-AAV (2xFlx-TetTox AAV) encodes bicistronic expression of EGFP for visualizing infected neurons and of TetTox for blocking synaptic transmission. The coding region of the double-floxed inverted TetTox-AAV is not translated until cre-recombinase flips the inverted coding region into the correct orientation. WGA-cre AAV mediates bicistronic expression of mCherry and WGA-cre. When this AAV infects a neuron, WGA-cre is trans-neuronally transferred to connected neurons, whereas mCherry is only expressed in the infected neuron. (B) Coronal brain section of a mouse injected with 2xFlx-TetTox AAV in the mPFC and with WGA-cre AAV in the dorsomedial striatum. The green EGFP fluorescence in the mPFC indicates that trans-synaptically transported WGA-cre activated expression of TetTox and EGFP in the mPFC. For high-magnification images, additional examples, and quantification of the trans-synaptic transport efficiency, see figs. S3 to S5. (C) Experimental protocol for analyzing the behavioral effects of selective TetTox expression in mPFC neurons that project to specific targets. 2xFlx-TetTox AAV was stereotactically injected into the mouse mPFC, and WGA-cre AAV was injected into the striatum, mediodorsal thalamic nucleus, NR, or mPFC (control, no WGA-cre AAV injection). Mice were tested 4 weeks later for contextual fear conditioning (context test), fear conditioning in an altered context to measure memory precision, and cued fear conditioning (tone test). For additional information, see fig. S6. (D) Fear conditioning measured with the experimental strategy described in (C) in multiple independent experiments (in the left panel, numbers in bars denote the number of mice analyzed). The discrimination index was calculated as the difference between the percentage of freezing in the training context and the altered context, divided by the sum of the two percentages. Data are means \pm SEM (error bars); statistical significance (* P < 0.05; ** P < 0.01) was assessed by (i) two-way mixed-model analysis of variance (ANOVA) with Bonferroni's post-hoc test comparing the freezing levels or (ii) one-way ANOVA followed by Turkey's post-hoc test for the discrimination index. Horizontal dashed lines indicate the level of control groups.

anatomical link between the mPFC and the hippocampus (13, 14), both of which are essential for memory specificity (4–6), and because the NR has been shown to play a possible role in hippocampus-dependent learning and memory (15, 16).

Four weeks after viral injections, we performed fear conditioning tests (Fig. 2C and fig. S6). We trained the injected mice with three tone-foot-shock pairs in a conditioning chamber and then measured “freezing” sequentially, first in the training chamber to assess contextual fear memory, then in a similar but altered chamber to examine fear memory generalization, and finally, in response to the conditioning tone, in the altered chamber to measure cued fear memory (6). We quantified fear memory generalization as the discrimination index (the difference between freezing in the training and the altered context, divided by the sum of freezing in both conditions).

Global inactivation of the mPFC with TetTox did not impair cued or contextual fear conditioning but did induce overgeneralization of fear memories (Fig. 2D). Activation of TetTox, specifically in only mPFC neurons that projected to the striatum or the mediodorsal thalamic nucleus, had no effect on any parameter during fear conditioning, including memory generalization. However, activation of TetTox in only mPFC neurons that projected to the NR caused overgeneralization of fear memories, similar to what we observed with direct expression of TetTox in the mPFC (Fig. 2D). Given the incomplete efficiency of the retrograde transport of WGA-cre, our results do not exclude the possibility that the striatum and mediodorsal thalamic nucleus also play a more limited role in memory generalization, but our findings suggest that this role is not inhibited by partial inactivation of the mPFC projection to these nuclei. In contrast, partial inactivation of the mPFC projection to the NR is sufficient to produce overgeneralization of fear memories.

The NR bidirectionally controls fear memory generalization. To explore the control of fear memory generalization by the NR, we injected into the NR recombinant lentiviruses encoding either EGFP alone (control), TetTox, or a short hairpin RNA that suppresses *neurexin-2* expression (NL2 KD) (Fig. 3A and fig. S7A) (17–20). Whereas TetTox suppressed propagation of synaptic signals from the NR, the *neurexin-2* knockdown decreased synaptic inhibition of NR neurons (the NR lacks intrinsic inhibitory neurons releasing γ -aminobutyric acid and receives inhibitory inputs from other brain regions), thereby increasing propagation of synaptic signals from the NR (Fig. 3 and fig. S7).

Two weeks after viral injections, we measured fear conditioning (Fig. 3, D and E). Similar to the effects induced by TetTox in the mPFC, expression of TetTox in the NR caused an overgeneralization of contextual fear memory without significant effects on contextual or cued fear conditioning. This overgeneralization was specific for contextual memories, as the generalization of cued memories was not affected (fig. S8). In contrast to the effect of TetTox, suppression of *neurexin-2* expression reduced memory generalization (Fig. 3E).

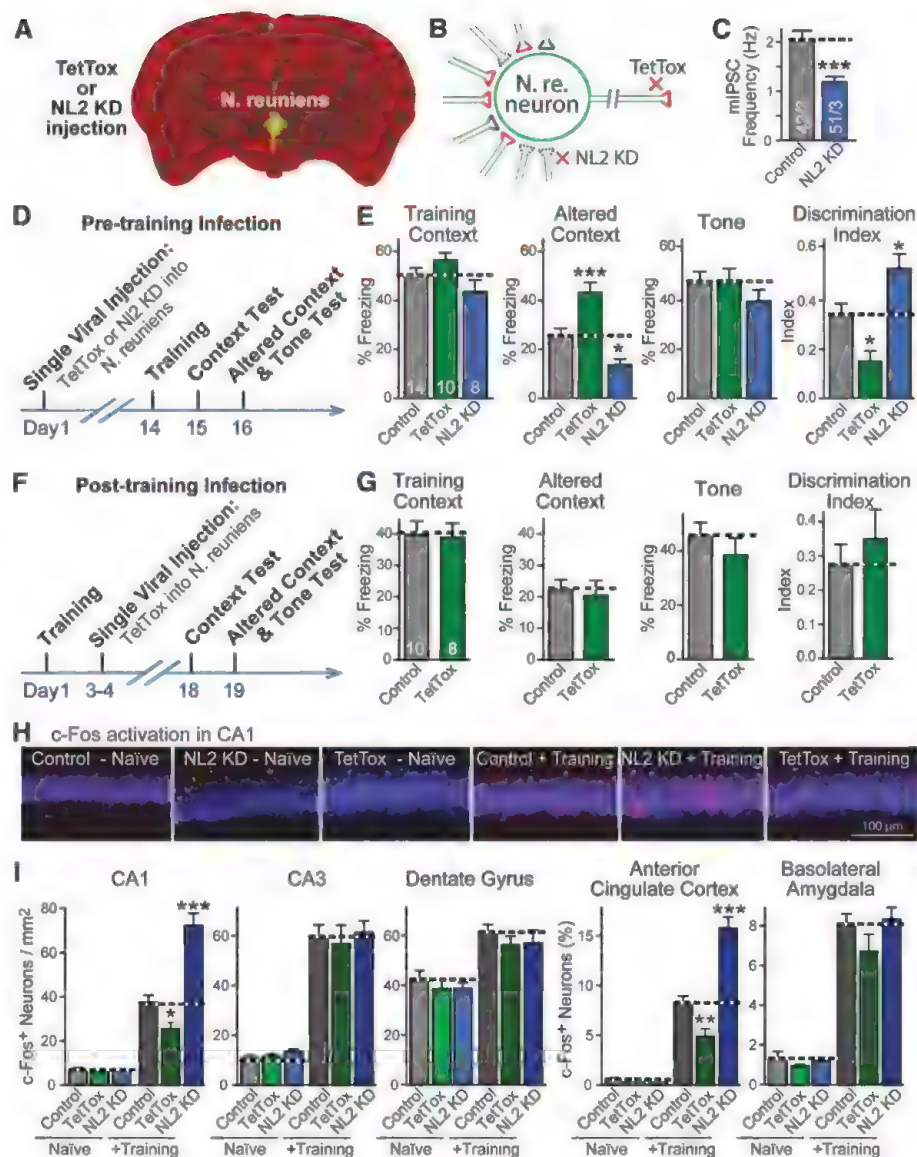


Fig. 3. The NR bidirectionally controls fear memory generalization. (A) Representative coronal brain section showing local expression of EGFP (green) after stereotaxic injection into the NR of lentiviruses encoding EGFP and TetTox or the *neurexin-2* knockdown (NL2 KD). (B) Schema of the effects of TetTox expression or of the *neurexin-2* knockdown on the activity of neurons in the NR. The *neurexin-2* knockdown decreases inhibition of NR neurons, thereby activating these neurons, whereas TetTox blocks synaptic outputs from NR neurons. (C) Effect of *neurexin-2* knockdown on the frequency of spontaneous inhibitory miniature synaptic events (mIPSCs), recorded in acute NR slices from mice that were injected with *neurexin-2* knockdown lentivirus (numbers in bars denote the number of neurons and mice analyzed, respectively). (D) Experimental protocol for testing fear memory after TetTox expression or *neurexin-2* knockdown in the NR. (E) Bidirectional changes in fear memory generalization by neuronal silencing with TetTox or neuronal activation with the *neurexin-2* knockdown. Mice injected with lentivirus expressing only EGFP were used as controls (numbers of mice are indicated in bars). (F and G) Same as (C) and (D), except that mice were injected with control or TetTox virus after fear conditioning training. (H and I) Effect of fear conditioning training and of TetTox expression or *neurexin-2* knockdown in the NR on the activity levels of neurons in different target brain regions. Control, TetTox, or the *neurexin-2* knockdown lentiviruses were injected into the NR of adult mice. Mice were subjected to fear conditioning training (+Training) or received no training (naïve) and were sacrificed 90 min after training. Brain sections were stained for c-Fos (red) to measure neuronal activation and NeuN to label all neuronal nuclei (blue). (H) Representative images of the hippocampal CA1 region. (I) Quantification of c-Fos expression in the indicated brain regions ($n = 12$ to 18 brain sections from four mice in each group; for additional data, see figs. S11 and S12). Data shown are means \pm SEM (error bars). Statistical significance (* $P < 0.05$; ** $P < 0.01$; *** $P < 0.001$) was assessed by two-tailed Student's t test [(C) and (G)], two-way ANOVA followed by Bonferroni's post-hoc test [(E), comparing freezing levels, and (I)], or one-way ANOVA followed by Turkey's post-hoc test [discrimination index in (E)]. Horizontal dashed lines indicate the level of control groups.

Does the NR determine the precision of memory during memory acquisition and/or during memory retrieval? To address this question, we injected lentiviruses expressing TetTox into the NR after fear conditioning and measured fear memories 2 weeks later (Fig. 3, F and G). Expression of TetTox after training had no effect on memory generalization, establishing the specificity of the effects observed by TetTox on the generalization of fear memory during the acquisition stage.

The mPFC, NR, and hippocampus constitute a memory generalization circuit. The NR directly projects to the hippocampus and back to the mPFC (13, 14), and the hippocampus, in turn, also projects to the mPFC (21), thus creating a closed loop with the projection from the mPFC to the NR (Fig. 1). In mapping experiments using SynapTag AAV injections into the NR and the hippocampus, we confirmed these conclusions (figs. S9 and S10). A major question, however, is how much the activity of NR neurons actually influences neuronal excitation in the hippocampus; that is, whether this is a major signaling pathway during memory acquisition.

Previous studies indicate that memories with high specificity involve a high level of engagement of the hippocampus (22). Thus, we examined whether enhanced fear generalization upon TetTox expression or reduced fear generalization following neuroligin-2 suppression in the NR are associated with corresponding changes in the activation of hippocampal neurons and whether such changes are specific to these neurons. We subjected control mice and mice with TetTox expression or neuroligin-2 knockdown in the NR to fear conditioning training, and we analyzed c-Fos expression in multiple brain regions 90 min afterward.

Consistent with previous reports (23, 24), c-Fos-positive neurons were increased after training in multiple brain regions, including the hippocampus, mPFC, amygdala, ventral tegmental area, and periaqueductal gray in control mice (Fig. 3, H and I, and figs. S11 and S12). Expression of TetTox or knockdown of neuroligin-2 in the NR had little effect on the basal c-Fos expression in any brain region. However, TetTox expression significantly and selectively decreased c-Fos

activation in the CA1 region of the hippocampus and in the ACC of the mPFC, whereas the neuroligin-2 knockdown significantly enhanced the effects of training on c-Fos expression in these two brain regions (Fig. 3I and fig. S12).

Activity patterns of NR neurons control memory specificity. To directly test the role of the NR in balancing the precision of contextual fear memories, we stimulated firing of NR neurons in behaving mice during memory acquisition using optogenetics. We expressed the channelrhodopsin-derivative ChIEF (25) in the NR and stimulated NR neurons via an implanted optical fiber (Fig. 4A). Electrophysiological experiments have shown that ChIEF exhibits fast kinetics and allows action-potential stimulation at frequencies of up to 50 Hz (25).

We used either tonic 4-Hz stimulus trains or phasic 15-pulse stimulus bursts to stimulate NR neurons during fear conditioning training (Fig. 4B) (26, 27). Similar to the TetTox and neuroligin-2 knockdown manipulations in the NR, neither the phasic nor the tonic NR stimulation had detectable effects on contextual or cued fear conditioning (Fig. 4C). However, these stimulations induced opposite changes in fear memory generalization. Phasic NR stimulation during training caused increased freezing in the altered context (i.e., produced overgeneralization of fear memory). In contrast, tonic NR stimulation induced decreased freezing in the altered context (i.e., a reduction in fear generalization) (Fig. 4C).

Because the two stimulation patterns we used represent, in principle, the same manipulation—optogenetic stimulation of NR firing—but result in opposite effects, these patterns control for each other, ruling out the possibility that the optogenetic manipulation simply impairs the functions of the NR instead of specifically stimulating it. Previous studies have shown that stimulation of the inputs from the NR to the hippocampus produces sub-threshold depolarization of CA1 pyramidal cells but above-threshold stimulation of inhibitory interneurons (28). The different behavioral phenotypes produced by the distinct stimulation patterns of NR neurons might arise from the relative impact of their stimulation on their downstream excitatory versus inhibitory neurons. Recent evidence indicates that the activity of the NR correlates with hippocampal oscillations, suggesting that the different behavioral effects may be related to changes in hippocampal oscillations (29).

Summary. Here, we establish that the mPFC controls memory specificity via signaling to the NR that, in turn, signals to the hippocampus and also back to the mPFC. The generalization of hippocampus-dependent memories is often discussed in the framework of complementary learning systems theory (30, 31). In this theory, the hippocampus keeps separate representations of individual memory episodes (specific memories), whereas the cortex abstracts common features from multiple memories. Through systems consolidation, in which memories are transferred from the hippocampus to the cortex, memories become generalized. Highly specific memories are proposed

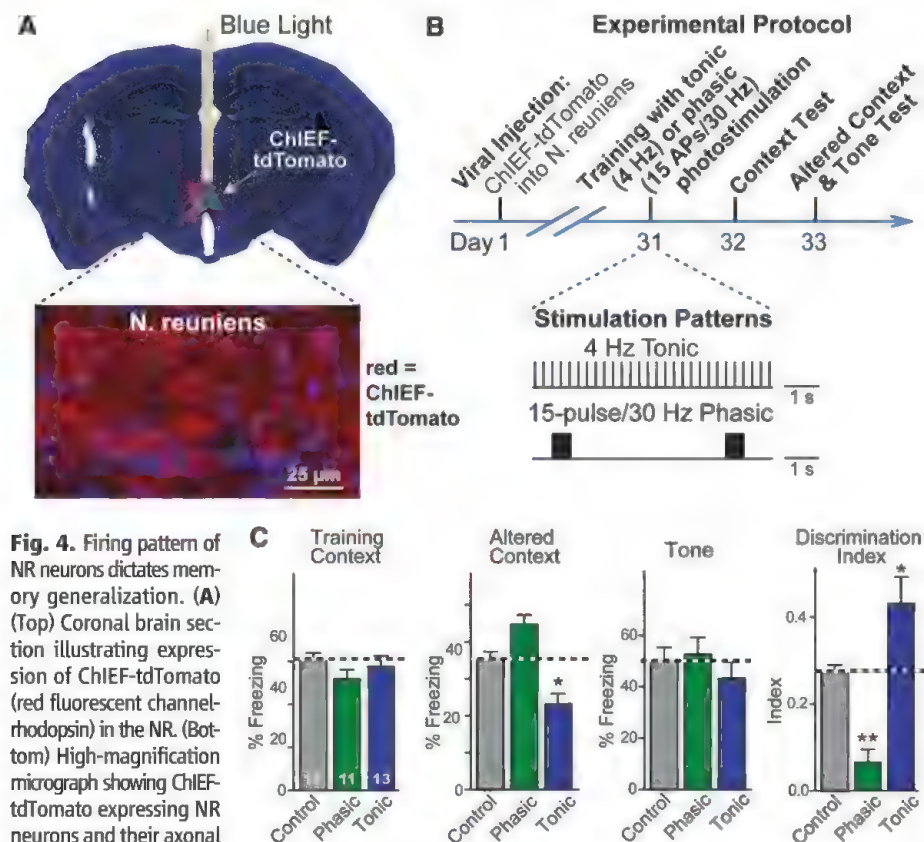


Fig. 4. Firing pattern of NR neurons dictates memory generalization. (A) (Top) Coronal brain section illustrating expression of ChIEF-tdTomato (red fluorescent channelrhodopsin) in the NR. (Bottom) High-magnification micrograph showing ChIEF-tdTomato expressing NR neurons and their axonal fibers. (B) Experimental protocol for testing the effect of different optogenetic stimulation patterns of NR neurons on fear conditioning behavior, with the stimulation patterns illustrated below the time diagram. NR neurons were stimulated throughout the 6-min training period by either a 4-Hz tonic stimulation or a 30-Hz phasic stimulation administered for 0.5 s every 5 s. Stimulus light pulses lasted 15 ms. (C) Tonic and phasic optogenetic stimulation produced opposite effects on fear memory generalization. Control mice also expressed channelrhodopsin and contained an implanted optical fiber, but were not stimulated. Data shown are means \pm SEM (error bars); numbers in bars indicate the number of mice analyzed. Statistical significance (* P < 0.05; ** P < 0.01) was assessed by two-way mixed-model ANOVA followed by Bonferroni's post-hoc test comparing the freezing levels or by one-way ANOVA followed by Turkey's post-hoc test for the discrimination index. Horizontal dashed lines indicate the level of control groups.

to be maintained through “pattern separation,” but can be generalized during retrieval through “pattern completion” (32, 33). Complementary learning systems theory provides a plausible account of the time-dependent generalization of memories after memory acquisition and their generalization upon memory retrieval (34–36), but this theory does not explain how memory generalization is controlled during acquisition. Taking advantage of the temporal precision of optogenetic stimulations, we found that the mPFC-NR-hippocampus circuit controls memory specificity and generalization during acquisition (Fig. 4).

Because memories are not composed of simple unitary traces but rather of flexible combinations of attributes or features of the remembered objects or situations (37, 38), generalization of memories may stem from overlap between the representations of the attributes and/or features of memories (39, 40). Different attributes of an object may not be remembered equally. For example, after seeing a baseball with a player's autograph (Fig. 5B), readers may memorize distinct combinations of the baseball's features to form memories with different levels of specificity. When only the most prominent attributes are remembered, its memory representation is more likely to overlap with that of another memory and become generalized. But when more features are remembered, the overall representation is less likely to overlap with other memory representations and, hence, becomes more specific. A plausible model that accounts for our

findings is that the NR may exert a persistent regulation of the excitability of hippocampal neurons, thereby controlling memory generalization (28). Increased excitability may allow less prominent memory features to be incorporated into overall memories by facilitating the firing or synaptic plasticity of CA1 neurons (fig. S13). Memories with more detailed attributes will then become more specific. This overall idea agrees with the general functions proposed for midline thalamic structures: Instead of relaying specific sensory information, they are thought to adjust the activity level of cortical structures (including the hippocampus and mPFC) (41). Studies of hippocampal place cells indicate that these cells undergo substantial “remapping” when encoding similar memories, especially in the CA3 region. Through remapping, subtle changes in the environment could produce profound alterations of a memory representation in the hippocampus, thereby increasing the distinction between similar memories (42). Thus, the mPFC-NR-hippocampus circuit may regulate memory generalization by actively controlling remapping. Notably, hippocampal remapping is modulated by motivational and emotional states (42, 43). Because the mPFC is centrally involved in the motivational and emotional states of an animal (7, 8), the mPFC-NR pathway may convey the motivational and emotional value of the attributes of a memory to the hippocampus for memory encoding, which, in turn, may underlie the regulation of memory generalization during acquisition.

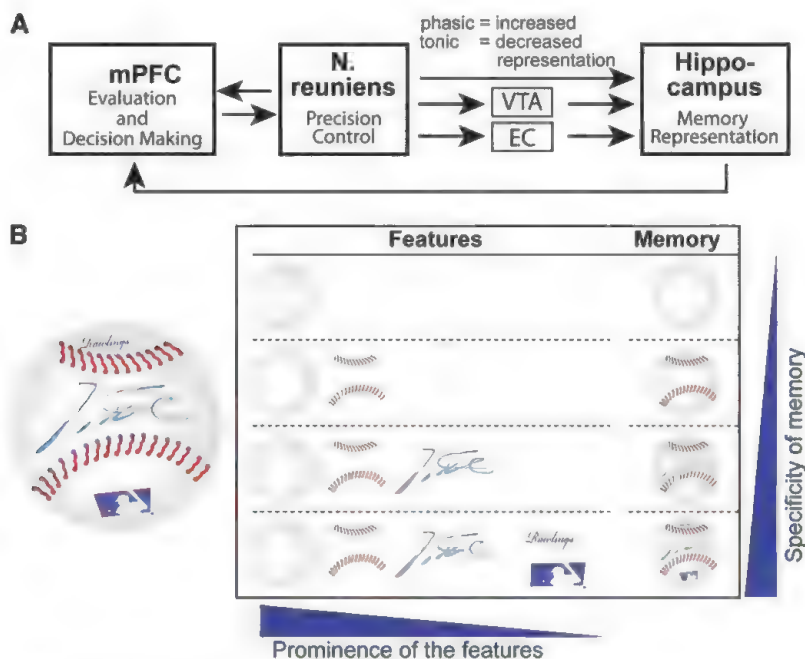


Fig. 5. Model for the mechanism of the NR's control of memory generalization. **(A)** Schematic diagram of the synaptic interactions between the mPFC, NR, and hippocampus in controlling memory generalization. VTA, ventral tegmental area; EC, entorhinal cortex. **(B)** Illustration of the modular composition of memory features. We posit that memories differentially incorporate a composite of specific attributes. The more prominent a feature is, the more likely it is to be included in memory, as illustrated here with a baseball containing additional features besides “ballness.” We propose that NR neurons control memory generalization by regulating the number of features that are incorporated into a memory. For a more detailed discussion, see fig. S13.

References and Notes

- A. L. Mahan, K. J. Ressler, *Trends Neurosci.* **35**, 24 (2012).
- I. H. Gotlib, J. Joormann, *Annu. Rev. Clin. Psychol.* **6**, 285 (2010).
- J. B. Watson, R. Rayner, *Am. Psychol.* **55**, 313 (2000).
- P. W. Frankland, V. Cestari, R. K. Filipkowski, R. J. McDonald, A. J. Silva, *Behav. Neurosci.* **112**, 863 (1998).
- F. G. Freeman, N. R. Kramarcy, J. Lee, *Physiol. Behav.* **11**, 273 (1973).
- W. Xu et al., *Neuron* **73**, 990 (2012).
- J. W. Dalley, R. N. Cardinal, T. W. Robbins, *Neurosci. Biobehav. Rev.* **28**, 771 (2004).
- S. P. Wise, *Trends Neurosci.* **31**, 599 (2008).
- Experimental procedures are explained in the materials and methods section of the supplementary materials on Science Online.
- J. M. Braz, B. Rico, A. I. Basbaum, *Proc. Natl. Acad. Sci. U.S.A.* **99**, 15148 (2002).
- V. Gradinaru et al., *Cell* **141**, 154 (2010).
- F. Osakada et al., *Neuron* **71**, 617 (2011).
- R. P. Vertes, *Neuroscience* **142**, 1 (2006).
- R. P. Vertes, W. B. Hoover, K. Szigeti-Buck, C. L. Lanthorn, *Brain Res. Bull.* **71**, 601 (2007).
- M. J. Dolleman-van der Weel, R. G. Morris, M. P. Witter, *Brain Struct. Funct.* **213**, 329 (2009).
- M. Loureiro et al., *J. Neurosci.* **32**, 9947 (2012).
- We chose lentiviruses for these experiments because they infect a small area of less than 0.8 mm in diameter (Fig. 3A). TetTox inactivates all synaptic outputs from the NR. Neuroligin-2 is a synaptic adhesion molecule that is exclusively expressed in inhibitory synapses (18), and inactivation of neuroligin-2 depresses the function of a subset of inhibitory synapses (19, 20).
- F. Varoqueaux, S. Jamain, N. Brose, *Eur. J. Cell Biol.* **83**, 449 (2004).
- J. R. Gibson, K. M. Huber, T. C. Südhof, *J. Neurosci.* **29**, 13883 (2009).
- A. Poullopoulos et al., *Neuron* **63**, 628 (2009).
- L. W. Swanson, *Brain Res.* **217**, 150 (1981).
- B. J. Wiltgen et al., *Curr. Biol.* **20**, 1336 (2010).
- I. Goshen et al., *Cell* **147**, 678 (2011).
- S. Milanovic et al., *Brain Res.* **784**, 37 (1998).
- J. Y. Lin, M. Z. Lin, P. Steinbach, R. Y. Tsien, *Biophys. J.* **96**, 1803 (2009).
- Because only limited information about the natural firing patterns of NR neurons is available (27–29), we first explored stimulation patterns to identify an optimal regimen. We found that tonic 4-Hz stimulus trains and phasic 15-pulse stimulus bursts (delivered at 30 Hz with 5-s intervals) produced significant but distinct behavioral effects, leading us to use these two stimulation paradigms for our experiments.
- G. J. Morales, E. J. Ramcharan, N. Sundaraman, S. D. Morgera, R. P. Vertes, *Conf. Proc. IEEE Eng. Med. Biol. Soc.* **2007**, 2480 (2007).
- M. J. Dolleman-Van der Weel, F. H. Lopes da Silva, M. P. Witter, *J. Neurosci.* **17**, 5640 (1997).
- Y. Zhang, T. Yoshida, D. B. Katz, J. E. Lisman, *J. Neurophysiol.* **107**, 3181 (2012).
- D. Kumaran, J. L. McClelland, *Psychol. Rev.* **119**, 573 (2012).
- J. L. McClelland, B. L. McNaughton, R. C. O'Reilly, *Psychol. Rev.* **102**, 419 (1995).
- T. J. McHugh et al., *Science* **317**, 94 (2007).
- T. Nakashiba et al., *Cell* **149**, 188 (2012).
- C. C. Perkins Jr., R. G. Weyant, *J. Comp. Physiol. Psychol.* **51**, 596 (1958).
- B. J. Wiltgen, A. J. Silva, *Learn. Mem.* **14**, 313 (2007).
- Y. Zhou, D. C. Riccio, *Learn. Motiv.* **27**, 400 (1996).
- H. Eichenbaum, *Neuron* **44**, 109 (2004).
- H. Eichenbaum, P. Dudchenko, E. Wood, M. Shapiro, H. Tanila, *Neuron* **23**, 209 (1999).
- M. W. Howard, M. S. Fotedar, A. V. Datey, M. E. Hasselmo, *Psychol. Rev.* **112**, 75 (2005).
- S. M. McTighe, R. A. Cowell, B. D. Winters, T. J. Bussey, L. M. Saksida, *Science* **330**, 1408 (2010).
- H. J. Groenewegen, H. W. Berendse, *Trends Neurosci.* **17**, 52 (1994).
- L. L. Colgin, E. I. Moser, M. B. Moser, *Trends Neurosci.* **31**, 469 (2008).
- M. A. Moita, S. Rosis, Y. Zhou, J. E. LeDoux, H. T. Blair, *J. Neurosci.* **24**, 7015 (2004).

Acknowledgments: We thank the following colleagues for providing plasmids and advice: M. Fucillo and J. Ko (neuroligin-2 knockdown constructs), J. Burre (EGFP-synaptobrevin-2 construct), C. Acuna and R. Tsien (ChIEF-tdTomato), S. Lammel (advice on optogenetics), and K. Diesseroth (WGA-cre plasmid). This study was supported by grants from the Simons Foundation (177850), the

National Institute of Mental Health (P50 MH086403), and the National Institute of Neurological Disorders and Stroke (NS077906).

Supplementary Materials

www.sciencemag.org/cgi/content/full/339/6125/1290/DC1
Materials and Methods

Figs. S1 to S13
References

30 August 2012; accepted 1 February 2013
10.1126/science.1229534

REPORTS

Spin Torque–Generated Magnetic Droplet Solitons

S. M. Mohseni,^{1,2} S. R. Sani,^{1,2} J. Persson,² T. N. Anh Nguyen,¹ S. Chung,^{1,3}
Ye. Pogoryelov,³ P. K. Muduli,^{3,4} E. Iacocca,³ A. Eklund,⁵ R. K. Dumas,³ S. Bonetti,^{1,6}
A. Deac,⁷ M. A. Hoefer,⁸ J. Åkerman^{1,2,3*}

Dissipative solitons have been reported in a wide range of nonlinear systems, but the observation of their magnetic analog has been experimentally challenging. Using spin transfer torque underneath a nanocontact on a magnetic thin film with perpendicular magnetic anisotropy (PMA), we have observed the generation of dissipative magnetic droplet solitons and report on their rich dynamical properties. Micromagnetic simulations identify a wide range of automodulation frequencies, including droplet oscillatory motion, droplet “spinning,” and droplet “breather” states. The droplet can be controlled by using both current and magnetic fields and is expected to have applications in spintronics, magnonics, and PMA-based domain-wall devices.

Dissipative solitons are localized excitations realized by a balance between nonlinearity, dispersion, gain, and loss (*1, 2*). They can be experimentally observed in optical (*3, 4*), chemical (*5, 6*), granular (*7*), and liquid (*8*) dissipative systems. Large amplitude nanoscale dynamics in magnetic thin films with perpendicular magnetic anisotropy (PMA) inherently possess all mechanisms supporting dissipative solitons except for gain. Spin-transfer torque (STT) (*9–12*) provides for the injection of angular momentum from spin-polarized electrons into a magnet. Using STT as the gain mechanism in nanocontact (NC)-based spin-torque oscillators (STOs), a magnetic dissipative soliton—the so-called “magnetic droplet”—was recently proposed (*13–15*). Using NC-STOs, we created and investigated magnetic droplet dynamics experimentally.

Classical conservative solitons, such as light pulses in a virtually lossless optical fiber, preserve their shape by balancing the opposing ef-

fects of dispersion (spreading) and nonlinearity (focusing). Similarly, if damping is ignored the Landau-Lifshitz equation for an extended two-dimensional magnetic thin film with PMA can sustain a family of conservative magnetic solitons, known as “magnon drops” (*16, 17*). All spins in a magnon drop precess in phase around the film normal, with a precession angle $0 < \Theta(0) < \pi$ at the center of the drop and $0 < \Theta(r) < \Theta(0)$ decreasing exponentially fast, with radius to 0 in the far field. The family of stationary magnon drops can be parameterized by the precessional frequency f_0 , satisfying $f_{\text{Zeeman}} < f_0 < f_{\text{FMR}}$, where f_{FMR} is the ferromagnetic resonance (FMR) frequency, and f_{Zeeman} is the Zeeman frequency. Magnon drops can be strongly nonlinear, exhibiting almost fully reversed cores [$\Theta(0) \rightarrow \pi$] for f_0 close to f_{Zeeman} . Whereas conservative magnon drops balance exchange (dispersion) with anisotropy (nonlinearity) for each f_0 , the dissipative magnetic droplet must also balance energy gain (STT) with dissipation (damping), singling out a particular droplet precession frequency for a given drive current and applied field (Fig. 1C) (*13*). More generally, dissipative soliton systems, such as the NC-STOs studied here, are natural environments for studying pattern formation. Dissipative solitons are often robust attractors and can exhibit exotic dynamics, such as time-periodic breathing (*1*). It has been claimed that NC-STOs with in-plane anisotropy and applied field exhibit nonlinear localization in the form of a weakly nonlinear spin wave bullet with precession angles much less than 90° (*18, 19*). In contrast, the fully nonlinear dissipative droplet studied here neces-

sarily involves precession angles greater than 90° (*13*), exhibiting a clear experimental signature and rich nonlinear behavior.

To test the theoretical predictions for a magnetic droplet (*13*), we fabricated NC-STOs based on orthogonal pseudospin valve stacks (Fig. 1C), in which the magnetization of the Co fixed layer lies in the plane for zero applied field, whereas that of the Co/Ni multilayer free layer lies along the film normal because PMA is sufficiently strong to overcome the demagnetization field (*20–22*).

The field dependence of the microwave signal from a NC-STO with 63-nm NC diameter in low to moderate perpendicular fields (Fig. 1A) shows the expected linear FMR-like field dependence (*20, 21*). However, at a critical field of $\mu_0 H_{\text{droplet}} = 0.65$ T, the precession frequency exhibits a dramatic drop to a frequency that lies between the Zeeman and FMR frequencies, with a simultaneous jump in the integrated power (*P*). A similarly dramatic transition can be observed (Fig. 1B) as a function of current in a constant field of 0.8 T with similar changes in frequency and power. To gain further insight into the magnetic state as a function of field and current, the magnetoresistance $\{MR = [R(H) - R(H = 0)] / R(H = 0)\}$, where R is the device resistance was measured both at -6 mA and at a lower current of -1 mA (Fig. 1A, inset). Below 0.65 T, the MR exhibits an identical linear decrease for both currents, which is consistent with a linearly increasing out-of-plane component of the fixed layer magnetization and an increasingly parallel state of the NC-STO. At exactly $\mu_0 H_{\text{droplet}} = 0.65$ T, MR [current (I) -6 mA] exhibits a jump of 0.1%, and its field dependence changes sign; the NC-STO state thus becomes increasingly antiparallel with increasing field. Contrarily, MR ($I = -1$ mA) does not show any sign of transition and continues to decrease linearly, eventually saturating in a field of 1.6 to 1.8 T (fig. S1) (*22*), which is consistent with the expected saturation field for the Co layer.

Both the dynamic and static observations are consistent with the formation of a magnetic droplet in the free layer. The large drop in frequency and the sign change of the field-dependent resistance further indicate a substantially reversed central region. This is corroborated by the large increase in microwave power because a reversed droplet will have a large area of spins precessing around the equator, whereas the precession angle of the FMR-like mode is very limited close to the threshold for STO dynamics (*10, 13*). Last, according to the theory of the magnetic droplet, its

¹Materials Physics, School of Information and Communication Technology, KTH Royal Institute of Technology, Electrum 229, 164 40 Kista, Sweden. ²NanOsc AB, Electrum 205, 164 40 Kista, Sweden. ³Department of Physics, University of Gothenburg, 412 96 Gothenburg, Sweden. ⁴Department of Physics, Indian Institute of Technology Delhi, New Delhi 110016, India. ⁵Devices and Circuits, School of Information and Communication Technology, KTH Royal Institute of Technology, Electrum 229, 164 40 Kista, Sweden. ⁶Department of Physics, Stanford University, Stanford, CA 94305, USA. ⁷Institute of Ion Beam Physics and Materials Research, Helmholtz-Zentrum Dresden-Rossendorf e. V., 01314 Dresden, Germany. ⁸Department of Mathematics, North Carolina State University, Raleigh, NC 27695, USA.

*To whom correspondence should be addressed. E-mail: johan.akerman@physics.gu.se

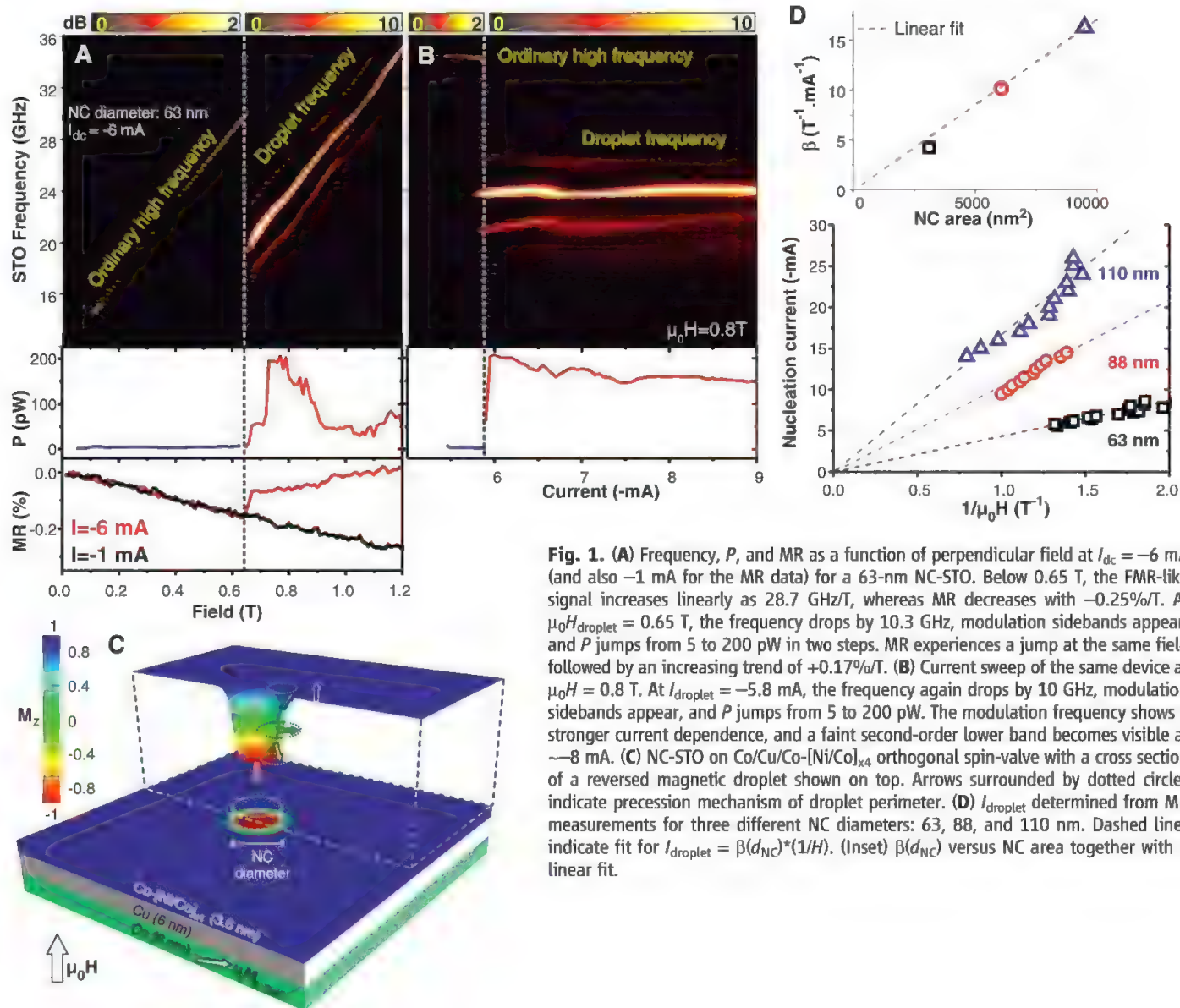


Fig. 1. (A) Frequency, P , and MR as a function of perpendicular field at $I_{\text{dc}} = -6$ mA (and also -1 mA for the MR data) for a 63-nm NC-STO. Below 0.65 T, the FMR-like signal increases linearly as 28.7 GHz/T, whereas MR decreases with $-0.25\%/T$. At $\mu_0 H_{\text{droplet}} = 0.65$ T, the frequency drops by 10.3 GHz, modulation sidebands appear, and P jumps from 5 to 200 pW in two steps. MR experiences a jump at the same field followed by an increasing trend of $+0.17\%/T$. (B) Current sweep of the same device at $\mu_0 H = 0.8$ T. At $I_{\text{droplet}} = -5.8$ mA, the frequency again drops by 10 GHz, modulation sidebands appear, and P jumps from 5 to 200 pW. The modulation frequency shows a stronger current dependence, and a faint second-order lower band becomes visible at ~ 8 mA. (C) NC-STO on Co/Cu/Co-(Ni/Co)_{x4} orthogonal spin-valve with a cross section of a reversed magnetic droplet shown on top. Arrows surrounded by dotted circles indicate precession mechanism of droplet perimeter. (D) I_{droplet} determined from MR measurements for three different NC diameters: 63, 88, and 110 nm. Dashed lines indicate fit for $I_{\text{droplet}} = \beta(d_{\text{NC}}) \cdot (1/H)$. (Inset) $\beta(d_{\text{NC}})$ versus NC area together with a linear fit.

frequency (f_{droplet}) should increase linearly with field at a slope of $\gamma/2\pi$ (γ is the gyromagnetic ratio, so $\gamma/2\pi = 28.7$ GHz/T) and decrease very weakly with current, which is in agreement with Fig. 1, A and B, respectively.

From the MR value at the transition, we can conclude that the Co layer tilt angle required to nucleate a droplet at -6 mA is $\sim 50^\circ$. Assuming that the nucleation is primarily driven by the perpendicular component of the spin-polarized current density, we expect the required nucleation current to be inversely proportional to the perpendicular component M_z of the fixed layer magnetization. Because M_z is linearly proportional to the perpendicular field for the easy-plane Co (fig. S1) (22), we can directly test this assumption by plotting the nucleation current (I_{droplet}) versus inverse applied field, $1/H$ (Fig. 1D). We indeed observed that I_{droplet} is inversely proportional to the applied field and that the slope of this depen-

dence scales with NC area, confirming that the droplet nucleation is governed by the perpendicular component of the spin-polarized current density, regardless of the applied field and NC size.

We now turn to the modulation sidebands that appear simultaneously with the nucleation of the magnetic droplet. The droplet and its field dependence are very robust and reproducible from device to device; however, we found greater variation in the modulation, with some devices showing single (Fig. 2A) and multiple (Fig. 2B) well-defined sideband pairs, some showing strong peaks at $f_{\text{droplet}}/2$ (with some power at $3f_{\text{droplet}}/2$) (Fig. 2C) and others not showing any modulation at any current or field. In some cases, pure single-tone operation may be preceded by modulated behavior at lower currents (Fig. 2B); the onset current is dependent on the direction of the current sweep. The low-frequency (~ 1 GHz) modulating signal can be measured directly (Fig. 2A).

Because all of our measurements involved dc drive alone, the observed modulation is unrelated to ordinary STO modulation (23, 24), in which the drive current contains an intentionally superimposed modulating current. The observed automodulation must instead be intrinsic to the droplet.

With the aid of dissipative droplet theory and micromagnetic simulations (22), we can identify these complex dynamics with different dynamical wave states, including quasiperiodic and periodic structures. At nucleation, the dramatic drop in frequency is associated with droplet formation (13), in which all the spins in the droplet precess uniformly at a single fixed frequency (Fig. 3A). In (13), a droplet drift instability was identified when the droplet was ejected from the NC area, eventually succumbing to damping, leaving room for the nucleation of a new droplet in a periodic fashion. This process occurs on a nanosecond time scale, which is consistent with

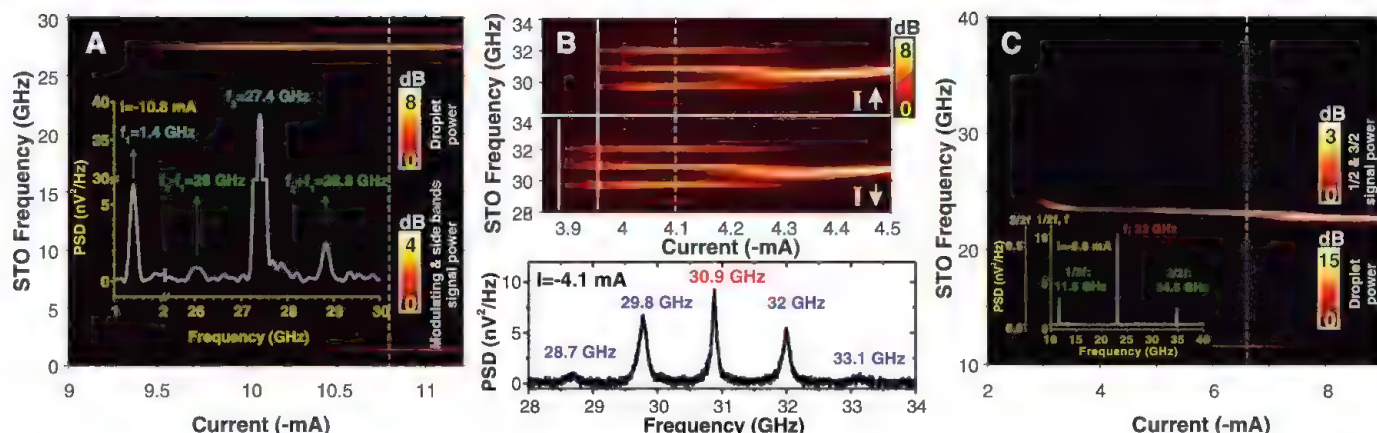


Fig. 2. (A) Droplet automodulation in an 88-nm NC-STO (perpendicular field of 0.9 T). (Inset) Power spectral density (PSD) at -10.8 mA showing both the modulating signal at 1.4 GHz and the resulting modulation sidebands. (B) Automodulation in a 60-nm NC-STO (perpendicular field of 0.9 T) leading to both first- and second-order sidebands (PSD at -4.1 mA shown in the inset

below). The onset current (solid white lines) exhibit a hysteresis of ~ 0.1 mA. (C) Observation of sidebands at $f_{\text{droplet}}/2$ and $3f_{\text{droplet}}/2$ (63-nm NC-STO, 0.8-T field applied at 30° to the plane), which is consistent with droplet breathing. (Inset) PSD at -6.6 mA. Shown is the different scale for the much weaker sideband signals.

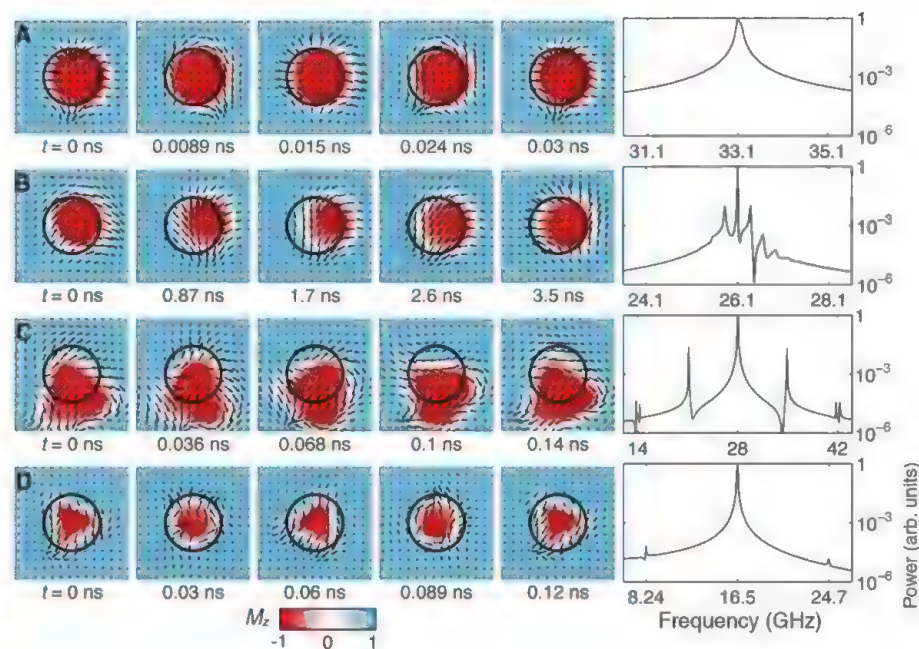


Fig. 3. Time sequences of out-of-plane, M_z (in color), and in-plane (vector field) magnetization component of free layer from micromagnetic simulation. (Right) The power spectrum associated with the NC-averaged projection of magnetization onto the polarization layer. Parameters are given as triples (field, NC diameter, and current). (A) Stationary droplet precession with a single spectral peak for large field (1.1 T, 80 nm, and -12 mA). (B) Droplet oscillation leading to prominent sidebands for moderate field (0.8 T, 63 nm, and -8 mA). (C) Spinning of an asymmetric droplet for moderate field (0.9 T, 50 nm, and -9 mA). (D) Droplet perimeter deformations (breathing) with period twice the precessional period (0.5 T, 80 nm, and -8 mA).

the experimentally observed modulation sidebands. However, this explanation is not consistent with the observed hysteresis (Fig. 2B), predicted for stable, nondrifting droplets (13), because it precludes the periodic death and re-birth of the droplet. Upon decrease of the current below the nucleation threshold, a new droplet cannot form once the first droplet has disappeared. Micromagnetic simulations reveal two

possible explanations for this discrepancy relying on the presence of a sufficiently canted polarizer for moderate fields. The drifting droplet may experience a restoring force leading to gyrotropic-like motion of the droplet within the NC area with a characteristic ~ 1 GHz frequency (Fig. 3B); depending on other parameters, micromagnetic simulations also reveal asymmetric droplets that “spin” on the edge of the NC area

while emitting spin waves (Fig. 3C), exhibiting sidebands with frequency spacings of several GHz. For strong canting of the polarizer away from the film normal (weak fields), we observed periodic dynamics with signals at $1/2$ and $3/2$ of the fundamental frequency (Fig. 3D). We identify these characteristic signals with a breathing mode whose observed breathing frequency is half the precessional frequency (Fig. 2C). Generally, micromagnetic simulations at larger fields tend to exhibit stable precessional dynamics, whereas lower fields can lead to unstable behavior or modulation sidebands by way of droplet oscillations, breathing, and spinning.

Besides the fundamental interest of the creation and control of dissipative solitons in magnetic systems—including, for example, surface magnetic drops expected in thick PMA films (25)—the observed magnetic droplet may have an impact on applications, in particular its influence on the emerging fields of STOs, domain-wall electronics, and magnonics. For STOs, the dramatic frequency drop enables ultra-broadband frequency-shift keying (26), in which the carrier frequency can be switched by ~ 10 GHz by varying the drive current a fraction of its absolute value. Micromagnetic simulations indicate nucleation on the sub-nanosecond time scale, but the definitive modulation rate should be determined experimentally. In the emerging field of domain-wall electronics with PMA materials (27), the magnetic droplet may be used as a current-controlled nanoscopic domain-wall injector and hence facilitate the implementation of compact domain-wall devices. By applying local field gradients, the magnetic droplet can be transported away from the nanocontact region (14, 15), carrying information on its own or spatially modifying local spin wave propagation in magnonic devices (28–30). These magnetic droplets hence may join domain walls and magnetic vortices as distinct and useful nanomagnetic objects.

References and Notes

- N. N. Akhmediev, A. Ankiewicz, *Lect. Notes Phys.* **751**, 1 (2008).
- N. J. Zabusk, M. D. Kruskal, *Phys. Rev. Lett.* **15**, 240 (1965).
- V. B. Tarananko, K. Staliunas, C. O. Weiss, *Phys. Rev. Lett.* **81**, 2236 (1998).
- S. Barland *et al.*, *Nature* **419**, 699 (2002).
- S. L. Lane, D. Luss, *Phys. Rev. Lett.* **70**, 830 (1993).
- H. H. Rotermund, S. Jakubith, G. Ertl, G. Ertl, A. von Oertzen, *Phys. Rev. Lett.* **66**, 3083 (1991).
- P. B. Umbanhowar, F. Melo, H. L. Swinney, *Nature* **382**, 793 (1996).
- F. Melo, S. Douady, *Phys. Rev. Lett.* **71**, 3283 (1993).
- J. C. Slonczewski, *J. Magn. Magn. Mater.* **159**, L1 (1996).
- J. C. Slonczewski, *J. Magn. Magn. Mater.* **195**, L261 (1999).
- L. Berger, *Phys. Rev. B* **54**, 9353 (1996).
- D. Ralph, M. Stiles, *J. Magn. Magn. Mater.* **320**, 1190 (2008).
- M. A. Hofer, T. J. Silva, M. W. Keller, *Phys. Rev. B* **82**, 054432 (2010).
- M. A. Hofer, M. Sommacal, *Physica D* **241**, 890 (2012).
- M. A. Hofer, M. Sommacal, T. J. Silva, *Phys. Rev. B* **85**, 214433 (2012).
- B. A. Ivanov, A. M. Kosevich, *Zh. Eksp. Teor. Fiz.* **72**, 2000 (1977).
- A. M. Kosevich, B. A. Ivanov, A. S. Kovalev, *Phys. Rep.* **194**, 117 (1990).
- A. Slavin, V. Tiberkevich, *Phys. Rev. Lett.* **95**, 237201 (2005).
- S. Bonetti *et al.*, *Phys. Rev. Lett.* **105**, 217204 (2010).
- W. H. Rippard *et al.*, *Phys. Rev. B* **81**, 014426 (2010).
- S. M. Mohseni *et al.*, *Phys. Status Solidi RRL* **5**, 432 (2011).
- Materials and methods are available as supplementary materials on Science Online.
- M. R. Puffall, W. H. Rippard, S. Kaka, T. J. Silva, S. E. Russek, *Appl. Phys. Lett.* **86**, 082506 (2005).
- P. K. Muduli *et al.*, *Phys. Rev. B* **81**, 140408(R) (2010).
- Yu. I. Bespyatykh, I. E. Dikhshtein, S. A. Nikitov, *Phys. Lett. A* **184**, 198 (1994).
- M. Manfrini *et al.*, *Appl. Phys. Lett.* **95**, 192507 (2009).
- O. Boule, G. Malinowski, M. Kläui, *Mater. Sci. Eng. Rep.* **72**, 159 (2011).
- V. V. Kruglyak, S. O. Demokritov, D. Grundler, *J. Phys. D Appl. Phys.* **43**, 264001 (2010).
- V. E. Demidov, S. Urazhdin, S. O. Demokritov, *Nat. Mater.* **9**, 984 (2010).
- M. Madami *et al.*, *Nat. Nanotechnol.* **6**, 635 (2011).

Acknowledgments: This work was supported by the European Commission FP7 contract ICT-257159 "MACALO," the Swedish Foundation for Strategic Research, the Swedish Research Council, and the Knut and Alice Wallenberg Foundation. J.Å. is a Royal Swedish Academy of Sciences Research Fellow supported by a grant from the Knut and Alice Wallenberg Foundation.

Supplementary Materials

www.sciencemag.org/cgi/content/full/339/6125/1295/DC1
Materials and Methods
Supplementary Text
Fig. S1
Reference (31)

13 September 2012; accepted 25 January 2013
10.1126/science.1230155

Flexible Minerals: Self-Assembled Calcite Spicules with Extreme Bending Strength

Filipe Natalio,^{1,2} Tomas P. Corrales,³ Martin Panthöfer,¹ Dieter Schollmeyer,⁴ Ingo Lieberwirth,³ Werner E. G. Müller,⁵ Michael Kappl,³ Hans-Jürgen Butt,³ Wolfgang Tremel^{1*}

Silicatein- α is responsible for the biomineralization of silicates in sponges. We used silicatein- α to guide the self-assembly of calcite "spicules" similar to the spicules of the calcareous sponge *Sycon* sp. The self-assembled spicules, 10 to 300 micrometers (μm) in length and 5 to 10 μm in diameter, are composed of aligned calcite nanocrystals. The spicules are initially amorphous but transform into calcite within months, exhibiting unusual growth along [100]. They scatter x-rays like twinned calcite crystals. Whereas natural spicules evidence brittle failure, the synthetic spicules show an elastic response, which greatly enhances bending strength. This remarkable feature is linked to a high protein content. With nano-thermogravimetric analysis, we measured the organic content of a single spicule to be 10 to 16%. In addition, the spicules exhibit waveguiding properties even when they are bent.

The organisms of various phyla have developed complex and intriguing strategies to deposit minerals in their structural frameworks. Most of them are directed by organic matrices, which control size, shape, organization, and even the mineral phase (1–3). A simple biological design strategy is to use single crystals. Amorphous precursors (4–7) are used to mold biominerals into their final forms (6–8) and to prevent unintentional calcification by rapid precipitation. (5) Organic macromolecules have been

shown to play a pivotal role. They stabilize the transient phases (9, 10), influence the shape, and overcome the intrinsic brittleness of the crystalline phase (11). Macromolecules create defects in the lattice, which strengthen the crystal against fracture by absorbing stress and stopping the propagation of cracks (12). Occluded macromolecules are—at least in part—responsible for the shape of biominerals by inhibiting their growth in certain directions. In addition, the observed anisotropic distribution of defects indicates that the macromolecules are arranged in certain crystal directions (3, 12). An early structural study of calcitic sponge spicules revealed a morphological and textural symmetry different from the hexagonal symmetry of calcite, indicating an additional level of biological control (13).

The intricate structures observed in biominerals have inspired the development of synthetic strategies to mimic nature. The precipitation of minerals in the presence of soluble organic additives has proven to be highly successful in the

regulation of crystal morphology and nanostructures (14). Although nature produces sophisticated structures with remarkable ease and fidelity, the synthesis of their artificial counterparts is still a challenge. The fabrication of materials that resemble spicules—calcareous or siliceous—is even more difficult because it involves dissimilar organic and inorganic nanophases. The principle of controlled nucleation occurs in both siliceous (noncrystalline) and calcareous (crystalline) biomineralization independently of their chemical nature.

One important protein responsible for the formation of siliceous spicules in sponges is silicatein- α . This ~23-kD protein, which has been shown to form oligomers and fibrous structures through self-aggregation (15), catalyzes and structurally directs the formation of silica spicules. (16) Here, we demonstrate that silicatein- α can also be used to form synthetic spicules of calcium carbonate. The mechanical properties of the synthetic spicules proved to be superior to those of biogenic material. For comparison, we used the spicules (monoaxa) of the calcareous sponge *Sycon* sp. (*Porifera, Calcarea*) (12, 13), which are morphologically very similar to our synthetic calcite spicules.

A solution of freshly prepared CaCl_2 (5 mM) was mixed on a cleaned mica surface with refolded recombinant silicatein- α (210 $\mu\text{g}/\text{mL}$, pH 7.4). This was then exposed to CO_2 partial pressure above solid ammonium carbonate $[(\text{NH}_4)_2\text{CO}_3]$ for 4 hours at room temperature (RT) in a sealed desiccator (17). Needle-like crystals ("synthetic spicules") with smooth surfaces, diameters of 5 to 10 μm , and lengths of 10 to 300 μm were formed (Fig. 1, A and B). A scanning electron microscopy (SEM) image (Fig. 1B, inset) of a cross section of a synthetic spicule prepared by use of a focused ion beam (FIB) revealed a uniform, homogeneous, and circular structure. In the absence of silicatein- α , only rhombohedral calcite crystals were formed (fig. S1A).

The presence of silicatein- α is evident from the Fourier transform infrared (FT-IR) spectrum

¹Institut für Anorganische Chemie und Analytische Chemie, Johannes Gutenberg-Universität, Duesbergweg 10-14, D-55099 Mainz, Germany. ²Institut für Chemie-Anorganische Chemie, Martin-Luther-Universität Halle-Wittenberg, Kurt Mothes Straße 2, 06120 Halle, Germany. ³Max-Planck-Institut für Polymerforschung, Ackermannweg 10, D-55128 Mainz, Germany. ⁴Institut für Organische Chemie, Johannes Gutenberg-Universität, Duesbergweg 10-14, D-55099 Mainz, Germany. ⁵Institut für Physiologische Chemie, Universitätsmedizin, Johannes Gutenberg-Universität, Duesbergweg 6, D-55099 Mainz, Germany.

*To whom correspondence should be addressed. E-mail: tremel@uni-mainz.de

(fig. S4B, blue line), in which the most substantial bands can be assigned to amide I, II, and III at 1650, 1580, and 1370 cm^{-1} , respectively (18). Because of the complexity of the FT-IR spectra, a specific three-dimensional conformation cannot be assigned to silicatein- α (such as α helix, β sheets, or random coils). The distribution of the amide I band (1650 cm^{-1}) and the ν_3 band of carbonate ions (1456 cm^{-1}) of a spicule over the mapped area are shown in Fig. 1C, top and bottom, respectively. The highest intensities (red) are observed both on the synthetic spicule, indicating the presence of silicatein- α and its participation in the control of the mineralization process.

To localize silicatein- α more precisely, we removed surface-bound silicatein- α by treating the synthetic spicules with NaOCl (1% v/v, 10 min). After washing with distilled water, the supernatant was kept, and the synthetic spicules were analyzed by means of SEM and immunocytochemistry. Fluorescence microscopy showed a positive cross-reaction between the synthetic spicules and polyclonal antibodies raised against axial filaments (PoAb-aSILIC) (Fig. 1D) (19). NaOCl treatment caused a minor decrease in the size of the synthetic spicule by rounding edges (Fig. 1E). No fluorescence was observed in the controls, in which the antibody was replaced by preimmune serum. Subsequently, the synthetic spicules were dissolved in acetic acid solution (5%, 10 min). The solution was analyzed by means of gel electrophoresis after neutralization. The presence of a band at ~23 kDa corresponding to silicatein- α is

shown in Fig. 1F, lane a, confirming that the protein was in fact occluded in the synthetic spicules. Electrophoretic analysis of the supernatant from the NaOCl treatment did not show any band, which demonstrates the absence of surface-bound silicatein- α (Fig. 1F, lane b and c).

To estimate the organic content of synthetic spicules, we used a nano-thermogravimetric analysis (nano-TGA) procedure on single, freshly prepared spicules (fig. S5). A single spicule was placed onto the end of an atomic force microscope (AFM) cantilever. Its mass was determined by measuring the resulting decrease in the resonance frequency of the cantilever. The density of the spicules, calculated from their mass and their dimension as determined with optical microscopy, was found to be 2.5 and 0.6 g/cm^3 for the natural and synthetic spicules, respectively. The density of a natural spicule is close to that of pure calcium carbonate (2.7 g/cm^3). Synthetic spiculae are highly porous on the microscopic scale. The spicules were then calcinated at 500°C for 10 min to remove all organic content, which was confirmed by means of attenuated total reflectance (ATR) μ FT-IR analysis (fig. S6A). The mass loss amounted to 1.5% for natural spicules and 10 to 16% for synthetic spicules. Macroscopically, the synthetic spiculae shrunk in size. Their density increased to 1.7 g/cm^3 (fig. S6B).

The CaCO_3 mineralization process in the presence of silicatein- α was monitored by taking transmission electron microscopy (TEM) “snapshots” at given time intervals. After 5 min, CaCO_3 nanocrystals with diameters of ~5 nm were formed

[Fig. 2A and fig. S7, high-resolution (HR) TEM image]. After 30 min, fractal-like structures were formed (Fig. 2B) proceeding through a continuous oriented assembly process (Fig. 2C) until elongated, compacted, amorphous, and granular microsized structures had grown (Fig. 1A).

The amorphous nature of the immature spicules and the subsequent aging of the synthetic spicules were demonstrated by means of a series of x-ray diffraction experiments at different aging stages. Synthetic spicules that had matured for more than 6 months diffracted, whereas spicules younger than 5 months were amorphous, as shown with optical polarization microscopy (fig. S8A). Despite their smooth surface, mature synthetic spicules scattered like a calcite twin crystal. According to reconstructed layers from reciprocal space (“precession plots,” $hk0$, $hk1$, $0kl$, and $1kl$), virtually all reflections are split into separated maxima as typically observed for non-merohedral twins with slightly skewed lattices (Fig. 2D). The individual maxima of the split reflections are relatively broad [full width at half maximum (FWHM) of 0.6 to 0.8°] pointing to small coherent scattering domains of 5 to 7 nm. Such small crystalline domains were also observed with TEM (Fig. 2E and fig. S7). This indicates that the synthetic spicules consist of crystallographically aligned nanodomains (20). The growth direction of the synthetic spicule is [100], which corresponds to no naturally observed morphology of calcite, thus suggesting the presence of mesocrystallinity (20). Because no Mg^{2+} was incorporated into the crystal (supplementary materials), one may attribute the reflection splitting in mature synthetic spicules to lattice strain from the occluded protein.

To further analyze the structure, we prepared ion-milled cross sections of natural spicules (fig. S9) as well as of immature and mature synthetic spicules (Fig. 2E). In *Sycon* sp. monoaxons, we observed filamentous structures and voids (fig. S9A). Electron diffraction (ED) patterns of different areas showed a mixture of amorphous and crystalline domains (fig. S9D). This, together with HRTEM images (fig. S9E), proves the mesocrystalline nature of the calcitic structures. Thin cuts of immature synthetic spicules showed no clear boundaries between organic and inorganic material, thus confirming the virtually amorphous character (fig. S10A). HRTEM analysis of mature synthetic spicules revealed the presence of small crystalline domains surrounded by an amorphous layer that we attribute to protein (Fig. 2E and fig. S10B), reflecting the mesocrystalline ultrastructure of mature synthetic spicules.

Although the outward appearance of a synthetic spicule kept under ambient conditions for 10 months remained virtually unchanged (fig. S11, SEM and AFM), polarized light microscopy (Fig. 2F and fig. S8A) and ATR μ FT-IR spectra (fig. S8B) revealed a transition from a non-crystalline to a crystalline phase. The crystalline phase grows at the expense of transient spherical amorphous calcium carbonate (ACC) particles

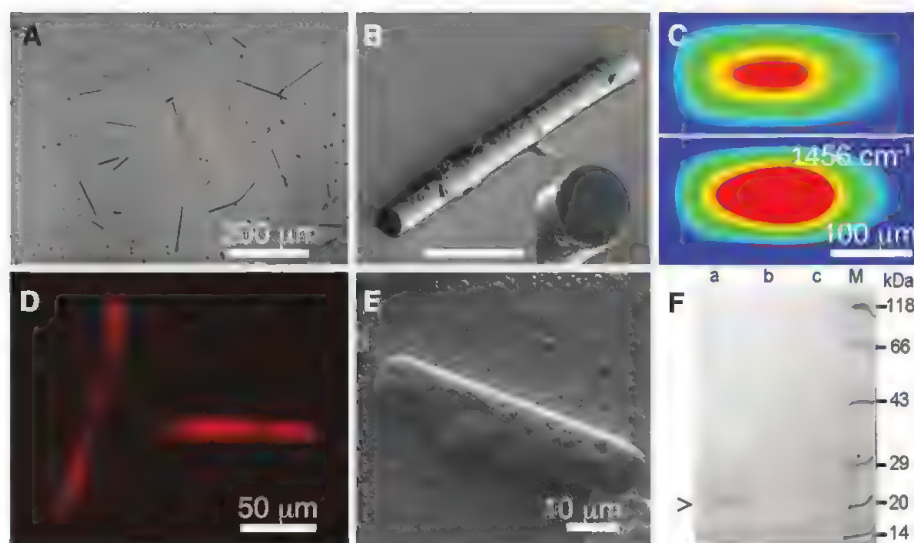
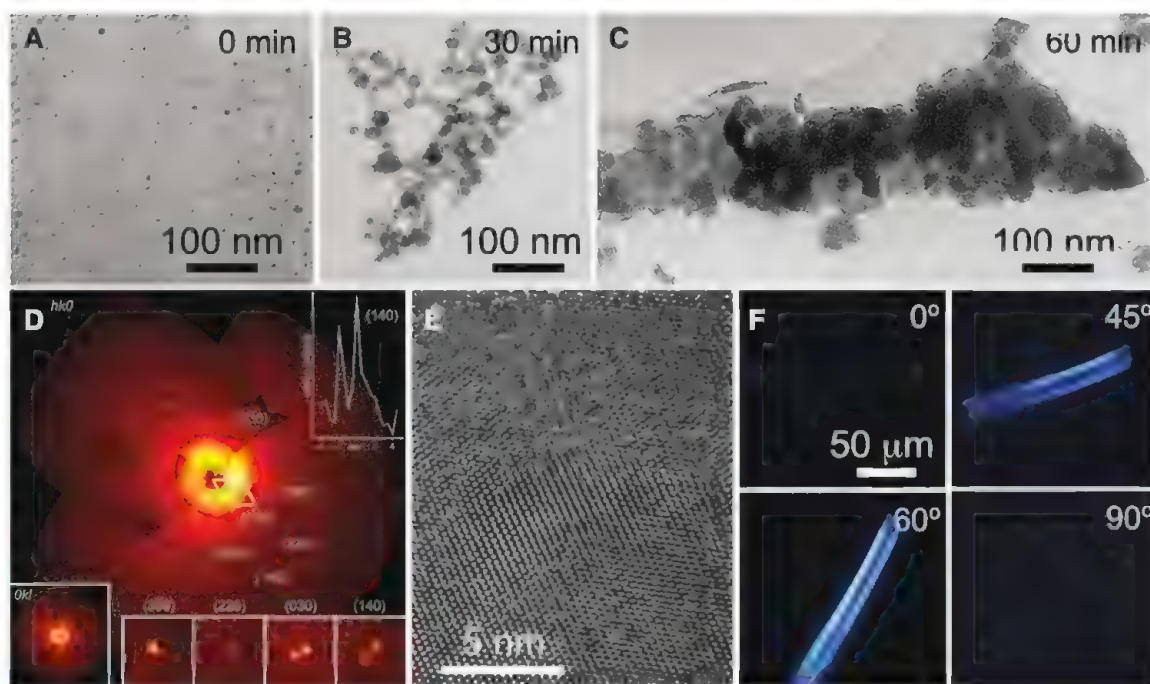


Fig. 1. (A) Light microscopy overview of synthetic spicules. (B) SEM image of a representative synthetic spicule. (Inset) SEM image of a cross section through a synthetic spicule prepared with a FIB. (C) FT-IR mapping for amide I band at 1650 cm^{-1} and ν_3 of carbonate ions in calcite at 1456 cm^{-1} on a synthetic spicule. High intensity is indicated in red. (D) Confocal microscopy image of immunostained synthetic spicules after cross-reaction with polyclonal antibodies (PoAb-aSILIC) raised against natural silicatein- α . (E) SEM of a synthetic spicule after NaOCl treatment. (F) Gel electrophoresis (SDS–polyacrylamide gel electrophoresis, 12%) analysis after NaOCl treatment (1% v/v, 10 min). A band with a molecular weight of ~23 kDa after Coomassie staining shows the presence of silicatein (lane a). After the second and third washing steps (lanes b and c), no protein was observed. M, molecular markers for calibration.

Fig. 2. TEM “snapshots” of synthetic spicule formation. (A) Overview of nanocrystals after 5 min, (B) 30 min, and (C) 1 hour. (D) Reconstructed x-ray diffraction pattern of the (hk0)-plane of a mature synthetic spicule (10 months). (Inset) Reconstructed diffraction pattern of the (0kl)-plane (bottom left), rocking curve of the (104) reflection displaying a split peak with peak widths (FWHM) of ≈ 0.6 to 0.7° , respectively (top right), and zoom of the intensity distribution of some selected reflections (bottom right). Data from which the rocking curve was derived are reconstructed from the full volume of the Ewald sphere. Therefore, they show the reflections of all domains. As a consequence, we see



only a few broad maxima rather than multiple sharp maxima. (E) HRTEM image of a cross section of a mature spicule showing small calcite crystals (~ 5 nm) embedded into an amorphous protein matrix. (F) Cross-polarized light microscopy images of the aged synthetic spicule (10 months) at different angles (0° to 90°).

according to Ostwald's step rule via a dehydration step combined with a dissolution-recrystallization process (fig. S12), as described before for sea urchin larvae (21).

The mechanical properties of single spicules have been studied before. These studies were, however, limited to spicules large enough to allow macroscale testing. The Young's modulus of siliceous sponge spicules was found to be close to 40 GPa in most cases (22–24), but values of 14 (25) and 68 GPa (26) have also been reported. Little is known about the mechanical properties of calcareous spicules from marine species; a value of 36 GPa has been reported for spicules from echinoderm larvae (27).

We probed the mechanical properties of natural and synthetic spicules with an AFM. Individual spicules were attached to the edge of a silicon wafer by using a small drop of two-component epoxy glue. The spicule acted as a flexible beam of length L (Fig. 3A). A tipless AFM cantilever was used to apply a force at a distance x from the wafer edge (Fig. 3A, inset). We recorded force-versus-beam deflection curves for a series of positions along the spicules. According to beam theory, the applied force F and the induced beam deflection δ at the loading position x of a one-sided clamped beam with a circular cross section are related by $F = 3\pi ER^4\delta/(4x^3)$. Here, E is the Young's modulus of the beam, and R is its radius. We observed a linear relation between applied force and induced beam deflection (Fig. 3A). The effective stiffness $k_s = F/\delta$ increases with decreasing distance x . From linear fits of many such force-versus-deflection curves, we obtained plots of the effective stiffness

as a function of the normalized position x/L (Fig. 3, B and C). The Young's modulus of the spicules was calculated by fitting with

$$k_s = \frac{3\pi ER^4}{4(x - x_0)^3} \quad (1)$$

Fit parameters were E and x_0 , where x_0 is an offset to correct for uncertainties in the determination of the distance from the clamping point. Using this method, we obtained $E = (14.2 \pm 0.8)$ GPa for a synthetic spicule 1 month after synthesis (Fig. 3B). The Young's modulus of a natural spicule was (8.8 ± 0.9) GPa (Fig. 3C). The Young's modulus of our synthetic spicule was lower than the one found in natural echinoderm spicules (36 GPa) (27) but higher than for spicules from *Sycon* sp. monoaxons. The Young's modulus of the synthetic spicules increased with time, which is a strong indication of aging. We measured $E = (3.0 \pm 0.5)$ GPa for a fresh spicule (less than a week old) and $E = (19 \pm 4)$ GPa for a 7-month-old sample (fig. S13).

To probe fracture properties and ultimate strength, spicules were bent in an SEM by using a micromanipulator. Natural spicules fracture in a brittle way when deflected by $\delta/L \geq 11\%$ (Fig. 3D, top inset, and movie S1). Assuming a linear stress-strain curve up to fracture and using the measured E modulus for the natural spicules, we calculated a maximum stress of $\sigma = 89$ to 125 MPa at the clamping point before fracture. SEM analysis of the natural spicule shows, instead of a crystal fracture, a clear glassy conchoidal fracture (fig. S14A). Similar behavior has been observed for glass sponge fibers and echinoderm

spicules and attributed to a combination of mesocrystallinity and organic content (11).

Synthetic spicules (1 and 7 months) showed no signs of fracture or plastic deformation, at least up to $\delta/L = 18$ and 27% (Fig. 3D, bottom inset, 1 month, and fig. S15, 7 months). This corresponds to a maximum applied stress of $\sigma = 170$ and 442 MPa, respectively. Even when bending a synthetic spicule to a U shape, we were not able to fracture it. Instead of brittle failure, we observed elastic bending with a small plastic component; after 180° bending and release, the spicule showed a residual plastic deformation of $\delta/L \sim 10\%$ (Fig. 3D, bottom inset, and movie S2) and cannot be broken even under extreme deformations (fig. S14, C and D). We attribute the remarkable bending strength of synthetic spicules as compared with that of natural spicules to the almost 10-times-higher content of organic material (10 to 16% in contrast to 1.5% for natural spicules). Furthermore, AFM imaging revealed a partial fusion of the initial granular structural units. This “sintering” effect can be attributed to a structural reorganization (fig. S16, A to I).

Using a micromanipulator (such as the one described above), we performed bending experiments on a calcinated (at 500°C) synthetic spicule that was partially glued with epoxy onto a silicon surface. (fig. S16J, i to vi for sequence, and movie S3). The calcinated synthetic spicule could still be bent to some extent before fracturing near its clamping point (fig. S16J, i to vi for sequence, and M, and movie S3). The fact that the synthetic spicule is composed of nanoscale calcite building blocks that are (to some extent) displaceable to each other because of interspersed protein contributes to the

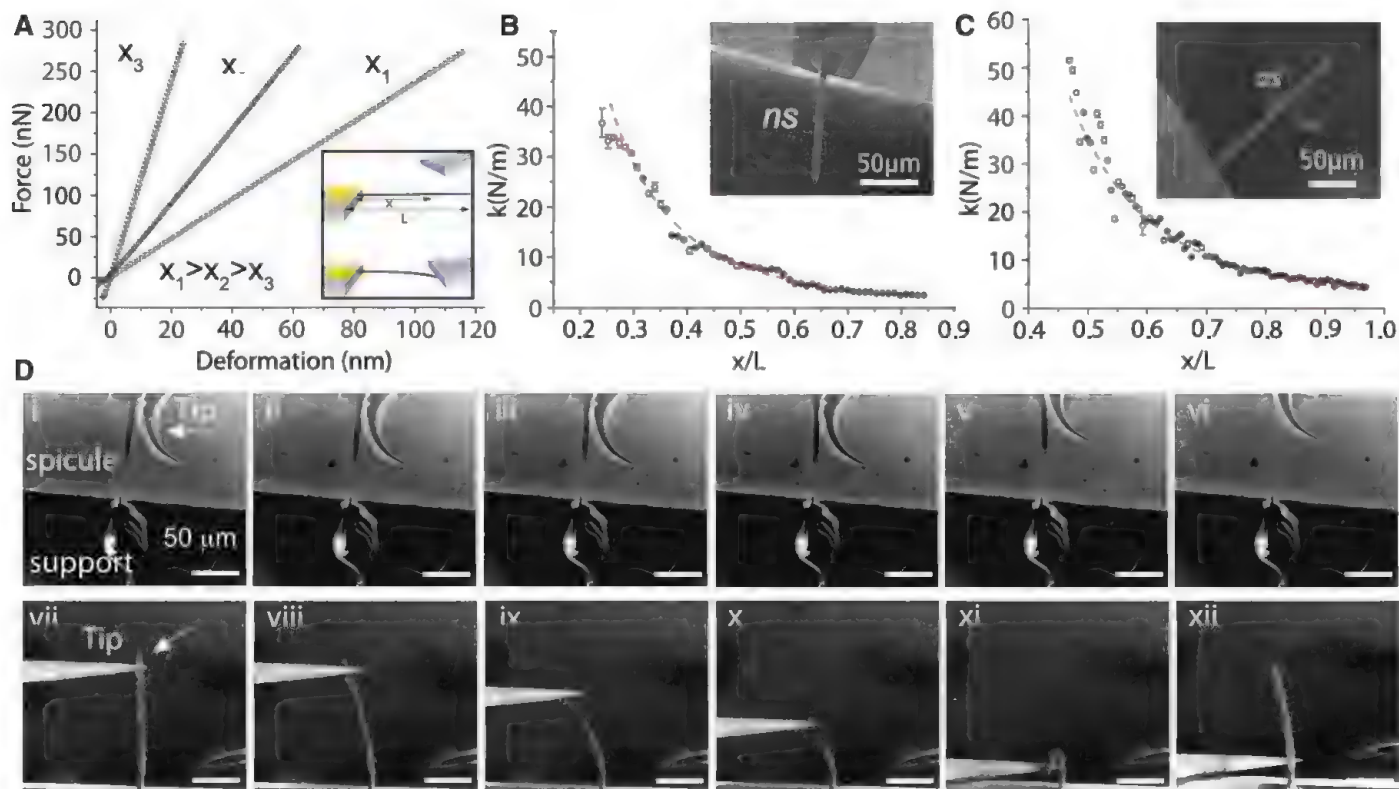


Fig. 3. (A) The flexural response of a fixed synthetic spicule of length L to a well-defined load applied at different positions x along its main axis (inset) was probed by using a tipless AFM cantilever. From the linear relationship between applied force and deformation, the stiffness k_s of the clamped spicule was obtained. (B and C) Measured values of k_s versus x/L and the fit (red dashed)

for (B) a synthetic spicule sample and for (C) a biogenic *Sycon sp.* monoaxon. (D) The fracture properties of spicules were probed with a micromanipulator and recorded in situ with SEM for natural (i to vi) and synthetic spicules (vii to xii). The synthetic spicule did not fracture even under extreme loading and deformation conditions (xi) that lead to plastic deformation.

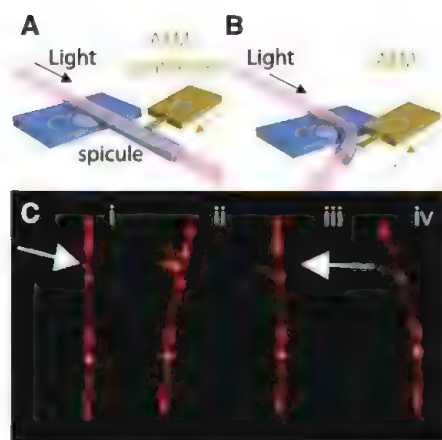


Fig. 4. (A and B) Schematic of a spicule (A) fixed at one end and (B) bent by an AFM cantilever to test its waveguiding properties. (C) Microscopy images of the waveguiding capacity of the synthetic spicule during deformation by (i and ii) pushing and (iii and iv) pulling it away from its original position (i).

remarkable mechanical properties of the synthetic spicules before calcination (fig. S17).

A high flexibility in calcite biomaterials has been reported before—for example, in sea urchin

spines (11) or the ossicles of the sea star *Echinaster spinulosus* (28). The flexibility of the sea urchin spine is due in part to the entrapment of proteins in the crystal. Similarly, echinoderms possess a rigid endoskeleton composed of calcite and small amounts of occluded matrix proteins. In the synthetic spicules, the mineral phase is composed of ACC, which then transforms to an anhydrous ACC and eventually to calcite. (29)

The uniform circular cross section of mature synthetic spicules with a diameter of a few micrometers is an optimal range for efficient waveguiding of visible light. To demonstrate the ability to guide light, a continuous laser ($\lambda = 632$ nm, incident spot size $44 \mu\text{m}$ at an angle of $\theta = 16^\circ$) was focused onto the fixed end of an epoxy-clamped mature synthetic spicule (Fig. 4A and fig. S18). The free end of the spicule was bent with an AFM cantilever ($k_c = 42$ N/m, tip length of $17 \mu\text{m}$) mounted on a three-axis micromanipulator (Fig. 4B). The bending process was recorded with an optical microscope placed above the sample. In a typical experiment, we pushed the synthetic spicule with the front side of the AFM tip (Fig. 4C, ii), allowed it to return to its initial position (Fig. 4C, iii), and then pulled it with the back side of the AFM tip (Fig. 4C, iv). Even after deformations of $\delta/L = 24$ to 33% , the synthetic spicule was still light guiding, without considerable loss of inten-

sity at its free end. We attribute the light-guiding properties of synthetic mature spicules to a gradient in the refractive index due to the protein content, as apparent from our data.

We have described the formation of needle-like calcite crystals that resemble naturally occurring *Sycon sp.* monoaxons by using the self-assembly properties of silicatein- α . Synthetic spicules are composed initially of amorphous building blocks that undergo an aging process. At the mature stage, these spicules consist of aligned calcite nanocrystals with silicatein- α occluded in the domain boundaries. The Young's modulus of 14 GPa for synthetic spicules is at least as high as that for natural spicules. Synthetic spicules sustain a fracture stress at least three times higher than that of natural spicules, without any sign of brittle fracture. The presence of 10 to 16% organic components accounts for these remarkable mechanical properties.

References and Notes

1. S. Weiner, P. M. Dove, *Rev. Mineral. Geochem.* **54**, 1 (2003).
2. A. M. Belcher et al., *Nature* **381**, 56 (1996).
3. A. Berman et al., *Science* **259**, 776 (1993).
4. E. Beniash, J. Aizenberg, L. Addadi, S. Weiner, *Proc. Biol. Sci.* **264**, 461 (1997).
5. J. Rieger, E. Hädicke, I. U. Rau, D. Boeckh, *Tens. Surf. Deterg.* **34**, 430 (1997).
6. L. B. Gower, D. J. Odom, *J. Cryst. Growth* **210**, 719 (2000).

7. L. Addadi, S. Raz, S. Weiner, *Adv. Mater. (Deerfield Beach Fla.)* **15**, 959 (2003).
8. Y. Politi, T. Arad, E. Klein, S. Weiner, L. Addadi, *Science* **306**, 1161 (2004).
9. E. D. Eanes, I. H. Gillissen, A. S. Posner, *Nature* **208**, 365 (1965).
10. V. Pipich, M. Balz, S. E. Wolf, W. Tremel, D. Schwahn, *J. Am. Chem. Soc.* **130**, 6879 (2008).
11. A. Berman *et al.*, *Science* **250**, 664 (1990).
12. J. Aizenberg *et al.*, *FASEB J.* **9**, 262 (1995).
13. J. Aizenberg *et al.*, *Chemistry* **1**, 414 (1995).
14. F. C. Meldrum, H. Cölfen, *Chem. Rev.* **108**, 4332 (2008).
15. M. M. Murr, D. E. Morse, *Proc. Natl. Acad. Sci. U.S.A.* **102**, 11657 (2005).
16. H. C. Schröder, X. Wang, W. Tremel, H. Ushijima, W. E. G. Müller, *Nat. Prod. Rep.* **25**, 455 (2008).
17. J. Küther, R. Seshadri, W. Knoll, W. Tremel, *J. Mater. Chem.* **8**, 641 (1998).
18. P. R. Carey, *Biochemical Applications of Raman and Resonance Raman Spectroscopies* (Academic Press, New York, 1982), chap. 4.
19. W. E. G. Müller *et al.*, *Cell Tissue Res.* **321**, 285 (2005).
20. H. Cölfen, M. Antonietti, *Mesocrystals and Nonclassical Crystallization* (Wiley, Chichester, 2008).
21. Y. Politi *et al.*, *Proc. Natl. Acad. Sci. U.S.A.* **105**, 17362 (2008).
22. C. Levi, J. L. Barton, C. Guillemet, E. Lebras, P. A. Lehuède, *J. Mater. Sci. Lett.* **8**, 337 (1989).
23. M. Sarikaya *et al.*, *J. Mater. Res.* **16**, 1420 (2001).
24. A. Woesz *et al.*, *J. Mater. Res.* **21**, 2068 (2006).
25. M. Johnson, S. L. Walter, B. D. Flinn, G. Mayer, *Acta Biomater.* **6**, 2181 (2010).
26. A. Miserez *et al.*, *Adv. Funct. Mater.* **18**, 1241 (2008).
27. R. B. Emlett, *Biol. Bull.* **163**, 264 (1982).
28. P. L. O'Neill, *Science* **213**, 646 (1981).
29. P. U. P. A. Gilbert, F. H. Wilt, in *Molecular Biomineralization*, W. E. G. Müller, Ed. (Springer-Verlag, Heidelberg, 2011), pp. 199–223.

Acknowledgments: This work was partially supported by the Deutsche Forschungsgemeinschaft within the SPP 1420. T.P.C. was supported by a Deutscher Akademischer Austauschdienst scholarship. We acknowledge the use of the facilities of the EM Center in Mainz (EZMZ) supported by the Center for Complex Matter and the SFB 625. We are grateful to R. Jung-Pothmann for performing single-crystal x-ray measurements and J. Ally for insightful discussions. The authors declare that they have no competing financial interests.

Supplementary Materials

www.sciencemag.org/cgi/content/full/339/6125/1298/DC1
Materials and Methods

Figs. S1 to S18

References

Movies S1 to S3

7 November 2011; accepted 24 January 2013
10.1126/science.1216260

Real-Time Observation of Surface Bond Breaking with an X-ray Laser

M. Dell'Angela,¹ T. Anniyev,² M. Beye,^{2,3} R. Coffee,⁴ A. Föhlisch,^{3,5} J. Gladh,⁶ T. Katayama,² S. Kaya,² O. Krupin,^{4,7} J. LaRue,² A. Møgelhøj,^{8,9} D. Nordlund,¹⁰ J. K. Nørskov,^{8,11} H. Öberg,⁶ H. Ogasawara,¹⁰ H. Öström,⁶ L. G. M. Pettersson,⁶ W. F. Schlotter,⁴ J. A. Sellberg,^{2,6} F. Sorgenfrei,¹ J. J. Turner,⁴ M. Wolf,¹² W. Wurth,¹ A. Nilsson^{2,6,8,10,*}

We used the Linac Coherent Light Source free-electron x-ray laser to probe the electronic structure of CO molecules as their chemisorption state on Ru(0001) changes upon exciting the substrate by using a femtosecond optical laser pulse. We observed electronic structure changes that are consistent with a weakening of the CO interaction with the substrate but without notable desorption. A large fraction of the molecules (30%) was trapped in a transient precursor state that would precede desorption. We calculated the free energy of the molecule as a function of the desorption reaction coordinate using density functional theory, including van der Waals interactions. Two distinct adsorption wells—chemisorbed and precursor state separated by an entropy barrier—explain the anomalously high prefactors often observed in desorption of molecules from metals.

The most fundamental elementary surface chemical process, the adsorption of a molecule, has been proposed to proceed through a weakly bound “precursor” state (*1–4*) that helps the molecule lose rotational and translation energy before forming a chemisorption bond to the surface. This transient state has never been directly detected in terms of a spectroscopic signature, although ultrafast vibrational spectroscopy measurements with pump-probe techniques have the potential to detect short-lived transient species on surfaces (*5–10*). A transient shift of the vibrational frequency of thermally highly excited adsorbed CO molecules has been detected by using pump-probe sum frequency generation (SFG) spectroscopy. However, the shifts were mostly attributed to excitation of frustrated rotational motions that led to diffusive motion parallel to the surface (hopping between adsorption sites), rather than to a weakly adsorbed precursor state (*7–9, 11*).

We show that ultrafast pump-probe x-ray fluorescence spectroscopic techniques based on an x-ray free-electron laser, the Linac Coherent Light Source (LCLS), can be used to probe the electronic structure of a transiently populated, weakly

adsorbed state in CO desorption from Ru(0001). An optical laser pump pulse increased the phonon temperature of the substrate on a sub-picosecond time scale (*12*) and rapidly populated the adsorbate transient state as an intermediate prior to desorption. The time evolution of the occupied and unoccupied valence electronic structure around the adsorbed CO molecule on Ru(0001) could be followed in an element-specific way during the desorption process with the use of oxygen-resonant x-ray emission spectroscopy (XES) and x-ray absorption spectroscopy (XAS), respectively. In particular, the CO molecules in the transient state had an electronic structure closer to the gas phase than to the chemisorbed state; however, the antibonding CO $2\pi^*$ states were still substantially affected by the interaction with the surface. Combining the experimental data with results of free energy calculations based on density functional theory (DFT) by using a new functional that includes van der Waals interactions identified a precursor state, a two-dimensional gas of CO molecules that weakly interacts with the surface but still affects desorption kinetics.

The principle of core-level excitation (XAS) and de-excitation (XES) (*13*) is illustrated in Fig. 1,

middle, together with the static spectra from the oxygen atom for CO chemisorbed on Ru(0001). Core-level spectroscopies constitute element-specific probes of the electronic structure, both the occupied (XES) and unoccupied (XAS) states, through the involvement of the local O 1s level (*14, 15*). Investigations of the chemical bonding of CO to late-transition metal and noble-metal surfaces by means of XES in combination with DFT calculations (*14, 16*) show that the key interaction is that of the 1π - and $2\pi^*$ -orbitals of the molecule with the metal *d*-states, resulting in an allylic configuration, as well as the polarization of the 5σ -orbital from the C to the O atom and a shift to higher-binding energy than gas phase. The lowest in energy of the three orbitals resulting from the π -interaction is the $1\tilde{\pi}$ orbital in a bonding configuration with the metal; the tilde denotes that the orbital has mixed with surface-metal orbitals. The middle orbital (denoted \tilde{d}_π) is non-bonding and mainly of *d*-character with a lone-pair contribution on the O atom, whereas the highest

¹University of Hamburg and Center for Free Electron Laser Science, Luruper Chaussee 149, D-22761 Hamburg, Germany.

²Stanford Institute for Materials Energy Sciences (SIMES), SLAC National Accelerator Laboratory, 2575 Sand Hill Road, Menlo Park, CA 94025, USA. ³Institute for Methods and Instrumentation in Synchrotron Radiation Research, Helmholtz-Zentrum Berlin für Materialien und Energie GmbH, Wilhelm-Conrad-Röntgen Campus, Albert-Einstein-Strasse 15, 12489 Berlin, Germany. ⁴Linac Coherent Light Source, SLAC National Accelerator Laboratory, 2575 Sand Hill Road, Menlo Park, CA 94025, USA. ⁵Institut für Physik und Astronomie, Universität Potsdam, Carl-Liebknecht-Strasse 24-25, 14476 Potsdam, Germany. ⁶Department of Physics, AlbaNova University Center, Stockholm University, SE-10691, Sweden. ⁷European X-Ray Free Electron Laser (XFEL) GmbH, Albert-Einstein-Ring 19, 22761 Hamburg, Germany. ⁸Sustainable Energy Through Catalysis (SUNCAT) Center for Interface Science and Catalysis, SLAC National Accelerator Laboratory, 2575 Sand Hill Road, Menlo Park, CA 94025, USA. ⁹Center for Atomic-Scale Materials Design (CAMD), Department of Physics, Technical University of Denmark, DK 2800 Lyngby, Denmark. ¹⁰Stanford Synchrotron Radiation Lightsource, SLAC National Accelerator Laboratory, 2575 Sand Hill Road, Menlo Park, CA 94025, USA. ¹¹SUNCAT Center for Interface Science and Catalysis, Department of Chemical Engineering, Stanford University, Stanford, CA 95305, USA. ¹²Fritz-Haber Institute, Max Planck Society, Faradayweg 4-6, D-14195 Berlin, Germany.

*To whom correspondence should be addressed. E-mail: nilsson@slac.stanford.edu

orbital is the $2\pi^*$ level in an antibonding configuration lying mainly above the Fermi level E_F . The $2\pi^*$ level shifts toward E_F through mixing with the 1π orbital (17).

Dynamic information on the electronic structure obtained through resonant O $1s \rightarrow 2\pi^*$ excitation with a 100-fs pulse from the LCLS x-ray free-electron laser before and 12 ps after inducing

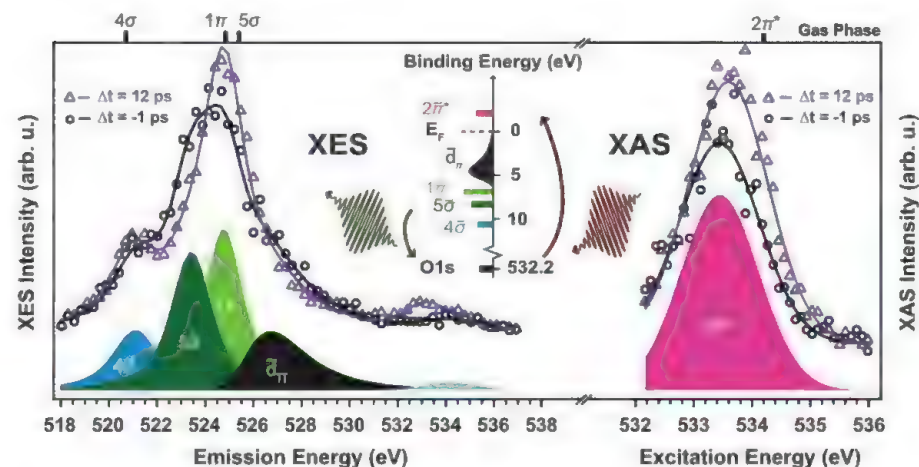


Fig. 1. Oxygen K-edge XES (left) and XAS (right) spectra (markers) of CO/Ru(0001) and corresponding fits (solid lines) measured at two selected pump-probe delays. At the bottom of the two panels, the peak deconvolution resulting from the fit of the spectra acquired at $\Delta t = -1$ ps is shown. The XAS data have been fitted with a Gaussian peak for the $O1s \rightarrow 2\pi^*$ resonance. The XES spectra have been fitted with three peaks of Voigt lineshape for the 1π , 5σ , and 4σ orbitals and an asymmetric Gaussian for the \tilde{d}_π states; the elastic peak is indicated in light blue around 534 eV. The fit of the spectra at $\Delta t = 12$ ps has been performed by varying only intensity and position of the previously determined components. **(Top)** The positions of the fitted components measured in previous resonant gas phase experiments are also indicated (26). **(Middle)** A schematic illustration of the excitation process from the $O1s$ level to the unoccupied $2\pi^*$ resonance in XAS and the core hole decay process from occupied molecular orbitals back to the $O1s$ in XES.

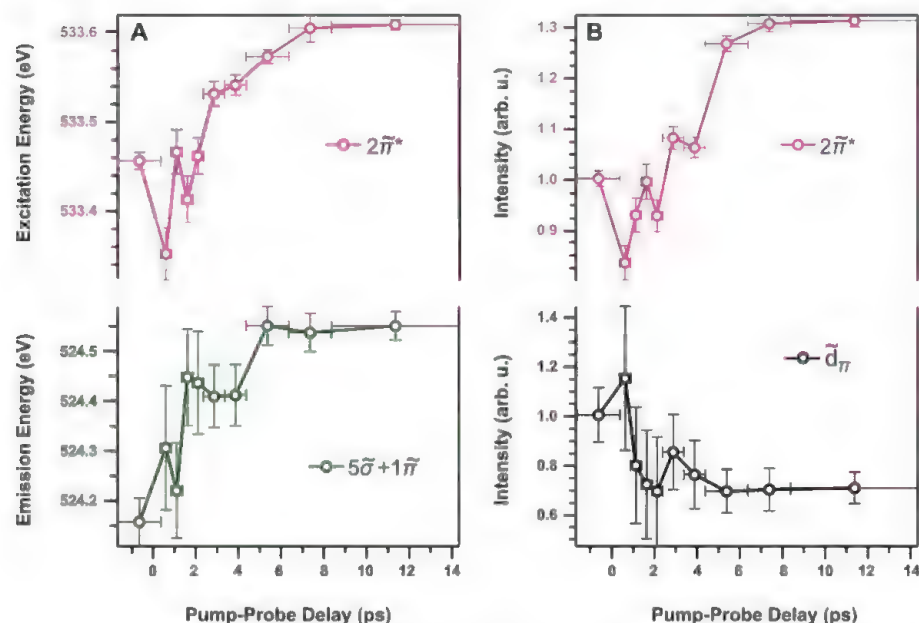


Fig. 2. (A and B) Experimental observations indicating the population of a weakly adsorbed precursor state before the desorption of CO from Ru(0001). The intensities in (B) have been normalized to the unpumped data ($\Delta t = -1$ ps). Because the pump-probe delay was continuously scanned during the measurement, the error bars in the plots along the time axis indicate the length of the time interval in which the data have been summed to produce the spectra of Fig. 1. The error bars on the other axis are evaluated from the fits (1 σ), where each point in the measured spectrum has been statistically weighted.

a surface-temperature jump with a 400-nm optical laser pulse of 50 fs duration (12) is shown in Fig. 1. In the XES spectra, there were four major changes after excitation: (i) The peak containing the 5σ and 1π orbitals became sharper with a decrease in intensity of the shoulder at 523.5 eV and a shift to higher emission energy; (ii) the dip between the 4σ and 5σ spectral features was better resolved; (iii) the broad shoulder around 527 eV, where the \tilde{d}_π was observed, decreased in intensity; and (iv) a peak centered around 533 eV appeared. This peak corresponds to participator decay, in which the excited electron remains on the CO molecule and returns to the core level with emission of an x-ray photon of similar energy as the excitation (12). In the XAS spectra, we observed both a shift toward higher absorption energies and higher intensities of the $2\pi^*$ resonance. All of the observed spectral changes in the electronic structure are consistent with a substantial fraction of CO molecules being more weakly bound to the surface.

We refined these spectral observations using peak fitting (12) and show the evolution of the peaks with pump-probe delay time in Fig. 2. In Fig. 2A, we display only the average of the 5σ and 1π peak positions in order to have a parameter that is independent of the details of the fitting procedure. All of the changes reached a maximum after 6 to 10 ps, after which they were nearly constant. The main peak in the XES spectra—the center of mass of the 1π and 5σ components—moves toward higher emission energy, toward that for gas-phase CO, which is consistent with a weakening of the bond between CO and metal. The overall shift of the combined 5σ and 1π peak mostly originates from changes in the 5σ position. Bond weakening is also consistent with the decrease in the intensity of the \tilde{d}_π spectral feature, in which only 70% of the intensity remains after long delay times (Fig. 2B). The $2\pi^*$ level (Fig. 2A) shifts toward the $2\pi^*$ value at 534.2 eV; the intensity at the gas-phase energy position is still low, indicating that few molecules have completely desorbed. The bonding to the surface leads to partial occupation of CO $2\pi^*$ character in the \tilde{d}_π orbital, resulting in a decrease of the $2\pi^*$ XAS resonance intensity (16, 17). The gas-phase $2\pi^*$ resonance intensity is also partly restored with increasing delay time. The latter is directly related to the observed increase in the participator peak because we use $O1s \rightarrow 2\pi^*$ excitation, and for a weaker interaction with the surface, the excited electron is less likely to couple to the metal and delocalize.

Laser-induced surface reactions on metals are driven by hot electrons excited in the substrate, which couple to the adsorbate and substrate phonons within the first picosecond (12). We observed some changes at early times (at 1 ps, as seen in Fig. 2) that we attribute to hot electrons exciting frustrated rotations and translation of the CO molecules on the surface in accordance with previous studies (7, 8, 18). However, the hot electron bath transfers energy to phonons within 1 to 2 ps that

subsequently couple to the CO molecule. Because the major bond-weakening occurred only after a few picoseconds, we can directly relate this change to an increase in the surface temperature (12).

Our DFT calculations of the adsorption energy of CO using the Bayesian error estimation functional (19) includes the nonlocal correlation effects, giving rise to van der Waals interactions (20). When plotted at 0 K as a function of the distance of the CO molecule to the surface (Fig. 3), the chemisorbed state has an adsorption energy of 1.4 eV versus an experimental value of 1.6 eV (21). The dynamics at elevated temperatures was explored following Doren and Tully (2, 22) by calculating $W(s)$, the potential of mean force (PMF), which is a free-energy curve including contributions from entropy as a function of the reaction coordinate s :

$$W(s) = -k_B T \ln[g(s)] + k_B T \ln[g(\infty)] \quad (1)$$

$$g(s) = \Gamma^{-1} \int e^{-\frac{V(s,q)}{k_B T}} dq \quad (2)$$

Here, k_B is Boltzmann's constant, T is the temperature, s is the distance from the surface to the center of mass of the CO molecule along the reaction coordinate, q represents all degrees of freedom except the reaction coordinate, $V(s,q)$ is the interaction potential, and Γ is an arbitrary normalization constant. All degrees of freedom except the reaction coordinate have been thermally averaged. Although Eq. 1 assumes that all degrees of freedom can be treated classically—which is a rather crude approximation, especially at low temperatures—it can provide qualitative insights; for example, Gibbs free energy (ΔG°) of the extrema directly provides the transition-state theory rate constant for desorption (or adsorption).

As shown in Fig. 3, as the temperature increases two minima develop in the potential of mean force: the chemisorption minimum and another minimum at greater distances that we associated with a precursor state for adsorption or desorption (2, 22). At high temperature, the loss of entropy in the strongly adsorbed state, in which the rotations and translations of the CO molecule are frustrated, means that the free energy increases substantially relative to the gas phase. In the precursor state, the CO molecule is nearly free to rotate and to move parallel to the surface to the extent allowed by the finite coverage. Here, the entropy loss is minimal.

The following qualitative explanation of the experimental results is suggested with Fig. 3. After the laser pulse, the adsorbate temperature increases to a value in the range of 1500 to 2000 K (12). Here, the free energy $W(s)$ of the precursor state becomes comparable with that of the chemisorbed state, and a substantial fraction of the adsorbed CO molecules shift to the precursor state. Do the observed changes in the XES and XAS spectra correspond to a population of CO molecules in the precursor state? The core hole state in XES is prepared by exciting an O1s electron to the $2\pi^*$ level. For chemisorbed CO, this electron transfers to the substrate faster than the core hole

decays and has no influence on the XES spectrum (14, 23), but in the gas phase, it is localized on the molecule and screens the various final valence hole states, giving rise to a spectator shift (24); an additional peak, due to participator decay in which the excited electron decays back to the ground state, furthermore appears at an energy similar to the exciting photon (24). Shown in Fig. 4, left, is a fit of the 12-ps XES spectrum in terms of a linear combination consisting of 70% chemisorbed unpumped CO spectrum and 30% of an appropriately adjusted gas-phase CO spectrum (12). Compared with gas phase, the 4σ and 1π peaks need to be shifted by 0.3 and 0.1 eV, respectively, toward higher energies, which indicates that the

spectator shift is smaller than in the gas phase; the larger shift of 4σ than 1π required for the fit of our data is consistent with the larger gas-phase spectator shift for 4σ (1.8 eV) than for 1π (0.8 eV). The participator decay of the excited electron is shifted by 0.5 eV toward lower energy and contributes with only half the intensity, showing that at long time delays, the excited $2\pi^*$ electron is less localized on the CO molecule in comparison with when in the gas phase. The down energy shift in the participator decay is also consistent with the fit of the XAS spectrum at 12-ps delay (Fig. 4, right), which results in a similar ratio of unpumped chemisorbed CO with the resonance shifted by 0.3 eV relative to gas phase.

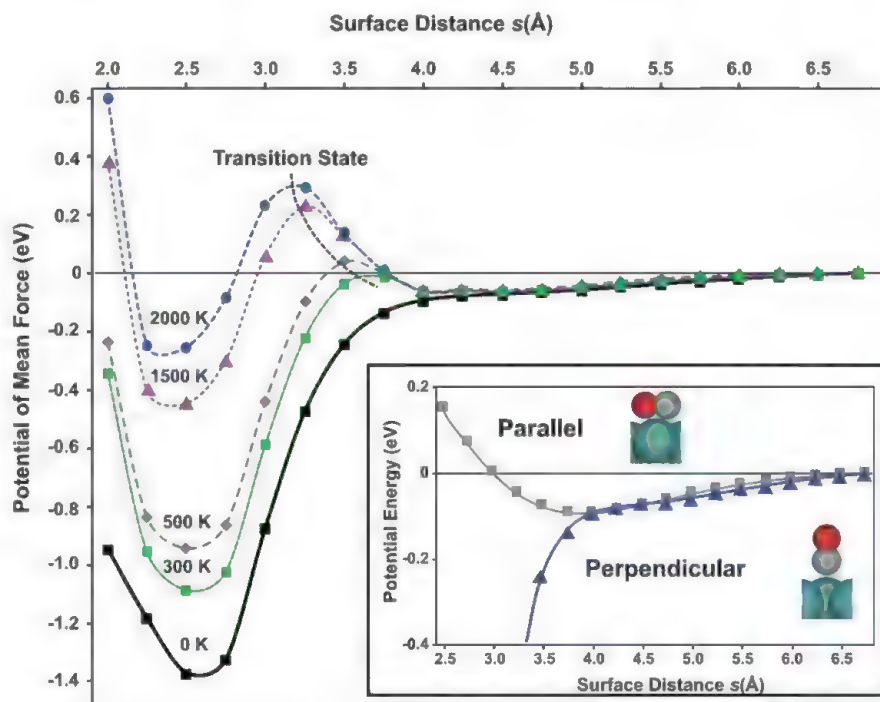


Fig. 3. The potential of mean force for CO adsorption/desorption on Ru(0001) at 0 K (minimum energy path) and 300, 500, 1500, and 2000 K. (Inset) The potential energy curve (0 K) of the CO molecule with orientation parallel and perpendicular to the Ru(0001) surface. The surface distance is measured between the CO center of mass and the surface. At 0 K and distances smaller than 2.5 Å, CO moves from on-top to bridge and hollow sites, giving less strong repulsion as compared with the finite temperatures at which more repulsive orientations are sampled.

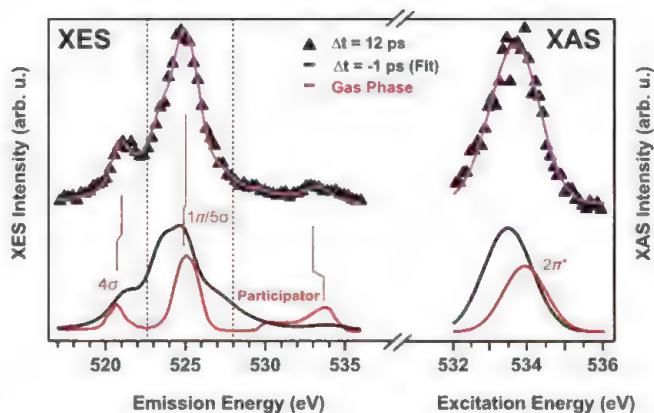


Fig. 4. (Left) XES and (Right) XAS at a pump-probe delay of 12 ps were represented by a sum of spectra corresponding to unpumped chemisorbed CO obtained from the spectra at negative delay and precursor state spectra represented by an appropriately adjusted gas-phase spectrum (12). The resulting fit (pink) and 12-ps experimental data are vertically offset for clarity.

The difference in XAS and participator decay positions of the $2\pi^*$ state can be related to nuclear dynamics during the core hole lifetime in XES (24). The smaller spectator shift in XES, lower participator intensity of the excited $2\pi^*$ electron, and less shifted $2\pi^*$ XAS resonance show that the CO molecules that have broken the direct CO metal bond have not yet desorbed into gas phase but still interact weakly with the surface.

Using DFT, we examined (figs. S9 and S10) the $1s \rightarrow 2\pi^*$ core-excited states and spectra for different points along the minimum energy path of Fig. 3. The computed XAS spectra reproduce the expected behavior with enhanced $2\pi^*$ intensity together with a shift to higher energy as the distance to the surface increases. In the precursor state, the antibonding CO orbitals, which have a large spatial extent, still interact with the metal states. The substrate interaction with the $2\pi^*$ has a distance dependence in the precursor state, and most likely, we are probing a distribution of distances in the experiment; rotation of the molecule in the precursor potential has only minor effects on the spectra (fig. S10).

Because 30% of the \tilde{a}_π intensity disappeared and the spectra could be fitted with 30% shifted gas-phase contributions at long delay times, it is likely that 30% of the molecules were pumped into the precursor state, supporting the notion that the two states have rather comparable free energies. Some of the molecules desorb during the experiment, but when the system cools, the remaining molecules can return from the precursor to the chemisorbed state. Previous SFG results showed that the C-O stretch intensity was reduced by one order of magnitude after a pump laser pulse that led to a final desorption of ~30% of the adsorbed CO molecules (8, 12). However, the SFG intensity recovered to half of its initial value after 170 ps (8) because roughly half of the molecules readsorbed into the chemisorbed state. We suggest that the initial drop of intensity in the SFG experiment corresponds to essentially all of the molecules being pumped into the precursor state, in which the SFG signal would disappear because of orientational disordering of the CO molecules (25, 26). Because the laser fluence in the SFG experiment and in the present experiment are similar, we propose that also in the present case, ~50% of the molecules return to the chemisorbed state from the precursor state as the substrate cools down and the temperature-induced entropic barrier to the chemisorbed state vanishes. The molecules in the precursor state have very weak interactions perpendicular to the surface, which leads to a small probability of obtaining the perpendicular momentum needed for desorption. Considering, on the other hand, the time-reversed situation, a similar trapping in the precursor state due to the entropic barrier must also occur in chemisorption.

The prefactors in Arrhenius expressions for desorption rates of molecules such as CO are often anomalously large (27). For instance, the prefactor for CO desorption on Ru(0001) has

been found to be of the order 10^{14} to 10^{19} s^{-1} , depending on coverage (21), versus typical values between 10^{12} and 10^{13} s^{-1} ; this has generally been explained by the difference in entropy between the initial (adsorbed) state and the final (gas) state (21). We instead found that it is the entropy gain at the free-energy barrier between the chemisorbed and precursor state that is decisive. In the present case, this leads to a computed prefactor on the order of 10^{17} s^{-1} and, consequently, to the efficient population of the precursor state observed in our experiment.

References and Notes

1. A. Cassuto, D. A. King, *Surf. Sci.* **102**, 388 (1981).
2. D. J. Doren, J. C. Tully, *Langmuir* **4**, 256 (1988).
3. P. Kisliuk, *J. Phys. Chem. Solids* **3**, 95 (1957).
4. J. B. Taylor, I. Langmuir, *Phys. Rev.* **44**, 423 (1933).
5. C. Frischkorn, M. Wolf, *Chem. Rev.* **106**, 4207 (2006).
6. H. Arnolds, M. Bonn, *Surf. Sci. Rep.* **65**, 45 (2010).
7. E. H. G. Backus, A. Eichler, A. W. Kleyn, M. Bonn, *Science* **310**, 1790 (2005).
8. M. Bonn *et al.*, *Phys. Rev. Lett.* **84**, 4653 (2000).
9. F. Fournier, W. Zheng, S. Carrez, H. Dubost, B. Bourguignon, *J. Chem. Phys.* **121**, 4839 (2004).
10. I. M. Lane, D. A. King, Z. P. Liu, H. Arnolds, *Phys. Rev. Lett.* **97**, 186105 (2006).
11. K. Inoue, K. Watanabe, Y. Matsumoto, *J. Chem. Phys.* **137**, 024704 (2012).
12. Materials and methods, and supporting analysis of the experimental and theoretical data, are available as supplementary materials on Science Online.
13. A. Föhlisch, W. Wurth, M. Stichler, C. Keller, A. Nilsson, *J. Chem. Phys.* **121**, 4848 (2004).
14. A. Nilsson, L. G. M. Pettersson, *Surf. Sci. Rep.* **55**, 49 (2004).
15. A. Nilsson *et al.*, *Phys. Rev. Lett.* **78**, 2847 (1997).
16. A. Föhlisch *et al.*, *J. Chem. Phys.* **112**, 1946 (2000).
17. O. Björneholm *et al.*, *Phys. Rev. B* **46**, 10353 (1992).
18. L. Bartels, F. Wang, D. Möller, E. Knoesel, T. F. Heinz, *Science* **305**, 648 (2004).
19. J. Wellendorff *et al.*, *Phys. Rev. B* **85**, 235149 (2012).
20. M. Dion, H. Rydberg, E. Schröder, D. C. Langreth, B. I. Lundqvist, *Phys. Rev. Lett.* **92**, 246401 (2004).
21. H. Pfnür, P. Feulner, D. Menzel, *J. Chem. Phys.* **79**, 4613 (1983).
22. D. J. Doren, J. C. Tully, *J. Chem. Phys.* **94**, 8428 (1991).
23. C. Keller *et al.*, *Phys. Rev. Lett.* **80**, 1774 (1998).
24. P. Skytt *et al.*, *Phys. Rev. A* **55**, 134 (1997).
25. Y. R. Shen, *Principles of Non-Linear Optics* (Wiley-Interscience, New York, 2003).
26. J. H. Hunt, P. Guyot-Sionnest, Y. R. Shen, *Chem. Phys. Lett.* **133**, 189 (1987).
27. I. Chorkendorf, H. Niemantsverdriet, *Concepts of Modern Catalysis and Kinetics* (Wiley-VCH, Weinheim, Germany, 2003).

Acknowledgments: This work is supported by the U.S. Department of Energy (DOE), Office of Basic Energy Sciences, Division of Materials Sciences and Engineering, under contract DE-AC02-76SF00515; the DOE, Basic Energy Science through the SUNCAT Center for Interface Science and Catalysis; the Swedish National Research Council; the Danish Center for Scientific Computing; the Volkswagen Stiftung; the Alexander von Humboldt Foundation; and the Lundbeck Foundation. The spectrum calculations were performed on resources provided by the Swedish National Infrastructure for Computing (SNIC) at the High Performance Computing Center North. Portions of this research were carried out on the SXR Instrument at LCLS, a division of SLAC National Accelerator Laboratory and an Office of Science user facility operated by Stanford University for the DOE. The SXR Instrument is funded by a consortium whose membership includes the LCLS, Stanford University through SIMES, Lawrence Berkeley National Laboratory, University of Hamburg through the BMBF priority program FSP 301, and the Center for Free Electron Laser Science.

Supplementary Materials

www.sciencemag.org/cgi/content/full/339/6125/1302/DC1
Materials and Methods
Figs. S1 to S12
References (28–50)

18 October 2012; accepted 27 December 2012
10.1126/science.1231711

Evidence for Microbial Carbon and Sulfur Cycling in Deeply Buried Ridge Flank Basalt

Mark A. Lever,^{1,2*} Olivier Rouxel,^{3,4} Jeffrey C. Alt,⁵ Nobumichi Shimizu,³ Shuhei Ono,⁶ Rosalind M. Coggon,⁷ Wayne C. Shanks III,⁸ Laura Lapham,^{2,†} Marcus Elvert,⁹ Xavier Prieto-Mollar,⁹ Kai-Uwe Hinrichs,⁹ Fumio Inagaki,¹⁰ Andreas Teske^{1*}

Sediment-covered basalt on the flanks of mid-ocean ridges constitutes most of Earth's oceanic crust, but the composition and metabolic function of its microbial ecosystem are largely unknown. By drilling into 3.5-million-year-old subseafloor basalt, we demonstrated the presence of methane- and sulfur-cycling microbes on the eastern flank of the Juan de Fuca Ridge. Depth horizons with functional genes indicative of methane-cycling and sulfate-reducing microorganisms are enriched in solid-phase sulfur and total organic carbon, host $\delta^{13}\text{C}$ - and $\delta^{34}\text{S}$ -isotopic values with a biological imprint, and show clear signs of microbial activity when incubated in the laboratory. Downcore changes in carbon and sulfur cycling show discrete geochemical intervals with chemoautotrophic $\delta^{13}\text{C}$ signatures locally attenuated by heterotrophic metabolism.

Subseafloor basaltic crust represents the largest habitable zone by volume on Earth (1). Chemical reactions of basalt with sea-

water flowing through fractures release energy that may support chemosynthetic communities. Microbes exploiting these reactions are known

from basalt exposed at the seafloor, where the oxidation of reduced sulfur (S) and iron (Fe) from basalt with dissolved oxygen and nitrate

from seawater supports high microbial biomass and diversity (2, 3). Multiple lines of indirect evidence that include textural alterations (4), depletions in $\delta^{34}\text{S}$ -pyrite (FeS_2) (5) and $\delta^{13}\text{C}$ -dissolved inorganic carbon (DIC) (6), and DNA sequences from borehole observatories (7, 8) suggest active microbial communities in subsurface basalt.

We combined sequencing of genes diagnostic of microbial methane and S cycling with geochemical and isotopic analyses of C and S pools and laboratory-based incubations to directly identify microbial ecosystem components in deep subsurface basalt. The 3.5-million-year-old basement at site U1301 was sampled during Integrated Ocean Drilling Program (IODP) Expedition 301 in 2004 (fig. S1) (9). Site U1301, off the eastern flank of the Juan de Fuca Ridge, is covered by a 265-m-thick sediment layer and lies ~2 km south of ODP Site 1026, which it resembles in temperature profile, lithology, and sediment chemistry (9). Given anticipated poor recovery due to brecciation of the upper basement [265 to 350 m below sea-

floor (mbsf)], coring was restricted to an interval of pillow basalts and massive lavas (351 to 583 mbsf). Sulfate concentrations (~16 mM) and vein carbonates indicate that basalt fluids are derived from seawater, which enters ~55 km south at Grizzly Bare outcrop and discharges near U1301, at Baby Bare and Mama Bare outcrops (9, 10) (fig. S1B). Yet, the basement at U1301 differs from seafloor-exposed basalt in its uniformly high temperature (~64°C) (9) and lack of fresh photosynthesis-derived organic matter, dissolved oxygen, and nitrate (7, 11). These conditions preclude oxygen- or nitrate-dependent microbial S and Fe oxidation (12) but may enable growth of anaerobes, such as sulfate reducers and methanogens, which use sulfate and DIC as electron acceptors.

We sequenced genes encoding the α subunit of methyl coenzyme M reductase (*mcrA*), a gene unique to methanogens and anaerobic methane oxidizers (13), and the β subunit of dissimilatory sulfite reductase (*dsrB*), a gene found in sulfate- and sulfite-reducing microbes (14), to indicate the presence of methane-cycling

¹Department of Marine Sciences, University of North Carolina at Chapel Hill, Chapel Hill, NC 27599, USA. ²Center for Geomicrobiology, Department of BioScience, Aarhus University, DK-8000 Aarhus C, Denmark. ³Woods Hole Oceanographic Institution, Woods Hole, MA 02543, USA. ⁴IFREMER, Centre de Brest, 29280 Plouzané, France. ⁵Department of Earth and Environmental Sciences, University of Michigan, Ann Arbor, MI 48109, USA. ⁶Department of Earth, Atmospheric, and Planetary Sciences, Massachusetts Institute of Technology, Cambridge, MA 02139, USA. ⁷Department of Earth Science and Engineering, Imperial College London, South Kensington Campus, London SW7 2AZ, UK. ⁸U.S. Geological Survey, Denver, CO 80225, USA. ⁹Organic Geochemistry Group, Department of Geosciences and MARUM Center for Marine Environmental Sciences, University of Bremen, D-28334 Bremen, Germany. ¹⁰Geomicrobiology Group, Kochi Institute for Core Sample Research, Japan Agency for Marine-Earth Science and Technology, Nankoku, Kochi 783-8502, Japan.

*To whom correspondence should be addressed. E-mail: mark.lever@biology.au.dk (M.A.L.); teske@email.unc.edu (A.T.)

†Present address: University of Maryland Center for Environmental Science, Solomons, MD 20688, USA.

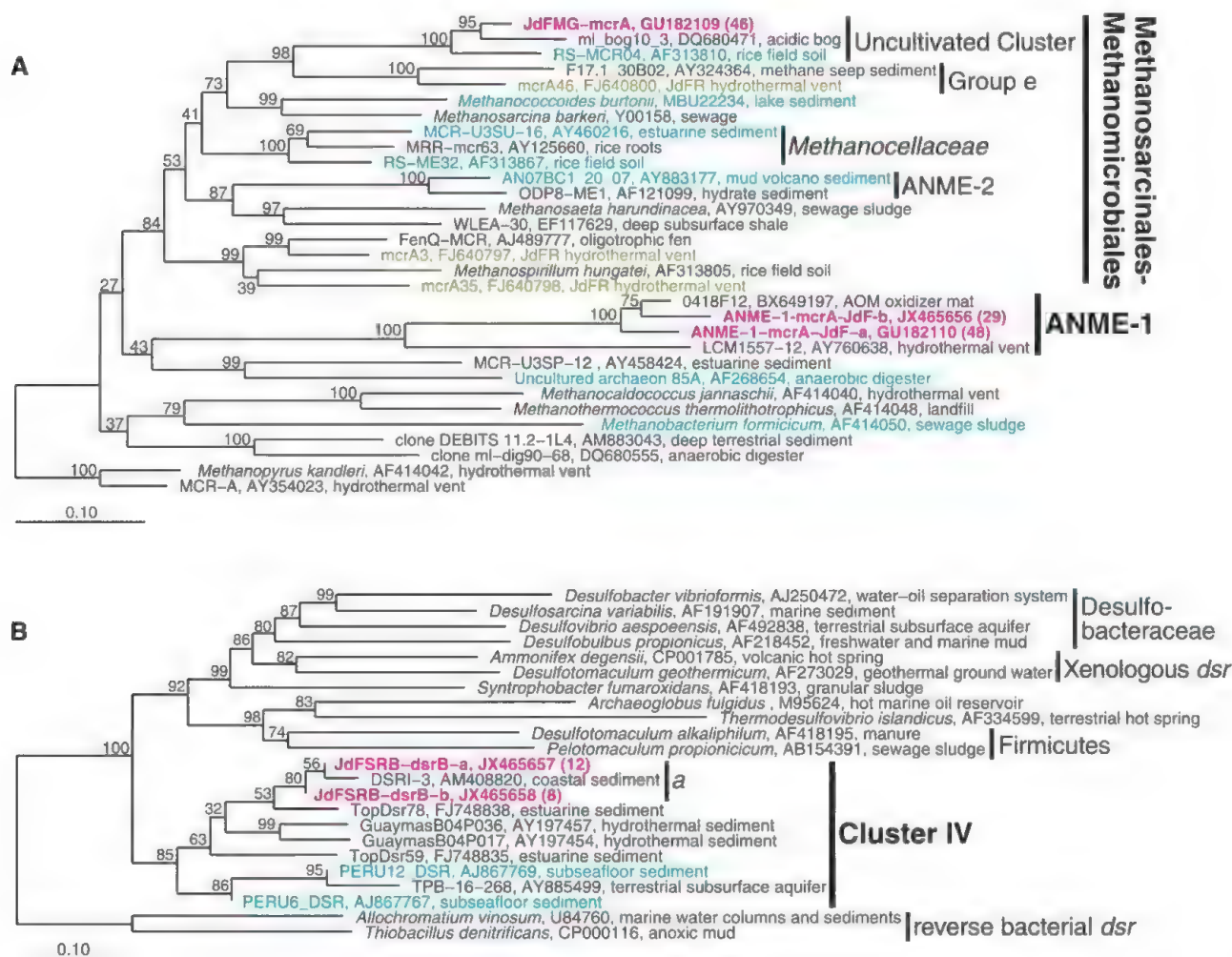


Fig. 1. Phylogenetic trees of functional genes. (A) *McrA* sequences from borehole U1301B are in bold magenta. Close relatives based on microarray analyses of JdF Ridge hydrothermal vent chimneys and seafloor basalt are in green (18) and cyan

(19), respectively. (B) *DsrB* sequences from borehole U1301B are in bold magenta and sequences from subsurface sediment off Peru in cyan (22). Bootstrap support (in %, 1000 replications) is indicated at each branching point.

and sulfate-reducing microbes. We detect *mcrA* in 5 of the 10 samples and *dsrB* in 4 of the 6 samples tested (table S1), which suggests that these metabolisms are present in this environment.

The phylogenetic diversity of *mcrA* genes that we identified is restricted to two groups: the Juan de Fuca Methanogen Group (JdFMG), which falls into an uncultivated cluster within the *Methanosarcinales*, and anaerobic methane-oxidizing archaea (ANME-1) (Fig. 1A). Close relatives of the JdFMG have been identified from paddy and wetland soil (15, 16) and also have been found in marine habitats, including Juan de Fuca Ridge hydrothermal vent chimneys and seafloor-exposed basalt ~100 km west of U1301 (fig. S2) (17, 18). ANME-1 occur widely in marine sediments and methane seeps and are believed to gain energy from the anaerobic oxidation of methane (AOM) (19). Two distinct ANME phylotypes occur at U1301, one closely related to ANME-1 from methane seeps and another clustering with only one other sequence, from seafloor sediment (fig. S3). We

detected JdFMG in 4 and ANME-1 in 3 out of 10 basalt samples. Two samples contained both groups (table S1).

The phylogenetic diversity of *dsrB* in these samples is limited to one group, the Juan de Fuca Sulfate Reducing Group (JdFSRG), which falls into Cluster IV, a deeply branching *dsrB* cluster without cultured members, first reported from hydrothermal sediment (Fig. 1B, fig. S4, and table S1) (20). Remarkably, the only other *dsrB* sequences reported so far from the seafloor—in sediment of the Peru Margin (21)—also fall into this cluster, which is widespread in shallow marine sediment and terrestrial aquifers.

We studied solid-phase S pools by analyzing acid-volatile sulfide (AVS), chromium-reducible S (CRS), and sulfate-S ($\text{SO}_4\text{-S}$) as a proxy to redox processes and correlate to microbial metabolisms (5, 22). We found *dsrB* sequences only in a relatively reduced “intermediate depth interval” (~430 to 520 mbsf, samples 14R to 26R) in samples with AVS as the main S pool in alteration halos (14R-1-11)—the visually conspicuous zone

surrounding fractures (fig. S1C)—or in host rock (17R-170, 20R-1-57, and 23R-2-21) (fig. S5 and table S1). Samples from this interval have higher AVS, CRS, and total S (fig. S5 and table S2); contain large pyrite fronts (14R-1-65P, 15R-4-142P) (fig. S5); and have lower $\delta^{34}\text{S}$ -AVS, -CRS, and - $\text{SO}_4\text{-S}$, compared with the more oxidized upper (1R to 12R) and lower coring intervals (30R to 36R) (fig. S6 and table S1). Consistent with higher $\text{Fe}^{3+}/\text{Fe}^{\text{Total}}$ ratios, which indicate halos to be more oxidized than host rock (table S1), pyrite is generally absent from halos or veins. Outside the intermediate depth interval, the near absence of pyrite from host rock, and mixed clay-Fe-oxyhydroxide-dominated halos and veins, are further evidence of pervasive oxidative alteration.

We analyzed the $\delta^{34}\text{S}$ signature of pyrite grains to examine micro- and macroscale variations in microbial S cycling (tables S1 and S3 and Fig. 2). Although variable, the $\delta^{34}\text{S}$ -pyrite grains [−72.4 to 1.2 per mil (‰)] (table S3) are typically lower than those of AVS (−9.3 to −0.2‰),

Fig. 2. Macro- and microscale distribution of S-isotopic data. On the left, $\delta^{34}\text{S}$ -depth profile of pyrite granules, analyzed by laser ablation and secondary ion mass spectrometry (SIMS), and bulk S pools (AVS and CRS). On the right, thin-section micrograph showing individual pyrite granules and their $\delta^{34}\text{S}$. The dashed magenta line indicates the sampling depth of the thin section. The dashed black lines mark the intermediate depth interval. Pyrite grains with a sufficient diameter for $\delta^{34}\text{S}$ determination (10 μm) were limited to this interval. Scale bar, 200 μm .

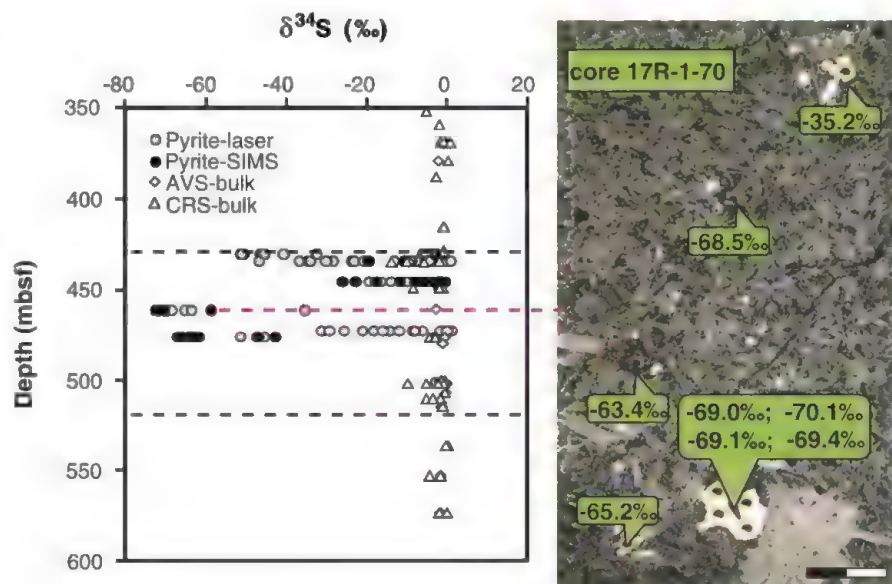
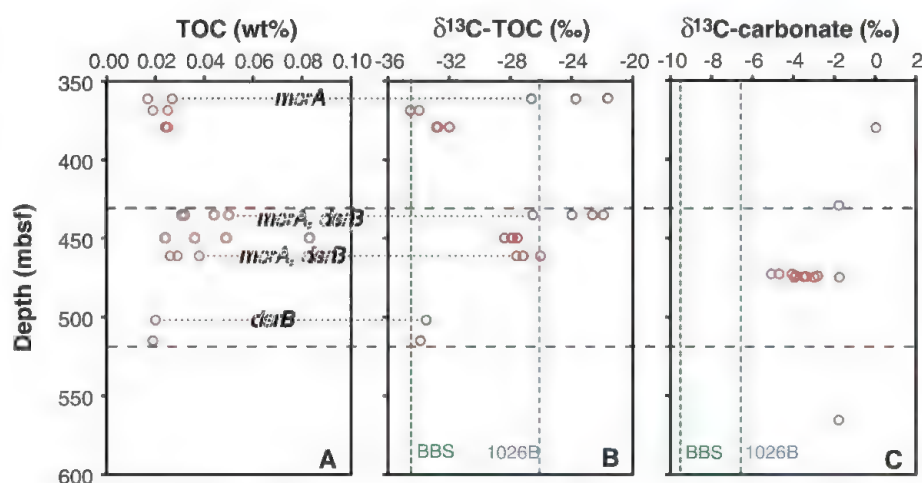


Fig. 3. Depth-related trends in (A) TOC content, (B) $\delta^{13}\text{C}$ -TOC, and (C) $\delta^{13}\text{C}$ -carbonate. Cores with functional gene detection are indicated in (A) and (B). Dashed vertical lines indicate $\delta^{13}\text{C}$ -DOC (B) and $\delta^{13}\text{C}$ -DIC (C) values from 1026B and BBS. Because the carbonate content of rock samples used in (A) and (B) was too low for analyses, $\delta^{13}\text{C}$ from carbonate veins are shown in (C). The reduced intermediate depth interval falls between the dashed horizontal lines. All $\delta^{13}\text{C}$ are in ‰ versus Vienna Pee Dee belemnite (VPDB).



CRS (−13.7 to 0‰), SO₄-S (−6.5 to 0‰), mantle S (0‰) (5), dissolved sulfate in bottom sediments at ODP Site 1026 (+30‰) (23), or seawater (+21‰) (Fig. 2). Locally, the δ³⁴S of pyrite grains reach very negative values (−72‰), consistent with the addition of highly ³⁴S-depleted secondary sulfide to basement rock (22). These low δ³⁴S-pyrite values indicate single-step sulfate reduction (24) or repeated cycles of sulfate reduction and S oxidation (25). The co-occurrence of low δ³⁴S-pyrite, *dsrB*, and *mcrA* of ANME-1 in two samples (14R-1-11, 17R-1-70) suggests local coupling between methane and S cycling by sulfate-dependent AOM.

Depth profiles of total organic carbon (TOC) content, δ¹³C-TOC, and δ¹³C-carbonate at U1301B are consistent with functional gene and ³⁴S data (Fig. 3). The TOC content is highest in the intermediate depth interval in cores with *mcrA*, *dsrB*, and low δ³⁴S-pyrite (Fig. 3A and table S4). The δ¹³C-TOC is in the range of dissolved organic C (DOC) in fluids from nearby 1026B and Baby Bare Springs (BBS) (Fig. 3B and table S4) and lower than seawater DOC (−21.1‰) (6). The δ¹³C-carbonate is higher than δ¹³C-DIC at Site 1026B or BBS (Fig. 3C and table S5) and overlaps with δ¹³C-DIC of bottom seawater (−1.4‰) (10).

δ¹³C-TOC values in the upper coring interval (4R to 5R) and near the bottom (23R to 26R; −34.6 to −32.0‰) are close to δ¹³C-DOC from nearby BBS (−34.6‰) (Fig. 3B). The absence of O₂ and the high ¹³C-TOC depletion relative to carbonate (−30 to −35‰) suggest C fixation by the reductive acetyl CoA pathway—an anaerobic pathway found in all methanogens and acetogens and certain sulfate and iron reducers (fig. S7 and tables S6 and S7) (26). The presence of *dsrB* but not *mcrA* in these samples suggests that sulfate reducers or other groups, but not methanogens, produce this low δ¹³C-TOC.

δ¹³C-TOC at the top (2R) and in the intermediate depth interval (−28.4 to −21.6‰) are close to δ¹³C-DOC from borehole 1026B (−26.1‰) (Fig. 3B) (6). The ¹³C depletion relative to carbonate is lower than in the other layers (−20 to −26‰), but also falls in the range of the reductive acetyl CoA pathway (table S7), and, consistent with *mcrA* detection, could be affected by autotrophic methanogenesis. In addition, elevated heterotrophic activity is possible, because degradation of chemoautotrophy-derived OC—for example, by AOM, methanogenesis, or fermentation—would lower the δ¹³C-carbonate and potentially raise the δ¹³C-TOC. In fact, the lowest δ¹³C-carbonate values (to −5.1‰) were measured in the intermediate depth interval (18R) (Fig. 3 and table S5), consistent with a locally conspicuous input of IC from the degradation of chemoautotrophy-derived OC. The alternative explanation, enhanced breakdown of photosynthesis-derived OC in the intermediate depth interval, is unlikely given that sediment inclusions are absent (9). Similarly, influx

of labile DOC or unaltered DIC from seawater is incompatible with the 7 to 11 thousand year greater DOC age compared with bottom seawater and the 4 to 8‰ decrease in δ¹³C-DIC along the flowpath from Grizzly Bare outcrop to 1026B and BBS, respectively (6, 10).

To rule out a fossil origin of functional genes and the chemical and isotopic signatures, we incubated pieces from the interior of three rock samples used for functional gene analyses (1R-1-79, 14R-1-11, and 23R-2-21) at 65°C in anoxic, sulfate-rich media containing H₂, acetate, methanol, and dimethyl sulfide as energy substrates (table S8). After 2 years, aliquots were transferred to fresh media and incubated for another 5 years using triple-autoclaved basalt pieces as substrata. By then, low concentrations of ¹³C-depleted methane (−54 to −65‰) had formed, indicating the presence of active methanogenic microorganisms (table S9).

The variability in δ³⁴S-pyrite, δ¹³C-TOC, and δ¹³C-carbonate indicates that micro- and macro-scale geochemical changes related to mineralogy, fracturing, and/or fluid flow strongly influence microbial activity. These chemical microniches may explain the coexistence of sulfate reducers and methanogens at U1301 and in other igneous habitats, despite higher energy yields of sulfate reduction compared with methanogenesis (27). In addition, some methanogens can survive in the presence of sulfate reducers by consuming noncompetitive methylated substrates (28). Because methanogenic substrate usage follows *mcrA* phylogeny (28), this explanation is consistent with the ability of a close relative of JdFMG to use methanol (16); it is also consistent with the production of biogenic methane in basalt incubations containing sulfate and methanol (table S9 and fig. S8).

Inorganic electron donors used by sulfate reducers and methanogens—e.g., H₂—are likely to derive from serpentinization reactions, whereby Fe(II) minerals—e.g., olivine [(Mg, Fe)₂SiO₄], which is abundant in several basalt horizons at U1301 (9) (fig. S9 and tables S10 and S11)—are oxidized in abiotic reactions with seawater-derived fluids (1). Organic electron donors (for example, short-chain fatty acids and alcohols) are probably produced by breakdown of autochthonous OC (6, 27, 29) or Fischer-Tropsch-type synthesis (30) (table S10). Targeted investigations of potential carbon and energy sources will provide further insights to micro- and macro-scale heterogeneity of microbial C and S cycling and thus contribute to a better understanding of chemoautotrophic ecosystems within Earth's oceanic crust.

References and Notes

- W. Bach, K. J. Edwards, *Geochim. Cosmochim. Acta* **67**, 3871 (2003).
- K. J. Edwards, T. M. McCollom, H. Konishi, P. R. Buseck, *Geochim. Cosmochim. Acta* **67**, 2843 (2003).
- C. M. Santelli et al., *Nature* **453**, 653 (2008).
- M. R. Fisk, S. J. Giovannoni, I. H. Thorseth, *Science* **281**, 978 (1998).

- O. Rouxel, S. Ono, J. Alt, D. Rumble, J. Ludden, *Earth Planet. Sci. Lett.* **268**, 110 (2008).
- M. D. McCarthy et al., *Nat. Geosci.* **4**, 32 (2011).
- J. P. Cowen et al., *Science* **299**, 120 (2003).
- B. N. Orcutt et al., *ISME J.* **5**, 692 (2011).
- A. T. Fisher, T. Urabe, A. Klaus, Expedition 301 Scientists, *Proc. IODP 301* (2005).
- B. D. Walker, M. D. McCarthy, A. T. Fisher, T. P. Guilderson, *Mar. Chem.* **108**, 123 (2008).
- C. G. Wheat et al., *Geochim. Geophys. Geosyst.* **11**, Q07011 (2010).
- A. Schippers, B. B. Jørgensen, *Geochim. Cosmochim. Acta* **66**, 85 (2002).
- M. W. Friedrich, *Methods Enzymol.* **397**, 428 (2005).
- M. Wagner, A. J. Roger, J. L. Flax, G. A. Brusseau, D. A. Stahl, *Appl. Environ. Microbiol.* **75**, 7086 (1998).
- T. Lueders, K.-J. Chin, R. Conrad, M. Friedrich, *Environ. Microbiol.* **3**, 194 (2001).
- G. Zhang et al., *Environ. Microbiol.* **10**, 1850 (2008).
- F. Wang et al., *Proc. Natl. Acad. Sci. U.S.A.* **106**, 4840 (2009).
- O. U. Mason et al., *ISME J.* **3**, 231 (2009).
- K. Knittel, A. Boetius, *Annu. Rev. Microbiol.* **63**, 311 (2009).
- A. Dhillon, A. Teske, J. Dillon, D. A. Stahl, M. L. Sogin, *Appl. Environ. Microbiol.* **69**, 2765 (2003).
- G. Webster et al., *FEMS Microbiol. Ecol.* **58**, 65 (2006).
- S. Ono, N. S. Keller, O. Rouxel, J. C. Alt, *Geochim. Cosmochim. Acta* **87**, 323 (2012).
- M. D. Rudnicki, H. Elderfield, B. Spiro, *Geochim. Cosmochim. Acta* **65**, 777 (2001).
- M. S. Sim, T. Bosak, S. Ono, *Science* **333**, 74 (2011).
- D. E. Canfield, B. Thamdrup, *Science* **266**, 1973 (1994).
- A. L. Zerkle, C. H. House, S. L. Brantley, *Am. J. Sci.* **305**, 467 (2005).
- H.-T. Lin, J. P. Cowen, E. J. Olson, J. P. Amend, M. D. Lilley, *Geochim. Cosmochim. Acta* **85**, 213 (2012).
- W. B. Whitman, T. L. Bowen, D. R. Boone, *The Prokaryotes* **3**, 165 (2006).
- M. A. Lever et al., *Geomicrobiol. J.* **27**, 183 (2010).
- T. M. McCollom, J. S. Seewald, *Chem. Rev.* **107**, 382 (2007).

Acknowledgments: We thank B. Jørgensen, M. Sogin, and the IODP Expedition 301 Scientists for advice and support in this project. Funding was obtained from a Schlanger Ocean Drilling Fellowship, a University of North Carolina Dissertation Completion Fellowship, a Marie-Curie Intra-European Fellowship (255135) (all to M.A.L.); the Danish National Research Foundation and the Max Planck Society (both to B. Jørgensen); Europol Mer (to O.R.); the European Research Council Advanced Grant DARCLIFE (to K.-U.H.); the NASA Astrobiology Institute Subsurface Biospheres (to A.T.); the Japan Society for the Promotion of Science (JSPS) Funding Program for Next Generation World-Leading Researchers (NEXT Program) (to F.L.); and the National Science Foundation (NSF-OCE 0622949 and OCE 1129631 to J.C.A.; OCE-0753126 to S.O. and O.R.; and NSF-ODP 0727175 and NSF-STC for Dark Energy Biosphere Investigations to A.T.). We thank three anonymous reviewers for very helpful comments. The geochemical data are available in the supplementary tables. Any use of trade, firm, or product names is for descriptive purposes only and does not imply endorsement by the U.S. government. The functional gene sequence data are available from the GenBank database (accession numbers GU182109 to GU182110 and JX465656 to JX465658).

Supplementary Materials

www.sciencemag.org/cgi/content/full/339/6125/1305/DC1
Materials and Methods
Figs. S1 to S9
Tables S1 to S13
References (31–46)

23 August 2012; accepted 12 December 2012
10.1126/science.1229240

Hind Wings in Basal Birds and the Evolution of Leg Feathers

Xiaoting Zheng,^{1,2*} Zhonghe Zhou,³ Xiaoli Wang,¹ Fucheng Zhang,³ Xiaomei Zhang,² Yan Wang,¹ Guangjin Wei,¹ Shuo Wang,^{3,4} Xing Xu^{1,3*}

Recent discoveries of large leg feathers in some theropods have implications for our understanding of the evolution of integumentary features on the avialan leg, and particularly of their relevance for the origin of avialan flight. Here we report 11 basal avialan specimens that will greatly improve our knowledge of leg integumentary features among early birds. In particular, they provide solid evidence for the existence of enlarged leg feathers on a variety of basal birds, suggest that extensively scaled feet might have appeared secondarily at an early stage in ornithomorph evolution, and demonstrate a distal-to-proximal reduction pattern for leg feathers in avialan evolution.

A bizarre hind wing formed by large pennaceous feathers (feathers with stiff vanes) along the metatarsus is known in several non-avian dinosaurs (1–4) and may have played an important role in the evolution of flight on the line to birds (1–7). However, no examples of this unusual structure have so far been reported in basal birds, although *Archaeopteryx* and one enantiornithine specimen have been reported to have large pennaceous feathers along the tibiotarsus (8, 9), and the relevance of large leg feathers to the early evolution of flight has been questioned on this basis (10, 11). Here we describe 11 specimens of different avialan taxa that preserve exceptional integumentary structures associated with the hindlimb (Figs. 1 to 3 and figs. S1 to S8) (12). These specimens demonstrate the presence of hind wings in basal birds. All 11 specimens are from the Lower Cretaceous Jehol Group (13) and are housed in the Shandong Tianyu Museum of Nature (STM).

Among these specimens, STM16-18 and STM16-19 (Fig. 1) are referable to the basal avialan *Sapeornis*, because the elements preserved in these individuals are nearly identical in morphology to those of previously described specimens of this genus (12, 14). STM16-18 is a nearly complete articulated skeleton lacking the pectoral girdle and forelimbs. STM16-19 is a partial skeleton preserving only the pygostyle, the two pubes, and the left hindlimb.

In STM16-18, a series of parallel pennaceous feathers is preserved along the distal half of the tibiotarsus and nearly the whole length of the metatarsus in each hindlimb (Fig. 1, A to C). The longest ones exceed 50 mm in length and appear to be located close to the distal end of the tibio-

tarsus, whereas the metatarsal feathers are shorter but still measure more than 30 mm. The lengths of the tibiotarsus and metatarsus themselves are 65 and 33 mm, respectively. Leg feathers of similar morphology can also be recognized on both the tibiotarsus and the metatarsus of STM16-19 (Fig. 1D). The pennaceous feathers attached to the hindlimbs of these two specimens have rachises that are significantly curved and appear to have symmetrical vanes. The feathers are nearly perpendicular to the tibiotarsus and metatarsus in orientation

and form a planar surface as in some basal deinonychosaurs with large leg feathers (1–4).

The leg integument is poorly known in confuciusornithids (15, 16), but five confuciusornithid specimens housed in the STM (STM13-32, STM13-44, STM13-55, STM13-57, and STM13-331) contribute significant new information (Fig. 2A and figs. S1 to S5) (12). In these specimens, large pennaceous feathers occur along nearly the whole length of the tibiotarsus and are individually more than half as long as this bone (Fig. 2B). Most interestingly, some feathers occur on the proximal half of the left metatarsus in STM13-32, though these feathers are insufficiently well preserved for it to be possible to determine whether they are pennaceous.

STM7-50, STM7-161, and STM7-215 (Fig. 2C and figs. S6 to S8) are referable to the Enantiornithes and probably belong to two different taxa (12). Regularly arranged large feathers are preserved along the whole length of the tibiotarsus in each of these specimens (Fig. 2D). The feathers measure more than half of the tibiotarsal length, have curved rachises, and are nearly perpendicular to the tibiotarsus. These specimens provide further support for the existence of a reduced hind wing in enantiornithines (8). As in most bird specimens from Liaoning, no integumentary structures are preserved in association with the feet.

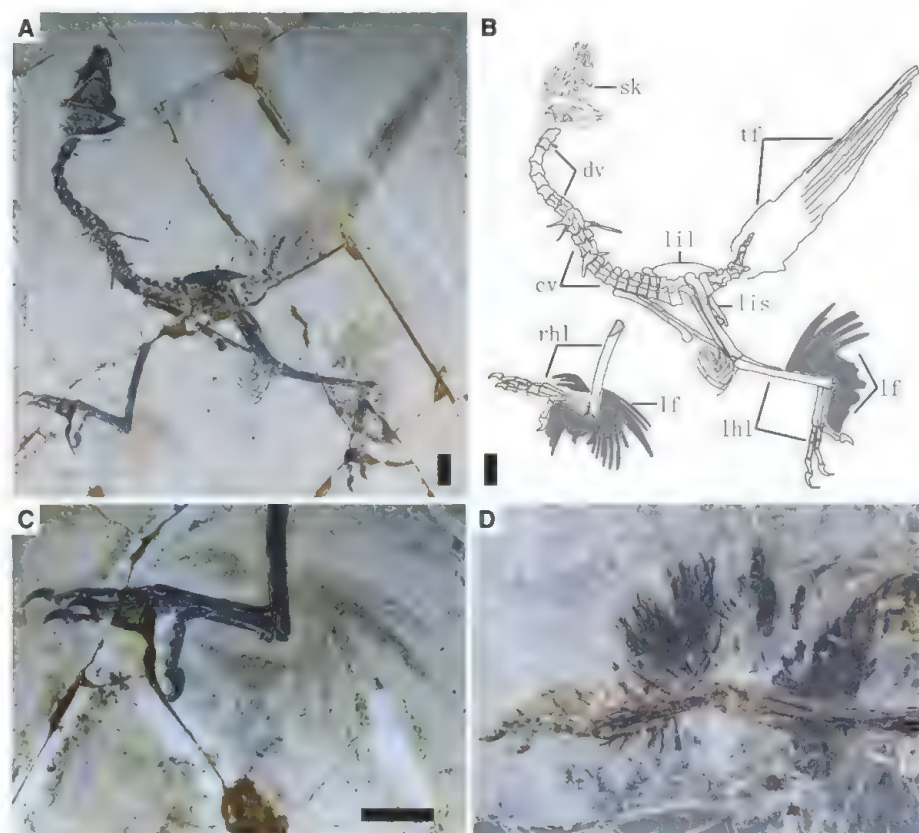


Fig. 1. Leg feathers in the basal avialan *Sapeornis*. Photograph (A) and drawing (B) of STM16-18; and close-up photographs of leg feathers of STM16-18 (C) and STM16-19 (D). Abbreviations: cv, cervical vertebrae; dv, dorsal vertebrae; lf, leg feathers; lhl, left hindlimb; lil, left ilium; lis, left ischium; rhl, right hindlimb; sk, skull; tf, tail feathers.

¹Institute of Geology and Paleontology, Linyi University, Shuangling Road, Linyi City, Shandong 276005, China. ²Shandong Tianyu Museum of Nature, Pingyi, Shandong 273300, China. ³Key Laboratory of Vertebrate Evolution and Human Origin of Chinese Academy of Sciences Institute of Vertebrate Paleontology and Paleoanthropology, Chinese Academy of Sciences, 142 Xiwai Street, Beijing 100044, China. ⁴Graduate University of the Chinese Academy of Sciences, 19 Yuquan Road, Beijing 100049, China.

*Corresponding author. E-mail: xingxu@vip.sina.com (X.X.); ty4291666@163.com (X.Z.)

STM9-5 (Fig. 3A), referable to *Yanornis* (12, 17, 18), is the first known basal ornithuromorph specimen in which both feathers and scales are well preserved on the legs. The femoral and crural feathers are short and plumulaceous (soft and downy), and the latter appear not to extend to the distal end of the tibiotarsus (Fig. 3, B and C). This is in stark contrast to the condition in other basal paravians, including basal deinonychosaurs (4), the basal avialan *Epidexipteryx*, *Sapeornis*, confuciusornithids, and enantiornithines (8, 19). In these taxa, the femoral and crural feathers are large, and in most cases they are pennaceous feathers that have curved rachises and extend nearly perpendicular to the limbs to form a planar surface.

However, STM9-5 differs from known specimens of the aforementioned taxa in having large scales that cover the anterior surfaces of the digits, including the fused metatarsals (Fig. 3, D and E). There appears to be a single row of large rectangular plates on the metatarsus, with a similar row extending along the phalangeal series of each of the three main digits. Each row of large plates is flanked by smaller scales. Tubercular skin, possibly representing interdigital telae (webs), is preserved between the pedal digits. However, this skin appears to be variable in extent: The putative web between digits III and IV extends close to the distal end of ungual III, whereas the one between digits II and III appears to extend only to the midpoint of digit III. The presence of webbing in this taxon will require confirmation on the basis of a better-preserved specimen.

The specimens described here collectively provide important new information about avialan hindlimb integumentary features, particularly in that they confirm the presence of a four-winged condition in basal birds. Large metatarsal feathers were first discovered in the basal dromaeosaurids *Microraptor* and *Sinornithosaurus* (1, 20–22), were subsequently reported in the enigmatic *Pedopenna* and the basal deinonychosaurs *Anchiornis* and *Xiaotingia* (2–4, 23), and can now also be definitively said to occur in the basal avialan *Sapeornis*. The morphology of the metatarsal feathers shows considerable variation among taxa known to possess these structures. In *Microraptor*, the metatarsal feathers are proportionally large with highly asymmetrical vanes (1), whereas in *Pedopenna*, *Anchiornis*, and *Sapeornis* they are proportionally smaller and have nearly symmetrical vanes (2, 3). In all cases, however, the metatarsal feathers are similar in general arrangement (nearly perpendicular to the metatarsus, forming a large flat surface) and in having stiff vanes and curved rachises. These features suggest that the metatarsal feathers were aerodynamic in function (12), providing lift, creating drag, and/or enhancing maneuverability, and thus played a role in flight (1–7, 24, 25). The presence of metatarsal feathers with a probable aerodynamic function in both deinonychosaurs and avialans strongly supports the interpretation that leg feathers were an important factor in the origin of avialan flight,

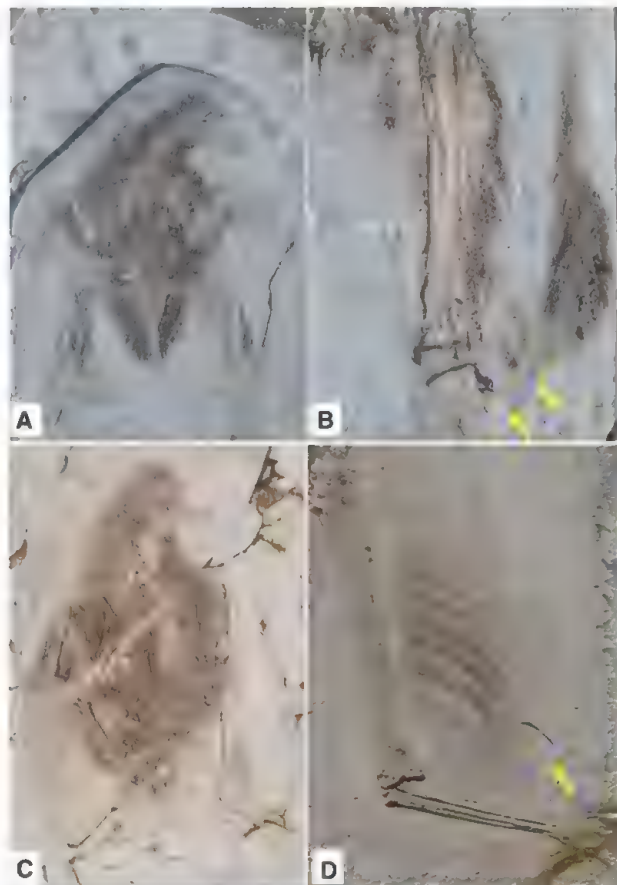
although the nature of their biomechanical contribution to flight ability in taxa that possessed them is debated (1–7, 24–26). It should be noted that preservational limitations make it difficult to reconstruct the precise location and orientation of the leg feathers in these basal paravians, including basal birds. Some limited evidence suggests that the large leg feathers of these taxa attach to the anterolateral margins of the hindlimb bones and are laterally directed (Fig. 4), but other possibilities exist (12).

Metatarsal feathers are also known in several other coelurosaurian dinosaurs, although in these cases they take the form of short filaments rather than large pennaceous feathers (27, 28). Short filamentous feathers have been reported to cover the metatarsus of the compsognathid *Sinocalliopteryx* (27), and similar feathers are also seen near the metatarsus of one specimen of the tyrannosauroid *Yutyrannus* (28). Metatarsal feathers are unknown in some other coelurosaurians that clearly bear femoral and crural feathers (8, 19), such as the therizinosauroid *Beipiaosaurus* (29), the oviraptorosaurians *Protarchaeopteryx* (30) and *Caudipteryx*, and enantiornithines. However, extensively scaled feet are unknown in any non-ornithuromorph coelurosaurian specimen, including the aforementioned taxa. Therefore, the lack in these taxa of known pedal feathers, including metatarsal ones, may be best regarded as a case of absence of evidence (perhaps resulting from the

vagaries of preservation) rather than evidence of absence. The point is underscored by the fact that the preservation of integumentary structures is typically inconsistent even within a given taxon. For example, of 273 confuciusornithid and 1065 enantiornithine specimens in the STM that preserve feathers on some part of the body, only 8 of the former and 143 of the latter preserve feathers on one or both hindlimbs. Consequently, the discovery of STM9-5, in combination with data from other recently reported coelurosaurian fossils (27, 28), implies that feathered feet might be primitive for the Coelurosauria, and extensively scaled feet might have appeared secondarily at an early stage of ornithuromorph evolution.

In almost all cases, the leg feathers of modern birds are less well developed than the arm feathers, and the difference is especially clear on the distal limb segments. The leg feathers of extant birds are generally small and fluffy, as in the basal ornithuromorph *Yanornis* (STM9-5), but differ considerably from the relatively large sheet-forming feathers seen in basal paravians, including such basal birds as sapeornithids, confuciusornithids, and enantiornithines (1–7, 24). Large contour feathers are present on the crural segment in some birds, especially predatory ones (31), but they are bunched and extend distally to lie at a low angle to the skin of the lower leg. A featherless pes is characteristic of most extant

Fig. 2. Leg feathers in the basal avialan *Confuciusornis* and the enantiornithine *Cathayornis*. (A) *Confuciusornis*, STM13-32. (B) Close-up of leg feathers of STM13-32. (C) *Cathayornis*, STM7-50. (D) Close-up of leg feathers of STM7-50. Yellow arrows indicate the distalmost preserved points on individual leg feathers.



birds, although some species (such as the golden eagle) have extensively developed fluffy pedal feathers (31). The probable function of leg feathers, including pedal feathers, in extant birds is to protect and/or insulate the leg (31, 32).

We incorporated information from the new specimens described in this paper into an analysis (12) that aimed to reconstruct the ancestral states of two key pedal integumentary characters for the major nodes across coelurosaurian phylogeny. The analysis was performed using Mesquite, a software package that offers a variety of functions for ancestral state reconstruction and other phylogeny-based analyses (33). Although the results are admittedly tentative because of the paucity of data available from the poorly known integuments of early birds and other extinct coelurosaurs, the analysis does suggest an interesting evolutionary pattern (Fig. 4). Short pedal filamentous feathers appeared early in the evolution of coelurosaurian dinosaurs (27), and the presence of extensively feathered feet is likely to be a diagnostic feature for Coelurosauria or a slightly more exclusive clade. Large femoral, crural, and pedal feathers are primitively present in the

Paraves. Large pedal feathers were lost early in avialan evolution, but large femoral and crural feathers persisted in derived non-ornithuromorph avialans and formed a reduced hind wing. Early in ornithuromorph evolution, extensively scaled feet appeared, and femoral and crural feathers became much smaller. The pedal scales of ornithuromorphs represent either a reversal to the pre-coelurosaurian primitive condition or novel structures that are not fully homologous to typical reptilian scales.

The evolution of leg feathers parallels that of arm feathers in basal paravians, which is not surprising given that forelimbs and hindlimbs share fundamental similarities both developmentally and morphologically (34). However, leg feathers were gradually reduced in a distal-to-proximal direction in avialan evolution, with eventual loss of the distal feathers and appearance of pedal scales in ornithuromorphs. The interpretation that the pedal scales of ornithuromorph birds are a secondarily derived feature is consistent with the fact that scale formation in extant birds requires inhibition of feather formation that would otherwise occur, and with developmental

evidence from the feathered feet of the scaleless (High-line) and Silkies strains of chicken (35). In the ontogenetic development of a modern bird, feathered feet can be changed into scaled feet or vice versa by changing the expression pattern of either one gene or a set of genes (36–38). A similar genetic change might have occurred early in avialan evolution.

Changes in the extent and morphology of the leg feathers were probably linked to the evolution of paravian locomotion in that the distribution and structure of leg feathers would have affected the aerodynamic properties of the limb (1, 4). Although early bird flight might initially have involved four wings, as strongly indicated by the basal avialan specimens STM16-18 and STM16-19, the locomotor system of ornithuromorph birds is characterized by a combination of flight using feathered arms and bipedal terrestrial locomotion using the legs. The reduction and loss of distal feathers on the legs reflect decoupling of the forelimbs from the hindlimbs in the locomotor system of ornithuromorph birds, in which the arms became specialized for flight and the legs for terrestrial locomotion (39).

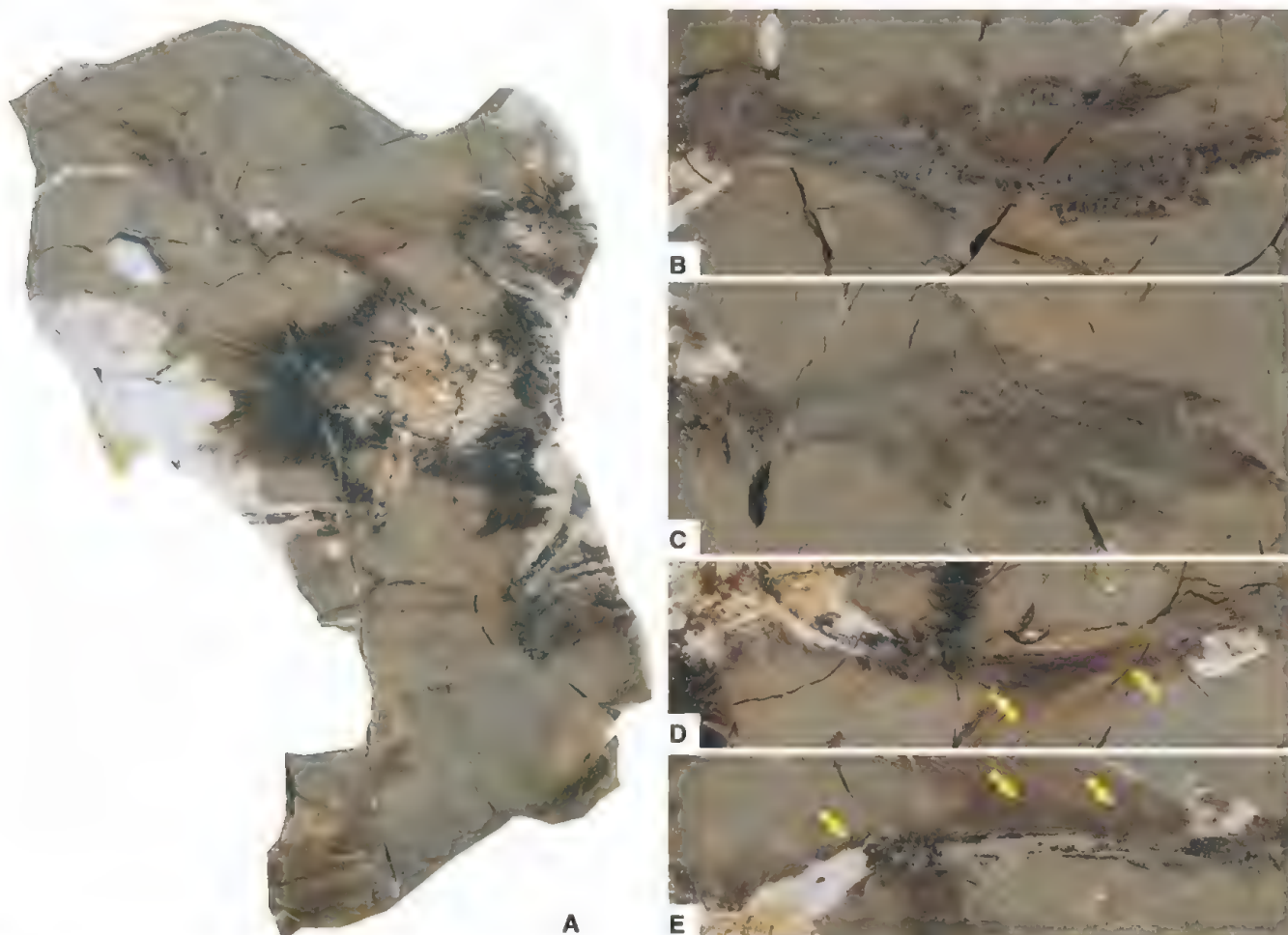
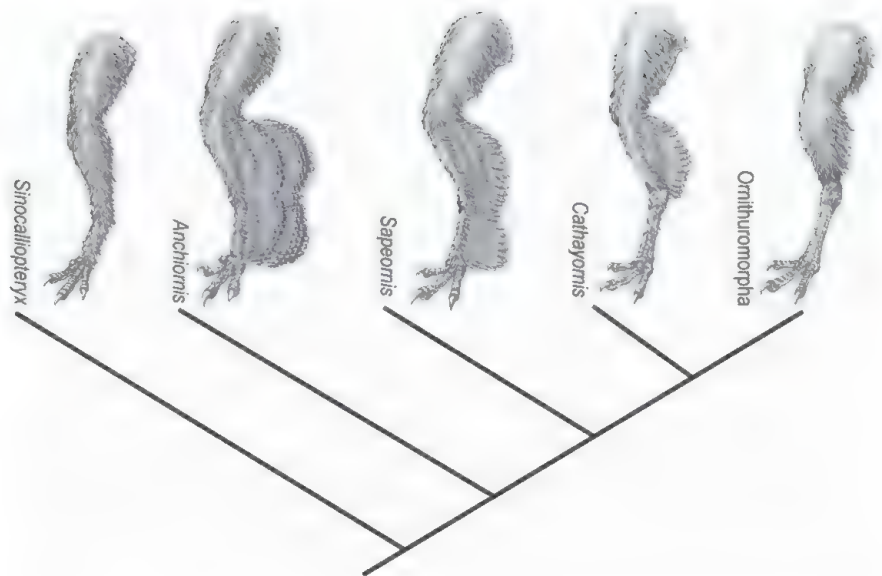


Fig. 3. Integumentary features of the hindlimb in the basal ornithuromorph *Yanornis*. (A) Photograph of STM9-5. Pedal integument of STM9-5 as seen in the slab (B) and counter slab (C). Femoral and crural feathers of STM9-5 as seen in the slab (D) and counter slab (E). Yellow arrows indicate the distalmost preserved points on individual leg feathers.

Fig. 4. Evolution of leg feathers in coelurosaurian dinosaurs. Four major stages in the evolution of integumentary structures on the hindlimb are represented by the compsognathid *Sinocalliopteryx* (short filamentous feathers covering legs, including feet); the basal deinonychosaurian *Anchiornis* and the basal avialan *Sapeornis* (large pennaceous feathers on legs, including feet, forming a winglike structure); the enantiornithine *Cathayornis* (large femoral and crural feathers forming a reduced winglike structure); and ornithuromorphs (small femoral and crural feathers and featherless feet).



References and Notes

- X. Xu *et al.*, *Nature* **421**, 335 (2003).
- X. Xu, F.-C. Zhang, *Naturwissenschaften* **92**, 173 (2005).
- D. Y. Hu, L.-H. Hou, L. J. Zhang, X. Xu, *Nature* **461**, 640 (2009).
- X. Xu, H. You, K. Du, F. Han, *Nature* **475**, 465 (2011).
- D. E. Alexander, E. Gong, L. D. Martin, D. A. Burnham, A. R. Falk, *Proc. Natl. Acad. Sci. U.S.A.* **107**, 2972 (2010).
- S. Chatterjee, R. J. Templin, *Proc. Natl. Acad. Sci. U.S.A.* **104**, 1576 (2007).
- R. O. Prum, *Nature* **421**, 323 (2003).
- F. C. Zhang, Z. H. Zhou, *Nature* **431**, 925 (2004).
- N. R. Longrich, *Paleobiology* **32**, 417 (2006).
- K. Padian, *Bioscience* **53**, 451 (2003).
- K. Padian, K. P. Dial, *Nature* **438**, E3, discussion E3 (2005).
- See the supplementary materials on Science Online.
- Z. Zhou, P. M. Barrett, J. Hilton, *Nature* **421**, 807 (2003).
- Z. H. Zhou, F. C. Zhang, *Can. J. Earth Sci.* **40**, 731 (2003).
- L. H. Hou, C. M. Chuong, A. Yang, X. L. Zeng, J. F. Hou, *Fossil Birds of China* (Yunnan Science and Technology Press, Kunming, China, 2003).
- L. M. Chiappe, S.-A. Ji, Q. Ji, M. A. Norell, *Bull. Am. Mus. Nat. Hist.* **242**, 1 (1999).
- Z. Zhou, F. C. Zhang, *Proc. Natl. Acad. Sci. U.S.A.* **102**, 18998 (2005).
- H. L. You *et al.*, *Science* **312**, 1640 (2006).
- F. C. Zhang, Z. H. Zhou, *Nature* **438**, E4 (2005).
- X. Xu, *Deinonychosaurian Fossils from the Jehol Group of Western Liaoning and the Coelurosaurian Evolution* (Chinese Academy of Sciences, Beijing, China, 2002).
- M. Norell *et al.*, *Nature* **416**, 36 (2002).
- Q. Ji, M. A. Norell, K.-Q. Gao, S.-A. Ji, D. Ren, *Nature* **410**, 1084 (2001).
- X. Xu *et al.*, *Chin. Sci. Bull.* **54**, 430 (2009).
- M. A. R. Koehl, D. Evangelista, K. Yang, *Integr. Comp. Biol.* **56**, 1002 (2011).
- J. Hall, H. J. Habib, M. Hone, L. Chiappe, *J. Vertebr. Paleontol.* **32**, 105B (2012).
- C. W. Beebe, *Zool. Sci. Contrib. N.Y. Zool. Soc.* **2**, 39 (1915).
- S. A. Ji, Q. Ji, J. C. Lu, C. X. Yuan, *Acta Geol. Sin.* **81**, 8 (2007).
- X. Xu *et al.*, *Nature* **484**, 92 (2012).
- X. Xu, Z.-L. Tang, X.-L. Wang, *Nature* **399**, 350 (1999).
- Q. Ji, P. J. Currie, M. A. Norell, S.-A. Ji, *Nature* **393**, 753 (1998).
- A. M. Lucas, P. R. Stettenheim, *Avian Anatomy: Integument* (U.S. Department of Agriculture, Washington, DC, 1972).
- L. Kelso, E. H. Kelso, *Auk* **53**, 51 (1936).
- W. P. Maddison, D. R. Maddison (2011), <http://mesquiteproject.org>.
- M. Logan, *Development* **130**, 6401 (2003).
- R. H. Sawyer, L. W. Knapp, *J. Exp. Zool.* **298B**, 57 (2003).

- M. P. Harris, B. L. Linkhart, J. F. Fallon, *Dev. Dyn.* **231**, 22 (2004).
- R. B. Wideltz, T.-X. Jiang, J.-F. Lu, C. M. Chuong, *Dev. Biol.* **219**, 98 (2000).
- F. Prin, D. Dhoulailly, *Int. J. Dev. Biol.* **48**, 137 (2004).
- S. M. Gatesy, K. P. Dial, *Evolution* **50**, 331 (1996).

Acknowledgments: Support for this research was provided by the National Natural Sciences Foundation of China (NNSFC grant nos. 41172016, 41120124002, and 41125008), the National Basic Research Program of China (grant no. 2012CB821900), and the Chinese Academy of Sciences (grant no. KZCX2-EW-105). We thank K. Padian and C. Sullivan for critical comments; C.-M. Chuong and T. Stidham for discussions;

R. Li and H. Zang for illustrations; X. Ding for preparation of some of the specimens; and O. Rauhut, M. Koehl-Ebert, and M. Roeper for access to *Archaeopteryx* specimens.

Supplementary Materials

www.sciencemag.org/cgi/content/full/339/6125/1309/DC1

Supplementary Text

Figs. S1 to S10

Tables S1 to S3

References (40–60)

13 August 2012; accepted 20 December 2012

10.1126/science.1228753

Adaptive Evolution of Multiple Traits Through Multiple Mutations at a Single Gene

Catherine R. Linnen,^{1*} Yu-Ping Poh,^{2,4,6} Brant K. Peterson,^{2,3} Rowan D. H. Barrett,² Joanna G. Larson,² Jeffrey D. Jensen,^{5,6} Hopi E. Hoekstra^{2,3*}

The identification of precise mutations is required for a complete understanding of the underlying molecular and evolutionary mechanisms driving adaptive phenotypic change. Using plasticine models in the field, we show that the light coat color of deer mice that recently colonized the light-colored soil of the Nebraska Sand Hills provides a strong selective advantage against visually hunting predators. Color variation in an admixed population suggests that this light Sand Hills phenotype is composed of multiple traits. We identified distinct regions within the *Agouti* locus associated with each color trait and found that only haplotypes associated with light trait values have evidence of selection. Thus, local adaptation is the result of independent selection on many mutations within a single locus, each with a specific effect on an adaptive phenotype, thereby minimizing pleiotropic consequences.

Darwin believed that adaptation occurred through “slight successive variations” (1). Fisher later elaborated on this idea by proposing the geometric model of adaptation (2), which assumes that most mutations are pleiotropic and therefore that mutations of small phenotypic effect are more likely than those of large effect to bring a population closer to its fitness optimum. To test

Fisher’s model, we must identify individual mutations and assess both their phenotypic effects and their degree of pleiotropy. Although recent years have seen considerable progress in identifying loci or genes underlying adaptive phenotypes [reviewed in (3, 4)], few have genetically dissected these loci to the level of individual mutations [but see (5–8)], and none have examined multiple traits at this level

of resolution. Thus, it remains unclear whether genes that contribute to complex phenotypes (i.e., those composed of multiple traits) tend to do so through single pleiotropic mutations or multiple mutations with independent effects.

Deer mice (*Peromyscus maniculatus*) living on the light-colored soils of the Nebraska Sand Hills, a massive dune field formed only 8000 to 15,000 years ago (9), are lighter than conspecifics living on the surrounding dark soils (10, 11) (Fig. 1, A and B). To test the hypothesis that this light pelage is an adaptation for crypsis, we measured attack rates on light and dark plasticine mouse models (Fig. 1C) at multiple Sand Hills sites [following (12); also see (13)]. We found that conspicuous, dark models were attacked significantly more often than cryptic, light models ($P < 0.05$) (Fig. 1D). Together with previous experiments using avian predators and live mice (14), these results strongly suggest that the overall light color of Sand Hills mice is a recent adaptation driven, at least in part, by visually hunting predators.

The light dorsal fur of Sand Hills mice is largely caused by a change at the *Agouti* locus. Specifically, a derived cis-acting increase in the duration and magnitude of *Agouti* expression during hair growth leads to a concomitant increase in the width of light pigmented bands on individual hairs (11). However, upon closer inspection of phenotypic variation, we found that Sand Hills and wild-type mice differ in multiple pigmentation traits that together give rise to the overall cryptic appearance of the Sand Hills mice (Fig. 2A). In addition to having a significantly lighter dorsum (one-tailed t test; $N = 10$ lab-reared mice; $P = 8.2 \times 10^{-4}$), Sand Hills mice also have a lighter ventrum, an upward shift in the dorsal-ventral (d-v) boundary, and a less pronounced tail stripe compared with the ancestral form (one-tailed t tests; $N = 10$ mice; ventral color: $P = 3.9 \times 10^{-5}$; d-v boundary: $P = 1.4 \times 10^{-4}$; tail stripe: $P = 5.5 \times 10^{-7}$). Because these derived light-color traits are all associated with *Agouti* in laboratory strains, they could be explained by either a single pleiotropic mutation of large effect or multiple mutations of smaller, more modular effect in this locus.

To distinguish between these alternatives, we collected phenotypic (color and color pattern) and genotypic data from 91 wild-caught mice from a phenotypically diverse population located near the edge of the Sand Hills. We measured three color traits derived from a principal com-

ponent analysis (PCA) of spectrophotometric data (dorsal hue, dorsal brightness, and ventral color) (table S1) and two color pattern traits (d-v boundary and tail stripe). Phenotypes in this wild population were largely independent (R^2 range: 0.04 to 0.27) (table S2). In fact, several trait pairs lacked a significant correlation in spite of a large sample size (e.g., dorsal hue and d-v boundary, $P = 0.69$, $N = 91$ mice). These data suggest that these pigment traits are likely under independent genetic control.

To dissect the molecular basis of these traits, we combined a targeted enrichment strategy with next-generation sequencing [following (15)] to generate polymorphism data for ~2100 unlinked regions averaging 1.5 thousand base pairs (kbp) in length and a 185-kbp region containing *Agouti* and all known regulatory elements (Fig. 2B) (16).

Using a genetic PCA on genome-wide polymorphism data (13), we identified four significant genetic principal components, none of which were associated with color (table S3). These data indicate that light and dark mice interbreed freely, and genetic structure is not associated with color variation in this population. Next, we examined linkage disequilibrium (LD) across *Agouti* (fig. S1) and found that the 95th percentile of r^2 falls below 0.4 within 3 kbp (fig. S2). The extremely low level of LD is considerably less than reported for wild populations of *Mus musculus* (17); however, this is not surprising given the large effective population size we estimated for *P. maniculatus* ($N_e > 50,000$ mice) (13). Together, these data suggest that there has been sufficient recombination for fine-scale mapping color traits within *Agouti*.



Fig. 1. Selective advantage of crypsis against predation. (A) Typical habitat in the Sand Hills (left) and the adjacent region (right). Insets show representative substrate from each habitat. (B) Typical mouse color phenotypes from on (left) and off (right) the Sand Hills, shown on light Sand Hills substrate. (C) Typical cryptic (left) and conspicuous (right) models, shown on Sand Hills substrate. (D) Proportion of predation events occurring over 2700 model nights in the Sand Hills habitat. Conspicuous models were attacked significantly more often than cryptic models (selection index = 0.545, $\chi^2 = 6.546$, $df = 1$, $P = 0.011$).

¹Department of Biology, University of Kentucky, 200A Thomas Hunt Morgan Building, Lexington, KY 40506, USA. ²Department of Organismic and Evolutionary Biology, the Museum of Comparative Zoology, Harvard University, 26 Oxford Street, Cambridge, MA 02138, USA. ³Department of Molecular and Cellular Biology, Harvard University, 26 Oxford Street, Cambridge, MA 02138, USA. ⁴Program in Bioinformatics and Integrative Biology, University of Massachusetts Medical School, Worcester, MA, USA. ⁵School of Life Science, Ecole Polytechnique Fédérale de Lausanne (EPFL), Lausanne, Switzerland. ⁶Swiss Institute of Bioinformatics (SIB), Lausanne, Switzerland.

*To whom correspondence should be addressed. E-mail: catherine.linnen@uky.edu (C.R.L.); hoekstra@oeb.harvard.edu (H.E.H.)

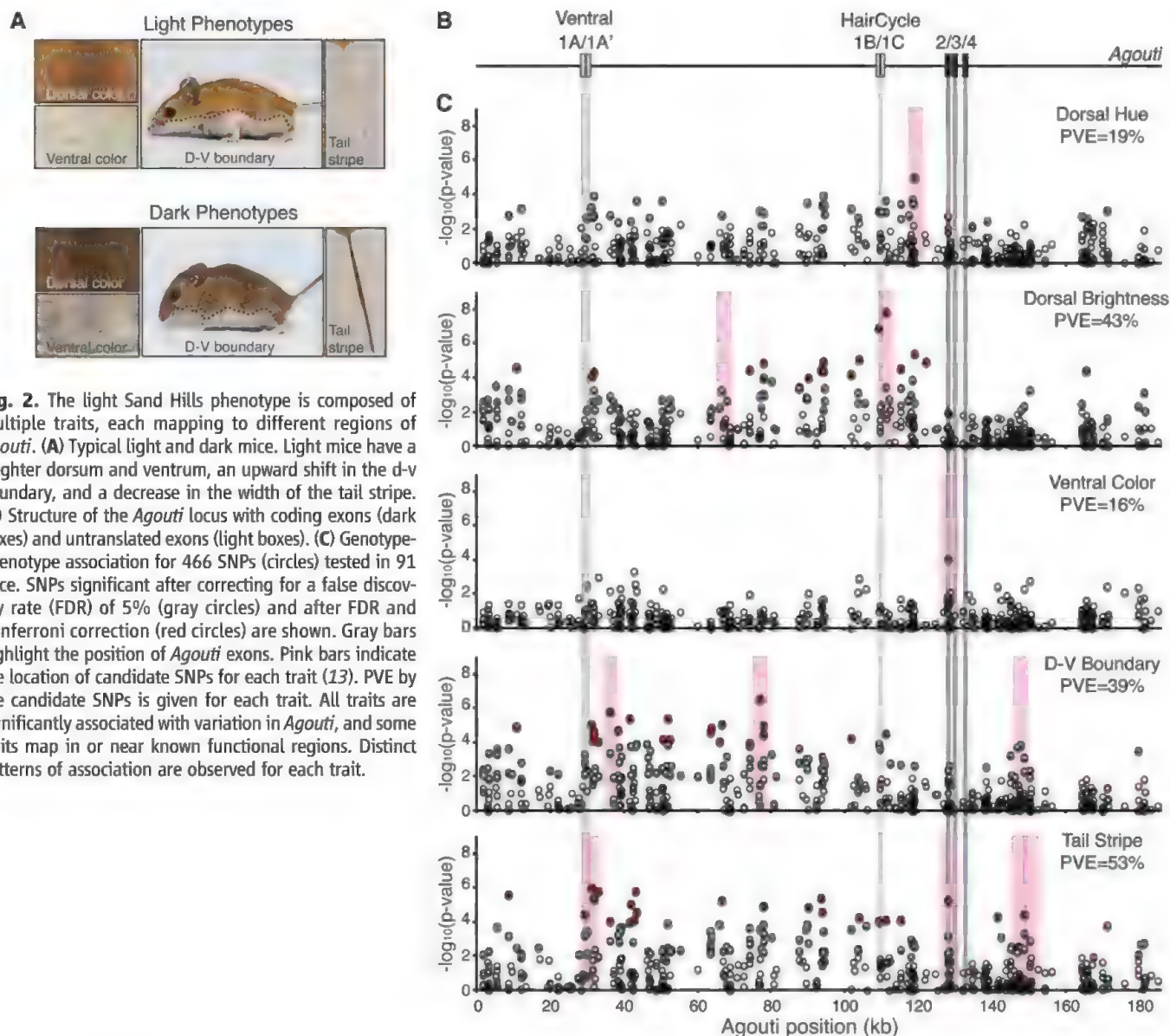


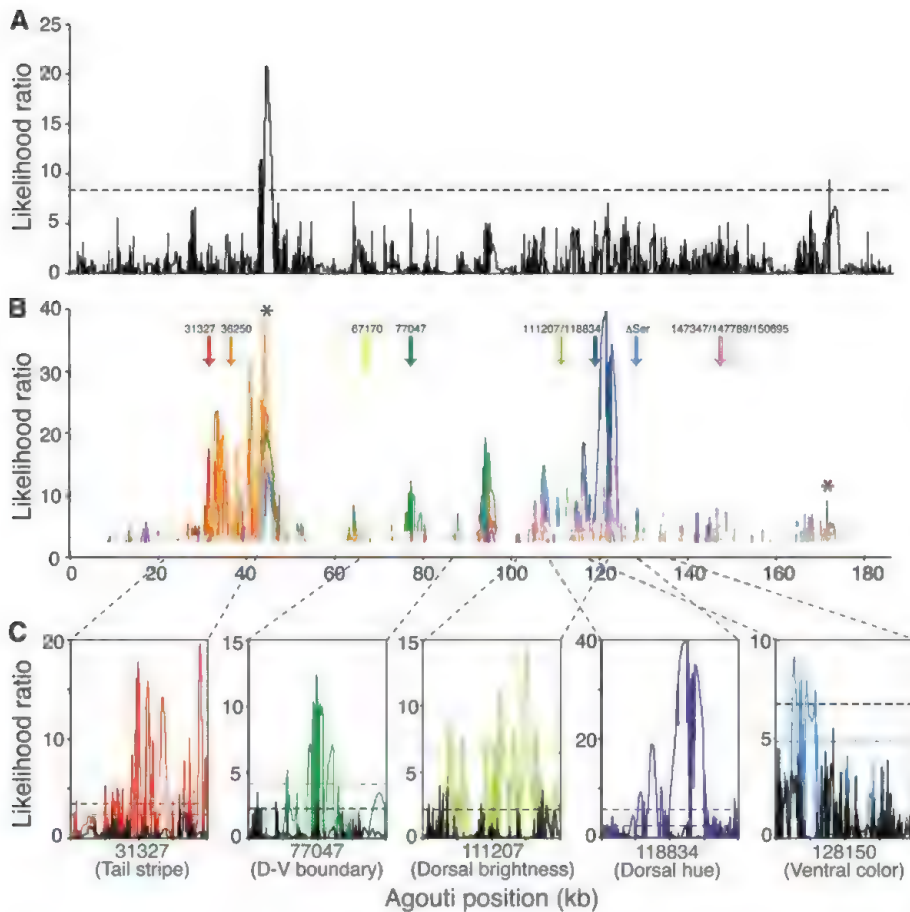
Fig. 2. The light Sand Hills phenotype is composed of multiple traits, each mapping to different regions of *Agouti*. **(A)** Typical light and dark mice. Light mice have a brighter dorsum and ventrum, an upward shift in the d-v boundary, and a decrease in the width of the tail stripe. **(B)** Structure of the *Agouti* locus with coding exons (dark boxes) and untranslated exons (light boxes). **(C)** Genotype-phenotype association for 466 SNPs (circles) tested in 91 mice. SNPs significant after correcting for a false discovery rate (FDR) of 5% (gray circles) and after FDR and Bonferroni correction (red circles) are shown. Gray bars highlight the position of *Agouti* exons. Pink bars indicate the location of candidate SNPs for each trait (13). PVE by the candidate SNPs is given for each trait. All traits are significantly associated with variation in *Agouti*, and some traits map in or near known functional regions. Distinct patterns of association are observed for each trait.

To identify associations between these *Agouti* genotypes and color phenotypes, we used both single-SNP (single-nucleotide polymorphism) linear regressions and a multiple-SNP Bayesian approach (13, 18). Based on these analyses, we found each of the five color traits was statistically associated with a unique set of SNPs that together explained 16 to 53% of the variation (Fig. 2C and fig. S3). There was one exception: a serine deletion (Δ Ser) in exon 2 was associated with both ventral color ($P = 8.5 \times 10^{-5}$) and tail stripe ($P = 5.4 \times 10^{-6}$). Notably, no single set of polymorphisms could account for variation across all five traits (table S4). These findings demonstrate that there are multiple mutations that contribute to different aspects of the light Sand Hills phenotype.

Additionally, several traits were associated with SNPs that fell in or near regions of known functional importance. Two *Agouti* isoforms under the

control of different promoters have been identified: The ventral isoform containing noncoding exons 1A/1A' is restricted to the ventral dermis and is required to establish the dorsal-ventral boundary during embryogenesis, and the hair-cycle-specific isoform containing noncoding exons 1B/1C is expressed in adults during hair growth and leads to the formation of light, pheomelanin bands on individual hairs (19, 20) (Fig. 2B). In our data, the d-v boundary and tail stripe traits mapped near the ventral promoter; dorsal brightness mapped near the hair-cycle promoter; and ventral color and tail stripe mapped to a deletion (Δ Ser) in exon 2, which is a conserved residue located in a protein domain that interacts with another pigment protein Attractin (21) (Fig. 2C, fig. S3, and table S5). These results suggest that multiple molecular mechanisms—including both protein-coding and cis-regulatory changes—are involved in color adaptation in these Sand Hills mice.

Having identified multiple regions contributing to coat-color lightness, we tested for positive selection on *Agouti* and these specific polymorphisms. We used *dadi* (22) to estimate a demographic model and parameters for our ecotonal population. We found evidence suggesting that the population experienced a recent (~2900 years ago) bottleneck, in which the population was reduced to 0.4% of its original size, followed by an exponential recovery to ~65% of its original size. Using this demographic model and the Sweepfinder framework (23), we evaluated patterns of selection in both the entire data set (i.e., all sampled individuals) and 10 polarized data sets (i.e., in which light and dark haplotypes are defined by the genotype at the candidate SNP of interest), following (11, 13, 24). We identified two regions with evidence of selection acting on all mice collected from this location, independent of coat color (Fig. 3A). By comparison, in polarized data



thresholds (black, dark only; colored, light only). (D) Strength of selection (s) is significantly correlated with PVE ($R^2 = 0.56$; Spearman's $\rho = 0.76$; $P = 0.0071$). Color of each SNP as in (B).

Table 1. Selection on candidate regions identified using association mapping. PVE (R^2) after controlling for population structure is given for each polymorphism. Asterisk denotes the Δ Ser in exon 2 that was associated with more than one trait. These SNPs were then used to classify haplotypes as "light" or "dark" depending on observed phenotype-genotype correlations; selection analyses were performed separately on light and dark haplotypes. The distance (in base pairs) to the nearest site with a significant LR and the number of significant sites within a 20-kbp window surrounding the polarizing site are given for both light and dark alleles. Selection coefficients [s ; assuming $N_e = 53,080$ mice (13)] and average $2Ns$ are also provided. Selection coefficients vary among traits; within each trait, SNPs with higher PVE have higher s .

Candidate	Trait	PVE	Light allele				Dark allele			
			Distance	No. of sites	$2Ns$	s	Distance	No. of sites	$2Ns$	s
118834	Dorsal hue	18.8	2393	2769	32,038	0.302	2607	207	2348	0.022
67170	Dorsal brightness	8.9	641	91	3926	0.037	2935	170	3977	0.038
111207	Dorsal brightness	28.7	881	588	15,296	0.144	1532	161	3047	0.029
Δ Ser*	Ventral color	16	4084	802	13,366	0.126	41831	0	3121	0.029
36250	d-v boundary	22.4	7	5476	44,598	0.420	2880	1237	7122	0.067
77047	d-v boundary	21.7	0	1446	20,855	0.197	76	102	4959	0.047
147789	d-v boundary	13.3	2657	26	1921	0.018	741	369	2262	0.021
31327	Tail stripe	25	0	2986	30,324	0.286	3898	155	3992	0.038
Δ Ser*	Tail stripe	21.3	4084	802	13,366	0.126	41,831	0	3121	0.029
147347	Tail stripe	4.7	733	1360	3447	0.033	24	176	1254	0.012
150695	Tail stripe	8	318	803	6730	0.063	1980	244	2399	0.023

sets, we found significant likelihood peaks clustered around the location of the polarizing SNPs (Fig. 3B and Table 1), consistent with recent selec-

tion acting on, or near, color-associated SNPs. Using one-tailed Wilcoxon signed-rank tests for our 10 candidate SNPs, we found that, compared with

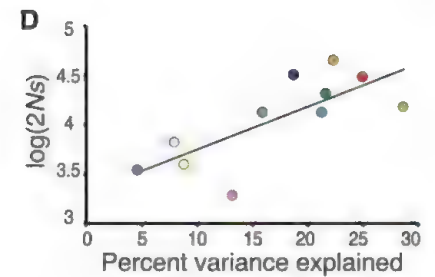


Fig. 3. Evidence of selection on light *Agouti* alleles. (A) Likelihood surface for all haplotypes with significance threshold [dotted line; determined by simulation (13)]. (B) Likelihood surface for only light haplotypes. Arrows indicate the positions of 10 candidate polymorphisms identified by association mapping (Fig. 2), and likelihood surfaces are colored according to the haplotypes determined by the corresponding polymorphism (e.g., the red LR trace was estimated using only those chromosomes carrying the light allele at position 31327). Significance thresholds were determined separately for each data set, and only LRs that are above these thresholds are shown. Asterisks give the location of peaks identified using all haplotypes (A). (C) Twenty-kbp windows (13) centered on the most strongly associated polymorphism for each trait (31327, tail stripe; 77047, dorsal-ventral boundary; 111207, dorsal brightness; 118834, dorsal hue; 128150 (Δ Ser), tail stripe and ventral color). Likelihood surface for dark haplotypes only (solid black line) compared with those for light haplotypes only (solid colored lines). Dotted lines are significance

thresholds (black, dark only; colored, light only). (D) Strength of selection (s) is significantly correlated with PVE ($R^2 = 0.56$; Spearman's $\rho = 0.76$; $P = 0.0071$). Color of each SNP as in (B).

the dark-associated alleles (Fig. 3C and Table 1), light-associated alleles have a significantly better correspondence between the location of the polarizing SNP and the nearest significant likelihood-ratio (LR) peak ($P = 0.037$), a significantly greater number of sites surrounding the polarizing SNP that reject neutrality ($P = 0.0063$), and a significantly higher selection coefficient ($P = 0.0063$). Also, these differences are robust to choice of window size (tables S6 and S7). These observations are consistent with multiple targets of selection among the light, but not dark, alleles of *Agouti*. We next estimated the strength of selection acting on these light-associated SNPs, using a maximum likelihood approach implemented in Sweepfinder (13, 23). Selection coefficients (s) ranged from 0.018 to 0.42 (Table 1), suggesting very strong selection in some cases. Selection strength varied as a function of both color trait and phenotypic effect size: We observed especially strong selection on SNPs associated with dorsal hue, dorsal-ventral boundary, and tail stripe (Table 1) and a positive correlation between the percent variation explained (PVE) and s across all light-associated SNPs (Spearman's Rank correlation = 0.76, $P = 0.0071$, one-tailed) (Fig. 3D). Moreover, within each trait, we see a perfect rank correlation between PVE and s (e.g., for tail stripe

associated SNPs Spearman's $\rho = 1$, $P = 0$, $N = 4$ SNPs). Thus, for each candidate SNP, the stronger its effect on color phenotype, the stronger the estimate of selection strength, suggesting that these mutations likely have minimal pleiotropic consequences. These results, when combined with results from the clay model experiment, the extensive recombination across this region, and the association mapping study, all support a scenario in which multiple independent *Agouti* mutations—each contributing to a distinct trait associated with the light phenotype—have been selected for cryptic coloration on the Sand Hills.

Although it has been suggested that pigmentation is an unusually simple trait (25), when deconstructed, we find both phenotypic and genetic complexity. The light pigmentation of the Sand Hills mice is composed of several genetically independent traits, and we find that mutations associated with each show clear signatures of selection. These results imply that each color trait, from dorsal color to tail stripe, independently affects fitness. We also demonstrate how a large-effect locus can fractionate into many small- to moderate-effect mutations. Moreover, although the gene *Agouti* has widespread effects on pigmentation, measurable pleiotropic effects are largely absent at the mutational level, serving as a reminder that, although it is commonplace to discuss the degree of pleiotropy of individual genes, it is individual mutations, not genes, that bring a population closer to its phenotypic optimum. Together, our results suggest that small, minimally pleiotropic mutations—even those occurring with-

in a single gene—may provide a rapid route to adaptation along multiple phenotypic axes.

References and Notes

1. C. Darwin, *On the Origin of Species by Means of Natural Selection, or the Preservation of Favoured Races in the Struggle for Life* (John Murray, London, 1859).
2. R. A. Fisher, *The Genetical Theory of Natural Selection* (Oxford Univ. Press, Oxford, 1930).
3. N. J. Nadeau, C. D. Jiggins, *Trends Genet.* **26**, 484 (2010).
4. J. Stapley *et al.*, *Trends Ecol. Evol.* **25**, 705 (2010).
5. H. E. Hoekstra, R. J. Hirschmann, R. A. Bunday, P. A. Insel, J. P. Crossland, *Science* **313**, 101 (2006).
6. M. Rebeiz, J. E. Pool, V. A. Kassner, C. F. Aquadro, S. B. Carroll, *Science* **326**, 1663 (2009).
7. N. Frankel *et al.*, *Nature* **474**, 598 (2011).
8. K. V. S. K. Prasad *et al.*, *Science* **337**, 1081 (2012).
9. D. B. Loope, J. Swinehart, *Great Plains Res.* **10**, 5 (2000).
10. L. R. Dice, *Contrib. Lab. Vertebr. Genet. Univ. Mich.* **15**, 1 (1941).
11. C. R. Linnen, E. P. Kingsley, J. D. Jensen, H. E. Hoekstra, *Science* **325**, 1095 (2009).
12. S. N. Vignieri, J. G. Larson, H. E. Hoekstra, *Evolution* **64**, 2153 (2010).
13. Materials and methods are available as supplementary materials on Science online.
14. L. R. Dice, *Contrib. Lab. Vertebr. Biol. Univ. Mich.* **34**, 1 (1947).
15. V. S. Domingues *et al.*, *Evolution* **66**, 3209 (2012).
16. E. P. Kingsley, M. Manceau, C. D. Wiley, H. E. Hoekstra, *PLoS ONE* **4**, e6435 (2009).
17. C. C. Laurie *et al.*, *PLoS Genet.* **3**, e144 (2007).
18. Y. Guan, M. Stephens, *Ann. Appl. Stat.* **5**, 1780 (2011).
19. S. J. Bultman *et al.*, *Genes Dev.* **8**, 481 (1994).
20. H. Vrieling, D. M. J. Duhl, S. E. Millar, K. A. Miller, G. S. Barsh, *Proc. Natl. Acad. Sci. U.S.A.* **91**, 5667 (1994).
21. P. J. Jackson *et al.*, *Chem. Biol.* **13**, 1297 (2006).
22. R. N. Gutenkunst, R. D. Hernandez, S. H. Williamson, C. D. Bustamante, *PLoS Genet.* **5**, e1000695 (2009).
23. R. Nielsen *et al.*, *Genome Res.* **15**, 1566 (2005).

24. C. D. Meiklejohn, Y. Kim, D. L. Hartl, J. Parsch, *Genetics* **168**, 265 (2004).
25. M. V. Rockman, *Evolution* **66**, 1 (2012).

Acknowledgments: We thank K. Duryea and G. Goncalves for laboratory assistance; J. Chupasko, E. Kay, E. Kingsley, M. Manceau, and J. Weber for field assistance; J. Demboski and the Denver Museum of Nature and Science for logistical support; and J. Chupasko for curation assistance. C.R.L. was supported by a Ruth Kirschstein National Research Service Award from NIH; B.K.P. by a Jane Coffins Child Postdoctoral Fellowship; J.D.J. and Y.-P.P. by grants from the Swiss National Science Foundation, the European Research Council, and Defense Advanced Research Projects Agency; R.D.H.B. by a Natural Sciences and Engineering Research Council of Canada Banting Postdoctoral Fellowship and a Foundational Questions in Evolutionary Biology Postdoctoral Fellowship. Laboratory and fieldwork was funded by Putnam Expedition Grants from the MCZ Museum of Comparative Zoology (MCZ), the Swiss National Science Foundation, Harvard University, and the National Science Foundation (DEB-0749958 to H.E.H.). *P. maniculatus* were collected under the Nebraska Game and Parks Commission Scientific and Educational Permit 901, and voucher specimens were deposited in the MCZ's Mammal Department. Sequence data were deposited in the NCBI Short Read Archive (accession no. SRP017939). **Author contributions:** C.R.L., J.D.J., and H.E.H. designed the project; C.R.L. conducted field work; B.K.P. designed capture array and short-read analysis pipeline; C.R.L. and B.K.P. collected genomic data; C.R.L. and J.G.L. collected phenotypic data; C.R.L., Y.-P.P., and B.K.P. analyzed the data; R.D.H.B. and C.R.L. conducted the plasticine model experiment; and C.R.L. and H.E.H. wrote the paper with input from the other authors.

Supplementary Materials

www.sciencemag.org/cgi/content/full/339/6125/1312/DC1
Materials and Methods
Figs. S1 to S3
Tables S1 to S9
References (26–47)

27 November 2012; accepted 4 February 2013
10.1126/science.1233213

Circadian Control of Chloroplast Transcription by a Nuclear-Encoded Timing Signal

Zeenat B. Noordally,¹ Kenyu Ishii,² Kelly A. Atkins,³ Sarah J. Wetherill,³
Jelena Kusakina,⁴ Eleanor J. Walton,³ Maiko Kato,² Miyuki Azuma,⁵ Kan Tanaka,⁶
Mitsumasa Hanaoka,² Antony N. Dodd^{4*}

Circadian timekeeping in plants increases photosynthesis and productivity. There are circadian oscillations in the abundance of many chloroplast-encoded transcripts, but it is not known how the circadian clock regulates chloroplast transcription or the photosynthetic apparatus. We show that, in *Arabidopsis*, nuclear-encoded SIGMA FACTOR5 (SIG5) controls circadian rhythms of transcription of several chloroplast genes, revealing one pathway by which the nuclear-encoded circadian oscillator controls rhythms of chloroplast gene expression. We also show that SIG5 mediates the circadian gating of light input to a chloroplast-encoded gene. We have identified an evolutionarily conserved mechanism that communicates circadian timing information between organelles with distinct genetic systems and have established a new level of integration between eukaryotic circadian clocks and organelles of endosymbiotic origin.

Circadian clocks coordinate biological systems with the Earth's day-night cycles. Because circadian regulation increases photosynthesis and productivity (1), we wished to understand how the circadian clock controls the timing of events within chloroplasts. Chloroplasts contain small cyanobacteria-derived genomes

that encode essential components of the photosynthetic apparatus. Interrogation of four circadian transcript profiles from *Arabidopsis thaliana* indicates that 62 (70%) of the 88 protein-coding genes encoded by the chloroplast genome can be circadian regulated (spreadsheet S1) (2). Chloroplast genes are transcribed by either nuclear-encoded

plastid RNA polymerase (NEP) or plastid-encoded plastid RNA polymerase (PEP). PEP comprises five core plastid-encoded subunits and requires one of several nuclear-encoded sigma factors of prokaryotic ancestry to confer promoter specificity to PEP (3). The *Arabidopsis* genome encodes six sigma factors (3), and all sigma factors can be circadian regulated, depending on experimental conditions (spreadsheet S1). In *Arabidopsis*, some sigma factors are required for gene expression during chloroplast biogenesis [e.g., SIGMA FACTOR2 (SIG2) and SIG6], and others adjust the photosynthetic apparatus during steady-state photosynthesis (e.g., SIG1 and SIG5) (4–7). We hypothesized that sigma factors might communicate circadian timing information from the nucleus to chloroplasts, if there are oscillations in

¹SynthSys, University of Edinburgh, C H Waddington Building, Mayfield Road, Edinburgh EH9 3JD, UK. ²Graduate School of Horticulture, Chiba University, 648 Matsudo, Matsudo, Chiba 271-8510, Japan. ³Department of Biology, University of York, York YO10 5DD, UK. ⁴School of Biological Sciences, University of Bristol, Bristol BS8 1UG, UK. ⁵Institute of Molecular and Cellular Biosciences, The University of Tokyo, 1-1-1 Yayoi, Bunkyo-ku, Tokyo 113-0032, Japan. ⁶Chemical Resources Laboratory, Tokyo Institute of Technology, 4259 Nagatsuta, Midori-ku, Yokohama 226-8503, Japan.

*To whom correspondence should be addressed. E-mail: antony.dodd@bristol.ac.uk

the abundance of transcripts encoding both the sigma factor and its chloroplast target gene(s). These criteria are met by *SIG1* and its target *psaA*, *SIG3* and *psbN*, *SIG4* and *ndhF*, and *SIG5* and *psbD* (4, 7, 8) (spreadsheet S1).

We investigated this by using *SIG5* control of *psbD* as a model to investigate circadian signaling to chloroplasts. *SIG5* regulates transcription from the well-characterized *psbD* blue light-responsive promoter (*psbD* BLRP) of the chloroplast *psbDC* operon in mature chloroplasts (4, 9, 10). Control of *psbD* BLRP by *SIG5* lacks the functional redundancy common to regulators of chloroplast transcription. Therefore, the specificity and degree of characterization make this pathway attractive for studies of circadian signaling. *psbDC* encodes the D2 and CP43 reaction center proteins of photosystem II (PSII). There are circadian oscillations in the abundance of *psbD* BLRP transcripts (Fig. 1A), and *SIG5* increases photosynthetic efficiency in fluctuating light environments and under abiotic stress (4).

To investigate whether *SIG5* contributes to circadian regulation of chloroplasts, we monitored circadian rhythms of delayed chlorophyll fluorescence (DF) in two homozygous transfer DNA mutants of *SIG5* (*sig5-2* and *sig5-3*) (11). DF provides information concerning the circadian regulation of PSII (12). In three experiments, the circadian peak of DF occurred earlier in *sig5* mutants than in Col-0 wild type (3.6 to 5.6 hours earlier and 4.0 to 5.9 hours earlier for *sig5-2* and *sig5-3*, respectively) (Fig. 1B and fig. S1). The earlier peak was not caused by a period alteration (table S1). DF is elevated by inhibitors of photosynthesis (13), so the earlier DF peak in *sig5* mutants may represent earlier deactivation of PSII.

Because *SIG5* modifies the shape of circadian rhythms of DF, we investigated the role of *SIG5* in circadian timing of chloroplast *psbDC* transcription. Circadian oscillations of *psbD* BLRP transcripts

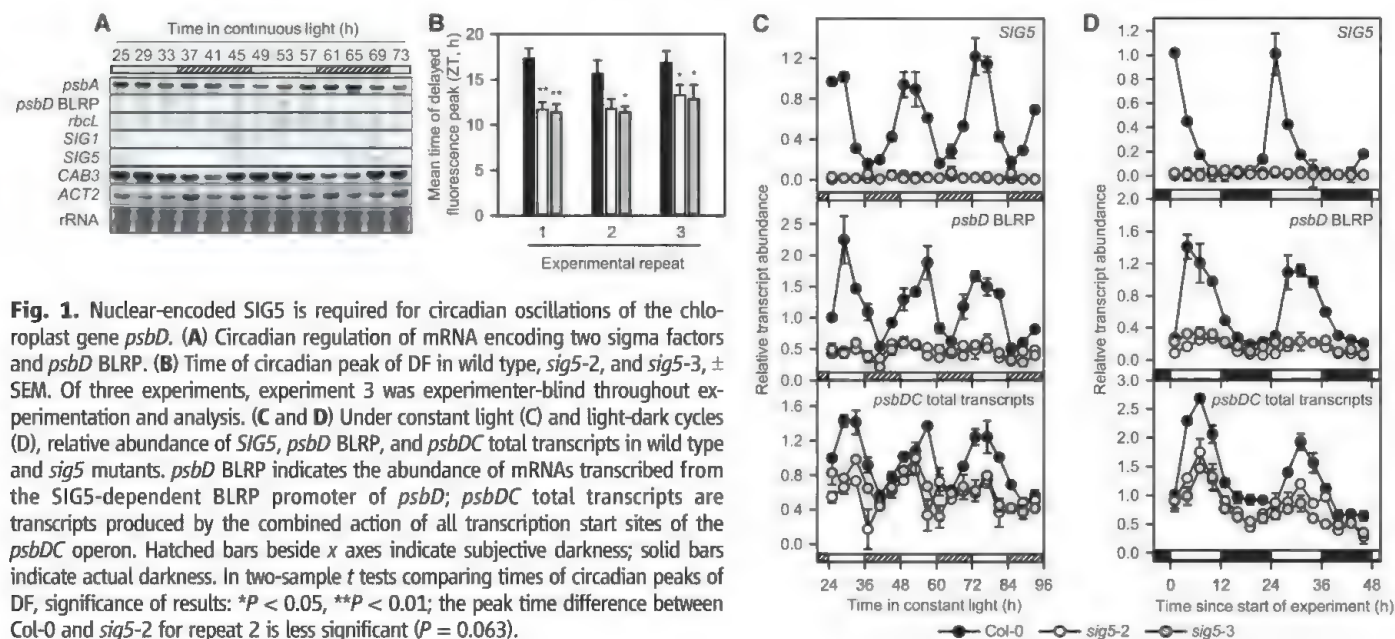
ceased in *sig5* mutants (Fig. 1C and fig. S2). Oscillations of transcripts encoding *CHLOROPHYLL A/B BINDING PROTEIN3*, *SIG1*, and a *SIG5*-independent plastid transcript (*rbcL*) were unaltered in *sig5-2*, which indicated that *SIG5* is not a global regulator of plastid or nucleus transcription (fig. S2). We also investigated the involvement of *SIG5* in circadian regulation of transcripts accumulating from all *psbDC* transcription start sites, which form the pool of translatable *psbDC* mRNA (Fig. 1C). The pMMC- β rhythmicity values from cosinor analysis (14) for *psbDC* oscillations were 0.06 (Col-0), 0.60 (*sig5-2*), and 0.38 (*sig5-3*), and transcripts with pMMC- β < 0.10 are considered rhythmic (15). Nuclear-encoded *SIG5* is therefore required for robust circadian oscillations in the abundance of transcripts encoded by the chloroplast *psbDC* operon.

Plants evolved under cycles of light and dark (LD), so we investigated the role of *SIG5* regulation of *psbDC* under LD. In wild-type plants, gradual predawn induction of *SIG5* transcripts combined with peak transcript abundance immediately after dawn indicates that light and circadian cues combine to control *SIG5* transcript abundance under LD (Fig. 1D). Daily cycles of *psbD* BLRP transcripts depend almost entirely on *SIG5* (Fig. 1D), and *SIG5* regulation accounts for half of *psbDC* total transcripts accumulated in the light (Fig. 1D). This is reminiscent of the way that maximum circadian amplitude of *psbA1* transcription is maintained by *rpoD2* in the cyanobacterium *Synechococcus* sp. PCC7942 (16). Daily timing of transcription by sigma factors is therefore a conserved mechanism that likely became integrated with the eukaryotic circadian timing system after the endosymbiosis that gave rise to chloroplasts.

We investigated whether the circadian timing of *SIG5* transcription controls the timing of *psbD* BLRP transcription. In the wild type, *SIG5* transcript abundance peaks around subjective dawn

(Fig. 1C). This likely arises from circadian oscillations of *SIG5* promoter activity, caused by three types of circadian-regulated cis elements within the *SIG5* promoter (fig. S3, A and B). We delayed the phase of *SIG5* transcripts by expressing *SIG5* fused to the evening-phased promoter of *TIMING OF CAB2 EXPRESSION1* (*TOC1*) in the *sig5-3* mutant. In two transgenic lines expressing *TOC1::SIG5*, the phase of *SIG5* transcripts was later than wild type [COSOPT relative phases -3.9 ± 0.4 hours (Col-0), 6.6 ± 0.6 hours (*TOC1::SIG5* line 1), and 8.1 ± 1.7 hours (*TOC1::SIG5* line 2)] (Fig. 2A and fig. S4, A and B). In *TOC1::SIG5* line 1, which expressed *SIG5* strongly, the phase of *psbD* BLRP transcripts was 9 hours later than the wild type's [relative phase -7.45 ± 0.7 hours (Col-0) and 1.94 ± 0.9 hours (*TOC1::SIG5* line 1)] (Fig. 2A). Although *TOC1::SIG5* line 2 also had delayed-phase *SIG5* oscillations, *SIG5* transcript abundance was below the wild type's, and *psbD* BLRP transcripts were arrhythmic (fig. S4B) (pMMC- β for *psbD* BLRP oscillations: 0.06, 0.02, and 0.46 for Col-0, *TOC1::SIG5* line 1, and *TOC1::SIG5* line 2, respectively). The altered phase of *SIG5* and *psbD* BLRP transcripts was not caused by altered oscillator function: Rhythms of the oscillator component *LATE ELONGATED HYPOCOTYL* (*LHY*) were unaltered in *TOC1::SIG5* (fig. S4C). The timing of transcription of *SIG5*, therefore, controls the timing of transcription of a chloroplast gene, and *psbD* BLRP induction requires a threshold dose of *SIG5* transcripts.

In addition to transcription-translation loops, circadian rhythms arise from posttranslational oscillators (17, 18). We therefore investigated whether the circadian timing of chloroplast transcription is controlled by the nuclear-encoded oscillator or by an independent mechanism within chloroplasts. The *toc1-1* and *ztl-1* mutations of



the circadian oscillator cause short and long periods, respectively (19, 20) (fig. S5, A and B). In these mutants, the circadian period of *SIG5* transcript abundance reflects the period of the mutant oscillator (Fig. 2B and fig. S5, C and D). The period of oscillation of chloroplast *psbD* BLRP transcripts was also determined by the core oscillator: *psbD* BLRP period was 20.9 ± 0.3 hours in *toc1-1* and 26.9 ± 0.9 hours in *ztl-1*, compared with 23.6 ± 0.6 hours in the wild type (Fig. 2B and fig. S5D). Together with our *TOC1::SIG5* experiments, this demonstrates that the nuclear-encoded

circadian clock controls the circadian timing of specific chloroplast genes by using a sigma factor.

Regulators of circadian oscillator function in *Arabidopsis* include phytohormones, cytosolic free Ca^{2+} , cyclic adenosine diphosphate ribose, sugars, chromatin remodeling, and protein phosphorylation (21–25). We tested whether *SIG5* is part of a circadian feedback loop incorporating the chloroplast. The circadian period, phase, and amplitude of transcripts encoding the oscillator components *CIRCADIAN CLOCK ASSOCIATED1* (*CCA1*), *CCA1 HIKING EXPEDITION* (*CHE*), *GIGANTEA*

(*GI*), *PSEUDO-RESPONSE REGULATOR7* (*PRR7*), *TOC1*, and *LHY* were largely unaltered in *sig5-3* (Fig. 3A and table S2). Moreover, rhythms of promoter activity of *CCA1*; *TOC1*; and peripheral oscillator component *COLD*, *CIRCADIAN RHYTHM*, *AND RNA BINDING2* (*CCR2*) were unaltered (Fig. 3, B and C, and table S3). Under our experimental conditions, *SIG5* communicates timing information unidirectionally from the eukaryotic circadian oscillator to specific chloroplast genes.

Circadian gating is thought to ensure that the magnitude of stimulus-induced responses is appro-

Fig. 2. The circadian timing of *SIG5* transcription by the eukaryotic circadian oscillator controls circadian rhythms of transcription of the chloroplast *psbD* BLRP. (A) The circadian phase of *SIG5* transcripts was advanced relative to the wild type by expressing *SIG5* under the control of the *TOC1* promoter in the *sig5-3* background (*TOC1::SIG5* line 1, top), and the circadian timing of *SIG5* can control the timing of *psbD* BLRP transcripts (bottom). (B) Short- and long-period circadian clock mutants cause short and long circadian periods of *SIG5* and *psbD* BLRP transcripts. Period estimated from cosinor analysis is plotted against pMMC- β measure of rhythmic robustness.

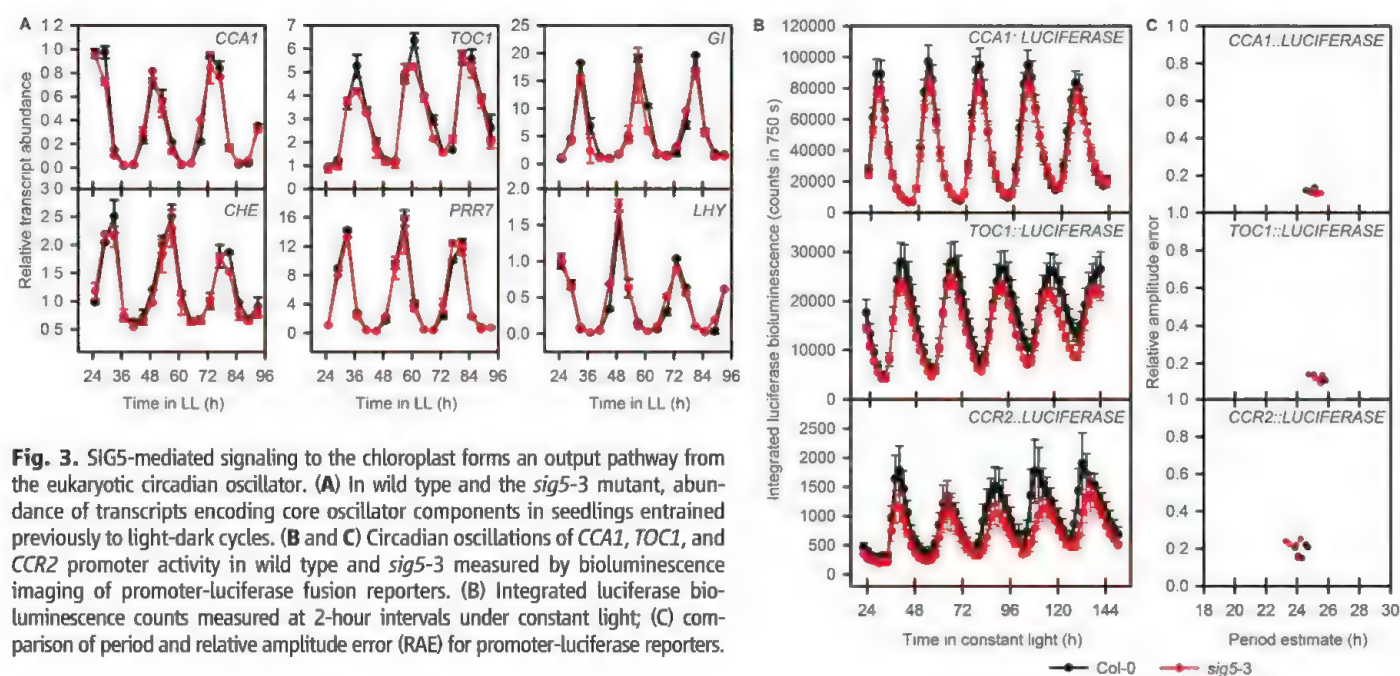
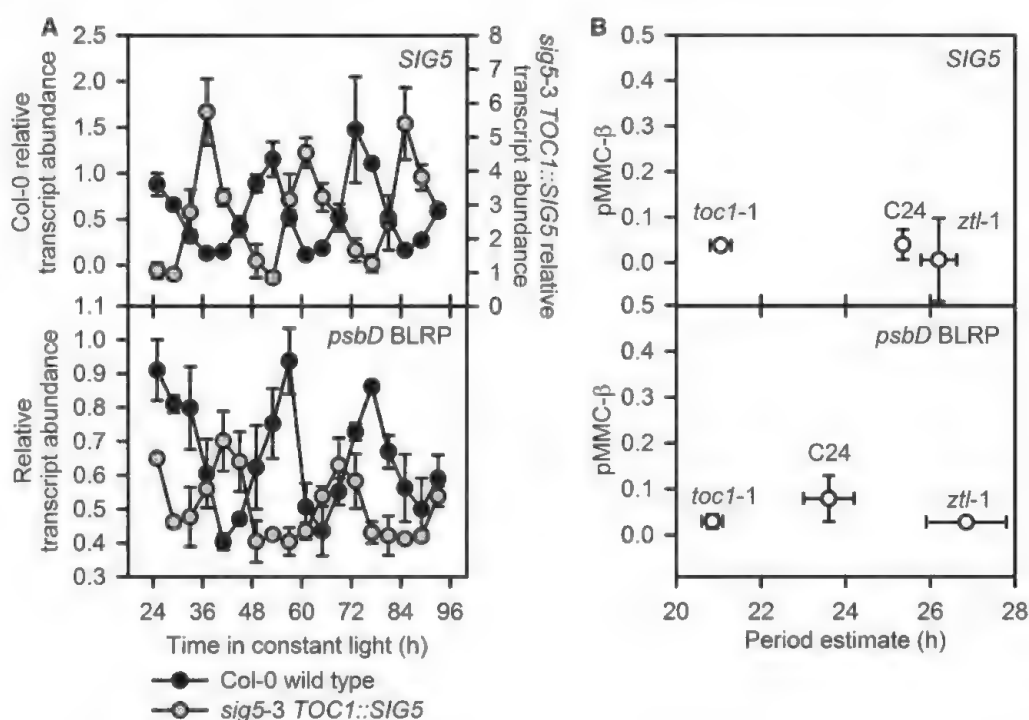


Fig. 3. *SIG5*-mediated signaling to the chloroplast forms an output pathway from the eukaryotic circadian oscillator. (A) In wild type and the *sig5-3* mutant, abundance of transcripts encoding core oscillator components in seedlings entrained previously to light-dark cycles. (B and C) Circadian oscillations of *CCA1*, *TOC1*, and *CCR2* promoter activity in wild type and *sig5-3* measured by bioluminescence imaging of promoter-luciferase fusion reporters. (B) Integrated luciferase bioluminescence counts measured at 2-hour intervals under constant light; (C) comparison of period and relative amplitude error (RAE) for promoter-luciferase reporters.

appropriate for the time of day (26). We hypothesized that circadian gating of light signals is important for chloroplasts, which function within a light environment incorporating predictable circadian components and unpredictable components (e.g., a cloud passing the sun). We investigated whether the circadian clock gates light induction of *SIG5* and *psbD* BLRP transcripts. Blue light (BL) induces *SIG5* and *psbD* (9, 27, 28) (fig. S6, A and B), *SIG5* is required for BL induction of *psbD* BLRP (10) (fig. S6B), and *SIG5* transcript abundance falls rapidly in darkness (fig. S6C). *SIG5* transcripts are induced more strongly during subjective day than subjective night, with the smallest induction 4 hours before subjective dawn (Fig. 4A). The magnitude of BL induction of *psbD* BLRP transcripts is greater during subjective day than subjective night (Fig. 4B). Therefore, the circadian oscillator gates *SIG5*-mediated BL regulation of chloroplast transcription.

Some *Arabidopsis* sigma factors (e.g., *SIG1* and *SIG6*) recognize multiple chloroplast gene promoters (6, 29), so we investigated whether *SIG5* communicates circadian timing information to other chloroplast genes. We used chromatin immunoprecipitation–quantitative polymerase chain reaction (ChIP–QPCR) to screen chloroplast promoters for potential targets of *SIG5* (fig. S7)

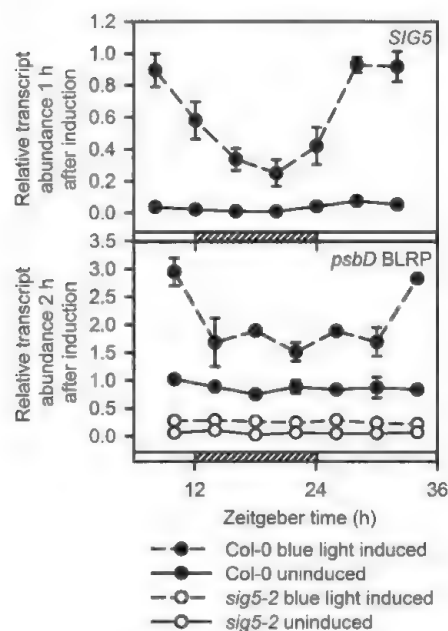


Fig. 4. Circadian gating of blue light induction of *SIG5* and *psbD* BLRP. The magnitude of *SIG5* transcript induction by blue light has a circadian oscillation (top), and the magnitude of *psbD* BLRP induction by blue light is circadian regulated and *SIG5*-dependent (bottom). *SIG5* and *psbD* BLRP transcripts were measured 1 hour and 2 hours after induction with $50 \mu\text{mol m}^{-2} \text{s}^{-1}$ blue light, respectively. Seedlings were entrained previously to light/dark cycles, then transferred to $5 \mu\text{mol m}^{-2} \text{s}^{-1}$ red light to maintain oscillator rhythmicity during the experiment. Hatched bars above x axes indicate subjective dark period.

(29) and identified *psaAB*, *psbA*, and *psbBT* as candidates with the greatest DNA recovery. Of these, *psaAB* and *psbA* transcript abundance was reduced consistently at certain times in the *sig5-2* mutant (fig. S8). This suggests that *SIG5* contributes to circadian rhythms of additional chloroplast-encoded genes that encode the reaction centers of PSI and PSII.

Our experiments indicate that individual sigma factors communicate timing information to multiple chloroplast genes. It also appears that several sigma factors might underlie circadian regulation of a single chloroplast gene, because of the functional redundancy of sigma factors. For example, oscillations of *psaA* transcripts persist with reduced amplitude in a *sig5* mutant (fig. S8A). This may be because *psaA* is also transcribed by *SIG1* (29), which has dawn-phased rhythmic transcripts. Finally, multiple pathways communicate circadian timing information to chloroplasts. We estimate that *SIG5* regulates operons incorporating at least 12% of rhythmic chloroplast transcripts, calculated as the number of rhythmic transcripts (eight, namely, *psaA*, *psaB*, *psbB*, *psbH*, *petB*, *petD*, *psbD*, and *psbC*) (spreadsheet S1) encoded within the four operons receiving circadian timing information from *SIG5* (fig. S8), as a proportion of all rhythmic chloroplast transcripts (62) (spreadsheet S1). This is a parsimonious estimate because there is likely functional redundancy between *SIG5* and other sigma factors, and our ChIP examined a representative gene set. Additional pathways, therefore, likely account for other rhythmic transcripts. *SIG1*, *SIG3*, and *SIG4* have rhythmic transcripts and rhythmic chloroplast targets, and so they are potential circadian regulators of chloroplast transcription for future study, especially in multiple mutant combinations to unravel redundancy. *SIG1* and *SIG5* are phased to subjective dawn, whereas *SIG3* and *SIG4* are phased to subjective dusk (spreadsheet S1). Distinct sigma factors therefore might communicate specific phase information to subsets of chloroplast genes. Circadian-gated light inputs, redox oscillations, and circadian Ca^{2+} signals (18, 30) may also signal timing information to chloroplasts. *SIG5* occurs within mitochondria of certain reproductive tissues (31), and chloroplast retrograde signals can alter circadian rhythms (32). Therefore, a sophisticated network of interactions incorporating multiple sigma factors and other signals appears to underlie crosstalk between the nuclear-encoded circadian clock and genome-bearing organelles.

Our findings demonstrate that, during evolution, prokaryotic transcriptional regulators in chloroplasts were recruited by the eukaryotic circadian system in higher plants. This mechanism appears to be conserved through the green lineage, because sigma factors in cyanobacteria and moss contribute to circadian modulation of photosynthesis gene expression (16, 33, 34). We have shown that circadian timing information is exchanged between organelles with distinct genetic systems having separate evolutionary origins, by using a signaling mechanism that appears to be a common feature of photosynthetic life.

References and Notes

1. A. N. Dodd et al., *Science* **309**, 630 (2005).
2. T. P. Michael et al., *PLoS Genet.* **4**, e14 (2008).
3. K. Kanamaru, K. Tanaka, *Biosci. Biotechnol. Biochem.* **68**, 2215 (2004).
4. A. Nagashima et al., *Plant Cell Physiol.* **45**, 357 (2004).
5. K. Kanamaru et al., *Plant Cell Physiol.* **42**, 1034 (2001).
6. Y. Ishizaki et al., *Plant J.* **42**, 133 (2005).
7. M. Shimizu et al., *Proc. Natl. Acad. Sci. U.S.A.* **107**, 10760 (2010).
8. J.-J. Favory et al., *Nucleic Acids Res.* **33**, 5991 (2005).
9. P. H. Hoffer, D. A. Christopher, *Plant Physiol.* **115**, 213 (1997).
10. Y. Tsunoyama et al., *Proc. Natl. Acad. Sci. U.S.A.* **101**, 3304 (2004).
11. Materials and methods are available as supplementary materials on Science Online.
12. P. D. Gould et al., *Plant J.* **58**, 893 (2009).
13. B. L. Strehler, W. Arnold, *J. Gen. Physiol.* **34**, 809 (1951).
14. S. Panda et al., *Cell* **109**, 307 (2002).
15. S. L. Harmer et al., *Science* **290**, 2110 (2000).
16. N. F. Tsinoremas et al., *EMBO J.* **15**, 2488 (1996).
17. J. Tomita, M. Nakajima, T. Kondo, H. Iwasaki, *Science* **307**, 251 (2005).
18. J. S. O'Neill et al., *Nature* **469**, 554 (2011).
19. A. J. Millar, I. A. Carré, C. A. Strayer, N. H. Chua, S. A. Kay, *Science* **267**, 1161 (1995).
20. D. E. Somers, T. F. Schultz, M. Milnamow, S. A. Kay, *Cell* **101**, 319 (2000).
21. S. Hanano, M. A. Domagalska, F. Nagy, S. J. Davis, *Genes Cells* **11**, 1381 (2006).
22. A. N. Dodd et al., *Science* **318**, 1789 (2007).
23. N. Dalchau et al., *Proc. Natl. Acad. Sci. U.S.A.* **108**, 5104 (2011).
24. P. Más, *Trends Cell Biol.* **18**, 273 (2008).
25. S. Sugano, C. Andronis, M. S. Ong, R. M. Green, E. M. Tobin, *Proc. Natl. Acad. Sci. U.S.A.* **96**, 12362 (1999).
26. C. T. Hotta et al., *Plant Cell Environ.* **30**, 333 (2007).
27. T. Mochizuki, Y. Onda, E. Fujiwara, M. Wada, Y. Toyoshima, *FEBS Lett.* **571**, 26 (2004).
28. Y. Onda, Y. Yagi, Y. Saito, N. Takenaka, Y. Toyoshima, *Plant J.* **55**, 968 (2008).
29. M. Hanaoka, M. Kato, M. Anma, K. Tanaka, *Int. J. Mol. Sci.* **13**, 12182 (2012).
30. C. H. Johnson et al., *Science* **269**, 1863 (1995).
31. J. Yao, S. Roy-Chowdhury, L. A. Allison, *Plant Physiol.* **132**, 739 (2003).
32. M. Hassidim et al., *Plant J.* **51**, 551 (2007).
33. K. Ichikawa, A. Shimizu, R. Okada, S. B. Satthai, S. Aoki, *FEBS Lett.* **582**, 405 (2008).
34. M. Hanaoka et al., *J. Biol. Chem.* **287**, 26321 (2012).

Acknowledgments: A.N.D. thanks the Royal Society for awarding a University Research Fellowship. Funding comprised a Royal Society Research Grant; a Royal Society Anglo-Japanese Daiwa Foundation International Joint Project (A.N.D. and M.H.); Biotechnology and Biological Sciences Research Council grant BB/I005811/1 (A.N.D.); the Nuffield Foundation (A.N.D. and K.A.A.); the University of York (A.N.D.); a Special Coordination Fund for Promoting Science and Technology (M.H.); Grants-in-Aid [21770034, 24117505, and 24770037 (M.H.); 23120505 and 24248061 (K.T.)] from the Ministry of Education, Culture, Sports, Science and Technology of Japan or Japan Society for the Promotion of Science, and the Sumitomo Foundation (M.H.). We thank A. Hall for delayed fluorescence advice and luciferase reporters; S. Penfield for period mutants; S. Kay for COSOPT; M. Kobayashi for technique development; and A. Webb, A. Hetherington, and K. Franklin for constructive criticism. The data described are in the main and supplementary figures. There are no conflicts of interest.

Supplementary Materials

www.sciencemag.org/cgi/content/full/339/6125/1316/DC1
Materials and Methods
Figs. S1 to S9
Tables S1 to S5
References (35–37)
Spreadsheet S1

18 September 2012; accepted 22 January 2013
10.1126/science.1230397

Quantitative Phosphoproteomics Reveal mTORC1 Activates de Novo Pyrimidine Synthesis

Aaron M. Robitaille,¹ Stefan Christen,² Mitsugu Shimobayashi,¹ Marion Cornu,¹ Luca L. Fava,^{1*} Suzette Moes,¹ Cristina Prescianotto-Baschong,¹ Uwe Sauer,² Paul Jenoe,¹ Michael N. Hall^{1†}

The Ser-Thr kinase mammalian target of rapamycin (mTOR) controls cell growth and metabolism by stimulating glycolysis and synthesis of proteins and lipids. To further understand the central role of mTOR in cell physiology, we used quantitative phosphoproteomics to identify substrates or downstream effectors of the two mTOR complexes. mTOR controlled the phosphorylation of 335 proteins, including CAD (carbamoyl-phosphate synthetase 2, aspartate transcarbamylase, and dihydroorotase). CAD catalyzes the first three steps in de novo pyrimidine synthesis. mTORC1 indirectly phosphorylated CAD-S1859 through S6 kinase (S6K). CAD-S1859 phosphorylation promoted CAD oligomerization and thereby stimulated de novo synthesis of pyrimidines and progression through S phase of the cell cycle in mammalian cells. Thus, mTORC1 also stimulates the synthesis of nucleotides to control cell proliferation.

The conserved Ser-Thr kinase target of rapamycin (TOR) controls growth and metabolism by regulating several anabolic and catabolic processes (1, 2). Deregulation of the mammalian TOR (mTOR) signaling network is associated with aging and various disorders, including cancer, diabetes, obesity, cardiovascular disease, inflammation, and neurodegeneration (3).

Allosteric mTOR inhibitors such as rapamycin are clinically approved for treatment of allograft rejection, cancer, and cardiovascular disease; and a new generation of adenosine triphosphate (ATP) competitive mTOR inhibitors are now in development as anticancer drugs (4). The identification of new mTOR targets may reveal further therapeutic strategies.

TOR forms two structurally and functionally distinct multiprotein complexes, TORC1 and TORC2, that are conserved from yeast to human (5). Rapamycin acutely inhibits TORC1. In mammals, nutrients (amino acids), growth factors (insulin), and cellular energy [high ATP:adenosine monophosphate ratio] activate mTORC1, whereas growth factors alone activate mTORC2, through phosphoinositide 3-kinase-dependent association of mTORC2 with the ribosome (6, 7). mTORC1 and mTORC2 directly phosphorylate several members of the AGC kinase family, including S6 kinase (S6K), protein kinase B (PKB) (also called Akt), serum and glucocorticoid regulated kinase, and canonical protein kinase C. Although mTOR direct substrates and downstream effectors are known, more are expected because of the broad role of mTOR in cell physiology.

To identify mTOR targets, we determined the phosphoproteome of mouse embryonic fibroblasts (MEFs) lacking raptor or rictor (fig. S1A). Raptor and rictor are specific and essential components of mTORC1 and mTORC2, respectively. Floxed

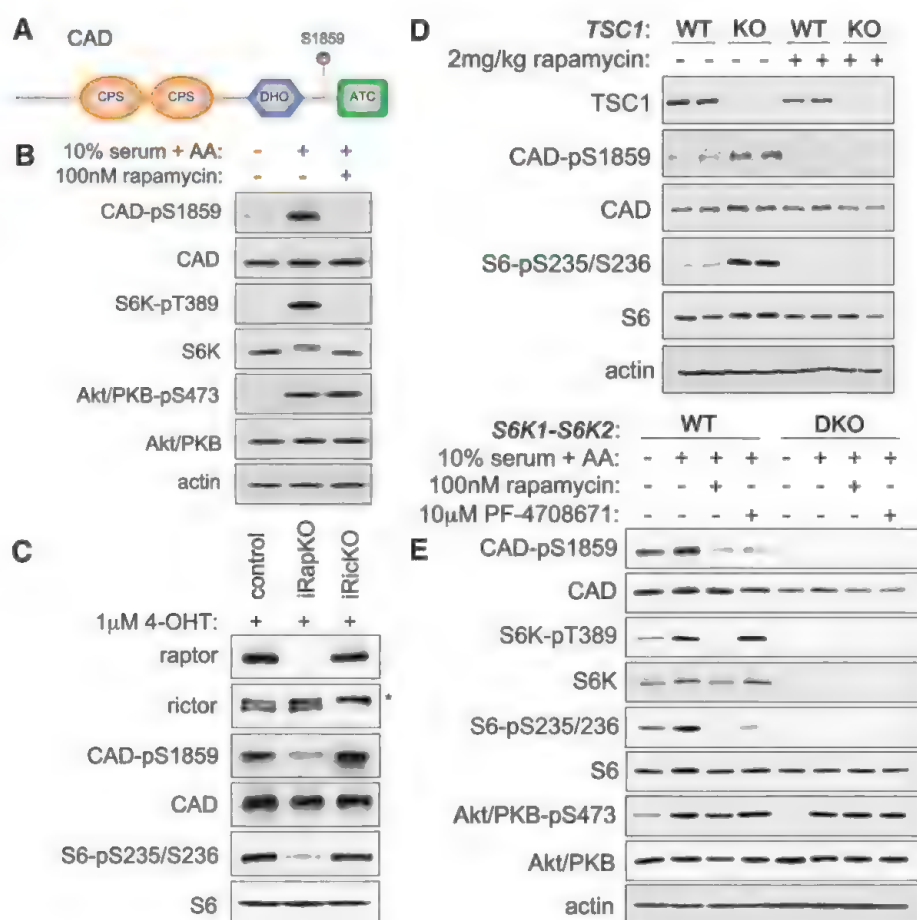
¹Biozentrum, University of Basel, 4056 Basel, Switzerland.

²Institute of Molecular Systems Biology, Eidgenössische Technische Hochschule (ETH) Zürich, 8093 Zürich, Switzerland.

*Present address: Biocenter, Division of Developmental Immunology, Innsbruck Medical University, A-6020 Innsbruck, Austria.

†Corresponding author. E-mail: m.hall@unibas.ch

Fig. 1. CAD as a target of mTORC1. (A) Diagram of CAD protein, including CPS (carbamoyl-phosphate synthetase), ATC (aspartate transcarbamylase), and DHO (dihydroorotase) enzymatic domains. (B) HeLa cells were deprived of serum for 16 hours in Dulbecco's minimum essential medium (DMEM) and incubated for 15 min without amino acids (AA) in 1× phosphate-buffered saline. Cells were then stimulated in DMEM with 10% dialyzed fetal calf serum (D-FCS) and 2× AA for 1 hour with or without rapamycin. (C) iRapKO and iRictKO MEFs were treated as in fig. S1B. The asterisk indicates a nonspecific band. (D) Mouse liver extract from wild-type (WT) (*TSC1*-fl/fl) or knockout (KO) (*TSC1*-fl/fl; *Albumin-Cre*) mice. Twelve-week-old littermates were starved overnight and treated with rapamycin or sham (0.9% NaCl) for 6 hours before killing. (E) WT (control) and DKO (*S6K1*-*S6K2* double knockout) MEFs were deprived of serum for 2 hours and then stimulated for 1 hour in modified Hank's buffered salt solution plus 10% D-FCS, glucose, vitamins, and 2× AA, with or without rapamycin or PF-4708671.



raptor or *riCTOR* genes in MEFs, referred to as iRapKO and iRicKO, respectively, were deleted by tamoxifen (4-OHT)-induced activation of CreERT2 recombinase (fig. S1B) (8). In total, we detected and quantified 4584 phosphorylation sites on 1398 proteins (fig. S1, C to E, and table S1), including 18 validated phosphorylation sites in nine known mTORC1 or mTORC2 target proteins (table S2). We also detected mTOR-regulated phosphorylation of 326 proteins that had not been

previously identified as mTOR targets (table S3). Two recent studies described the phosphoproteome of cells treated with an ATP-competitive mTOR inhibitor (9, 10). A comparison of the three mTOR phosphoproteomes revealed only ~30% overlap between any two data sets with regard to both validated and previously unknown mTOR-regulated proteins, although the three data sets are similar in size (fig. S1F and tables S4 and 5). Taken together, the three independent studies

suggest that mTOR directly or indirectly regulates the phosphorylation of at least 803 distinct proteins. This corresponds to 3.9% of all mammalian genes, consistent with the broad role of mTOR in regulating cell physiology.

Phosphorylation motif analysis (fig. S2A) and immunoblotting (fig. S2B) suggested that the mTOR-regulated proteins we identified include both direct substrates and indirect effectors. Peptide array in vitro kinase assays indicated that mTOR

Fig. 2. Activation of de novo pyrimidine synthesis by mTORC1. (A) Diagram of de novo pyrimidine synthesis pathway. CAP, carbamoyl phosphate; CAA, carbamoyl aspartic acid; OMP, orotidine monophosphate. (B) HeLa cells were metabolically labeled with 4 mM ¹⁵N-amide glutamine. Metabolites were measured with targeted ultra high-performance liquid chromatography–tandem mass spectrometry. Values are expressed as mean ± SD. Asterisks indicate a statistical difference between stimulated and rapamycin treatment: **P* < 0.05, ***P* < 0.01, ****P* < 0.001 (Student's *t* test) *n* = 3 to 6. (C) Inhibition of growth factor–stimulated increase in DHOA, OA, and UTP cellular concentrations by rapamycin. (D) Rapamycin did not inhibit growth factor–stimulated increase in GDP or GTP cellular concentrations.

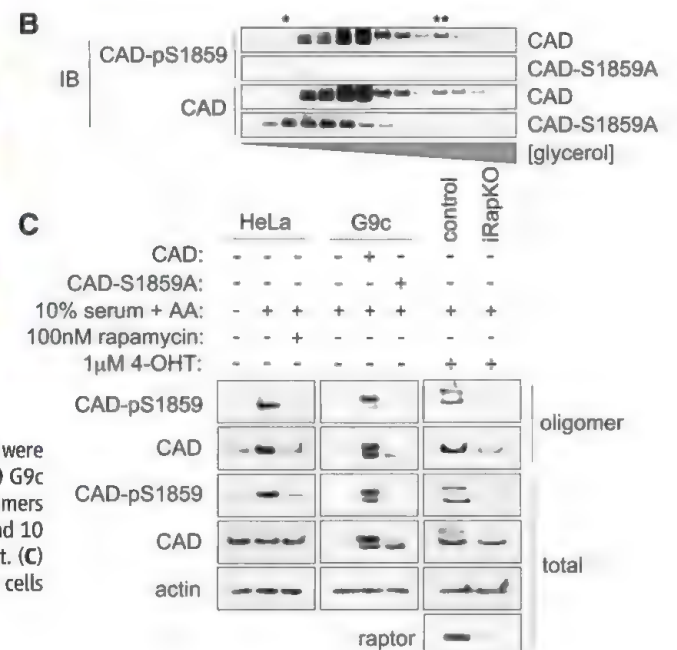
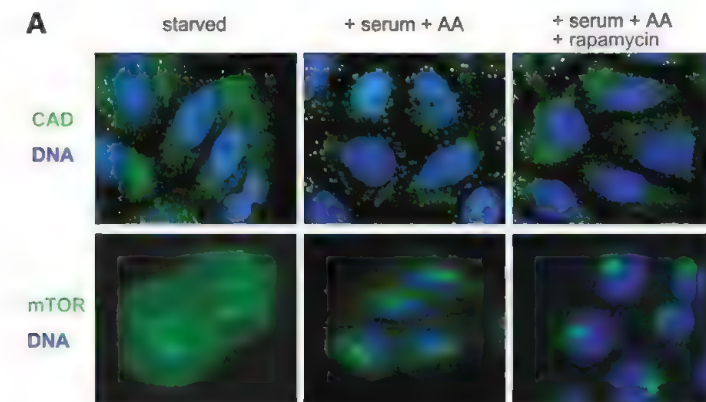
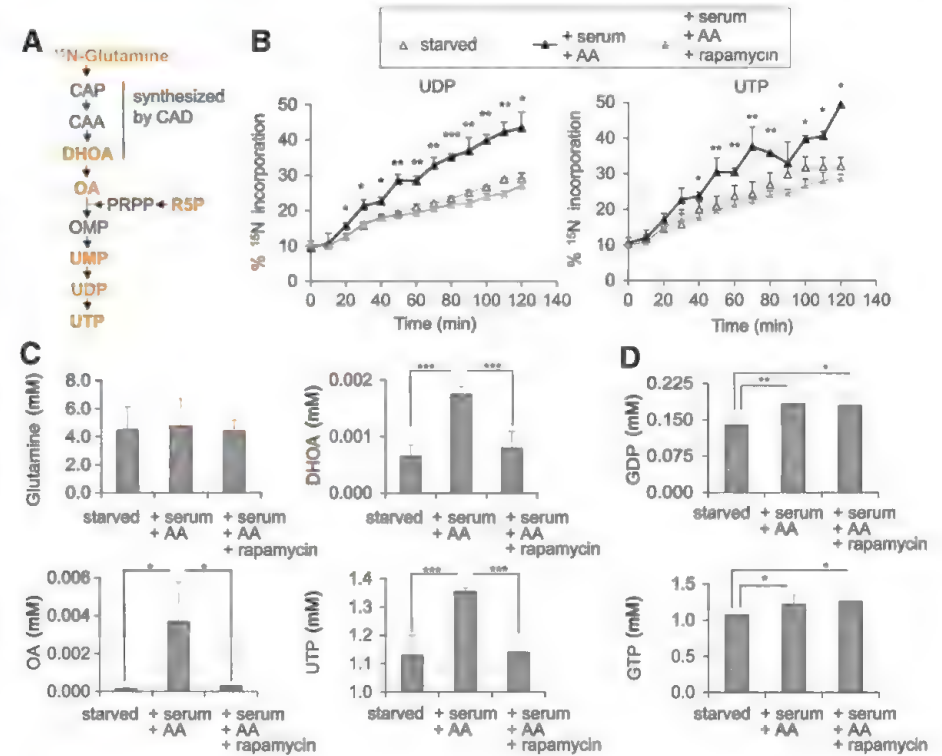


Fig. 3. Effects of mTORC1 on CAD localization and oligomerization. (A) HeLa cells were treated as in Fig. 1B. Endogenous CAD was visualized by immunocytochemistry. (B) G9c cells were transfected with plasmid-encoding, wild-type or mutant CAD. CAD oligomers were detected by sedimentation in 10 to 35% glycerol gradients. Fractions 2 (*) and 10 (**) correspond to 250-kD and 1.5-MD size standards, respectively. IB, immunoblot. (C) HeLa cells were treated as in Fig. 1B, G9c cells were treated as in (B), and iRapKO cells were treated as in fig. S1B. Oligomer is fraction 10 (**).

directly phosphorylated 26 newly identified sites, corresponding to 21 potential mTOR substrate proteins (fig. S2, C to E, and tables S6 and S7), and confirmed that mTOR phosphorylates mainly but not exclusively S/T-P (where S is Ser, T, Thr, and P, Pro) and hydrophobic motif (Φ -X-X- Φ -S/T- Φ) sites. Thus, mTOR appears to be a promiscuous kinase that phosphorylates diverse target sites.

Gene Ontology (GO) analysis of mTOR-regulated proteins revealed enrichment of KEGG-annotated insulin signaling, mTOR signaling, cancer, and ribosome biogenesis pathways (fig. S3A). GO analysis also identified RNA metabolism and DNA replication as mTOR-regulated processes, yet few mTOR targets involved in these processes are known. We therefore investigated CAD (carbamoyl-phosphate synthetase 2, aspartate transcarbamylase, and dihydroorotase) as a potential mTORC1 effector. CAD functions in pyrimidine synthesis, a conserved metabolic pathway essential for S phase progression (fig. S3B). In mammals, de novo pyrimidine synthesis is activated by growth factors (11, 12). However, despite the central importance of pyrimidine synthesis, its regulation by growth cues is incompletely understood. Our phosphoproteomic analysis indicated that mTORC1 mediates phosphorylation of CAD at S1859 (Fig. 1A). To confirm that mTORC1 controls CAD-S1859 phosphorylation, we generated a phosphospecific antibody to CAD-pS1859. The antibody failed to recognize a S1859→A1859 (S1859A, where A is Ala) mutant version of CAD (fig. S3C). Western immunoblotting showed that CAD-S1859 phosphorylation was stimulated by growth factors (dialyzed serum) and amino acids in a rapamycin-sensitive manner in HeLa and U2OS cells (Fig. 1B and fig. S3, D and E). CAD-S1859 phosphorylation was inhibited in MEFs depleted of raptor but not those depleted of rictor (Fig. 1C). We examined CAD phosphorylation in the livers of liver-specific *tuberous sclerosis 1* (*TSC1*) knockout mice (L-*TSC1* KO). Deletion of the tumor suppressor *TSC1* hyperactivates mTORC1 (13, 14). CAD-S1859 phosphorylation was increased in *TSC1*-deficient liver in a rapamycin-sensitive manner (Fig. 1D). CAD-S1859 is part of a sequence, R-I-H-R-A-S¹⁸⁵⁹ (where R is Arg; I, Ile, and H, His), that weakly resembles a consensus target site for AGC protein kinases, suggesting that mTORC1 may phosphorylate S1859 through S6K (15). Pharmacological inhibition of S6K with PF-4708671 (fig. S3F) or depletion of S6K1 and S6K2 prevented growth factor and amino acid-stimulated CAD-S1859 phosphorylation (Fig. 1E). Furthermore, recombinant S6K directly phosphorylated immunopurified CAD at S1859 (fig. S3G). Thus, mTORC1 phosphorylates CAD-S1859 through S6K.

CAD is a 250-kD protein containing three distinct enzymatic activities that catalyze the initial three steps in de novo pyrimidine synthesis, including the rate-limiting first step. In particular, CAD uses glutamine, bicarbonate, and aspartic acid to form a pyrimidine ring that is subsequently attached to ribose to generate a pyrimidine

nucleotide. To measure de novo pyrimidine synthesis, we labeled HeLa cells with ¹⁵N-amide-labeled glutamine and measured ¹⁵N incorporation into uridine diphosphate (UDP) and uridine triphosphate (UTP) (16) (Fig. 2A and fig. S4, A and B). Growth conditions did not affect glutamine uptake into cells, and ¹⁵N incorporation was not detected in aspartic acid or the pentose phosphate pathway intermediate 6-phospho-gluconate (fig. S4C). Furthermore, we did not detect ¹⁵N incorporation into UDP or UTP in G9c cells, a Chinese hamster ovary cell line lacking endogenous CAD activity (fig. S4D). The above results indicate that the analysis was specific for CAD-dependent de novo pyrimidine synthesis. HeLa cells deprived of nutrients exhibited a low basal rate of de novo pyrimidine synthesis, whereas growth factors and amino acids stimulated synthesis of UDP and UTP. Rapamycin or PF-4708671 treatment inhibited growth factor-stimulated de novo pyrimidine synthesis, decreasing the absolute synthesis of UDP and UTP by about 60% (Fig. 2B and fig. S4, E and F). Rapamycin also inhibited growth factor-stimulated increase in the intracellular concentrations of dihydroorotate (DHOA), the final CAD-synthesized metabolite, and the downstream products orotate (OA) and UTP (Fig. 2C). In contrast, rapamycin had no effect on purine synthesis as measured by guanosine diphosphate (GDP) and guanosine triphosphate (GTP) concentrations (Fig. 2D). Thus, mTORC1 activates de novo pyrimidine synthesis in response to growth factors and amino acids.

To test the role of CAD-S1859 phosphorylation, we examined de novo pyrimidine synthesis

in CAD-deficient G9c cells reconstituted with CAD-S1859A or wild-type CAD. CAD-S1859A-expressing cells exhibited reduced incorporation of ¹⁵N into UDP and UTP (fig. S4, G and H) compared with cells expressing wild-type CAD. The small effect of CAD-S1859A likely reflects a high basal rate of de novo pyrimidine synthesis in the reconstituted G9c cells that overexpress wild-type and mutant CAD about four- to fivefold. Thus, we conclude that mTORC1 activates de novo pyrimidine synthesis through phosphorylation of CAD-S1859.

mTORC1 transcriptionally enhances the pentose phosphate pathway (17) which produces 5-phosphoribosyl-1-pyrophosphate (PRPP). PRPP in turn is required for a late step in de novo pyrimidine synthesis (Fig. 2A and fig. S4B). Thus, mTORC1 may regulate de novo pyrimidine synthesis by acute stimulation of CAD and by delayed transcriptional activation of the pentose phosphate pathway. One-hour treatment of HeLa cells with growth factors increased cellular concentrations of DHOA and OA, metabolites synthesized before the PRPP requirement in pyrimidine synthesis, whereas the cellular concentration of ribose 5-phosphate (R5P), a PRPP precursor, remained unchanged (fig. S5A). Furthermore, 1-hour rapamycin treatment inhibited CAD phosphorylation and de novo pyrimidine synthesis before changes in expression of pentose phosphate pathway genes were observed (fig. S5B and table S8). Lastly, *TSC1*-deficient liver displayed a rapamycin-sensitive increase in the amount of OA and increased transcriptional expression of glucose-6-phosphate dehydrogenase, a pentose phosphate pathway enzyme (fig. S5, C

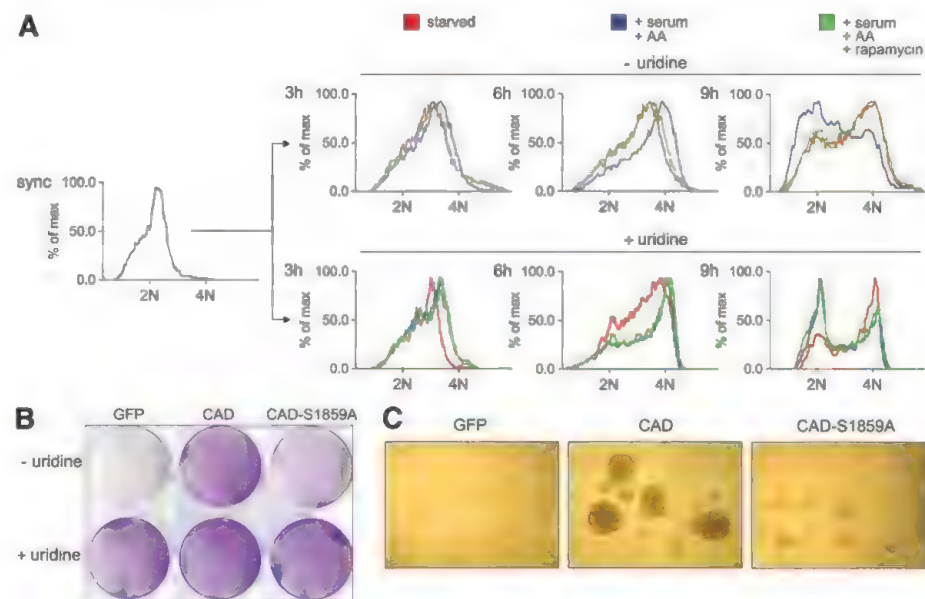


Fig. 4. Promotion of S phase progression by mTORC1. (A) HeLa cells were synchronized in early S phase by using a double-thymidine block. Cells were then released in DMEM (starved) (red); DMEM, 10% D-FCS, and 2× AA (stimulated) (blue); or DMEM, 10% D-FCS, 2× AA, and 100 nM rapamycin (rapamycin) (green); in the absence (top) or presence (bottom) of 30 μM uridine. DNA content was analyzed by flow cytometry. (B and C) G9c cells were transfected with equal amounts of plasmid-encoding green fluorescent protein (GFP), WT, or mutant CAD. Cells were visualized with crystal violet 5 days after transfection (B), or proliferation was assayed via soft agar colony formation (C). Colonies were visualized after 8 days growth in the absence of uridine.

and D), indicating that mTORC1 activates de novo pyrimidine synthesis by both acute stimulation of CAD activity and delayed activation of genes encoding enzymes of the pentose phosphate pathway.

We examined the cellular distribution of endogenous CAD in HeLa cells. As visualized by immunofluorescence with antibody to CAD, growth factors and amino acids stimulated the formation of intracellular punctate structures in a rapamycin-sensitive manner (Fig. 3A and fig. S6, A and B). Growth factors and amino acids failed to stimulate formation of puncta in MEFs depleted for raptor (fig. S5C) or S6K1 and S6K2 (fig. S6, D and E). The puncta did not colocalize with the nucleus, endosomes, lysosomes, peroxisomes, or mitochondria (fig. S6F). Visualization of CAD in stimulated HeLa cells by immunogold electron microscopy revealed cytoplasmic clusters containing six to eight particles (fig. S6, G and H). CAD forms higher-order oligomers in vitro (18, 19). Thus, the puncta may represent CAD oligomers in vivo.

We investigated a possible role of mTORC1-mediated CAD-S1859 phosphorylation in CAD oligomerization. CAD oligomerization was assayed by sedimentation of a cell extract through a glycerol gradient and subsequent immunoblotting of gradient fractions (Fig. 3B and fig. S6I). Treatment of HeLa cells with growth factors and amino acids stimulated the formation of CAD oligomers in a rapamycin-sensitive manner. CAD oligomerization was reduced in MEFs depleted for raptor and in CAD-deficient G9c cells reconstituted with CAD-S1859A (Fig. 3C). Thus, mTORC1-mediated CAD-S1859 phosphorylation appears to promote CAD oligomerization.

CAD is essential for progression through S phase of the cell cycle because of the increased requirement for pyrimidines during DNA synthesis (20). We examined whether mTORC1-

mediated CAD activation is also important for cell cycle progression. HeLa cells were synchronized in early S phase by using a double-thymidine block, and cell-cycle progression of released cells was monitored by flow cytometry. Similar to cells deprived of serum, cell treated with rapamycin showed a 32% delay in S phase progression upon release from the thymidine block (Fig. 4A, top). As cells entered G₂ and M phase, the delay in cell cycle progression increased to 52%, consistent with an additional requirement for mTORC1 in G₂-M (21). The rapamycin-induced delay in cell-cycle progression was suppressed by addition of exogenous uridine (Fig. 4A, bottom). Inhibition of S6K with PF-4708671 delayed cell-cycle progression (fig. S7A). Overexpression of wild-type CAD restored proliferation in G9c cells in the absence of exogenous uridine. In contrast, overexpression of CAD-S1859A only weakly restored cell proliferation (Fig. 4, B and C, and fig. S7, B and C), although CAD-S1859A was slightly less expressed than wild-type CAD in the corresponding reconstituted G9c cells (figs. S4G and S7C). Thus, mTORC1 appears to promote pyrimidine synthesis and S phase progression through S6K-mediated phosphorylation and stimulation of CAD (fig. S7D), consistent with reports that rapamycin inhibits DNA synthesis and cell proliferation independently of eukaryotic initiation factor 4E-binding proteins (22, 23).

References and Notes

1. S. Wullschlegel, R. Loewith, M. N. Hall, *Cell* **124**, 471 (2006).
2. M. Laplante, D. M. Sabatini, *Cell* **149**, 274 (2012).
3. E. Dazert, M. N. Hall, *Curr. Opin. Cell Biol.* **23**, 744 (2011).
4. D. Benjamin, M. Colombi, C. Moroni, M. N. Hall, *Nat. Rev. Drug Discov.* **10**, 868 (2011).
5. J. Kim, K. L. Guan, *Annu. Rev. Biochem.* **80**, 1001 (2011).

6. V. Zinzalla, D. Stracka, W. Oppliger, M. N. Hall, *Cell* **144**, 757 (2011).
7. W. J. Oh et al., *EMBO J.* **29**, 3939 (2010).
8. N. Cybulski, V. Zinzalla, M. N. Hall, *Methods Mol. Biol.* **821**, 267 (2012).
9. P. P. Hsu et al., *Science* **332**, 1317 (2011).
10. Y. Yu et al., *Science* **332**, 1322 (2011).
11. M. L. Smith, J. M. Buchanan, *J. Cell. Physiol.* **101**, 293 (1979).
12. L. M. Graves et al., *Nature* **403**, 328 (2000).
13. X. Gao et al., *Nat. Cell Biol.* **4**, 699 (2002).
14. K. Inoki, Y. Li, T. Zhu, J. Wu, K. L. Guan, *Nat. Cell Biol.* **4**, 648 (2002).
15. E. A. Carrey, D. G. Campbell, D. G. Hardie, *EMBO J.* **4**, 3735 (1985).
16. M. Rühl et al., *Biotechnol. Bioeng.* **109**, 763 (2012).
17. K. Düvel et al., *Mol. Cell* **39**, 171 (2010).
18. P. Zhang et al., *Biochemistry* **48**, 766 (2009).
19. L. Lee, R. E. Kelly, S. C. Pastra-Landis, D. R. Evans, *Proc. Natl. Acad. Sci. U.S.A.* **82**, 6802 (1985).
20. A. D. Mitchell, N. J. Hoogenraad, *Exp. Cell Res.* **93**, 105 (1975).
21. F. Ramírez-Valle, M. L. Badura, S. Braunstein, M. Narasimhan, R. J. Schneider, *Mol. Cell Biol.* **30**, 3151 (2010).
22. R. J. Dowling et al., *Science* **328**, 1172 (2010).
23. C. Espeillac et al., *J. Clin. Invest.* **121**, 2821 (2011).

Acknowledgments: We acknowledge support from the Werner Siemens Foundation (A.M.R.), the Société Francophone du Diabète-Association de Langue Française pour l'Étude du Diabète et des Maladies Métaboliques (M.C.), the Swiss Cancer League, the Louis Jeantet Foundation, the Swiss National Science Foundation, and the SystemsX.ch project YeastX. We declare no conflicts of interest. The phosphoproteomic data, including UniProt accession numbers reported in this paper, are deposited in the supplementary materials.

Supplementary Materials

www.sciencemag.org/cgi/content/full/science.1228771/DC1
Materials and Methods
Supplementary Text
Figs. S1 to S7
Tables S1 to S8
References (24–42)

13 August 2012; accepted 29 January 2013
Published online 21 February 2013;
10.1126/science.1228771

Stimulation of de Novo Pyrimidine Synthesis by Growth Signaling Through mTOR and S6K1

Issam Ben-Sahra,^{1*} Jessica J. Howell,^{1*} John M. Asara,² Brendan D. Manning^{1†}

Cellular growth signals stimulate anabolic processes. The mechanistic target of rapamycin complex 1 (mTORC1) is a protein kinase that senses growth signals to regulate anabolic growth and proliferation. Activation of mTORC1 led to the acute stimulation of metabolic flux through the de novo pyrimidine synthesis pathway. mTORC1 signaling posttranslationally regulated this metabolic pathway via its downstream target ribosomal protein S6 kinase 1 (S6K1), which directly phosphorylates S1859 on CAD (carbamoyl-phosphate synthetase 2, aspartate transcarbamoylase, dihydroorotase), the enzyme that catalyzes the first three steps of de novo pyrimidine synthesis. Growth signaling through mTORC1 thus stimulates the production of new nucleotides to accommodate an increase in RNA and DNA synthesis needed for ribosome biogenesis and anabolic growth.

Cells closely monitor the availability of growth factors, nutrients, and energy and respond accordingly by differentially regu-

lating catabolic and anabolic metabolism. The mechanistic target of rapamycin complex 1 (mTORC1) signaling pathway senses and integrates cellular

growth signals and may act as a conduit between these signals and the control of specific energy- and nutrient-consuming processes (1). mTORC1 stimulates protein synthesis through effects on mRNA translation and ribosome biogenesis (1, 2). mTORC1 signaling also promotes de novo lipid and sterol synthesis through the activation of the sterol-response element-binding protein (SREBP) transcription factors, which stimulate the expression of the enzymes driving this biosynthetic process (3, 4). Through such effects on macromolecular synthesis, mTORC1 is a major driver of anabolic cell growth and proliferation conserved throughout eukaryotes.

To reveal additional inputs from the mTORC1 pathway into the control of cellular metabolism,

¹Department of Genetics and Complex Diseases, Harvard School of Public Health, Boston, MA 02115, USA. ²Division of Signal Transduction, Beth Israel Deaconess Medical Center, Department of Medicine, Harvard Medical School, Boston, MA 02115, USA.

*These authors contributed equally to this work.

†To whom correspondence should be addressed. E-mail: bmmanning@hsph.harvard.edu

we used unbiased metabolomic profiling in cells lacking the tuberous sclerosis complex 2 (TSC2) tumor suppressor, which is a key negative regulator of mTORC1 (5). TSC2-deficient cells exhibit growth factor-independent activation of mTORC1 signaling. Of 224 small metabolites identified through liquid-chromatography (LC) tandem mass spectrometry (MS/MS), the steady-state levels of 20 metabolites were significantly increased

($P < 0.01$) in *Tsc2*^{-/-} mouse embryo fibroblasts (MEFs) relative to those in their littermate-derived wild-type counterparts (Fig. 1A and table S1). The *Tsc2*^{-/-} cells were treated with the mTORC1 inhibitor rapamycin (15 hours) so as to identify changes dependent on mTORC1. We identified five metabolites whose abundance significantly decreased ($P < 0.01$) in response to rapamycin (Fig. 1B). Amongst those that were both increased

in abundance in the *Tsc2*^{-/-} cells and sensitive to rapamycin were metabolites of the pentose phosphate pathway. mTORC1 signaling induces global transcription of pentose phosphate pathway genes and thus increases metabolic flux through this pathway (4).

To identify metabolites that are more acutely affected by changes in mTORC1 signaling, we also conducted metabolite profiling 1 hour after

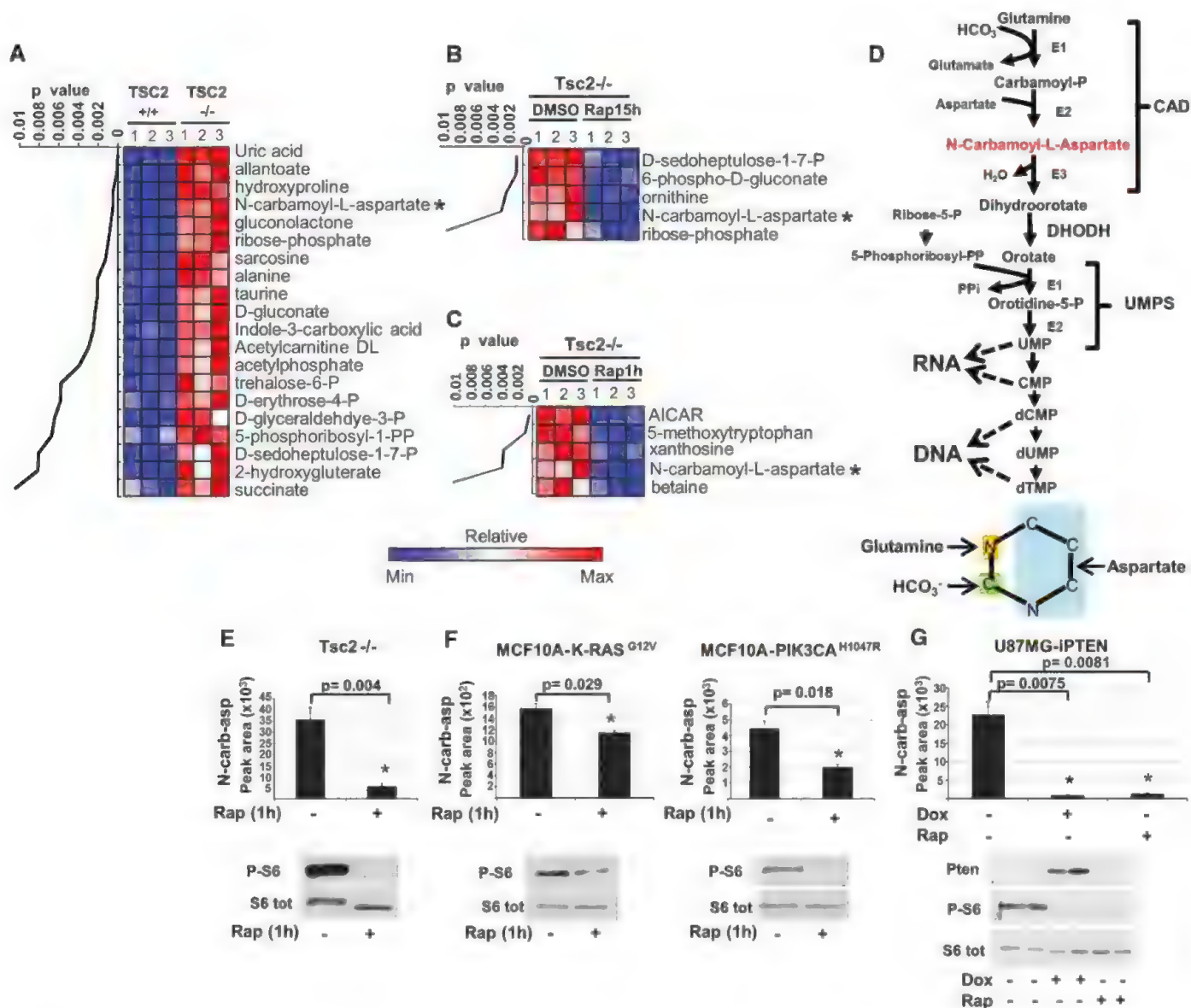


Fig. 1. Influence of mTORC1 on the abundance of *N*-carbamoyl-aspartate. (A to C) Steady-state metabolite profiles from *Tsc2*^{+/+} and *Tsc2*^{-/-} MEFs grown in the absence of serum for 15 hours and treated with either vehicle [dimethyl sulfoxide (DMSO)] or rapamycin (20 nM). Intracellular metabolites from three independent samples per condition were profiled by means of liquid chromatography (LC)/MS/MS, and those (A) significantly increased in *Tsc2*^{-/-} relative to *Tsc2*^{+/+} cells or decreased in *Tsc2*^{-/-} cells by either (B) 15 hours or (C) 1 hour of Rapamycin treatment are shown as row-normalized heat maps ranked according to *P* value. The complete metabolite profiles from these samples are provided in table S1. (D) Schematic of the de novo pyrimidine synthesis pathway and the source of carbon and nitrogen incorporated into the pyrimidine ring (bottom). (E and F) The effects of mTORC1 inhibition on the

steady-state levels of *N*-carbamoyl-aspartate, measured via LC/MS/MS, in (E) *Tsc2*^{-/-} MEFs or (F) MCF10A cells stably expressing K-Ras^{G12V} or PI3KCA^{H1047R} after 15 hours of serum starvation and 1 hour of treatment with rapamycin (20 nM) or DMSO. (G) *N*-carbamoyl-aspartate levels were measured, as above, in U87MG cells stably expressing a doxycycline-inducible PTEN after 15 hours of serum starvation and treatment with doxycycline (1 μg/mL) or rapamycin (20 nM) for the final 8 hours. In (E) to (G), data are shown as the mean ± SEM from triplicate samples, with immunoblots below. MetaboAnalyst (Jianguo Xia, University of Alberta, Edmonton, Canada) and GENE-E (Joshua Gould, Broad Institute, Cambridge, Massachusetts, USA) software were used to assist metabolite data analyses. All *P* values for pairwise comparisons were calculated by using a two-tailed Student's *t* test ($n = 3$ samples/condition).

treatment of *Tsc2*^{-/-} cells with rapamycin. Of the five metabolites whose abundance significantly decreased ($P < 0.01$) after short-term rapamycin (Fig. 1C), only *N*-carbamoyl-aspartate was also both increased in abundance in the *Tsc2*^{-/-} cells relative to wild type (Fig. 1A) and sensitive to longer-term rapamycin (Fig. 1B), indicating that mTORC1 signaling positively influences the abundance of this metabolite. These changes are not due to differences in cell proliferation or cell cycle progression, which were similar between the *Tsc2*^{+/-} and *Tsc2*^{-/-} cells and unchanged after 1 hour of rapamycin treatment (fig. S1, A and B). *N*-carbamoyl-aspartate is generated in the first committed step of de novo pyrimidine biosynthesis, a pathway that combines nitrogen and carbon from glutamine, bicarbonate (HCO_3^-), and aspartate with ribose, derived from the pentose phosphate pathway, to form pyrimidine nucleotides (Fig. 1D).

To confirm the sensitivity of this metabolite to short-term rapamycin, as detected in *Tsc2*^{-/-} MEFs (Fig. 1E), we compared its abundance in other genetic settings with activated mTORC1 signaling after treatment with either vehicle or rapamycin.

In a normal human breast epithelial cell line, MCF10A—stably expressing either K-Ras^{G12V} or PI3K^{H1047R}, oncogenes that activate mTORC1 signaling (6)—*N*-carbamoyl-aspartate levels were also decreased after 1 hour of rapamycin treatment (Fig. 1F). In a *PTEN* null human glioblastoma cell line expressing doxycycline-inducible *PTEN* (U87MG-iPTEN) (7), *PTEN* reexpression or rapamycin treatment—both of which inhibit mTORC1 signaling in these cells—greatly reduced the abundance of *N*-carbamoyl-aspartate (Fig. 1G). Therefore, mTORC1 signaling affects the abundance of this metabolite in multiple cell settings.

To determine whether the effects of mTORC1 signaling on the steady-state abundance of *N*-carbamoyl-aspartate reflect regulation of metabolic flux through the de novo pyrimidine synthesis pathway, we measured relative flux with a 15-min pulse of stable-isotope-labeled ¹⁵N-glutamine, labeled on the amide nitrogen that is incorporated into the pyrimidine ring. Enhanced incorporation of label into multiple intermediates of pyrimidine synthesis was detected in *Tsc2*^{-/-} MEFs, and this was inhibited by short-term

rapamycin treatment (Fig. 2A). Although *Tsc2*^{-/-} cells exhibited increased glutamine uptake, this uptake was not sensitive to rapamycin at 1 hour (fig. S2A), demonstrating that the mTORC1-regulated flux is not a result of increased glutamine availability. Flux through pyrimidine synthesis was stimulated by insulin in wild-type MEFs (Fig. 2B and fig. S2B) or HeLa cells (fig. S2C) and was blocked by mTORC1 inhibition with rapamycin, or in response to amino acid starvation (fig. S2, D and E). mTORC1 signaling thus induces this metabolic pathway in response to both genetic and physiological stimuli. A 15-min pulse labeling with ¹³C-aspartate, which labels at the second step in the pathway (Fig. 1D), further confirmed the mTORC1-regulated flux (Fig. 2C). Because the pentose phosphate pathway converges with pyrimidine synthesis through ribose-5-phosphate and 5-phosphoribosyl-1-pyrophosphate (PRPP) (Fig. 1D), which can influence upstream steps in pyrimidine synthesis (8), and mTORC1 signaling promotes flux through the oxidative branch of this pathway through transcriptional effects (4), we analyzed de novo synthesis of pentose phosphate pathway products after exposure of cells

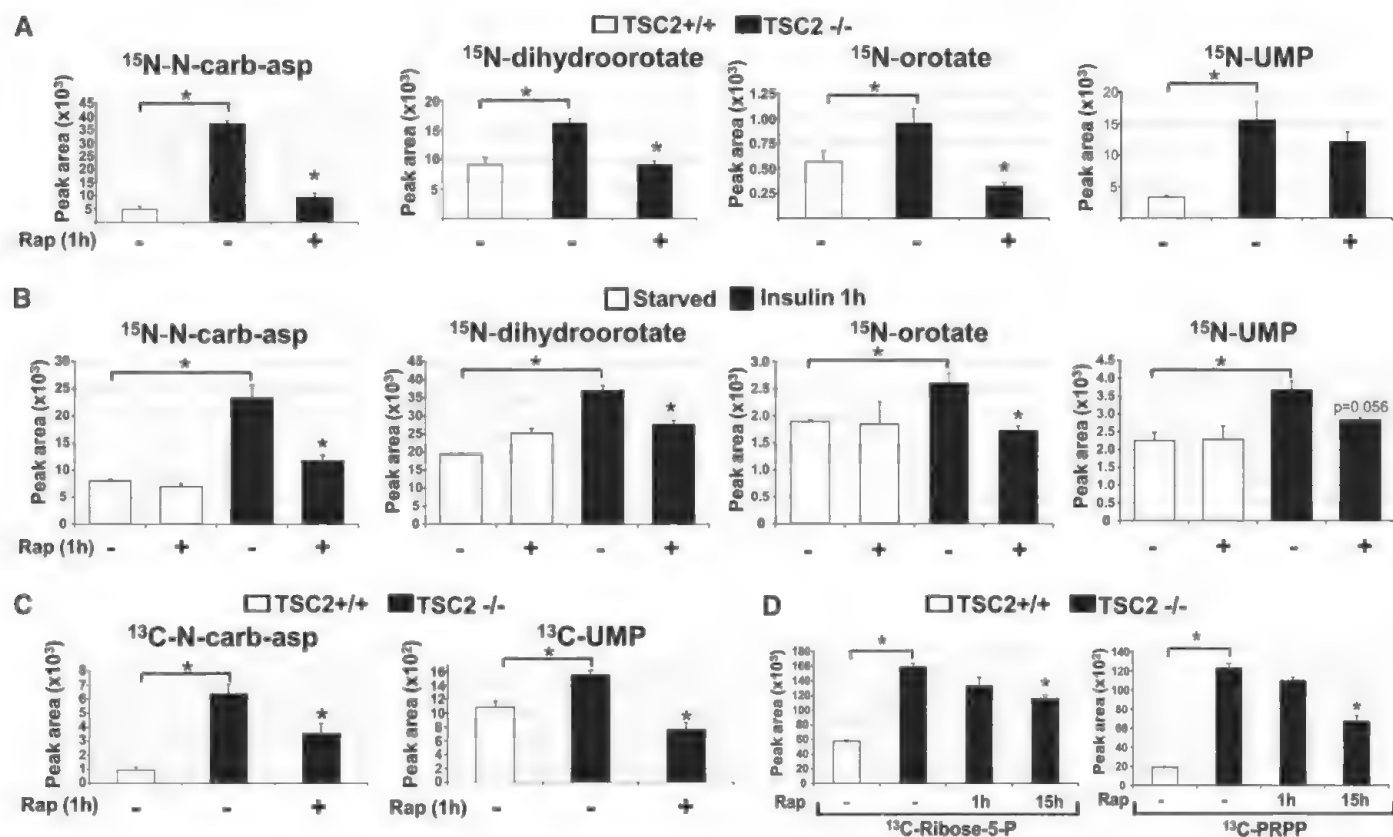


Fig. 2. Effects of genetic or insulin-stimulated activation of mTORC1 on metabolic flux through the de novo pyrimidine synthesis pathway. (A) Normalized peak areas of ¹⁵N-labeled metabolites, measured by means of LC/MS/MS, extracted from *Tsc2*^{+/-} and *Tsc2*^{-/-} MEFs grown in the absence of serum for 15 hours, with vehicle (DMSO) or rapamycin (20 nM) treatment over the last 1 hour and a 15-min pulse label of ¹⁵N-glutamine. (B) Normalized peak areas of ¹⁵N-labeled metabolites from wild-type MEFs treated as above, but stimulated with insulin (100 nM) for 1 hour where indicated. (C) Normalized peak

areas of ¹³C-labeled metabolites from cells treated as in (A), but with a 15-min pulse label of [4-¹³C]-aspartate before metabolite extraction. (D) Normalized peak areas of singly ¹³C-labeled metabolites from cells treated as in (A) but with rapamycin treatment for either 1 hour or 15 hours and 15-min pulse label with [1,2-¹³C]-glucose before metabolite extraction. In (A) to (D), all data are presented as mean \pm SEM over three independent samples per condition. * $P < 0.05$ for pairwise comparisons calculated by using a two-tailed Student's *t* test ($n = 3$ samples/condition), with all *P* values provided in table S3.

to a pulse of [1,2- 13 C]-glucose. *Tsc2*^{-/-} cells exhibited increased flux through the oxidative pentose phosphate pathway, leading to increased synthesis of ribose-5-phosphate and PRPP, and this was significantly sensitive to 15-hour (4), but not 1-hour, treatment with rapamycin (Fig. 2D). Therefore, the acute effects of mTORC1 signaling on pyrimidine synthesis are not through parallel effects on the pentose phosphate pathway.

To identify the mechanism by which mTORC1 signaling stimulates pyrimidine synthesis, we focused on the enzymes this pathway comprises. We found that neither the transcript nor protein levels of CAD (carbamoyl-phosphate synthetase 2, aspartate transcarbamoylase, dihydroorotase) and dihydroorotase dehydrogenase (DHODH), the first two enzymes of the pathway, were altered in settings in which mTORC1-dependent increases in flux through pyrimidine synthesis were detected (fig. S3, A to F). Rapamycin and a DHODH inhibitor [A771726 (9)] had opposing effects on both the steady-state—(fig. S3G) and de novo-synthesized (fig. S3H) amounts of *N*-carbamoyl-aspartate, with the DHODH inhibitor greatly increasing the abundance of this metabolite in *Tsc2*^{-/-} cells, suggesting that mTORC1 signaling does not influence DHODH activity but rather steps upstream.

Because CAD catalyzes the first three steps of the pathway (Fig. 1D), we performed MS/MS analyses on CAD immunopurified from insulin-stimulated cells in the presence or absence of rapamycin in order to identify potential mTORC1-regulated phosphorylation sites. Despite 85% coverage of the protein, we only identified two high stoichiometry phosphorylation sites in this analysis, S1859 and S1900 (fig. S4A). Whereas the ratio of peptides containing S1900 that were phosphorylated remained unchanged with insulin and rapamycin treatment, peptides phosphorylated on S1859 were only detected in samples from insulin-stimulated cells and were absent from those also treated with rapamycin (Fig. 3A). S1859 lies within a conserved linker region between the dihydroorotase (DHO; E3) and aspartate transcarbamoylase (ATC; E2) domains, and the phosphorylation site is conserved amongst vertebrate CAD orthologs (fig. S4B). This site can be phosphorylated in vitro by adenosine 3',5'-monophosphate (cAMP)-dependent protein kinase (PKA) (10) and was identified in two recent phospho-proteomic screens for mTORC1-regulated phosphorylation sites (11, 12). However, the cellular regulation and function of S1859 phosphorylation on CAD has not been described.

To characterize the mechanism of S1859 phosphorylation, we took advantage of its sequence context, which is recognized by an available phospho-Ser-motif antibody. The phospho-Ser-motif antibody recognizes CAD from cells stimulated with insulin, whereas a phosphorylation site mutant of CAD affecting S1859 was not detected by this antibody, establishing the specificity of the antibody for phospho-S1859 on CAD (Fig. 3B). The insulin-stimulated phosphorylation of CAD on this site was sensitive to rapamycin, confirming the dependence on mTORC1 activation (Fig. 3C). Because the S1859 motif resembles that recognized by basophilic kinases, such as Akt and S6K (13, 14), rather than the motif reported for mTOR (11), we determined whether this site was phosphorylated by S6 kinase 1 (S6K1) or S6K2 downstream of mTORC1. Like rapamycin, an S6K1-specific inhibitor [PF-4708671 (15)] blocked the insulin-stimulated phosphorylation of CAD-S1859, along with that of an established S6K1 target site on Rictor (Fig. 3C) (16). Likewise, small interfering RNA (siRNA)-mediated knockdown of S6K1, but not S6K2, attenuated CAD phosphorylation on S1859 (Fig. 3D). CAD and endogenous S6K1 coimmunoprecipitated (fig. S4C), and S6K1, but not catalytically inactive S6K1, directly phosphorylated CAD

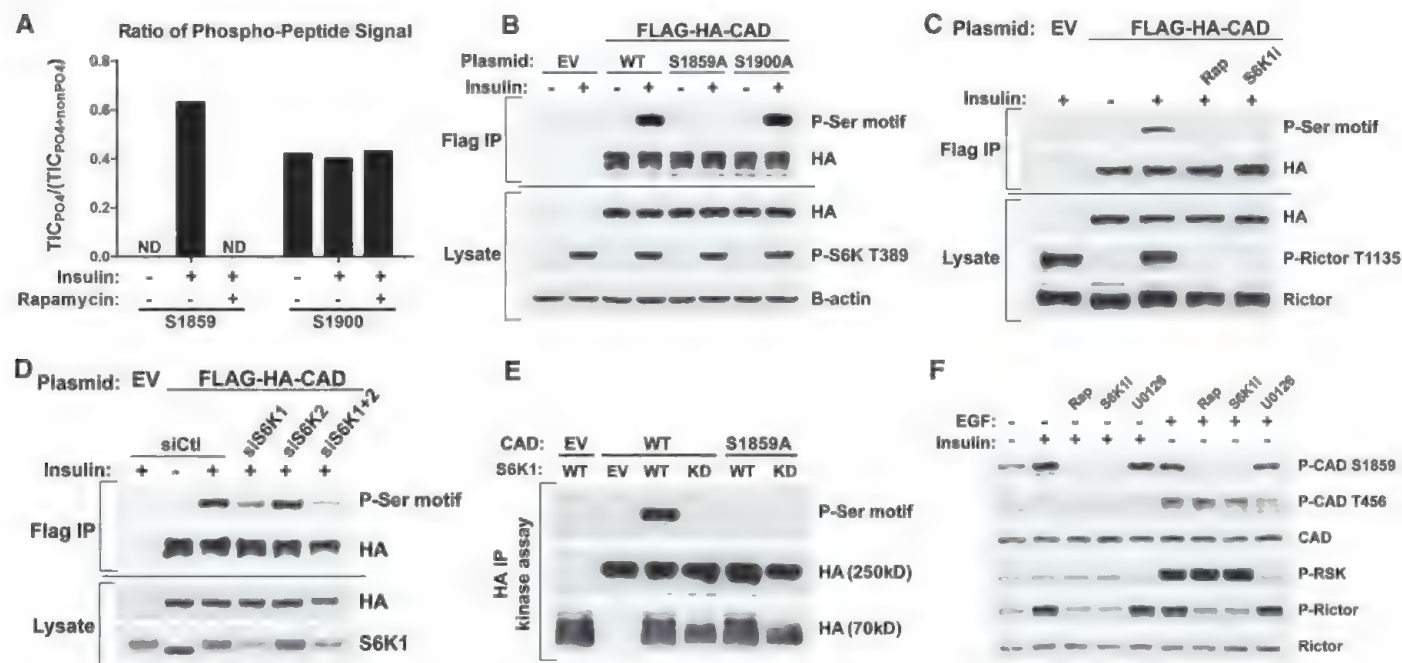


Fig. 3. CAD as a direct substrate of S6K1. (A) Effects of insulin and rapamycin on CAD phosphorylation sites. FLAG-hemagglutinin (HA)-CAD was immunopurified from serum-starved (16 hours) human embryonic kidney (HEK)-293E cells, treated for 1 hour with DMSO or rapamycin (20 nM), before stimulation with insulin (3 hours, 50 nM). The ratios of phosphorylated to total peptide levels, measured as total ion current (TIC) by means of LC/MS/MS, of the indicated sites on CAD under the different conditions are graphed. ND, phosphopeptide not detected. (B) HEK-293E cells expressing empty vector (EV) or wild-type (WT), S1859A, or S1900A versions of FLAG-HA-CAD were serum-starved (16 hours) and stimulated with insulin (1 hour, 100 nM). FLAG immunoprecipitates were immunoblotted with a phospho-14-3-3-binding motif

antibody (P-Ser motif). (C) Cells were treated as in (B) but pretreated for 1 hour with rapamycin (20 nM) or the S6K1 inhibitor PF-4708671 (10 μ M, S6K1i) before insulin stimulation. (D) Cells were treated as in (C) but were also transfected with siRNAs targeting S6K1, S6K2, or both, or nontargeting controls (siCtrl). (E) In vitro kinase assays were performed with FLAG-HA-CAD substrate (WT or S1859A) immunoprecipitated from serum-starved, rapamycin-treated HEK-293E cells and HA-S6K1 [WT or kinase dead (KD)] immunoprecipitated from insulin-stimulated HEK-293E cells. (F) HeLa cells were serum-starved (16 hours) and pretreated for 1 hour with rapamycin, S6K1i, or the MEK inhibitor U0126 (10 μ M) before 1 hour of stimulation with insulin (100 nM) or EGF (20 ng/mL).

on S1859 in vitro (Fig. 3E). A phospho-specific antibody to CAD-S1859 (fig. S4D) confirmed that endogenous CAD is phosphorylated on this residue in multiple cell lines in response to insulin or epidermal growth factor (EGF) in an mTORC1- and S6K1-dependent, but ERK- and RSK-independent, manner (Fig. 3F and fig. S4, E and F). S6K1 did not influence the phosphorylation of CAD on T456, which is phosphorylated by ERK in response to EGF (Fig. 3F) (17).

We sought to determine whether S6K1 activity influences flux through the pyrimidine synthesis pathway. Although long-term treatment with rapamycin can decrease glucose uptake and its flux through the oxidative pentose phosphate pathway (4), the S6K1-specific inhibitor did not affect glucose uptake in *Tsc2*^{-/-} cells (fig. S5A), and siRNA-mediated depletion of S6K1 did not influence pentose phosphate pathway flux in insulin-stimulated cells (fig. S5B). In contrast, the S6K1 inhibitor, like rapamycin, significantly decreased the insulin-stimulated flux from ¹⁵N-glutamine into metabolites of the pyrimidine synthesis pathway (Fig. 4A and fig. S5C), and this was also seen with siRNA-mediated depletion of S6K1,

but not S6K2 (Fig. 4B and fig. S5D). Similar effects of S6K1 depletion on pyrimidine flux were observed in *Tsc2*^{-/-} cells with constitutive mTORC1 signaling (fig. S5E). Thus, S6K1 is required for induction of de novo pyrimidine synthesis downstream of mTORC1.

To determine whether mTORC1 signaling influences the production of nucleic acids through its stimulation of de novo pyrimidine synthesis, we measured the incorporation of carbon from ¹⁴C-aspartate into RNA and DNA. To control for global effects on RNA and DNA synthesis, we also labeled cells with either ³H-uridine for RNA or ³H-thymidine for DNA, exogenous pyrimidines that bypass the de novo synthesis pathway. The DHODH inhibitor blocked the insulin-induced integration of ¹⁴C, but not ³H, into both RNA and DNA, validating the specificity of this assay for de novo pyrimidine synthesis (fig. S6A). The insulin-stimulated incorporation of both ¹⁴C-aspartate and ³H-uridine into RNA was inhibited by rapamycin (fig. S6, A and B), indicating that mTORC1 signaling influences both de novo pyrimidine synthesis and global RNA synthesis downstream of insulin. Because the

majority of cellular RNA is ribosomal, this finding is consistent with the multiple inputs from mTORC1 signaling into ribosomal RNA (rRNA) synthesis (2). However, the effects of rapamycin on the incorporation of pyrimidines into DNA was specific to those synthesized de novo (fig. S6, A and B). siRNA-mediated depletion of S6K1 also blocked the insulin-induced incorporation of ¹⁴C-aspartate into both RNA and DNA but, unlike rapamycin, did not affect the incorporation of exogenous pyrimidines (Fig. 4C). Ribosome purification from labeled cells depleted of S6K1 demonstrated that S6K1 was required for insulin to stimulate the incorporation of de novo-synthesized pyrimidines, but not exogenous pyrimidines, into rRNA (Fig. 4D). The role of S6K1 in the mTORC1-stimulated flux through pyrimidine synthesis into RNA and DNA was further confirmed in *Tsc2*^{-/-} cells depleted of S6K1 (fig. S6C).

To determine whether S6K1 regulates flux through the pyrimidine synthesis pathway through its direct phosphorylation of CAD-S1859, we used a chinese hamster ovary (CHO-K1)-derived cell line called G9C, which is auxotrophic for uridine because of a CAD deficiency (18). As in other

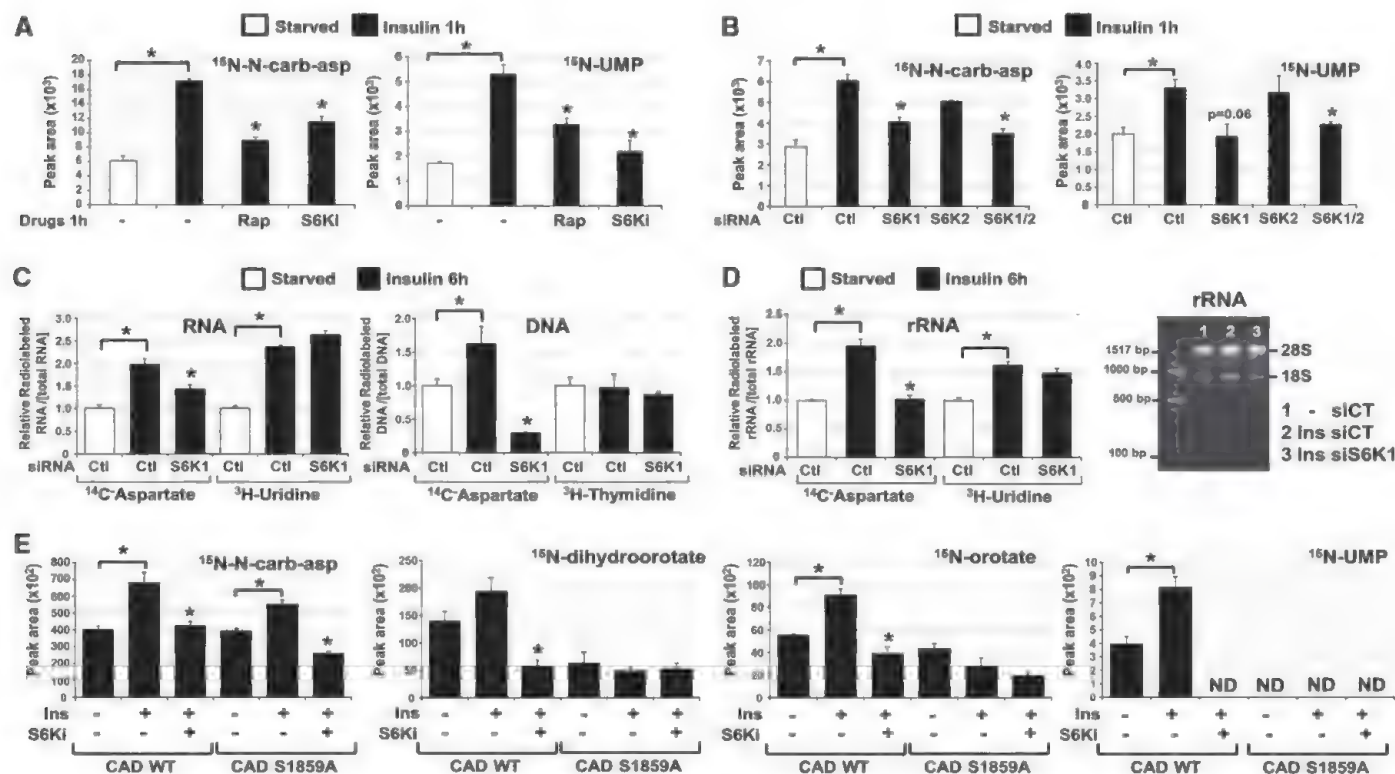


Fig. 4. Requirement of S6K1 and S1859 on CAD for the mTORC1-dependent stimulation of the de novo pyrimidine synthesis pathway. (A) Normalized peak areas of ¹⁵N-labeled metabolites, measured by means of LC/MS/MS, extracted from WT MEFs serum starved (15 hours) and insulin-stimulated (1 hour, 100 nM) in the presence of DMSO, rapamycin (20 nM), or PF-4708671 (10 μ M, S6K1), with a 15-min pulse label of ¹⁵N-glutamine. (B) Normalized peak areas of ¹⁵N-labeled metabolites from WT MEFs transfected with siRNAs targeting S6K1, S6K2, or both, or nontargeting controls (siCtl) were treated 48 hours after transfection as in (A). (C) The relative incorporation of radiolabel from ¹⁴C-aspartate, ³H-uridine, or ³H-thymidine into RNA and DNA from WT MEFs

transfected with siRNAs as in (B), serum starved (15 hours), and stimulated with insulin (6 hours, 100 nM), during which cells were radiolabeled. (D) The relative incorporation of radiolabel from ¹⁴C-aspartate or ³H-uridine into rRNA from WT MEFs treated as in (C). (Right) The purified rRNA was also assessed on an agarose gel. (E) Normalized peak areas of ¹⁵N-labeled metabolites in G9C cells expressing CAD WT or a S1859A mutant treated as in (A). ND, metabolite not detected. In (A) to (E), all data are presented as mean \pm SEM over three independent samples per condition. **P* < 0.05 for pairwise comparisons calculated by using a two-tailed Student's *t* test (*n* = 3 samples/condition), with all *P* values provided in table S4.

cell settings, insulin acutely stimulated an increase in labeling of intermediates in pyrimidine synthesis in G9C cells expressing wild-type CAD, and this was blocked by the S6K1 inhibitor (Fig. 4E and fig. S7, A and B). Although the synthesis of *N*-carbamoyl-aspartate increased in response to insulin in CAD-S1859A mutant-expressing G9C cells, the labeling of pyrimidine intermediates downstream of CAD was not stimulated by insulin, with these metabolites detected at amounts similar to that in wild-type cells treated with the S6K1 inhibitor (Fig. 4E). These data suggest that the S6K1-mediated phosphorylation of S1859 enhances the *in vivo* dihydroorotase (E3) activity of CAD, with additional points of regulation from insulin and S6K1 possibly affecting upstream steps in the pathway (fig. S7C). The cells expressing CAD-S1859A were no longer acutely sensitive to insulin for the stimulated incorporation of de novo-synthesized pyrimidines into RNA and DNA (fig. S7D).

This study demonstrates that mTORC1 serves as a molecular link between growth signals and acute control over pyrimidine synthesis. It is worth emphasizing that mTORC1 and S6K1 are not essential for de novo pyrimidine synthesis *per se* but are required to increase flux through this pathway in response to growth-promoting signals,

such as insulin and nutrients. The direct regulation of CAD by S6K1 serves as a mechanism to increase the pool of nucleotides available for the RNA and DNA synthesis that accompanies cell growth. In addition to protein and lipid synthesis, pyrimidine synthesis represents another major anabolic process that is responsive to changes in cellular growth conditions through mTORC1 signaling.

References and Notes

1. M. Laplante, D. M. Sabatini, *Cell* **149**, 274 (2012).
2. V. Iadevaia, Y. Huo, Z. Zhang, L. J. Foster, C. G. Proud, *Biochem. Soc. Trans.* **40**, 168 (2012).
3. T. Porstmann *et al.*, *Cell Metab.* **8**, 224 (2008).
4. K. Düvel *et al.*, *Mol. Cell* **39**, 171 (2010).
5. J. Huang, B. D. Manning, *Biochem. J.* **412**, 179 (2008).
6. S. Menon, B. D. Manning, *Oncogene* **27**, (Suppl 2), S43 (2008).
7. A. Radu, V. Neubauer, T. Akagi, H. Hanafusa, M. M. Georgescu, *Mol. Cell. Biol.* **23**, 6139 (2003).
8. M. Mori, M. Tatibana, *Methods Enzymol.* **51**, 111 (1978).
9. R. A. Williamson *et al.*, *Transplant. Proc.* **28**, 3088 (1996).
10. E. A. Carrey, D. G. Campbell, D. G. Hardie, *EMBO J.* **4**, 3735 (1985).
11. P. P. Hsu *et al.*, *Science* **332**, 1317 (2011).
12. Y. Yu *et al.*, *Science* **332**, 1322 (2011).
13. H. Flotow, G. Thomas, *J. Biol. Chem.* **267**, 3074 (1992).

14. D. R. Alessi, F. B. Caudwell, M. Andjelkovic, B. A. Hemmings, P. Cohen, *FEBS Lett.* **399**, 333 (1996).
15. L. R. Pearce *et al.*, *Biochem. J.* **431**, 245 (2010).
16. C. C. Dibble, J. M. Asara, B. D. Manning, *Mol. Cell. Biol.* **29**, 5657 (2009).
17. L. M. Graves *et al.*, *Nature* **403**, 328 (2000).
18. L. A. Musmanno, R. S. Jamison, R. S. Barnett, E. Buford, J. N. Davidson, *Somat. Cell Mol. Genet.* **18**, 309 (1992).

Acknowledgements: We thank M. Yuan and S. Breitkopf for technical assistance with MS/MS and D. Patterson, D. Kwiatkowski, and M. Zbinden for cell lines. This work was supported in part by a grant from the LAM Foundation (I.B.-S.); NIH grants F32-DK095508 (J.J.H.), P01-CA120964 (B.D.M. and J.M.A.), and R01-CA122617 (B.D.M.); Dana Farber/Harvard Cancer Center grant P30-CA006516 (J.M.A.); and a Sanofi Innovation Award (B.D.M.). I.B.-S. and J.J.H. conceived and performed all experiments, analyzed all experimental data, and prepared the manuscript. J.M.A. performed and analyzed the MS/MS experiments. B.D.M. directed the research, reviewed all experimental data, and prepared the manuscript. All authors have reviewed the manuscript and declare no competing financial interests.

Supplementary Materials

www.sciencemag.org/cgi/content/full/science.1228792/DC1
Materials and Methods
Figs. S1 to S7
Tables S1 to S4
References (19–23)

13 August 2012; accepted 25 January 2013
Published online 21 February 2013;
10.1126/science.1228792

Proteomic Mapping of Mitochondria in Living Cells via Spatially Restricted Enzymatic Tagging

Hyun-Woo Rhee,^{1*†} Peng Zou,^{1*} Namrata D. Udeshi,² Jeffrey D. Martell,¹ Vamsi K. Mootha,^{2,3,4} Steven A. Carr,² Alice Y. Ting^{1,2‡}

Microscopy and mass spectrometry (MS) are complementary techniques: The former provides spatiotemporal information in living cells, but only for a handful of recombinant proteins at a time, whereas the latter can detect thousands of endogenous proteins simultaneously, but only in lysed samples. Here, we introduce technology that combines these strengths by offering spatially and temporally resolved proteomic maps of endogenous proteins within living cells. Our method relies on a genetically targetable peroxidase enzyme that biotinylates nearby proteins, which are subsequently purified and identified by MS. We used this approach to identify 495 proteins within the human mitochondrial matrix, including 31 not previously linked to mitochondria. The labeling was exceptionally specific and distinguished between inner membrane proteins facing the matrix versus the intermembrane space (IMS). Several proteins previously thought to reside in the IMS or outer membrane, including protoporphyrinogen oxidase, were reassigned to the matrix by our proteomic data and confirmed by electron microscopy. The specificity of peroxidase-mediated proteomic mapping in live cells, combined with its ease of use, offers biologists a powerful tool for understanding the molecular composition of living cells.

We sought to develop a method that circumvents the limited specificity and loss of material associated with organelle purification in traditional mass spectrometry (MS)-based proteomics. Our approach involves tagging the proteome of interest with a chemical handle such as biotin while the cell

is still alive, with all membranes, complexes, and spatial relationships preserved. Thus, we required a genetically targetable labeling enzyme that covalently tags its neighbors, but not more distant proteins, in living cells. One candidate is promiscuous biotin ligase (1–3), but its labeling is extremely slow (requiring 24

hours) (fig. S1) (1, 2), and the proposed mechanism proceeds through a biotin-adenylate ester, which has a half-life of minutes, implying a large labeling radius. Horseradish peroxidase (HRP)-catalyzed nitrene generation is another possibility (4), but we were unable to detect this labeling (fig. S2), and HRP is inactive when expressed in the mammalian cytosol (5).

We recently introduced engineered ascorbate peroxidase (APEX) as a genetic tag for electron microscopy (EM) (5). Unlike HRP, APEX is active within all cellular compartments. In addition to catalyzing the H₂O₂-dependent polymerization of diaminobenzidine for EM contrast, APEX also oxidizes numerous phenol derivatives to phenoxyl radicals. Such radicals are short lived (<1 ms) (6, 7), have a small labeling radius (<20 nm) (8, 9), and can covalently react with electron-rich amino acids such as Tyr, Trp, His, and Cys (10–13). This chemistry forms the basis of tyramide signal amplification (14), but it has not been extended to living cells.

¹Department of Chemistry, Massachusetts Institute of Technology (MIT), Cambridge, MA 02139, USA. ²Broad Institute of MIT and Harvard, Cambridge, MA 02142, USA. ³Department of Molecular Biology, Massachusetts General Hospital, Boston, MA 02115, USA. ⁴Department of Systems Biology, Harvard Medical School, Boston, MA 02115, USA.

*These authors contributed equally to this work.

†Present address: Ulsan National Institute of Science and Technology, Ulsan, Korea.

‡To whom correspondence should be addressed. E-mail: ating@mit.edu

To examine whether APEX could be employed for proteomic labeling (Fig. 1A), we targeted APEX to the mitochondrial matrix of human embryonic kidney (HEK) cells and initiated labeling by adding biotin-phenol and 1 mM H_2O_2 to the cell medium. Labeling was terminated after 1 min by cell fixation or lysis. Imaging by confocal microscopy (Fig. 1B) or stochastic optical reconstruction microscopy (STORM) (Fig. 1C) (15) showed that biotinylated proteins overlapped tightly with the mito-APEX construct. Streptavidin blot analysis of cell lysates showed that numerous endogenous proteins were biotinylated in an APEX- and H_2O_2 -dependent manner (Fig. 1D and fig. S3).

To test the generality of our approach, we also analyzed other constructs that target APEX to different cellular regions (figs. S4 and S5). Seven different cytosol-facing APEX fusions gave distinct “fingerprints” in a streptavidin blot analysis, suggesting that targeted APEX biotinylates only a subset of cytosolic proteins, probably those in its close vicinity. We performed additional experiments to characterize the small-molecule specificity of APEX (fig. S2), the membrane permeability of the phenoxyl radical (fig. S6), and

the covalent adducts formed with amino acids in vitro (fig. S7; see also supplementary materials and methods).

We used mitochondrial matrix-targeted APEX to perform a proteomic experiment. Though mitochondria have been extensively characterized by MS proteomics, all previous studies have used mitochondrial purification, which is associated with sample loss and contamination. Consequently, the most comprehensive inventory of mitochondrial proteins (16) integrates MS proteomic data with green fluorescent protein imaging and computational analysis. Furthermore, proteome-scale maps of the matrix subcompartment in mammalian cells contain only a small number of proteins (17), representing very low coverage, probably because of the challenge of enriching for this subcompartment.

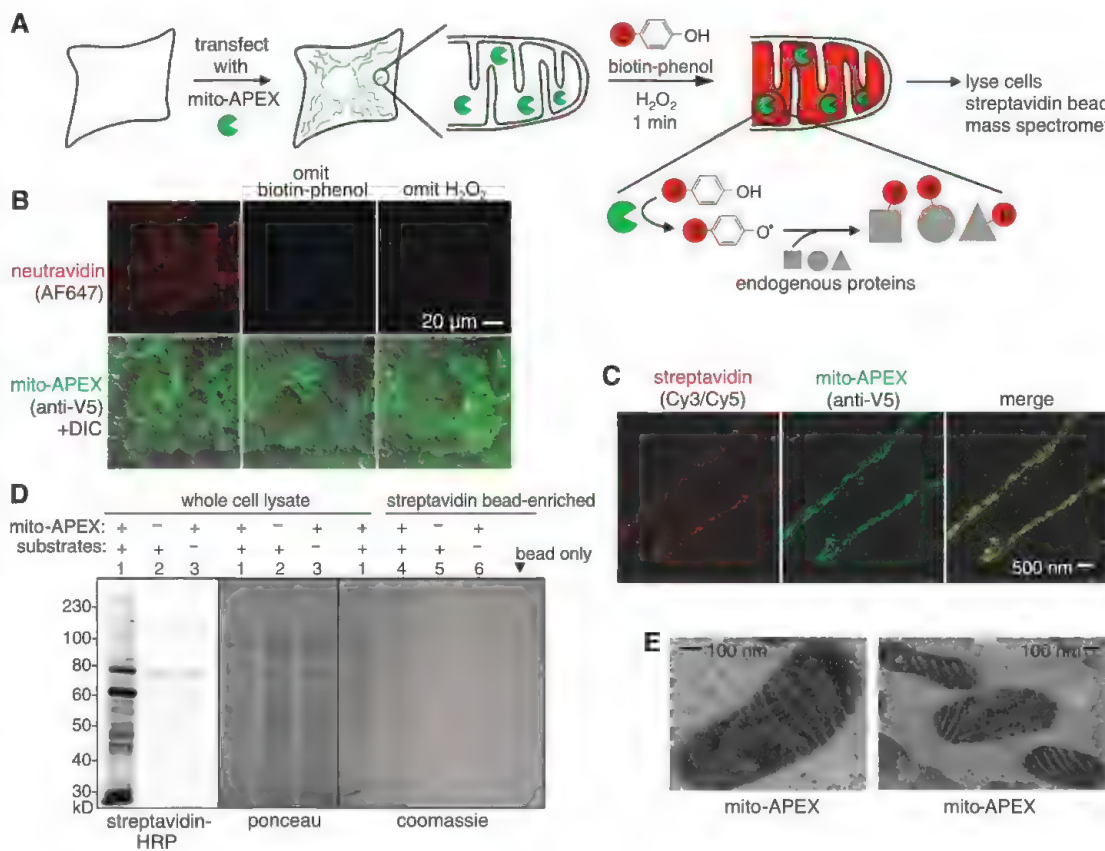
Endogenous proteins biotinylated by mito-APEX for 1 min in live HEK cells (as in Fig. 1) were purified using streptavidin beads, digested to peptides, and identified by tandem MS. We used stable isotope labeling (18) of experimental and control samples to distinguish between biotinylated proteins and nonspecific binders (fig. S8). We performed two independent replicates, each of

which produced a bimodal distribution of proteins based on isotope ratio (fig. S8C). The high-ratio distributions were strongly enriched for mitochondrial proteins, so we separated these hits and intersected the results from both replicates to obtain a list of 495 proteins (table S1), which we call our “matrix proteome.” This list is expected to contain both soluble matrix proteins and inner mitochondrial membrane (IMM) proteins that contact the matrix space.

Crossing our matrix proteome with earlier literature revealed that it was highly enriched for both mitochondrial and mitochondrial matrix proteins (Fig. 2A). Ninety-four percent (464 proteins) had prior mitochondrial annotation, leaving 31 “mitochondrial orphans” without any previously known connection to mitochondria (table S2). To further quantify the specificity of our matrix proteome, we examined the components of the electron-transport chain (Fig. 2C) and the TOM/TIM/PAM protein-import pathway (Fig. 2D), because they are structurally and/or topologically well characterized. In our matrix proteome, we detected only those subunits with exposure to the matrix space, illustrating the specificity and membrane-impermeability of our tagging.

Fig. 1. Labeling the mitochondrial matrix proteome in living cells.

(A) Labeling scheme. The APEX peroxidase was genetically targeted to the mitochondrial matrix via fusion to a 24-amino acid targeting peptide (5). Labeling was initiated by the addition of biotin-phenol and H_2O_2 to live cells for 1 min. Cells were then lysed, and biotinylated proteins were recovered with streptavidin-coated beads, eluted, separated on a gel, and identified by MS. The peroxidase-generated phenoxyl radical is short-lived and membrane-impermeant and, hence, covalently tags only neighboring and not distant endogenous proteins. **(B)** Biotin. Confocal fluorescence imaging of biotinylated proteins (stained with neutravidin) after live labeling of HEK cells expressing mito-APEX as in (A). Controls were performed with either biotin-phenol or H_2O_2 omitted. DIC, differential interference contrast. **(C)** Superresolution STORM images showing streptavidin and APEX (AF405/AF647) localization patterns at 22-nm resolution in U2OS cells. Samples were reacted as in (B). **(D)** Gel analysis of biotinylated mitochondrial matrix proteins, before (lanes 1 to 3) and after (lanes 4 to 6) streptavidin bead enrichment. Samples were labeled as in (B). Substrates are biotin-phenol and H_2O_2 . Mammalian cells have four endogenously biotinylated proteins, three of which were observed in the negative con-



control lanes (2 and 3) of the streptavidin blot. **(E)** Electron microscopy of HEK cells expressing mito-APEX. EM contrast was generated by treating fixed cells with H_2O_2 and diaminobenzidine. APEX catalyzes the polymerization of diaminobenzidine into a local precipitate, which is subsequently stained with electron-dense OsO_4 (5). Dark contrast is apparent in the mitochondrial matrix, but not the intermembrane space.

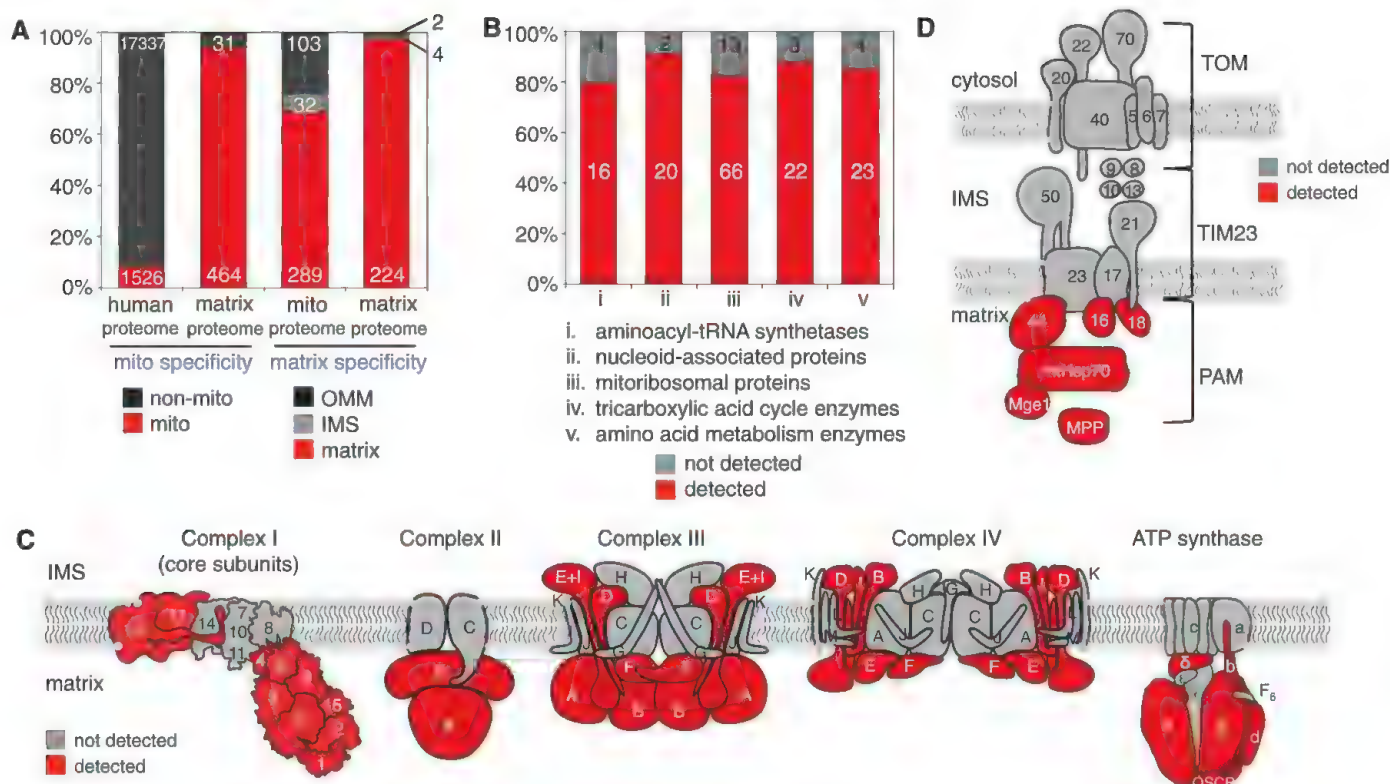


Fig. 2. Specificity and depth of coverage of the mitochondrial matrix proteome. (A) Analysis of specificity. The left two columns show the fraction of proteins with prior mitochondrial annotation in the entire human proteome (column 1) and in our matrix proteome (column 2). The right two columns show the distribution of proteins with prior submitochondrial localization information, for all mitochondrial proteins (column 3) and for our matrix proteome (column 4). See table S6 for details. (B) Analysis of depth of coverage. Five groups of well-established mitochondrial matrix proteins (i to v) were crossed with our proteomic list. For each group, 80 to 91% of proteins were detected in our matrix proteome. See table S7 for details. (C) Analysis of labeling specificity

for protein complexes of the IMM. The subunits of complexes I to IV and F_0F_1 adenosine triphosphate (ATP) synthase, for which structural information is available, are illustrated. Subunits detected in our matrix proteome are shaded red; those not detected are shaded gray. Note that because structural information is not available for all 45 subunits of complex I, some subunits that appear exposed here may not be exposed in the complete complex. OSCP, oligomycin sensitivity conferral protein. (D) Same analysis as in (C), for proteins of the TOM/TIM/PAM protein-import machinery that span the OMM and IMM. All proteins depicted in (C) and (D) are listed, with additional information, in table S8.

To analyze depth of coverage, we checked our matrix proteome for well-established groups of soluble matrix proteins (Fig. 2B). We detected members of each group at a rate of 80 to 90% and found nearly identical subsets of proteins in each of the two replicates, suggesting that coverage was high, but for only ~85% of proteins. The proteins we consistently did not detect were not low-abundance proteins (fig. S8F), nor did they lack surface-exposed tyrosine residues. We hypothesize that these proteins were sterically buried in macromolecular complexes, making them inaccessible to the phenoxyl radical.

For a subset of proteins in our proteome, we detected directly biotinylated peptides (fig. S9 and table S4). Tandem MS sequencing showed that biotin-phenol was conjugated to tyrosine side chains. In nearly all cases, the biotinylated tyrosine residue mapped to a surface-exposed site on a soluble protein or a matrix-exposed site on a transmembrane protein.

Our matrix proteome of 495 proteins provides a number of interesting insights. First, the 31 mitochondrial orphans may be newly discovered mitochondrial proteins. We selected and

imaged six of these at random and found complete or partial mitochondrial localization for all of them (fig. S10). Second, 240 proteins with unknown submitochondrial localization can now be assigned by our data to the matrix compartment (table S3). Third, we detected six proteins previously assigned to the intermembrane space (IMS) or outer mitochondrial membrane (OMM): PPOX, CPOX, PNPT1, CHCHD3, COASY, and SAMM50. To determine if our detection of these proteins in the matrix was accurate, we performed EM imaging, taking advantage of APEX's additional functionality as an EM tag (5). APEX fusions to five of the six proteins showed matrix staining by EM (Fig. 3 and fig. S11). We were unable to examine the final protein, SAMM50, because APEX insertion at four different sites abolished mitochondrial targeting.

The proteins PPOX and CPOX are particularly interesting in this group because they catalyze two of the later steps in heme biosynthesis (Fig. 3A). Previous studies on purified mitochondria or mitoplasts treated with proteases or membrane-impermeant inhibitors have localized both enzymes to the IMS (19–22). Structural anal-

ysis and modeling have indicated that PPOX docks to ferrochelatase (FECH), the final iron-inserting enzyme of heme biosynthesis, through the IMM (23) (Fig. 3F). This model is inconsistent with our EM data, because we found that both the C terminus and amino acid 205 of PPOX localize to the matrix (Fig. 3C). Our EM data on CPOX, on the other hand, are consistent with previous literature, because we found that residue 70 localizes to the matrix (explaining the detection of CPOX in our matrix proteome), whereas the C terminus and residue 120 flanking the active site localize to the IMS (Fig. 3D). Our reassignment of PPOX from the IMS to the matrix has implications for the nature of its interactions with CPOX and FECH and the mechanisms by which its substrates are transported across the IMM.

We have developed a method for mapping the proteomic composition of cellular organelles, using a genetically targetable peroxidase that catalyzes the generation of short-lived, highly reactive, and membrane-impermeant radicals in live cells. With a temporal resolution of 1 min, labeled proteins are harvested and identified by

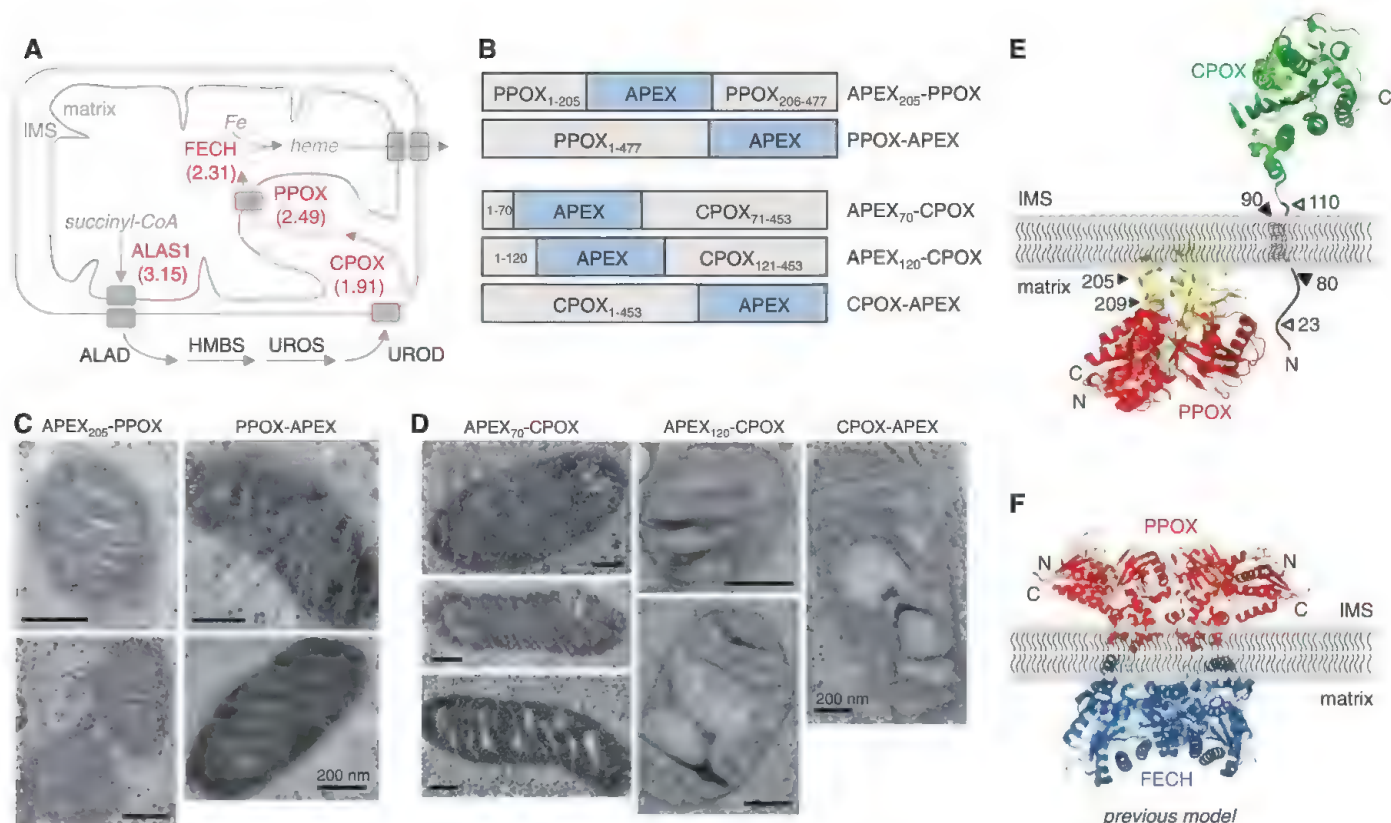


Fig. 3. Submitochondrial localization of the heme biosynthesis enzymes CPOX and PPOX. **(A)** Model showing the submitochondrial localizations of the eight core enzymes that catalyze heme biosynthesis, according to previous literature (24). Four of these enzymes are detected in our matrix proteome and are shown in red [with \log_2 (heavy/light) ratios from replicate 1. CoA, coenzyme A. Drawing adapted from (25). **(B)** Domain structures of PPOX and CPOX fusions to APEX, imaged by EM in **(C)** and **(D)**, respectively. Additional EM images of PPOX-APEX are shown in fig. S11B. Scale bars in **(C)** and **(D)**,

200 nm. **(E)** Our model for PPOX and CPOX localization, based on our EM data and previous literature (19–22). The predicted membrane-binding region of PPOX (residues 92 to 209) is shown in yellow (26). Hollow arrowheads point to predicted cleavage sites in CPOX. **(F)** Previous model showing the docking of a PPOX dimer and a FECH dimer through the IMM (23). N- and C-terminal ends of PPOX are labeled. Our data contradict this model, because the EM images in **(C)** show that the C terminus and residue 205 of PPOX are in the matrix, not the IMS.

MS with the use of well-established techniques. In addition to its simplicity, our method has no noticeable toxicity, requires far less material than conventional organellar proteomics, and takes hours to implement rather than days (as for subcellular fractionation). Our initial demonstration on the human mitochondrial matrix proteome shows that specificity is exceptionally high because labeling is performed in living cells while membranes and other structures are still intact. Depth of coverage is also high for the majority of proteins—most likely those that are sterically accessible to the phenoxyl radical. Notably, our method provides insight into the topology of identified proteins. Finally, the same peroxidase, APEX, can be used for both proteomic mapping and EM visualization (5).

References and Notes

- K. J. Roux, D. I. Kim, M. Raida, B. Burke, *J. Cell Biol.* **196**, 801 (2012).
- B. Morriswood *et al.*, *Eukaryot. Cell* **12**, 356 (2013).
- E. Choi-Rhee, H. Schulman, J. E. Cronan, *Protein Sci.* **13**, 3043 (2004).
- N. Kotani *et al.*, *Proc. Natl. Acad. Sci. U.S.A.* **105**, 7405 (2008).
- J. D. Martell *et al.*, *Nat. Biotechnol.* **30**, 1143 (2012).
- J. F. Wishart, B. S. Madhava Rao, in *Recent Trends in Radiation Chemistry* (World Scientific, Singapore, 2010), pp. 577–596.
- A. Mortensen, L. H. Skibsted, *J. Agric. Food Chem.* **45**, 2970 (1997).
- M. Bendayan, *Science* **291**, 1363 (2001).
- G. Mayer, M. Bendayan, *J. Histochem. Cytochem.* **45**, 1449 (1997).
- K. Minamihata, M. Goto, N. Kamiya, *Bioconjug. Chem.* **22**, 2332 (2011).
- M. S. Rogers *et al.*, *Biochemistry* **47**, 10428 (2008).
- B. Bhaskar *et al.*, *J. Mol. Biol.* **328**, 157 (2003).
- F. Amini, T. Kodadek, K. C. Brown, *Angew. Chem. Int. Ed. Engl.* **41**, 356 (2002).
- W. Schönhuber, B. Fuchs, S. Juretschko, R. Amann, *Appl. Environ. Microbiol.* **63**, 3268 (1997).
- H. Huang, M. Bates, X. Zhuang, *Annu. Rev. Biochem.* **78**, 993 (2009).
- D. J. Pagliarini *et al.*, *Cell* **134**, 112 (2008).
- F. Forner, L. J. Foster, S. Campanaro, G. Valle, M. Mann, *Mol. Cell. Proteomics* **5**, 608 (2006).
- S. E. Ong *et al.*, *Mol. Cell. Proteomics* **1**, 376 (2002).
- G. C. Ferreira, T. L. Andrew, S. W. Karr, H. A. Dailey, *J. Biol. Chem.* **263**, 3835 (1988).
- J.-C. Deybach, V. da Silva, B. Grandchamp, Y. Nordmann, *Eur. J. Biochem.* **149**, 431 (1985).
- G. H. Elder, J. O. Evans, *Biochem. J.* **172**, 345 (1978).
- B. Grandchamp, N. Phung, Y. Nordmann, *Biochem. J.* **176**, 97 (1978).
- M. Koch *et al.*, *EMBO J.* **23**, 1720 (2004).
- I. Hamza, H. A. Dailey, *Biochim. Biophys. Acta Mol. Cell Res.* **1823**, 1617 (2012).
- R. Nilsson *et al.*, *Cell Metab.* **10**, 119 (2009).
- X. Qin *et al.*, *FASEB J.* **25**, 653 (2011).

Acknowledgments: We thank N. Watson (Whitehead Institute Keck Microscopy Facility) and E. Vasil (Koch Institute Microscopy Core Facility) for performing EM imaging, H. B. Fraser for assistance with data analysis and manuscript editing, C. Uttamapinant for picoyl azide-AF647, X. Zhuang and her lab for advice on STORM, H. A. Dailey for advice on CPOX and PPOX, and S. Calvo for assistance with data analysis. Funding was provided by the NIH (grants DP1 OD003961 to A.Y.T. and R01 GM077465 to V.K.M.), the Dreyfus Foundation (A.Y.T.), the American Chemical Society (A.Y.T.), and the Broad Institute of MIT and Harvard (S.A.C.). The authors have no conflicting financial interests. A patent application relating to the use of enzymes for proteomic mapping in live cells has been filed by MIT. Proteomic data can be found in supplementary tables S1 to S9. The authors will make the genetic constructs used in this work widely available to the academic community through Addgene (www.addgene.org/).

Supplementary Materials

www.sciencemag.org/cgi/content/full/science.1230593/DC1
Materials and Methods
Figs. S1 to S11
Tables S1 to S9
References (27–53)

24 September 2012; accepted 11 January 2013
Published online 31 January 2013;
10.1126/science.1230593

The Genetic Basis for Bacterial Mercury Methylation

Jerry M. Parks,^{1*} Alexander Johs,^{2*} Mircea Podar,^{1,3*} Romain Bridou,⁴ Richard A. Hurt Jr.,¹ Steven D. Smith,⁴ Stephen J. Tomanicek,² Yun Qian,² Steven D. Brown,^{1,5} Craig C. Brandt,¹ Anthony V. Palumbo,¹ Jeremy C. Smith,^{1,5} Judy D. Wall,⁴ Dwayne A. Elias,^{1,5†} Liyuan Liang^{2†}

Methylmercury is a potent neurotoxin produced in natural environments from inorganic mercury by anaerobic bacteria. However, until now the genes and proteins involved have remained unidentified. Here, we report a two-gene cluster, *hgcA* and *hgcB*, required for mercury methylation by *Desulfovibrio desulfuricans* ND132 and *Geobacter sulfurreducens* PCA. In either bacterium, deletion of *hgcA*, *hgcB*, or both genes abolishes mercury methylation. The genes encode a putative corrinoid protein, HgcA, and a [2Fe-4S] ferredoxin, HgcB, consistent with roles as a methyl carrier and an electron donor required for corrinoid cofactor reduction, respectively. Among bacteria and archaea with sequenced genomes, gene orthologs are present in confirmed methylators but absent in nonmethylators, suggesting a common mercury methylation pathway in all methylating bacteria and archaea sequenced to date.

Mercury (Hg) is a pervasive global pollutant; in the form of methylmercury (CH_3Hg^+), it bioaccumulates in the food web and is highly toxic to humans and other organisms (1). Unlike inorganic forms of Hg, which originate from atmospheric deposition and point discharges, methylmercury is generated in the

environment predominantly by anaerobic microorganisms (2). Sulfate-reducing bacteria are the main producers of CH_3Hg^+ (3, 4), although iron-reducing bacteria (5–7) and methanogens (8, 9) can also be involved.

Production of CH_3Hg^+ by the model methylating bacteria *Desulfovibrio desulfuricans* ND132 and *Geobacter sulfurreducens* PCA involves cellular uptake of Hg(II) by active transport, methylation of Hg(II) in the cytosol, and export of CH_3Hg^+ from the cell (10). Hg methylation is an enzyme-catalyzed process proposed to be associated with the reductive acetyl-coenzyme A (CoA) pathway [also called the Wood-Ljungdahl pathway (11)] and potentially linked to corrinoid proteins involved in this pathway (12). However, no direct evidence firmly connects the acetyl-CoA pathway and the ability of bacteria to meth-

ylate Hg (13). Furthermore, phylogenetic analyses have not revealed any distinctive trends or clustering of methylating versus nonmethylating microorganisms (14–16).

To understand the genetic and biochemical basis of microbial Hg methylation, we analyzed the genomes of methylating and nonmethylating bacteria in the context of biochemical pathways involved in single-carbon metabolism. The well-characterized corrinoid iron-sulfur protein (CFeSP) is known to transfer methyl groups to a NiFeS cluster in acetyl-CoA synthase (17). Therefore, recognizing that a corrinoid protein associated with the acetyl-CoA pathway could be required for Hg methylation, we reasoned that a protein similar to CFeSP might transfer a methyl group to a Hg substrate to yield CH_3Hg^+ , and that genes encoding such a protein should be recognizable in the genome sequences of Hg-methylating bacteria. Complete genome sequences are available for six methylating and eight closely related nonmethylating bacterial species (tables S1 and S2). Furthermore, molecular structures and functions have been determined for various enzymes of the reductive acetyl-CoA pathway, including CFeSP from *Moorella thermoacetica* (18, 19) and *Carboxydothermus hydrogenoformans* (20, 21). Accordingly, we performed a BLASTP search with the sequence of the large subunit of CFeSP (CfsA, locus tag CHY_1223) from *C. hydrogenoformans* Z-2901 against the translated genome sequence of *D. desulfuricans* ND132 (22). Sequence similarity was found between the C-terminal corrinoid-binding domain of CfsA and the N terminus of DND132_1056 (fig. S1), although DND132_1056 lacks both the TIM barrel domain and the C-terminal [4Fe-4S] binding motif of CfsA. The C-terminal region showed no detectable similarity to any proteins of known structure, but exhibited

¹Biosciences Division, Oak Ridge National Laboratory, Oak Ridge, TN 37831, USA. ²Environmental Sciences Division, Oak Ridge National Laboratory, Oak Ridge, TN 37831, USA. ³Department of Microbiology, University of Tennessee, Knoxville, TN 37996, USA. ⁴Biochemistry Division, University of Missouri, Columbia, MO 65211, USA. ⁵Department of Biochemistry and Cellular and Molecular Biology, University of Tennessee, Knoxville, TN 37996, USA.

*These authors contributed equally to this work.

†To whom correspondence should be addressed. E-mail: liangl@ornl.gov (L.L.); eliasda@ornl.gov (D.A.E.)

D. desulfuricans ND132



D. aesopoeensis



D. africanus Walvis Bay



D. propionicus



G. sulfurreducens PCA



G. metallireducens

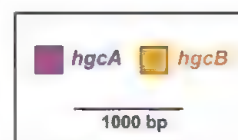


Fig. 1. Putative mercury methylation gene cluster and genomic context for six confirmed mercury methylators with sequenced genomes.

features characteristic of a transmembrane domain (fig. S2).

We also performed comparative genomic analyses of known Hg methylators and nonmethylators on the basis of Pfam classifications (23), with an emphasis on enzyme families known to be involved in methyl transfer reactions. The distribution of Pfam domains in the genomes is heterogeneous and, for the most part, does not coincide with the mercury methylation phenotype (table S3). However, the distribution of proteins of the CdhD family (PF03599, annotated as CO dehydrogenase/acetyl-CoA synthase delta subunit) encoded in the genomes correlates with the ability or inability of those organisms to methylate mercury. DND132_1056 is annotated as encoding a CdhD member, as are its close relatives in all five other confirmed methylators.

Analysis of the genomic context in the confirmed Hg methylators revealed genes similar to both the putative corrinoid protein-encoding gene and an additional, ferredoxin-like gene located downstream, which suggests that these two genes might be coexpressed and functionally related (Fig. 1). In *D. desulfuricans* ND132, the annotated coding sequences of the two genes (DND132_1056 and DND132_1057) are on the same strand and are separated by only 14 base pairs. Similar gene pairs were found in the genomes of 52 organisms with sequence translations available in public databases (table S4). The two genes are present in all sequenced, confirmed

methylators and absent in the sequenced, confirmed nonmethylators. The other 46 organisms in which the genes are present have not been tested for Hg methylation (table S4).

We hypothesized that these two genes are key components of the bacterial Hg methylation pathway, with the putative corrinoid protein facilitating methyl transfer and the ferredoxin carrying out corrinoid reduction. Therefore, we deleted these genes individually, and also together, from *D. desulfuricans* ND132 (supplementary text). Additionally, we deleted the orthologs GSU1440 and GSU1441 together, and GSU1440 individually, from *G. sulfurreducens* PCA. In both of these organisms, CH_3Hg^+ production decreased in the deletion mutants by >99% relative to the parental strains (Fig. 2). Complementation of the two-gene deletions by reincorporation of the genes into the chromosomes restored 26% and 87% of the wild-type methylation activity in *D. desulfuricans* ND132 and *G. sulfurreducens* PCA, respectively, as measured by inductively coupled plasma mass spectrometry (ICP-MS) (Fig. 2). Deletion of DND132_1057 alone yielded <0.2% of wild-type methylation activity, and subsequent complementation showed 97% methylation activity. Complementation of either gene alone into the double deletion mutant did not restore detectable methylation activity (Fig. 2). Restoration of $\Delta\text{DND132}_{1056}$ was not performed. Although the relative location of the two genes is consistent with cotranscription, reverse transcription poly-

merase chain reaction confirmed the transcription of DND132_1056 in the $\Delta\text{DND132}_{1057}$ strain and DND132_1057 in the $\Delta\text{DND132}_{1056}$ mutant (fig. S3).

The above findings are consistent with both genes being required for Hg methylation activity, although other unidentified genes are also likely to be involved. Hereafter, we refer to the DND132_1056 gene and its inferred orthologs as *hgcA*, encoding putative corrinoid proteins required for CH_3Hg^+ production, and DND132_1057 and its inferred orthologs as *hgcB*, encoding putative corrinoid protein-associated 2[4Fe-4S] ferredoxins. To determine whether gene loss impairs metabolism on a more general scale, we obtained comparative growth curves. The deletion mutants showed no impairment in rate or extent of growth (fig. S4). Thus, under the conditions tested, the construction of the deletions did not cause major growth aberrations that might interfere with the detection of methylation activity. The native functions of *hgcA* and *hgcB* remain unknown, but these genes are not essential for cell survival or proliferation.

The above findings merit some mechanistic considerations. The requirement for HgcA and HgcB in methylation is largely consistent with a previously proposed Hg methylation pathway by Bartha and co-workers (11), which we revise (fig. S5 and supplementary text). The methyl group in CH_3Hg^+ originates from $\text{CH}_3\text{-H}_4\text{-folate}$ in *D. desulfuricans* LS (11) and is likely first transferred (as CH_3^+) to cob(I)alamin-HgcA to form $\text{CH}_3\text{-cob(III)alamin-HgcA}$. This step may be catalyzed by a folate-binding methyltransferase similar to the $\text{CH}_3\text{-H}_4\text{-folate:CFeSP}$ methyltransferase (MeTr) from the reductive acetyl-CoA pathway (24, 25), or by an unknown enzyme (fig. S5 and supplementary text). The high affinity of thiolate ligands for Hg^{2+} [formation constants for $\text{Hg}(\text{SR})_2$, $\log K = 40$ to 43] (26) suggests that a possible substrate for HgcA could be a Hg(II) bis-thiolate complex involving either free cellular thiols or cysteine residues from a protein. Methyl transfer from $\text{CH}_3\text{-cob(III)alamin-HgcA}$ to a Hg substrate likely involves either CH_3^- or CH_3 . Although transfer of a carbanion from methylcobalamin to Hg(II) nonenzymatically is known to occur (27, 28), enzymatic transfer of CH_3^- by a corrinoid protein has never been observed.

Further sequence analysis of the 52 HgcA orthologs (Fig. 3) revealed a highly conserved motif, Asn-(Val/Ile)-Trp-Cys-Ala-(Ala/Gly)-Gly-Lys, in the region of highest similarity to the CfsA subunit of CFESP. This region corresponds to the cap helix of CFESP, which is located near the lower axial face of the corrin ring (20). In all HgcA sequences, a strictly conserved cysteine (Cys⁹³ in *D. desulfuricans* ND132) occupies the position corresponding to Thr³⁷⁴ in CFESP from *C. hydrogenoformans* Z-2901 (Fig. 3 and fig. S1). Although Thr³⁷⁴ is not considered a ligand for Co (19, 20), a cysteine might coordinate to Co, depending on its location relative to the cofactor and the Co oxidation state. Homology modeling

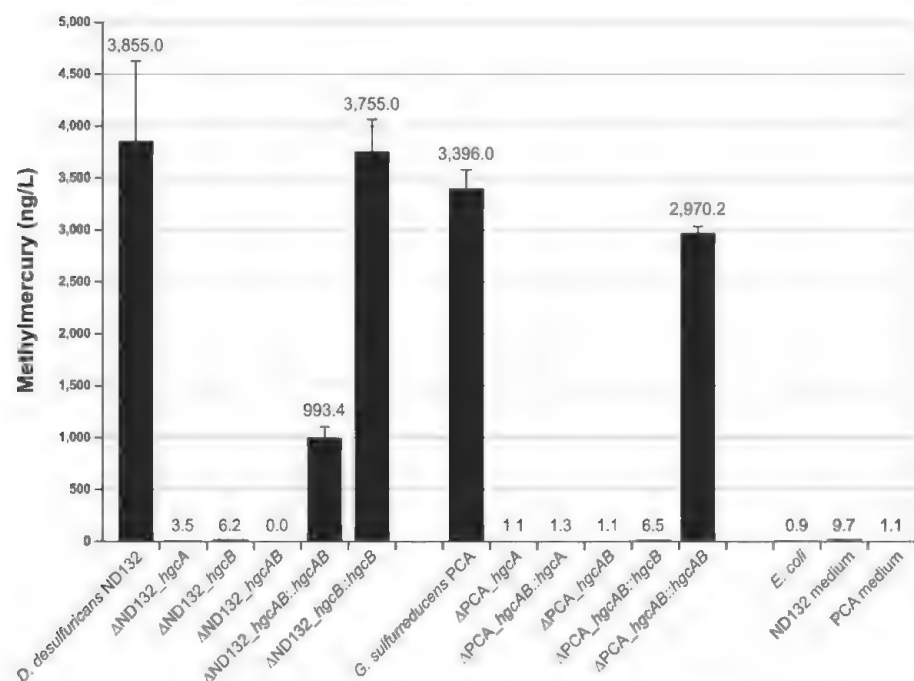


Fig. 2. Production of methylmercury by *D. desulfuricans* ND132 and *G. sulfurreducens* PCA, by deletions of *hgcA*, *hgcB*, and *hgcAB*, and by complements in both bacteria. CH_3Hg^+ concentrations (ng/liter) were determined after overnight incubations and measured by ICP-MS. The prefix Δ indicates a gene deletion; the symbol :: indicates complementation by chromosomal insertion. Values plotted are the average CH_3Hg^+ concentrations detected per strain from triplicate assays; error bars denote SD. Note that ΔPCA_{hgcAB} complemented with PCA_{hgcA}^+ or PCA_{hgcB}^+ is still deleted for PCA_{hgcB} or PCA_{hgcA} , respectively.

(fig. S6) and ultraviolet-visible spectra (fig. S7) of the cobalamin-binding domain of HgcA suggest that Co-S coordination may be present in HgcA. Lower axial coordination of alkyl-cob(III) alamin by a biological thiolate has been proposed previously (29) but has never been observed for a corrinoid protein. The likely role of the ferredoxin-like protein HgcB is to accomplish

the thermodynamically difficult reduction of Co(II) to Co(I) required for turnover, consistent with a previously suggested need for a ferredoxin as a reductant in Hg methylation (11). The mechanistic details of methyl transfer (supplementary text), the integration of these two gene products into carbon and energy metabolism, and their functioning with other poten-

tial, as yet unidentified, proteins remain to be determined.

In the absence of genome sequences for all Hg-methylating organisms, the generality of the present findings cannot yet be ascertained. However, our interpretation is in agreement with all currently available sequence information for methylating bacteria and archaea. The presence

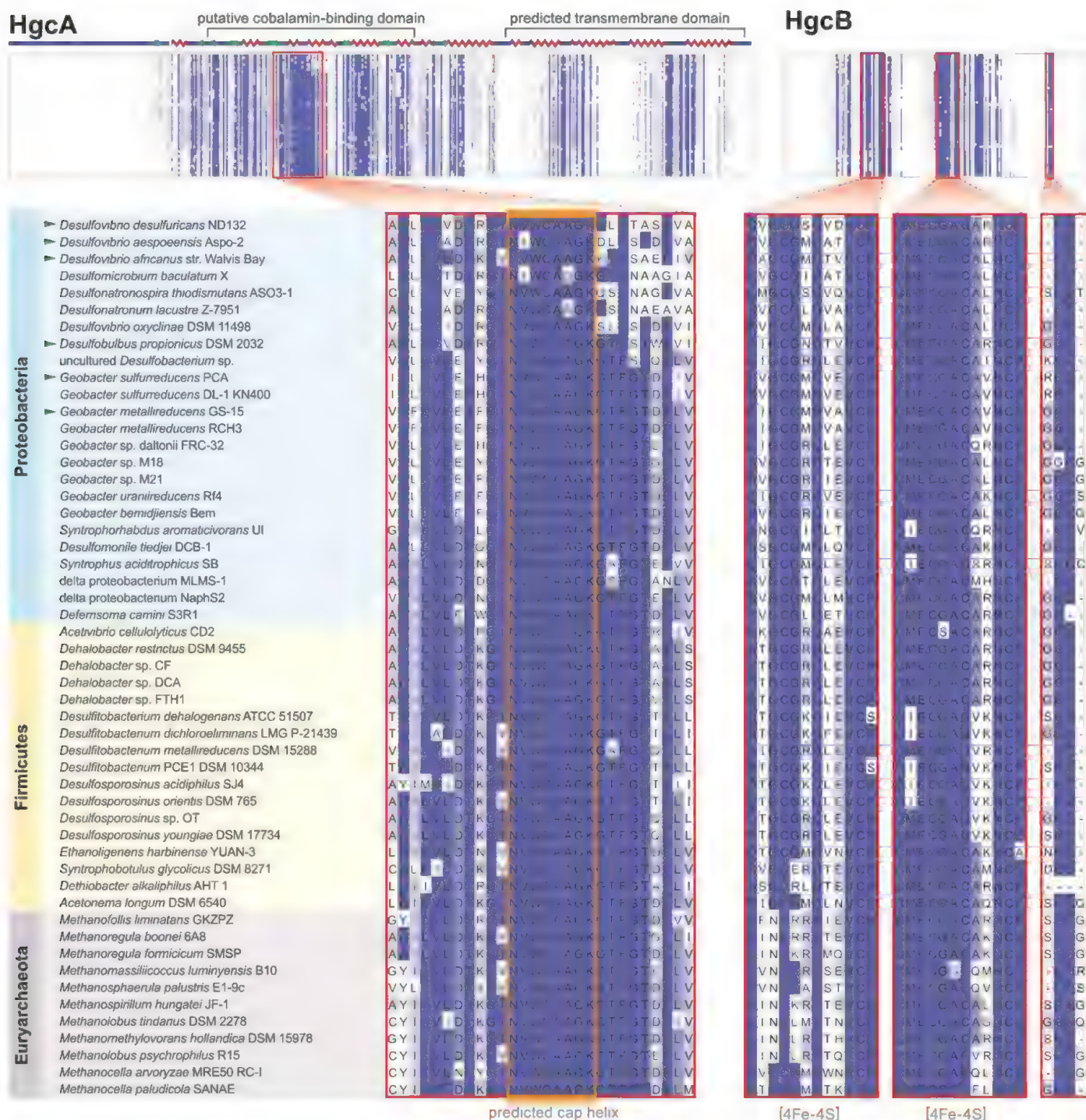


Fig. 3. Multiple sequence alignments of 52 HgcA and HgcB orthologs from bacteria and archaea, including six confirmed methylating bacteria (arrowheads). Red boxes indicate highly conserved regions including the putative cap helix [consensus sequence motif, N(V/I)WCA(A/G)GK] in HgcA, two strictly conserved

CX₂CX₂CX₃C motifs characteristic of [4Fe-4S] clusters, and a conserved vicinal pair of cysteines located at the C terminus of HgcB. Abbreviations for amino acid residues: A, Ala; C, Cys; D, Asp; E, Glu; F, Phe; G, Gly; H, His; I, Ile; K, Lys; L, Leu; M, Met; N, Asn; P, Pro; Q, Gln; R, Arg; S, Ser; T, Thr; V, Val; W, Trp; Y, Tyr; X, any amino acid.

of the *hgcAB* cluster in the genomes of several sequenced, but so far untested, microorganisms (table S4) leads us to hypothesize that these organisms are also capable of methylating mercury. The gene cluster appears to be quite sporadically distributed across two phyla of bacteria (Proteobacteria and Firmicutes) and one phylum of archaea (Euryarchaeota). Organisms possessing the two-gene cluster include 24 strains of Deltaproteobacteria, 16 Clostridia, 1 Negativicutes, and 11 Methanomicrobia. Interestingly, we also found these genes in a psychrophile (30), in a thermophile (31), and in a human commensal methanogen (32) (Fig. 3). The sparse phylogenetic gene distribution of the *hgcAB* system may be due to gene loss or lateral gene transfer (or both) across distant taxa and may be linked to environmental and community-structure factors. The sporadic distribution of these genes and the lack of an obvious selective advantage related to mercury toxicity (15) raise important questions regarding their physiological roles. Identification of these genes is a critical step linking specific microorganisms and environmental factors that influence microbial Hg methylation in aquatic ecosystems.

References and Notes

1. J. M. Wood, *Science* **183**, 1049 (1974).
2. H. Hintelmann, *Met. Ions Life Sci.* **7**, 365 (2010).
3. G. C. Compeau, R. Bartha, *Appl. Environ. Microbiol.* **50**, 498 (1985).
4. C. C. Gilmour, E. A. Henry, R. Mitchell, *Environ. Sci. Technol.* **26**, 2281 (1992).
5. E. J. Fleming, E. E. Mack, P. G. Green, D. C. Nelson, *Appl. Environ. Microbiol.* **72**, 457 (2006).
6. E. J. Kerin et al., *Appl. Environ. Microbiol.* **72**, 7919 (2006).
7. R. Q. Yu et al., *Environ. Sci. Technol.* **46**, 2684 (2012).
8. J. M. Wood, F. S. Kennedy, C. G. Rosen, *Nature* **220**, 173 (1968).
9. S. Hamelin, M. Amyot, T. Barkay, Y. P. Wang, D. Planas, *Environ. Sci. Technol.* **45**, 7693 (2011).
10. J. K. Schaefer et al., *Proc. Natl. Acad. Sci. U.S.A.* **108**, 8714 (2011).
11. S. C. Choi, T. Chase Jr., R. Bartha, *Appl. Environ. Microbiol.* **60**, 4072 (1994).
12. S. C. Choi, T. Chase Jr., R. Bartha, *Appl. Environ. Microbiol.* **60**, 1342 (1994).
13. E. B. Ekstrom, F. M. Morel, J. M. Benoit, *Appl. Environ. Microbiol.* **69**, 5414 (2003).
14. M. Ranchou-Peyruse et al., *Geomicrobiol. J.* **26**, 1 (2009).
15. C. C. Gilmour et al., *Appl. Environ. Microbiol.* **77**, 3938 (2011).
16. R.-Q. Yu et al., *Environ. Sci. Technol.* **46**, 2684 (2012).
17. T. I. Doukov, T. M. Iverson, J. Seravalli, S. W. Ragsdale, C. L. Drennan, *Science* **298**, 567 (2002).
18. Y. Kung et al., *Nature* **484**, 265 (2012).
19. S. W. Ragsdale, P. A. Lindahl, E. Münck, *J. Biol. Chem.* **262**, 14289 (1987).
20. T. Svetlichnaia, V. Svetlichnyi, O. Meyer, H. Dobbek, *Proc. Natl. Acad. Sci. U.S.A.* **103**, 14331 (2006).
21. S. Goetzl, J. H. Jeoung, S. E. Hennig, H. Dobbek, *J. Mol. Biol.* **411**, 96 (2011).
22. S. D. Brown et al., *J. Bacteriol.* **193**, 2078 (2011).
23. M. Punta et al., *Nucleic Acids Res.* **40** (database issue), D290 (2012).
24. H. L. Drake, S. I. Hu, H. G. Wood, *J. Biol. Chem.* **256**, 11137 (1981).
25. T. Doukov, J. Seravalli, J. J. Stezowski, S. W. Ragsdale, *Structure* **8**, 817 (2000).
26. P. Cardiano, G. Falcone, C. Foti, S. Sammartano, *J. Chem. Eng. Data* **56**, 4741 (2011).

27. R. E. DeSimone et al., *Biochim. Biophys. Acta* **304**, 851 (1973).
28. H. A. O. Hill, J. M. Pratt, S. Ridsdale, F. R. Williams, *J. Chem. Soc. Chem. Commun.* **1970**, 341 (1970).
29. G. N. Schrauzer, J. W. Sibert, *J. Am. Chem. Soc.* **92**, 3509 (1970).
30. G. S. Zhang, N. Jiang, X. L. Liu, X. Z. Dong, *Appl. Environ. Microbiol.* **74**, 6114 (2008).
31. G. B. Slobodkina et al., *Int. J. Syst. Evol. Microbiol.* **62**, 2463 (2012).
32. B. Dridi, M. L. Fardeau, B. Ollivier, D. Raoult, M. Drancourt, *Int. J. Syst. Evol. Microbiol.* **62**, 1902 (2012).

Acknowledgments: We thank S. Miller, C. Gilmour, and T. Barkay for helpful discussions, and K. Rush, X. Yin, G. Christensen, and Q. Gui for experimental assistance. Supported by the U.S. Department of Energy (DOE), Office of Science, Office of Biological and Environmental Research, through the Mercury Scientific Focus Area Program at Oak Ridge National Laboratory (ORNL). ORNL is managed by UT Battelle, LLC, for DOE under contract DE-AC05-00OR22725. All other data are available online in the supplementary materials. Author contributions: J.M.P., A.J., R.B., J.C.S., A.V.P., D.A.E., S.D.B., M.P., J.D.W., and L.L. designed the research. M.P., S.D.B., and C.C.B. performed the comparative genomic analyses. A.J. and J.M.P. performed the bioinformatics and biochemical interpretations. R.B., R.A.H., S.D.S., S.J.T., A.J., and Y.Q. performed the experiments. J.M.P., A.J., R.B., J.C.S., D.A.E., J.D.W., and L.L. wrote the paper.

Supplementary Materials

www.sciencemag.org/cgi/content/full/science.1230667/DC1
Materials and Methods
Supplementary Text
Figs. S1 to S9
Tables S1 to S8
References (33–69)

24 September 2012; accepted 23 January 2013

Published online 7 February 2013;

10.1126/science.1230667

The *C9orf72* GGGGCC Repeat Is Translated into Aggregating Dipeptide-Repeat Proteins in FTL/ALS

Kohji Mori,^{1*} Shih-Ming Weng,^{2*} Thomas Arzberger,³ Stephanie May,² Kristin Rentzsch,² Elisabeth Kremmer,⁴ Bettina Schmid,^{2,5} Hans A. Kretschmar,³ Marc Cruts,^{6,7} Christine Van Broeckhoven,^{6,7} Christian Haass,^{1,2,5†} Dieter Edbauer^{1,2,5†}

Expansion of a GGGGCC hexanucleotide repeat upstream of the *C9orf72* coding region is the most common cause of familial frontotemporal lobar degeneration and amyotrophic lateral sclerosis (FTLD/ALS), but the pathomechanisms involved are unknown. As in other FTLD/ALS variants, characteristic intracellular inclusions of misfolded proteins define *C9orf72* pathology, but the core proteins of the majority of inclusions are still unknown. Here, we found that most of these characteristic inclusions contain poly-(Gly-Ala) and, to a lesser extent, poly-(Gly-Pro) and poly-(Gly-Arg) dipeptide-repeat proteins presumably generated by non-ATG-initiated translation from the expanded GGGGCC repeat in three reading frames. These findings directly link the FTLD/ALS-associated genetic mutation to the predominant pathology in patients with *C9orf72* hexanucleotide expansion.

Frontotemporal lobar degeneration (FTLD) and amyotrophic lateral sclerosis (ALS) are the extreme ends of a spectrum of overlapping neurodegenerative disorders variably associated with dementia, personality changes, language abnormalities, and progressive muscle

weakness (1–3). The majority of patients show intracellular inclusions that are strongly positive for phosphorylated TDP-43 (classified as FTLD-TDP, FTLD/ALS-TDP, or ALS-TDP). Recently, expansion of a GGGGCC hexanucleotide repeat in the gene *C9orf72* has been identified as the

most common pathogenic mutation in families with autosomal dominant FTLD, FTLD/ALS, and ALS (4–6). The expansion is located upstream of the *C9orf72* coding region, either in the first intron or the promoter region, depending on the transcript isoform (fig. S1A). Although the extreme GC content precludes sequencing in patients, the number of GGGGCC repeat units is believed to be at least several hundred, compared with fewer than 25 in healthy controls (7).

Patients with a *C9orf72* repeat expansion mutation have clinical symptoms similar to other FTLD/ALS-TDP patients but show several unique

¹Adolf Butenandt-Institute, Biochemistry, Ludwig-Maximilians-University (LMU) Munich, Schillerstrasse 44, 80336 Munich, Germany. ²German Center for Neurodegenerative Diseases (DZNE), Munich, Schillerstrasse 44, 80336 Munich, Germany.

³Center for Neuropathology and Prion Research, Ludwig-Maximilians-University Munich, Feodor-Lynen-Strasse 23, 81377 Munich, Germany. ⁴Institute of Molecular Immunology, Helmholtz Zentrum München, Marchioninistrasse 25, 81377 Munich, Germany. ⁵Munich Cluster of Systems Neurology (SyNergy), Ludwig-Maximilians-University Munich, Schillerstrasse 44, 80336 Munich, Germany. ⁶Neurodegenerative Brain Diseases Group, Department of Molecular Genetics, VIB, Universiteitsplein 1, B-2610 Antwerp, Belgium. ⁷Laboratory of Neurogenetics, Institute Born-Bunge, University of Antwerp, Universiteitsplein 1, B-2610 Antwerp, Belgium.

*These authors contributed equally to this work.

†To whom correspondence should be addressed. E-mail: dieter.edbauer@dzne.de

pathological features (8–12). Aggregates of phosphorylated TDP-43 are accompanied by abundant dotlike and star-shaped phospho-TDP-43-negative neuronal cytoplasmic inclusions—in particular, in cerebellum, hippocampus, and frontotemporal neocortex—that can only be identified with antibodies for p62, ubiquitin, or the related ubiquilins (8–11). These phospho-TDP-43-negative aggregates are highly characteristic of diseased *C9orf72* mutation carriers and are absent in other variants of FTL/ALS-TDP (9–11). The identity of the disease protein(s) in these inclusions and their relation to the *C9orf72* hexanucleotide repeat expansion have remained elusive. Proposed pathomechanisms include haploinsufficiency through impaired transcription or splicing of the mutant *C9orf72* allele and RNA toxicity through the sequestration of unidentified RNA-binding proteins (3–7).

We hypothesized that the intronic GGGGCC repeat might be aberrantly translated into dipeptide-repeat (DPR) proteins. Although quite rare, two mechanisms of non-ATG-initiated translation have been described: Initiation from alternative start codons with a good Kozak sequence is possible (13–15), and hairpin formation in the repeat region may trigger so-called repeat-associated non-ATG-initiated (RAN) translation, as described for CAG repeats in ataxin 8 (*ATXN8*) (16–18). *ATXN8* encodes a natural poly-Q stretch that can cause poly-Q inclusions upon repeat expansion in spinocerebellar ataxia type 8 (SCA8) patients. Strikingly, the expanded CAG repeat is translated in all three reading frames (poly-Q, poly-A, and poly-S) even after removal of the endogenous start codon.

Translation of the GGGGCC repeat in all reading frames would result in three DPR proteins: poly-(Gly-Ala), poly-(Gly-Pro), and poly-(Gly-Arg). Poly-GA and poly-GP proteins are extremely hydrophobic and may form intracellular aggregates. We raised antibodies (anti-GA and anti-GP) against (GA)₁₅ and (GP)₁₅ peptides fused to maltose binding protein and tested a monoclonal antibody (anti-GR) that was originally raised against an EBNA2A epitope with a (GR)₆ repeat (19). All three affinity-purified DPR antibodies detected the respective repeat antigen by immunoblotting without cross-reaction with the other two DPR proteins (Fig. 1A).

To investigate whether such repeat proteins can be translated in the absence of a start codon, we cloned parts of the repeat region from *C9orf72* patients into a mammalian expression vector. For the longer constructs, we could only use restriction digest to estimate the repeat number ranging from ~28 to ~145 (Fig. 1B), because the extreme GC content precludes sequencing. The region upstream of the GGGGCC repeat lacks ATG start codons and contains four to five stop codons, depending on the reading frame. Upon transfection of these constructs into human embryonic kidney (HEK) 293 cells, anti-GA detected proteins of increasing size starting with a faint product from ~38 repeats, suggesting that the translation

mechanism becomes more efficient with increasing repeat length (Fig. 1B). We did not detect poly-GR products, and only the longest construct with ~145 repeats additionally expressed detectable amounts of poly-GP (Fig. 1B).

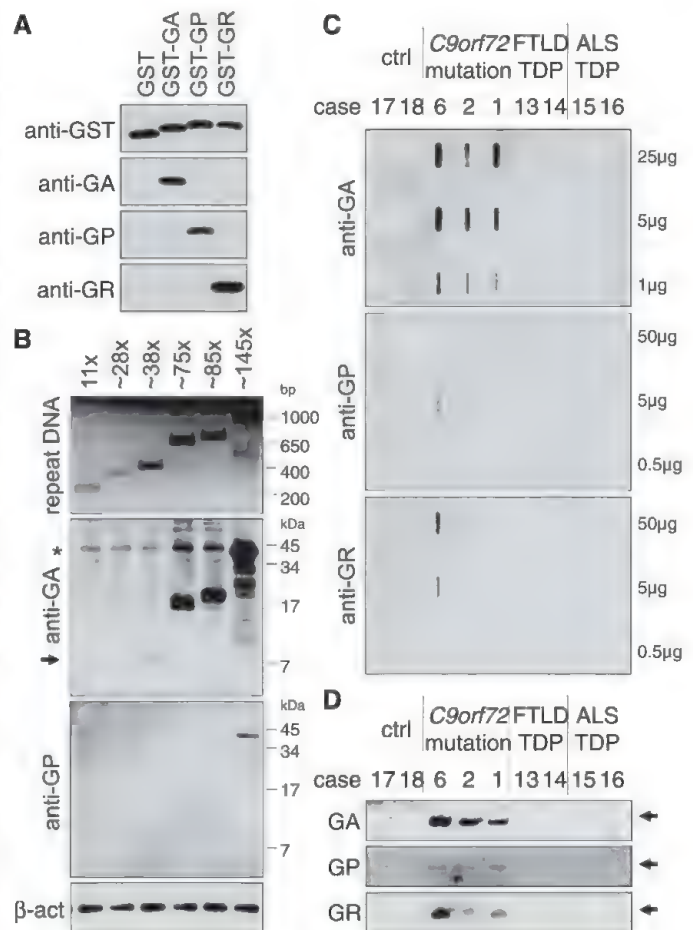
To analyze poly-GA aggregation, we performed filter trap assays (20) using 2% sodium dodecyl sulfate (SDS) extracts from human postmortem cerebellum of healthy controls and FTL/ALS-TDP patients with and without pathological *C9orf72* hexanucleotide repeat expansion. We observed strong poly-GA signal only in FTL/ALS patient with hexanucleotide repeat expansion (Fig. 1C), indicating that poly-GA forms SDS-insoluble aggregates in the cerebellum. We also detected insoluble poly-GP and poly-GR in *C9orf72* patients (Fig. 1C). The 2% SDS-insoluble material was partially solubilized upon boiling in 8% SDS and could be analyzed by immunoblotting. We detected high-molecular weight DPR aggregates in all three reading frames at the top of the gel specifically in patients with *C9orf72* mutation (Fig. 1D).

mRNA expression of the mutant *C9orf72* allele is reported to be repressed through impaired transcription or splicing (4, 6, 7). We also found

reduced *C9orf72* mRNA levels in patient cerebellum (fig. S1B). However, both sense and antisense transcripts containing intron 1 (where the GGGGCC repeat is located) were strongly increased in *C9orf72* patients (fig. S1C). This suggests a selective stabilization of repeat containing pre-mRNA (or the excised intron 1 alone) and raises the possibility that the antisense strand may be translated into poly-(Pro-Arg), poly-(Ala-Pro) and further poly-GP DPR proteins.

To determine the cellular distribution patterns of these DPR proteins in patients with pathological *C9orf72* repeat expansion, we focused on the cerebellum and hippocampus in the immunohistochemical analysis because these brain regions contain abundant inclusion pathology positive for p62 but negative for phospho-TDP-43 (9–11) (Fig. 2, A and B, and fig. S2A). In all patients with *C9orf72* mutation, poly-GA-specific antibodies detected dotlike neuronal cytoplasmic inclusions in the granular cell layer of the cerebellum (Fig. 2C and fig. S2B). Their shape and abundance were similar to the p62-positive/TDP-43-negative inclusions considered to be pathognomonic for *C9orf72* mutation patients.

Fig. 1. Extended GGGGCC repeats are translated into aggregating DPR proteins. (A) Validation of DPR-specific affinity-purified antibodies by immunoblotting with purified GST-fusion proteins containing (GA)₁₅, (GP)₁₅, or (GR)₁₅. **(B)** GGGGCC-repeat constructs with indicated repeat length lacking an upstream ATG were transfected into HEK293 cells. Restriction digest to estimate the repeat length of the transfected constructs (upper panel). Immunoblots show length-dependent expression of poly-GA and poly-GP proteins. Poly-GA products were detectable starting from ~38 repeats (arrow). Asterisk indicates nonspecific band. Poly-GR products were not detected (not shown). **(C)** Filter trap assay from patient cerebellum (table S1). Triton-X100 insoluble fractions were re-suspended in 2% SDS and filtered through cellulose acetate membranes, and retained proteins were detected with the indicated antibodies. **(D)** The SDS-insoluble fraction from (C) was boiled in 4x Laemmli buffer (containing 8% SDS) and analyzed by immunoblotting. Arrows mark the top of the gel. Single-letter abbreviations for the amino acid residues are as follows: A, Ala; C, Cys; D, Asp; E, Glu; F, Phe; G, Gly; H, His; I, Ile; K, Lys; L, Leu; M, Met; N, Asn; P, Pro; Q, Gln; R, Arg; S, Ser; T, Thr; V, Val; W, Trp; and Y, Tyr.



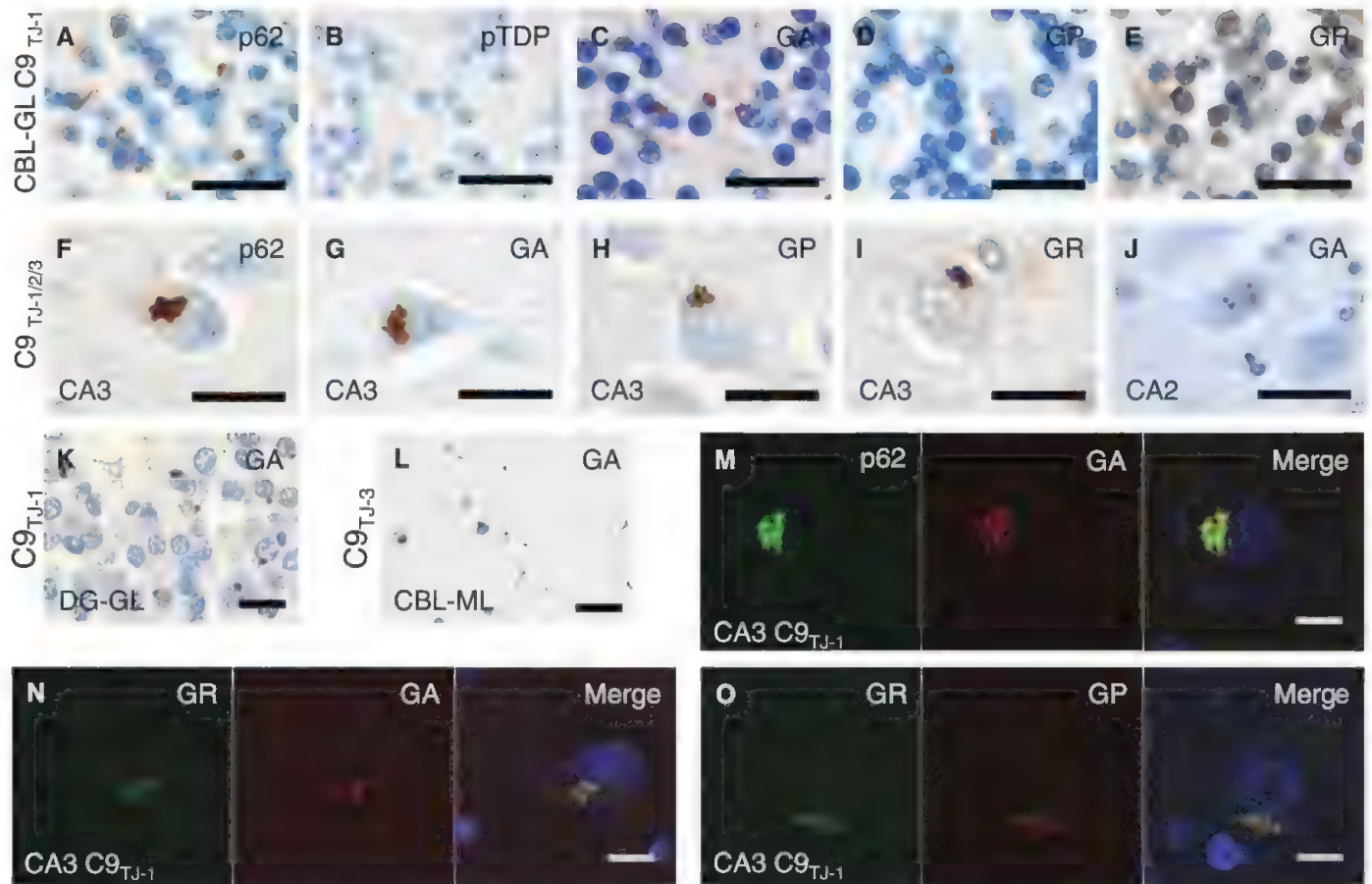
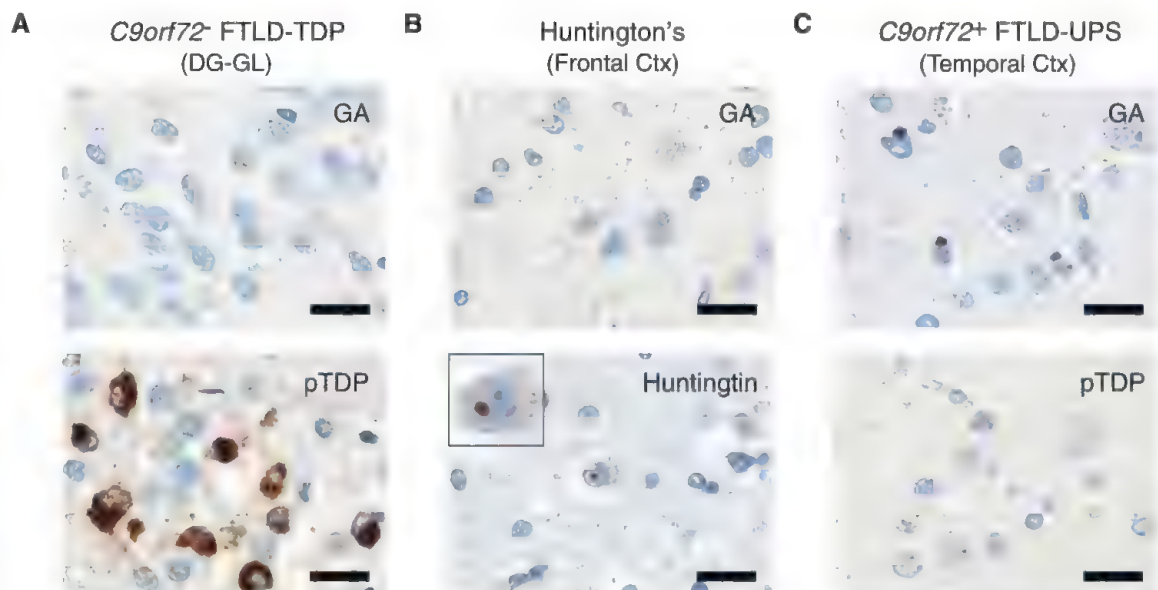


Fig. 2. DPR proteins form the characteristic TDP-43-negative inclusions in *C9orf72* patients. Immunohistochemistry with affinity-purified DPR-specific antibodies (GA, GP, and GR) reveals poly-GA, poly-GP, and poly-GR inclusions resembling the p62-positive aggregates in FTLD/ALS patients with *C9orf72* mutation (compare table S1). Dotlike and threadlike inclusions in cerebellar granular layer (CBL-GL) (A to E). Star-shaped cytoplasmic (F to I) and dot-like intranuclear (J) inclusions in hippocampal cornu ammonis regions 2 and 3 (CA2 and CA3). Inclusion of mixed morphology in dentate gyrus granular layer (DG-GL) and cerebellar molecular layer (CBL-ML) (K and

L). In patients and controls, poly-GR antibodies additionally showed faint nuclear and cytoplasmic staining. Scale bars, 20 μ m. Anti-GA and anti-GP specificity was confirmed by preincubation experiments with recombinant antigens (fig. S3, A to F). Validation of anti-GR was only possible by immunoblot experiments (Fig. 1A) because the poly-GR antigen itself bound to the tissue directly (fig. S3, G to K). (M to O) Double immunofluorescence reveals composition of DPR aggregates in *C9orf72* FTLD/ALS patient TJ-1. No colocalization of DPR proteins was observed with phospho-TDP-43 (fig. S4). Scale bars, 10 μ m.

Fig. 3. DPR pathology is specific to patients with *C9orf72* hexanucleotide repeat expansion. (A and B) Immunohistochemistry with poly-GA-specific antibodies (GA) detects no aggregates in an FTLD-TDP patient (TJ-13) without *C9orf72* repeat expansion and a case with Huntington's disease (TJ-11). Phospho-TDP-43 and Huntingtin inclusions are readily detectable. Granular layer of dentate gyrus (DG-GL) and frontal cortex, respectively. (C) Poly-GA-positive inclusions, but no phospho-TDP-43 inclusions, in temporal cortex of patient TJ-10 with *C9orf72* mutation diagnosed with FTLD-UPS (6). Scale bars, 20 μ m.



Furthermore, these types of inclusions were also detected by antibodies against poly-GP and poly-GR, however to a much lesser extent (Fig. 2, D and E, and fig. S2, C and D). In the hippocampus, most inclusions stained by the three DPR antibodies resembled the p62-positive star-shaped inclusions typical for *C9orf72* mutation patients (Fig. 2, F to I, and fig. S3). As reported for p62 stainings (9, 11), we also observed some DPR-positive neuronal intranuclear inclusions (Fig. 2J). Their relation to the RNA foci described previously remains to be determined (4). Similar DPR pathology was visible in other brain regions, including the granular layer of the dentate gyrus and the molecular layer of the cerebellum and neocortex (Fig. 2, K and L, and table S1).

We next analyzed whether the DPR-positive aggregates are identical to the p62-positive and phospho-TDP-43-negative aggregates. In hippocampal sections of a *C9orf72* mutation patient, poly-GA, poly-GP, and poly-GR colocalized with p62 in the characteristic starlike inclusions (Fig. 2, M to O, and fig. S4, D and E). However, there was no coaggregation of phospho-TDP-43 and DPR proteins (fig. S4, A to C). Occasionally, small spheric poly-GA aggregates were surrounded by aggregated phospho-TDP-43, forming a core inside phospho-TDP-43 inclusions (fig. S4F), which suggests that DPR aggregation may precede TDP-43 pathology. Quantitative analysis confirmed extensive colocalization of p62-positive inclusions with poly-GA aggregates and, to a lesser extent, with poly-GP and poly-GR (fig. S4G).

Consistent with the filter trap assay (Fig. 1C), such poly-GA aggregates were not detectable in FTLT-DTP patients without *C9orf72* mutation or with Huntington's disease, which features expanded poly-Q stretches (Fig. 3, A and B). In total, we identified poly-GA, poly-GP, and poly-GR aggregates in all 10 patients with a confirmed pathological *C9orf72* repeat expansion but not in 12 other cases with normal repeat length (table S1).

Some patients with *C9orf72* mutation show remarkably few phospho-TDP-43 inclusions throughout the brain. So far, only a single exceptional patient (TJ-10)—classified as FTLT-DTP (ubiquitin pro-

teasome system), with *C9orf72* mutation and prominent ubiquitin-pathology but without detectable TDP-43 pathology—has been reported (6, 7). We found abundant poly-GA and some poly-GP and poly-GR aggregates in the temporal cortex of this patient (Fig. 3C and table S1), suggesting that DPR proteins are crucial for FTLT pathogenesis in this case. Thus, we propose that poly-GA is the main aggregating species in FTLT-DTP patients with *C9orf72* repeat expansion.

Here, we have shown that non-ATG-initiated translation of the intronic GGGGCC-repeat expansion in FTLT/ALS patients leads to accumulation of insoluble DPR aggregates. In addition to DPR and TDP-43 pathology, the *C9orf72* expansion may lead to haploinsufficiency and trigger sequestration of GGGGCC-binding proteins. Such interacting proteins may even support nuclear export of the repeat RNA or its translation.

Ample evidence suggests a pathogenic role of DPR inclusions in FTLT patients with *C9orf72* hexanucleotide repeat expansion. First, DPR pathology is predominant in clinically relevant brain regions (hippocampus and frontotemporal neocortex) and may precede TDP-43 pathology. Second, *C9orf72* patients show cerebellar atrophy that does not occur in the other FTLT/ALS variants lacking cerebellar DPR inclusions (10, 12). Third, at least one *C9orf72* mutation carrier had abundant DPR pathology and behavioral-variant clinical FTLT but no detectable TDP-43 inclusion pathology. Finally, DPR pathology is a direct consequence of the pathological hexanucleotide repeat expansion, the most common genetic cause of FTLT/ALS. We therefore suggest the acronym FTLT/ALS-DPR to pathologically classify these patients in a revised nomenclature.

References and Notes

1. K. A. Josephs et al., *Acta Neuropathol.* **122**, 137 (2011).
2. I. R. Mackenzie, R. Rademakers, M. Neumann, *Lancet Neurol.* **9**, 995 (2010).
3. R. Rademakers, M. Neumann, I. R. Mackenzie, *Nat. Rev. Neurol.* **8**, 423 (2012).
4. M. DeJesus-Hernandez et al., *Neuron* **72**, 245 (2011).
5. A. E. Renton et al., *Neuron* **72**, 257 (2011).
6. I. Gijssels et al., *Lancet Neurol.* **11**, 54 (2012).
7. J. van der Zee et al., *Hum. Mutat.* **34**, 363 (2013).
8. A. L. Boxer et al., *J. Neurol. Neurosurg. Psychiatry* **82**, 196 (2011).

9. S. Al-Sarraj et al., *Acta Neuropathol.* **122**, 691 (2011).
10. C. J. Mahoney et al., *Brain* **135**, 736 (2012).
11. E. H. Bigio et al., *Neuropathology* (2012); 10.1111/j.1440-1789.2012.01332.x.
12. J. L. Whitwell et al., *Brain* **135**, 794 (2012).
13. I. P. Ivanov, A. E. Firth, A. M. Michel, J. F. Atkins, P. V. Baranov, *Nucleic Acids Res.* **39**, 4220 (2011).
14. D. S. Peabody, *J. Biol. Chem.* **264**, 5031 (1989).
15. C. Touriol et al., *Biol. Cell* **95**, 169 (2003).
16. T. Zu et al., *Proc. Natl. Acad. Sci. U.S.A.* **108**, 260 (2011).
17. C. E. Pearson, *PLoS Genet.* **7**, e1002018 (2011).
18. M. L. Moseley et al., *Nat. Genet.* **38**, 758 (2006).
19. E. Kremmer et al., *Virology* **208**, 336 (1995).
20. H. Li, T. Wyman, Z. X. Yu, S. H. Li, X. J. Li, *Hum. Mol. Genet.* **12**, 2021 (2003).

Acknowledgments: We thank I. Pigur for technical assistance, M. Neumann for genotyping of some of the LMU cases, and J. Banzhaf-Strathmann, F. van Bebber, E. Bentmann, D. Dormann, J. Herms, A. Hruscha, G. Kleinberger, J. McCarter, D. Orozco, and B. Schwenk for critical comments. This project was supported by a grant from the Centres of Excellence in Neurodegeneration Research (CoEN) to M.C., C.H., C.V.B., B.S., and D.E., and the Competence Network for Neurodegenerative Diseases (KNDD) of the Bundesministerium für Bildung und Forschung (BMBF) to C.H. K.M. was supported by a postdoctoral fellowship from the Alexander von Humboldt Foundation. D.E. was supported by the Helmholtz Young Investigator program. We thank all clinicians recruiting brain donors, in particular H.-H. Klünemann (Bezirksklinikum Regensburg) and, most notably, all brain donors and their next of kin. We acknowledge the Antwerp biobank of the Institute Born-Bunge for brain samples, as well as T. Van Langenhove, J. van der Zee, S. Engelborghs, P. P. De Deyn, A. Sieben, and J.-J. Martin for genetic, clinical, and pathological diagnoses. The Antwerp site is supported by the MetLife Foundation Award (to C.V.B.), the Belgian Science Policy Office Interuniversity Attraction Poles program, the Foundation for Alzheimer Research (SAO/FRA), the Medical Foundation Queen Elisabeth, the Flemish Government Methusalem excellence program, the Research Foundation Flanders (FWO), and the University Research Fund of the University of Antwerp. A patent application concerning DPR-based diagnosis and therapy of neurodegenerative disorders has been filed by K.M., S.-M.W., T.A., K.R., E.K., C.H., and D.E.

Supplementary Materials

www.sciencemag.org/cgi/content/full/science.1232927/DC1
Materials and Methods
Supplementary Text
Figs. S1 to S4
Table S1
References (21, 22)

19 November 2012; accepted 25 January 2013
Published online 7 February 2013;
10.1126/science.1232927

HANDHELD PIPETTING SYSTEM

Designed to enable labs to process samples simply and productively, the VIAFLO 384 is a new handheld 384-channel electronic pipette that enables fast, precise, and easy transfer of 384 samples simultaneously. Uniquely, the VIAFLO 384 offers all the benefits of increased sample throughput as well as lower sample and reagent use without the expense of having to invest in a robotic liquid handling system. The compact VIAFLO 384 comes with a choice of two 384-channel pipetting heads, which cover the volume ranges of 0.5–12.5 μ L and 5–125 μ L. The new system is fully compatible with VIAFLO 96-channel pipetting heads enabling easy switching between 96-channel and 384-channel pipetting using the same unit. The VIAFLO 384 features the company's popular Touch Wheel pipette user interface for simple and fast programming of a wide range of pipetting modes including repeat dispense, serial dilute, and mixing routines.

Integra Biosciences

For info: +41-(0)-81-286-95-30 | www.integra-biosciences.com

**LIGHT-SENSITIVE SAMPLE PROTECTION**

To protect light-sensitive samples, a selection of high-quality black microplates and seals are offered that eliminate sample degradation, even over long storage periods. Manufactured from ultrapure grade polypropylene, Porvair black microplates are resistant to a wide range of solvents and have near-zero leachates, ensuring long-term sample integrity. The black plates are supplied RNase/DNase free meaning they can be used with even the most sensitive biological samples. Available in a choice of 96-well formats, these plates are precisely manufactured to applicable ANSI/SLAS dimensions ensuring complete compatibility with almost all readers and automated equipment. To prevent evaporation and hydration of DMSO solutions and to completely eliminate light from samples, a choice of black light-absorbing sealing films, which can be applied to the top of the black plates, are also available.

Porvair Sciences

For info: +44-(0)-1372-824290 | www.porvair-sciences.com

TUBE DECAPPER

The Univo Electric Decapper DC480 enables researchers tasked with opening multiple sample storage tubes to achieve significant productivity gains. The Univo Electric Decapper DC480 is not only compatible with all Micronic tubes (up to 1.40 mL) but also with tubes and caps of other brands. Through an improved user interface the operator is able to select any rack to decap, without using different adapters for different tube sizes or brands. Easy to install and operate, the compact Univo Electric Decapper DC480 removes and disposes of the push caps from a full 96-tube storage rack in eight seconds. Operation is safe and user friendly: simply place a rack of capped tubes onto the access tray, push the start button, and the Univo Electric Decapper DC480 will gently remove all the caps in one action. The integrated cap disposal device ensures that caps cannot be reused. The decapper can be used as a stand-alone instrument or be simply integrated into a fully automated laboratory environment.

Micronic

For info: +31-320-277070 | www.micronic.com

AUTOMATED INCUBATOR

The new Cytomat 10 is a fully automated incubator and storage module for high-capacity cell growth and assay incubation. Designed to fit into the busiest of cell biology or screening laboratories, the Cytomat 10 offers superior environmental control and can be seamlessly integrated with existing automated assay hardware. The Cytomat 10 provides a fast plate access time of less than 10 seconds. Additionally, multiple transfer positions and an under-bench version allow flexible incubator placement within the laboratory. As the first generation of automated incubator with a fully validated thermal decontamination system, the Cytomat 10 is designed to significantly decrease the risk of contamination and reduce assay variability. An efficient thermal disinfection method practically eliminates germs and spore suspensions, even in areas that are difficult to reach via manual cleaning.

Thermo Fisher Scientific

For info: 905-332-2000 | www.thermoscientific.com/automate

MICROPIPETTES

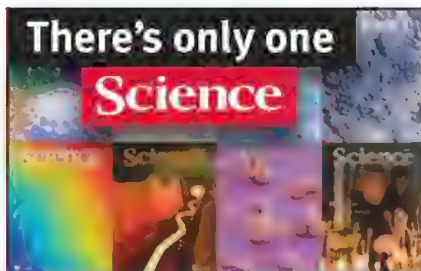
A new range of micropipettes are designed to provide optimal ease of use and assure a high level of user comfort during operation, minimizing the risk of repetitive strain injury. Integral to the design of the variable volume pipette is an innovative soft grip and safety device on the thumb-controlled plunger. This feature prevents accidental volume changes during use, facilitating maximum precision and accuracy. The universal two-step plunger allows reverse pipette techniques to be performed and enables last drop dispensing. The micropipettes may be safely autoclaved at 120°C and 1.05 bar/15 psi for 15 minutes. Maintenance and adjustment are simple procedures as the user can readily recalibrate the micropipette with the adjustment tool supplied. There are eight variable models covering volume ranges from 0.1–5,000 μ L. A further 14 fixed volume models compliment the range covering 5–10,000 μ L and four or six position bench racks are available for easy storage.

Medline Scientific

For info: +44-(0)-1865-400321 | www.medlinescientific.com

Electronically submit your new product description or product literature information! Go to www.sciencemag.org/products/newproducts.dtl for more information.

Newly offered instrumentation, apparatus, and laboratory materials of interest to researchers in all disciplines in academic, industrial, and governmental organizations are featured in this space. Emphasis is given to purpose, chief characteristics, and availability of products and materials. Endorsement by *Science* or AAAS of any products or materials mentioned is not implied. Additional information may be obtained from the manufacturer or supplier.



Science Careers Advertising

For full advertising details, go to ScienceCareers.org and click For Employers, or call one of our representatives.

Tracy Holmes

Worldwide Associate Director
Science Careers
Phone: +44 (0) 1223 326525

THE AMERICAS

E-mail: advertise@sciencecareers.org
Fax: 202-289-6742

Tina Burks

United States/Canada/South America
Phone: 202-326-6577

Marci Gallun

Sales Administrator
Phone: 202-326-6582

Online Job Posting Questions

Phone: 202-312-6375

EUROPE / INDIA / AUSTRALIA / NEW ZEALAND / REST OF WORLD

E-mail: ads@science-int.co.uk
Fax: +44 (0) 1223 326532

Lucy Nelson

Phone: +44 (0)1223 326527

Kelly Grace

Phone: +44 (0) 1223 326528

JAPAN

Yuri Kobayashi

Phone: +81-(0)90-9110-1719
E-mail: ykobayas@aaas.org

CHINA / KOREA / SINGAPORE / TAIWAN / THAILAND

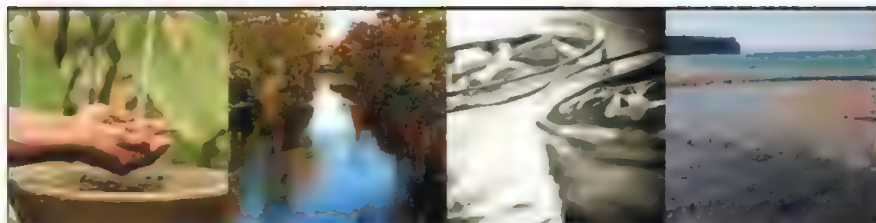
Ruolei Wu

Phone: +86-1367-1015-294
E-mail: rwu@aaas.org

All ads submitted for publication must comply with applicable U.S. and non-U.S. laws. *Science* reserves the right to refuse any advertisement at its sole discretion for any reason, including without limitation for offensive language or inappropriate content, and all advertising is subject to publisher approval. *Science* encourages our readers to alert us to any ads that they feel may be discriminatory or offensive.



ScienceCareers.org



Michigan State University Global Water Initiative Cluster Hire

Michigan State University announces the MSU Global Water Initiative, an effort to integrate and expand research expertise across the university and address the world's most compelling water issues. With more than 100 faculty working in water-related fields, the university has expertise spanning the natural, social, and engineering sciences. MSU's portfolio of external grants in water has grown over the past five years to \$86 million. MSU is committed to conducting research of the highest caliber, creating solutions, and expanding human understanding of the challenges related to water.

Over the next three years, the MSU Global Water Initiative will coordinate recruitment of 16 new faculty positions in the Colleges of Natural Science, Agriculture and Natural Resources, Social Science, and Engineering. Areas of interest for the cluster hire include, but are not limited to:

- Integrated Risk Analysis and Critical Decision Making
- Spatial and Social Dimensions of Water
- Water and Health
- Ecohydrology and Water Resource Engineering
- Aquatic Ecosystem Services

The new hires will collaborate with current faculty to enhance disciplinary expertise, strengthen linkages across disciplines, and create new advances in water science, technology, and policy. In seeking candidates at both junior and senior levels, MSU is focused on research excellence, global perspective, and leadership in interdisciplinary, collaborative approaches. Searches are under way for a Hannah Chair in Engineering and five positions in the College of Natural Science. Currently open positions include:

- Water Resources Economist: economic research to help inform public policy and decision making related to water resources. Open rank, Department of Economics and the Environmental Science and Policy Program
- Medical/Health Geographer: international health and infectious diseases. Assistant/Associate Professor, Department of Geography and Environmental Science and Policy Program
- Political Scientist: international relations, comparative politics, American politics or public policy related to water issues. Department of Political Science and Environmental Science and Policy Program

Potential applicants for these and future positions are directed to MSU Global Water Initiative website, water.msu.edu, which contains detailed information and will be updated regularly.

All applications must be submitted through the MSU Applicant Page website at jobs.msu.edu.

MICHIGAN STATE
UNIVERSITY

The Institute of Agriculture and Natural Resources (IANR) at the University of Nebraska-Lincoln (UNL) is seeking applicants to fill three tenure track faculty positions, which are directed to human health and well being in the areas of food safety, lipid chemistry and metabolic processes. These academic-year, state-funded positions are part of the strategic plans of IANR directed to expand world-class excellence in applications of agricultural and life sciences towards a sustained high quality of life. The university has state-of-the-art core facilities in food processing, proteomics and metabolomics, genomics, crystallography, bioimaging, flow cytometry, bioinformatics, biophysical spectroscopy, and trace elemental analysis. Opportunities exist for successful applicants to develop and participate in interdisciplinary research, teaching and extension programs addressing the mission of IANR and UNL.

Each position is at the Assistant Professor or advanced Assistant Professor level. It is expected that the individuals selected will have or establish nationally recognized and extramurally funded research programs (from the National Institutes of Health, National Science Foundation, and/or National Institute of Food and Agriculture) and possess a talent for teaching and/or extension programming.

Food Safety Risk Assessment (#F_130068). Will lead research activities aimed at the development and application of quantitative risk assessment methods applied particularly to various food safety issues including but not limited to food safety microbiology, food processing and engineering, food toxicology, and food biotechnology. The candidate should have a strong background in application of quantitative risk assessment to issues in epidemiology, human health, toxicology, food safety, food allergy and/or other similar fields of science and should have the ability to convey results from their research to the food industry. The incumbent will be expected to develop on-campus and distance learning courses and training programs to assist food processors and the food and agricultural biotechnology industry on risk analysis/assessments. Ph.D. or equivalent degree in food science, food engineering, mathematics, statistics, or a related discipline is required. Degree must be completed before employment begins.

Lipid Chemistry and Functionality (F_130075). Will lead research activities aimed at improving of the inclusion of functional lipids into foods and maximizing product quality and health effects. Research expertise is required in product functionality, food composition, lipid bioavailability, and biotransformation (i.e. lipidomics) as it pertains to raw materials, food product development, and lipid based nutraceuticals. Teaching expectations will include on-campus and distance learning in areas of food-lipid chemistry and lipid-processing technologies and undergraduate or graduate courses in food chemistry. Ph.D. or equivalent in Food Chemistry, Biochemistry, Chemistry, Nutrition Sciences or a closely related field is required. Degree must be completed prior to employment.

Lipid Metabolism and Health (F_130081). Will lead a nationally recognized research program focused at the interface between dietary lipids, metabolism and health outcomes, with emphasis on obesity-related metabolic diseases. Research expertise in cell differentiation, adipocyte biology, gene regulation, lipidomics/metabolomics, and/or cell signaling is preferred. Teaching expectations include courses in nutrient metabolism and/or nutrient/gene regulation. A Ph.D. or M.D. or equivalent degree in nutrition, biochemistry, food science, biology, or related field is required before employment begins.

Each position comes with highly competitive start-up packages. Lincoln Nebraska is a 2012 Top 10 College Town and boasts an outstanding quality of life that includes fine culinary and artistic treasures, a budding live music scene, and extensive parks, golf courses and bike trails. Applicants should go to <http://employment.unl.edu>, search for the position number noted above. Click on "Apply to this job." Complete application. Attach documents as identified in the position posting. Review of applications will begin on the date identified in the position posting and continue until the positions are filled or the searches are closed.

The University of Nebraska has an active National Science Foundation ADVANCE gender equity program, and is committed to a pluralistic campus community through Affirmative Action, Equal Opportunity, work-life balance, and dual careers.

CANADA EXCELLENCE RESEARCH CHAIR IN GEOFLUIDS IN SEDIMENTARY BASINS

Department of Geological Sciences and Geological Engineering
Faculty of Arts and Science and Faculty of Engineering and
Applied Science

One of Canada's leading universities, Queen's has a long-standing reputation for academic excellence, research, and a diverse and vibrant learning environment. With its strong tradition of public service, the University has helped to shape Canadian values and policies, educating notable political and cultural figures.

Queen's University is located in the heart of the community in historic Kingston, midpoint between Montreal, Toronto, and the nation's capital.

Queen's University is seeking an outstanding individual to take up a Canada Excellence Research Chair in GeoFluids in Sedimentary Basins. The CERC will be awarded to a world leading researcher, with selection based on the highest standards of research excellence. The CERC program dedicates \$10 million over seven years to each chair holder and his/her research team, to support the pursuit of excellence in research (www.cerc.gc.ca/hp-pa-eng.shtml). In addition, the incumbent will be provided with the opportunity to make an application to the Canada Foundation for Innovation (CFI) program (www.innovation.ca).

The CERC holder will complement existing strengths by examining the details of fluid-rock interactions on all scales, from modeling large scale fluid flow in (hydrocarbon-bearing) sedimentary basins, to the origin and character of both mineralizing and barren fluids associated with energy-related commodities, to the pressure and chemical evolution of strata-bound fluids during earth history and into the future, to geochemical interactions between fluids and both natural and engineered materials. The Chair holder would focus on one, or both, of two major themes: (1) Energy and Mineral Resources (fluid evolution of sedimentary basins that potentially host petroleum and mineral deposits and exploration for buried deposits in basins); (2) Protecting and Managing the Environment (assessing element cycles in the environment that involve basins on all scales, or evaluating factors that affect waste disposal in sedimentary basins).

The successful candidate will be required to maintain a leading-edge research program, take a leading role in developing the GeoFluids program at Queen's, actively engage with industry, supervise graduate students, teach undergraduate and graduate courses, and make administrative contributions through service to the University, Faculty, and Department. Candidates must hold a relevant Ph.D. degree and have a demonstrated excellence in research, teaching and training of highly qualified personnel. Established research collaborations with industry and engagement in public policy will be considered an asset. Registration as a Professional Geoscientist or as a Professional Engineer in Ontario, or eligibility to acquire registration in Ontario is strongly encouraged.

Interested applicants are directed to the full details of the advertisement at: www.queensu.ca/geol/departement/employment.html

Applicants should send their curriculum vitae, contact information, the names of three referees including their contact information, along with a statement of research and teaching interests, and three examples of relevant publications to:

Dr. Cynthia Fekken, Chair, CERC GeoFluids Appointment Committee
Associate Vice-Principal (Research), Office of the Vice-Principal (Research)
251 Richardson Hall, Queen's University, Kingston, ON, Canada K7L 3N6
By email: fekken@queensu.ca

Review of applications will begin on April 1st, 2013. Applications will be accepted until the position is filled.

The University invites applications from all qualified individuals. Queen's is committed to employment equity and diversity in the workplace and welcomes applications from women, visible minorities, aboriginal people, persons with disabilities, and persons of any sexual orientation or gender identity. All qualified candidates are encouraged to apply; however, Canadian citizens and permanent residents of Canada will be given priority. The academic staff at Queen's is governed by a collective agreement between QUFA and the University, which is posted at www.qufa.ca.

www.hr.queensu.ca

Science Careers is the forum that answers questions.



Science Careers is dedicated to opening new doors and answering questions on career topics that matter to you. With timely feedback and a community atmosphere, our careers forum allows you to connect with colleagues and experts to get the advice and guidance you seek as you pursue your career goals.

Science Careers Forum:

- » Relevant Career Topics
- » Timely Advice and Answers
- » Community, Connections, and More!

Visit the forum and join the conversation today!



Your Future Awaits.



ScienceCareers.org

THE GEORGE
WASHINGTON
UNIVERSITY
WASHINGTON DC

Faculty Positions in Computational Biology and Bioinformatics

The newly established Computational Biology Institute at the George Washington University seeks founding faculty members to establish vibrant, interdisciplinary and externally funded research programs in bioinformatics and/or computational biology. We have five open faculty positions at all academic levels and seek applicants especially in the areas of biodiversity informatics, translational medicine, and systems biology developing methods to address 'big data' issues from a computational perspective. Candidates are expected to establish an extramurally funded and internationally recognized research program.

Basic Qualifications: Applicants must have an MD and/or PhD in Bioinformatics, Computational Biology, Computer Science, Mathematics, Genomics, or related discipline with postdoctoral research experience, granting experience, and a solid publication track record. Successful candidates will enjoy joint appointments at the CBI and an academic department of their choosing (e.g., Biological Sciences, Computer Science, Mathematics, Biochemistry, Integrated Systems Biology, etc.) upon approval, and have opportunities to establish partnerships with regional research centers of excellence, including Children's National Medical Center, NIST, Janelia Farm, INOVA hospital system, Naval Research Laboratory, the Smithsonian, and the NIH intramural research program. Rank and contractual status, will be based on experience.

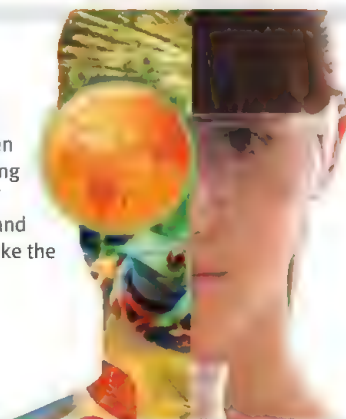
Application Procedure: Applicants should submit an electronic application, and upload a cover letter emphasizing specific qualifications, a curriculum vitae, a description of research interests, and names and contact information of 3 references at: <http://www.gwu.jobs/postings/14121>

Review of applications will begin on **April 15, 2013** and will continue until positions are filled. Only complete applications will be considered. For further information about the Computational Biology Institute at George Washington University, please see <http://cbi.gwu.edu>. For questions relating to this opportunity, please contact **Keith Crandall, Director, Computational Biology Institute, The George Washington University**, kcrandall@gwu.edu.

The George Washington University is an Equal Opportunity/Affirmative Action Employer and seeks to attract an active, culturally and academically diverse faculty of the highest caliber.

WOMEN IN SCIENCE forging new pathways in green science

Read inspiring stories of women working in "Green Science" who are blending a unique combination of enthusiasm for science and concern for others to make the world a better place.



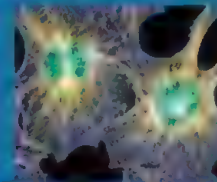
Download this free booklet
ScienceCareers.org/L'OrealWiS



This booklet is brought to you by the AAAS/Science Business Office in partnership with the L'Oreal Foundation

Associate Director for Data Science

Office of the Director, National Institutes of Health, Department of Health and Human Services



The NIH is the center of medical and behavioral research for the Nation

---making essential medical discoveries that improve health and save lives.

Are you a top-level Scientific Researcher or Scientific Administrator seeking a career at one of the preeminent biomedical research institutions in the Nation and the world? Are you at that point in your career where you're ready to "give back?" The position of Associate Director for Data Science (ADDS), Office of the Director (OD), National Institutes of Health (NIH), offers a unique and exciting opportunity to provide critical leadership for basic and translational research. The era of "Big Data" has arrived for the biomedical sciences. There is an urgent need and, with it, spectacular opportunities for NIH to enhance its programs in data science, such as those involving data emanating from different sources (e.g., genomics, imaging, and phenotypic information from electronic health records). The ADDS provides a vision for the utilization and extraction of knowledge from the data generated by, and relevant to, NIH research, and advises experts throughout the agency on a variety of complex, unique, and/or sensitive situations and issues in data science to ensure continual achievement of NIH's dynamic biomedical research mission.

We are looking for applicants with senior-level experience who have a commitment to excellence and the energy, enthusiasm, and innovative thinking necessary to lead a dynamic and diverse organization.

The successful candidate for this position will be appointed at a salary commensurate with his/her qualifications. Full Federal benefits will be provided including leave, health and life insurance, long-term care insurance, retirement, and savings plan (401k equivalent).

If you are ready for an exciting leadership opportunity, please see the detailed vacancy announcement at <http://www.jobs.nih.gov> (under Executive Careers). Applications will be reviewed starting May 13, 2013, and will be accepted until the position is filled.



**THE NATIONAL INSTITUTES OF HEALTH AND THE DEPARTMENT OF HEALTH AND HUMAN SERVICES
ARE EQUAL OPPORTUNITY EMPLOYERS**



Group leader position in bioinformatics

The Institute of genetic diseases *Imagine* at Necker Enfants-Malades Hospital, in Paris, is inviting applications for one group leader position in bioinformatics, computational biology, and/or statistical genetics.

imagine
INSTITUT DES MALADIES GÉNÉTIQUES

Imagine is an interdisciplinary research center in molecular medicine in the Necker Enfants-Malades University Hospital campus. *Imagine* has a new home which will open in 2013 in the heart of the left bank of Paris, and offer cutting-edge research facilities. *Imagine* has recently been designated as an "Institut Hospitalo-Universitaire", and is supported by a Foundation with a focus on rare diseases, their biology and their life-long outcomes to address unmet basic and clinical research questions. We expect this research to result in the development of new biological concepts, diagnostic tools, and innovative therapeutics. The Institute is currently composed of 250 members in 20 laboratories working in a variety of genetic disorders and systems.

Imagine has excellent core facilities in genomics, bioinformatics, cell imaging, flow cytometry, pathology, and animal housing. The current bioinformatics platform comprises 6 engineers and computer analysts, and additional recruitments are ongoing. The platform has already developed a number of tools to analyze high-throughput genotyping, sequencing, and transcriptomic data.

Imagine is now committed to further develop this domain of expertise by attracting one new research group with outstanding track record in the development, implementation, and application of innovative methods to analyze high dimensional data. This research group will closely interact with the *Imagine* laboratories and will have privileged access to a wide range of unique data. Applications can focus on any field related to bioinformatics, computational biology and/or statistical genetics, with a special emphasis on those that may offer strong opportunities of synergy with the present *Imagine* laboratories. Applications can be proposed at the level of either junior or senior group leader.

Applications should be submitted to Alain Fischer at the address below and must include:

- Complete CV including list of publications
- Past and current research interest (2 pages)
- Future research proposals (5 pages)
- At least three letters of recommendation

Address: newgroups@institutimagine.org (www.institutimagine.org)

Applications should be received by **May 15th 2013** at the latest.

There's only one GALILEO GALILEI

Born in 1564, Galileo Galilei once contemplated a career in the priesthood. It's perhaps fortunate for science that upon the urging of his father, he instead decided to enroll at the University of Pisa. His career in science began with medicine and from there he subsequently went on to become a philosopher, physicist, mathematician, and astronomer, for which he is perhaps best known. His astronomical observations and subsequent improvements to telescopes built his reputation as a leading scientist of his time, but also led him to probe subject matter counter to prevailing dogma. His expressed views on the Earth's movement around the sun caused him to be declared suspect of heresy, which for some time led to a ban on the reprinting of his works.

Galileo's career changed science for all of us and he was without doubt a leading light in the scientific revolution, which is perhaps why Albert Einstein called him the father of modern science.

Want to challenge the status quo and make the Earth move? At *Science* we are here to help you in your own scientific career with expert career advice, forums, job postings, and more — all for free. For your career in science, there's only one *Science*. Visit ScienceCareers.org today.



For your career in science, there's only one **Science**

AAAS

ScienceCareers.org

FACULTY POSITIONS AT THE ROCKEFELLER UNIVERSITY

The Rockefeller University seeks exceptional, interactive, and creative scientists to join its faculty. We invite applications from outstanding candidates for tenure-track positions.

The University has a laboratory-based organizational structure that fosters interdisciplinary research. We encourage applications in the following areas:

- Chemical & Structural Biology
- Genetics & Genomics
- Immunology, Virology & Microbiology
- Medical Sciences, Systems Physiology & Human Genetics
- Molecular Cell Biology
- Neurosciences & Behavior
- Organismal Biology, Evolution, Ethology & Ecology
- Physical, Mathematical & Computational Biology
- Stem Cells, Development, Regeneration & Aging

Details about specific subjects of research can be found at:
<http://www.rockefeller.edu/facultysearch>.

The Rockefeller University provides strong support for the research work of its faculty. The positions offer competitive salary, benefits and start-up funds, renovated laboratory space, access to state-of-the-art core facilities and extensive opportunities for collaboration both within the University and with neighboring institutions.

Applications are being accepted electronically through our **Online Application System** at <http://oas.rockefeller.edu>. Applicants should follow the online application procedure.

The deadline for application submission is April 22, 2013.



If you have questions regarding submitting an application, please contact our Administrator at facultysearch@rockefeller.edu.

The Rockefeller University is an Affirmative Action/Equal Opportunity/VEVRAA Employer and solicits applications from women and under-represented minorities.



蘇州大學

SOOCHOW UNIVERSITY

Full Professor and Academic Leader in Radiobiology

The School of Radiation Medicine and Protection (SRMP) and School of Radiological and Interdisciplinary Sciences (RAD-X) of Medical College of Soochow University in Suzhou, China, are seeking outstanding candidates for a position of Full Professor as the academic leader in the research field of radiobiology. The candidates should have demonstrated the distinguished academic leadership and the ability of developing original research programs with external funding.

Successful appointee will be offered an excellent package including sufficient lab space, start-up funding, relocation aid, competitive salary commensurate with experience, and other employee benefits.

Applicants should submit (i) a cover letter summarizing current research projects and future plans, (ii) a curriculum vitae, and (iii) names and contact info of 3 professional referees to: SRMP and RAD-X Search Committee, Soochow University, Dushu Lake Campus, 199 Ren-Ai Road, Industrial Park, Suzhou 215123, China; Email: bxzhu@suda.edu.cn



深圳大學

Opening positions for full-time talents

Shenzhen University (SZU) invites applications for full-time Distinguished Professor and lecturer positions for highly qualified candidates with special expertise in one of the following academic areas.

The University

The university is located in Shenzhen; a big city of over 8 million people in Southern China's Guangdong Province and directly adjacent to Hong Kong. Shenzhen is China's first Special Economic Zone, is well known for its economic, scientific and technological innovation, and is one of China's most advanced and prosperous cities. Shenzhen University was founded in 1983 and has been at the forefront and a central participant in the city's rapid development.

Shenzhen University consists of twenty-six colleges with a total enrollment over thirty-thousand undergraduate and graduate students. The university is highly committed to quality education and applied research across a number of fields important to the future development. We are aggressively seeking highly qualified international scholars to join us as we continue towards our mission of becoming a top-class research institution in China.

Areas of Interest for distinguished professors and lecturers

Economics, Law, Literature, Science, Engineering, Medicine, Management, Art

A. Distinguished professor

Qualifications

1. Candidates must have an earned doctorate in a closely related discipline with a track record of extraordinary accomplishment in teaching, research/scholarship, and professional service, judged by peers to be outstanding;
2. They should have at least associate-professor or above academic experience in world-renowned universities;
3. They should have been recognized nationally or internationally for the importance of their achievements and are expected to bring distinction to SZU and serve as a key contributor to achieving its strategic goal of becoming a World-Class university.
4. They should have strong research capability and great potential to become academic leader whose vision anticipates the development tendency of their field.
5. They should have a strong organizing and communicating ability to lead their research team to reach world-class level.

Salary/Benefits

Salary and benefits are very competitive; yearly salary starting from 100,000 to 200,000 US dollars and will be commensurate with qualifications and experience.

B. Lecturers (equivalent to the rank of Assistant Professor)

Qualifications

1. Candidates must have an earned doctorate in a closely related discipline;
2. Strong ability to conduct independent research and publish on peer-reviewed professional journals;
3. Fluent in communication with working language (Chinese and/or English) for teaching and research;
4. Satisfy the basic requirement on legal residence and work authorization (by the Chinese government) .

Salary/Benefits for Lecturer

Salary and benefits are competitive; and commensurate with qualifications and experience.

C. Scientific research team for Institute of Nanosurface Science and Engineering (INSE)

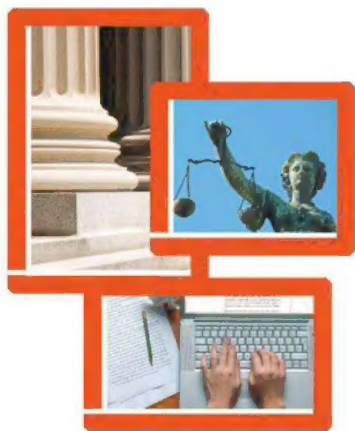
More details please see: <http://szuhr.szu.edu.cn/idxNewsView.asp?nID=166&page=...>

To Apply

1. Interested candidates for distinguished professor and lecturers should submit all application documents to the contacts below or submit all information to <http://szuhr.szu.edu.cn>. For more information please visit <http://www.szu.edu.cn/szu2007/indexe.asp>

Contact: Mr. Ren Qiang (szurse@sina.cn, 0086-755-26535295)
Ms. Yun LI (liyun@szu.edu.cn, 0086-755-26536111)

2. Interested candidates for INSE, please directly contact with Professor Diaoy Dongfeng (dfdiao@szu.edu.cn or dfdiao@mail.xjtu.edu.cn)



Nontraditional Careers: Opportunities Away From the Bench Webinar

Want to learn more about exciting and rewarding careers outside of academic/industrial research? View a roundtable discussion that looks at the various career options open to scientists and strategies you can use to pursue a nonresearch career.

Now Available On Demand
www.sciencecareers.org/webinar

Produced by the
 Science/AAAS Business Office.



POSITIONS OPEN



US DEPARTMENT OF AGRICULTURE Agricultural Research Service

Job Announcement opens March 4, 2013 thru April 12, 2013. Salary: \$68,809.00 to \$147,857.00/year.

The USDA-ARS, is seeking a **RESEARCH SCIENTIST** (Research Microbiologist/Physiologist [GI]) to work at the Arkansas Children's Nutrition Center in Little Rock, Arizona.

For the full Vacancy Advertisement and application requirements, please go to **website: https://www.usajobs.gov/** and use search# **ARS-X13W-0043**.

ASSISTANT/ASSOCIATE PROFESSOR or PROFESSOR

Department of Pharmaceutical Sciences

The College of Pharmacy, Washington State University (WSU) on Riverpoint campus in Spokane, invites applications for a full-time, tenure-track faculty position at the rank of Assistant Professor, Associate Professor, or Professor (commensurate with experience) in the Department of Pharmaceutical Sciences. Applicants must have an advanced degree (M.D., Pharm.D., or Ph.D. in Pharmacology, Pharmaceutical Sciences, or a related discipline) before start of employment. The Assistant Professor candidate must possess a track record of accomplishment to demonstrate the potential to become an outstanding scholar and educator. Associate Professor candidates must possess the a track record of accomplishment demonstrating he/she as an outstanding scholar and educator with an active, nationally recognized, extramurally funded, research program. The Professor candidate must possess the a track record of accomplishment demonstrating he/she is an outstanding scholar and educator with an active, internationally recognized, extramurally funded, research program. Preference will be given to applicants who have a demonstrated ability to teach pharmacology and/or pharmacogenetics at the graduate level. The successful candidate will be expected to maintain an active, extramurally funded research program in the general area of drug discovery, drug delivery, and novel targets, to mentor graduate students and fellows, and to teach in the professional and graduate curricula in topic areas related to Pharmaceutical Sciences.

Screening of applications will begin March 18, 2013 and will continue until a suitable candidate is identified. Applications must include the following materials: (1) A letter of application describing your professional goals, relevant academic preparation, and experience; (2) a current curriculum vitae; and (3) name, title, organization, telephone number, and e-mail address for four people willing to serve as employment references. To apply and see complete position description visit **website: http://www.wsujobs.com**.

WSU is an Equal Opportunity/Affirmative Action/ADA educator and employer.

☒ More scientists agree—we are the most useful website.



www.ScienceCareers.org

POSITIONS OPEN



Two **POSTDOCTORAL** positions are available to investigate the role of Nrf2 downstream Quinone Oxidoreductases (NQO1 and NQO2) in control of p53/p21 and other Growth and Differentiation Factors in prevention of (1) Lung Diseases including Asthma and COPD; and (2) Breast Cancer. These involve studying protein-protein interaction, protein modifications and degradation, apoptosis, cell proliferation, and knockout/transgenic mice disease models. Experience in lung or mammary biology, biochemical and molecular biology techniques and working with mice models is essential. Applicants should submit curriculum vitae, names, addresses, telephone numbers, and e-mail addresses of three references. Contact: **Anil Jaiswal, Ph.D., Professor, Department of Pharmacology, University of Maryland School of Medicine, 655 West Baltimore Street, Baltimore, M.D. 21201 or e-mail: ajaiswal@som.umaryland.edu.**

Your career is our cause.

Get help from the experts.

www.sciencecareers.org

- Job Postings
- Job Alerts
- Resume/CV Database
- Career Advice
- Career Forum



MARKETPLACE

ProMab Biotechnologies, Inc.

Custom Monoclonal Antibody \$3,900

> 3,000 CLONES WILL BE SCREENED

1-866-339-0871

www.ProMab.com | info@promab.com

Faculty Positions at ShanghaiTech University (上海科技大学)

ShanghaiTech University is a newly established research university located at Zhang-Jiang High-Tech Park in Pudong, Shanghai, China. Currently, it has four schools and several advanced research institutes: School of Physical Science and Technology, School of Life Science and Technology, School of Information Science and Technology and School of Entrepreneurship and Management with expected enrollment of 4,000 graduate and 2,000 undergraduate students. The new University is jointly supported by Chinese Academy of Sciences and Shanghai Municipal Government. The vision of ShanghaiTech is to be a globally recognized top research university for its size and profound integration of education, research and innovation by creating a dynamic people centered hub where innovative research, education, and community service meet to provide a multi-disciplinary approach to learning and to solving problems facing society. As a new university, we expect to set up new policies to support an academic environment for best practices of research, teaching and learning. The University will build state of art research and teaching facilities including large research instruments, modern library and classrooms. Our faculty will have the access to the research facilities and resources of Chinese Academy of Sciences. Shared governance will be a part of the campus culture.

We are currently seeking applicants for multiple tenure-track and tenured positions at all ranks.

Initial Research Support Package: University will provide internationally competitive start-up fund plus support of Research Associate and Post-Doctoral fellows. Laboratory space will be provided matching the research needs.

Compensation and Benefits: Salary is competitive and commensurate with experience and academic accomplishments. ShanghaiTech also offers a comprehensive benefit package including housing benefits.

1. School of Physical Science and Technology (SPST)

SPST is established to encourage interdisciplinary research particularly focused on Materials, Environment and Energy. The School is expected to have about 100 regular tenured and tenure-track faculty, 1,200 graduate and 750 undergraduate students.

Qualifications: Successful applicants should have a doctoral degree in Physical Science and Engineering as well as postdoctoral experience for junior level position. They will be expected to establish an independent, internationally recognized research program, to supervise students and to teach two courses a year. The senior position applicant is expected to be leading scientist in his/her research disciplinary. We particularly welcome those with research interests related to Energy, Materials and Environment Science and Engineering to apply.

2. School of Information Science and Technology (SIST)

SIST seeks faculty candidates in all cutting edge areas of information science and technology, with special focus on: advanced futuristic computer architecture and technology, nano-scale electronics, ultra-high speed and low power circuits, intelligent multimedia and integrated signal processing systems, next-generation computer systems, computational foundations, big data, data mining, visualization, computer vision, bio-computing, smart energy devices and systems, highly-scalable and multi-service heterogeneous networking, as well as various inter-disciplinary areas involving the foundation and applications of information science and technology.

Qualifications: Candidates must demonstrate: A strong interest in undergraduate and graduate education; Well-developed research plans and demonstrated strength; Ph.D. (Electrical Engineering, Computer Engineering, Computer Science, or closely related field); A minimum relevant research experience of 4 years.

3. School of Life Science and Technology (SLST)

SLST seeks early career scientists in these five research areas: Protein science and biotechnology; Stem cell research and regenerative medicine; Systems biology and translational medicine; Physical biology and molecular imaging; Chemical biology and innovative pharmacology.

Qualifications: The successful candidates should have an exceptional track record of research in life sciences or a closely related discipline within the last five years. Besides maintaining an active research program, the recruited candidates will also be expected to contribute to the educational missions of undergraduate and graduate programs within SLST.

Application Procedure: Submit a cover letter, a 2-3 page statement of research interests, a CV and the names and addresses of three individuals who can serve as references to the mail addresses given below:

School of Physical Science and Technology

School of Information Science and Technology

School of Life Science and Technology

School of Entrepreneurship and Management

The iHuman Institute

Shanghai Institute for Advanced Immunochemical Studies

SPST@shanghaitech.edu.cn

SIST@shanghaitech.edu.cn

SLST@shanghaitech.edu.cn

SEM@shanghaitech.edu.cn

iHuman@shanghaitech.edu.cn

SIAIS@shanghaitech.edu.cn

4. School of Entrepreneurship and Management (SEM)

SEM provides students with practical knowledge in strategic emerging industries where there is a high demand for commercialization of innovation that advances China's economic development. SEM programs focus on the applied fields of technology innovation management, entrepreneurship and MSE management, as well as venture capital management. SEM offers advanced studies through MBA, EMBA, and EDP programs.

Qualifications: An applicant should possess a doctoral degree in professional studies such as Economics, Finance, or Management. Industry experience is preferred but not necessary. Faculty responsibilities include teaching MBA or EMBA students and conducting applied research often working with companies. SEM especially welcomes applicants with interests related to Innovation, Entrepreneurship, and Venture Capital.

5. The iHuman Institute

The iHuman Institute is established to encourage interdisciplinary research focused on human cell signaling combining chemistry, biology, imaging, and structural biology. Integration of academic basic sciences and applied sciences with industry will be integrated together providing all researchers with unique scientific opportunities.

Qualifications: Successful applicants should have a doctoral degree in Physical or Life Sciences as well as postdoctoral experience for junior level position. Applicants will be expected to establish an independent, internationally recognized research program and supervise students. The senior position applicants are expected to be leading scientists in his/her research disciplinary. We particularly welcome those with research interests related to chemical biology and bioinformatics to apply.

6. Shanghai Institute for Advanced Immunochemical Studies (SIAIS)

SIAIS focuses on elucidating the most fundamental problems in life science research, particularly in immunochemistry. We are seeking highly motivated and outstanding candidates with strong interests in antibody design and engineering, antibody assay method and platform technology, antibody therapeutics, structural biochemistry, and translational medical research.

Qualifications: Qualified candidates should possess a doctoral degree in physical or life science with successful track records in academia and pharmaceutical industry. SIAIS particularly welcomes those with research interests that emphasize innovation and transformation.

ShanghaiTech University, Building 2, 319 Yueyang Road, Shanghai 200031, China

Review of applications will start immediately and will continue until positions are filled.

For more information, please visit our website: www.shanghaitech.edu.cn